Numerical Simulations of Neutron Star Mergers as the Central Engines of Short-Period Gamma-Ray Bursts

Richard Andrew Archibald

Doctor of Philosophy
University of Edinburgh
2008

Abstract

We present the results of fully three dimensional, post-Newtonian hydrodynamical simulations of the dynamical evolution of mergers between compact stellar remnants (neutron stars and black holes). Although the code is essentially Newtonian, we simulate gravitational wave emission and the corresponding effect on the fluid flow via a post-Newtonian correction. Also, we use a modified Newtonian potential which reproduces certain aspects of the Schwarzschild and Kerr solutions to improve the physics in the vicinity of the black hole. Changes to the energy by neutrino/anti-neutrino emission are accounted for by an extensive neutrino leakage scheme. The hydrodynamical equations are integrated using the piecewise parabolic method (PPM) and the neutron star matter is described by a tabulated equation of state (EoS). Since the physics of matter at the extreme densities found in neutron stars is not yet certain, we compare results computed using two such tables to ascertain whether this uncertainty in the micro-physics extends to an uncertainty in the energy available to power a short-period gamma-ray burst.

With an aim to including magnetic field physics to these simulations, we present a survey of approximate Riemann solvers which may be more easily extended to the system of equations of magnetohydrodynamics (MHD) than the exact or iterative Riemann solver used in the PPM scheme. Tests are performed using the linearised solver of Roe and the approximate Harten, Lax, van Leer and Einfeldt Riemann solvers (HLLE and HLLEM) with the PPM reconstruction scheme. Finally, we discuss the effectiveness of these approximate Riemann solvers in the simulation of mergers between compact stellar remnants.

Declaration

I declare that this thesis was composed by myself and that the work contained therein is my own, except where explicitly stated otherwise in the text.

(Richard Archibald)

Acknowledgements

This thesis would not have been possible without the help and support of many people. I would like to express my gratitute to my supervisor, Maximilian Ruffert for his guidance, encouragement and patience during my Ph.D studies. I am indebted to his attention to detail and constructive criticisms while proof reading this thesis. Our weekly meetings were always a great learning experience for me and provided me with fresh ideas and inspiration as well as all the shortbread I could handle!

Thanks to all those who helped to make the weekly "Astro Tea" meetings as fun as they were. Aside from the social aspect, I really enjoyed many of the challenging discussions on extremely varied topics from the world of astronomy, mathematics and computer science. Special thanks go to those who supplied the majority of the tea time treats, Douglas Heggie and Max.

On a personal level, I couldn't have completed this thesis without the help of so many people, especially during the months of most intensive writing. Thanks to my fellow choristers in the Edinburgh University Renaissance Singers and my friends in the postgraduate community of the School of Mathematics who made coming in to the office bearable, even in the darkest days of writing up. In particular I would like to thank David Urminsky and his wife Neyir, Otonyo Mangete, Enrique Covarrubias, Achim Nonnenmacher, the usual suspects of lunch and tea time banter, and everyone with whom I have shared the office in room 4620 over the years.

I would like to give special thanks to my family, in particular my parents, for their continuing support and encouragement in everything I do; without their help and belief in me, I doubt that I would have made it this far. Finally, a huge thank you to my wonderful girlfriend Rosemary Apple for sticking by me and for coping so well with me through those stressful last few months. I am truly lucky to have found someone who understands me and who thought nothing of selflessly giving up many of her evenings to keep me company as I worked late in the office.

To my parents and my girlfriend, Rosemary Apple for believing in me.

Contents

Abstract i

Declaration ii

Acknowledgements iii

Contents v

List of Figures vii

1 Introduction 1

1.1 Gamma-ray bursts: a brief history 1

1.2 Theoretical models: GRB progenitors and central engines 3

1.3 Modelling the merger of compact stellar remnants 4

1.4 Organisation of the thesis 5

2 Hydrodynamics: Numerical Treatment and Tests 6

2.1 Hydrodynamics 6

2.2 Numerical treatment 9

2.2.1 Discretization 9

2.2.2 Finite differences 10

2.2.3 Godunov's method 11

2.3 The Riemann problem and its solution 12

2.3.1 The shallow water equations 15

2.3.2 Computing the inter-cell fluxes in Godunov's method 18

2.4 Choosing the time step 23

2.5 Approximate Riemann solvers 24

2.5.1 Roe's linearised solver 24

2.5.2 Shortcomings of the Roe solver 27

2.5.3 The HLL, HLLE and HLLEM schemes 29

2.6 Higher Resolution Methods 31
2.6.1 Increasing the spatial accuracy of Godunov's method 31
2.6.2 PPM - the piecewise parabolic method 33
2.7 Numerical Tests 36
2.7.1 1D shock tube tests 37
2.7.2 Tests in two spatial dimensions 42

3 EoS: Numerical Treatment and Effects on GRB Simulations 48
3.1 Description of CHARYBDIS 49
3.1.1 Equation of state of nuclear material 49
3.1.2 Hydrodynamics 52
3.1.3 Neutron star model 55
3.1.4 Implementation of black holes 58
3.1.5 Gravitational waves in Newtonian setting 63
3.1.6 Neutrino emission 66
3.1.7 Nested, refined grid structure 67
3.2 Numerical simulations 70
3.2.1 Initial conditions 70
3.2.2 NSBH results and discussion 72
3.2.3 NSNS results and discussion 90

4 Application of Approximate Riemann Solvers in Charybdis 97
4.1 The challenge of magnetohydrodynamics 98
4.2 Implementation of the approximate schemes 99
4.3 Numerical results 100

5 Conclusions and Outlook 109
5.1 The importance of the equation of state in GRB simulations 110
5.2 Using approximate Riemann solvers in Charybdis 111
5.3 Outlook 112

A The interpolant of PPM 115

B Numerical results 117

C Two Dimensional Plots of NSBH Simulations 132

Bibliography 143

List of Figures

2.1 Graphical depiction of the discretization and cell averaged quantities in one spatial dimension. 11
2.2 (a) An example of the piecewise constant initial conditions in a Riemann problem showing a discontinuity in an arbitrary quantity as a function of x; (b) A possible solution (actually the mass density profile of the solution to the Sod shock tube Riemann problem) to the relaxation of the discontinuity in panel (a). From right to left the jumps correspond to a shock, a contact discontinuity and a rarefaction fan. 14
2.3 A space-time diagram of the self-similar solution of a Riemann problem showing the four zones which result and the three waves separating them. The waves shown here are, from left to right, a rarefaction wave, the contact discontinuity and a shock wave. 14
2.4 The Hugoniot curves associated with three arbitrary states (indicated by plus symbols) in the phase plane of the shallow water equations. The solution to the particular Riemann problem with left and right states marked by "L" and "R" respectively is shown by a circle with the label "$\star$". The characteristic waves referred to in the text are also highlighted by labelled arrows. 16
2.5 Godunov (1959) type methods advance the flow in time by solving local Riemann problems at cell interfaces to obtain inter-cell fluxes. This allows the fluid quantities to be updated in a conservative fashion. . . 19
2.6 The loci of all possible states in a Riemann problem with a rarefaction moving to the left and a shock moving to the right in the velocity-pressure plane. The initial states are at left with zero velocity and the state marked (u^*, p^*) is the constant state formed between the shock and rarefaction wave. 20

2.7 Graphical illustration of the iterative Riemann solver of Godunov. The true solution $(u^\star, p^\star)$ is the intersection of the black curves and the coloured lines show successive iterations $(u^\star_{(i)}, p^\star_{(i)})$ in search of this solution. Note how the intersection of one set of the coloured lines determines the gradient of the lines for the next iteration. 22

2.8 Illustration of the Roe linearisation using the two dimensional phase space of the shallow water equations as an example. Two Riemann problems are shown here. In (a) a single shock moves with constant speed from left to right. The Roe approximation to the solution (square box with solid black line) matches the exact solution in this case. The dashed line and box symbol illustrate the importance of the average used to define the linearisation. The plot in (b) shows how the Roe solver can fail in the presence of strong rarefactions. Not only are the approximate and true solutions far apart, but the Roe solver computes an unphysical, negative depth. 26

2.9 The failure of the Roe solver for trans-sonic flows is demonstrated here with the solution to a modified Sod shock tube problem (Toro test 1). In panel (a) we see the numerical solution with an iterative Riemann solver and, in (b), the solution as computed using a linearised Roe solver. The exact solution is shown as a solid line in both plots. The resolution for both simulations was 500 cells with a Courant number of 0.9. 28

2.10 The three states in the HLL family of approximate Riemann solvers. F and S are the speeds of the fastest and slowest waves respectively. Between these waves, a region opens separating the original left and right states of the Riemann problem (U_{L} and U_{R}) with a new constant state U_{HLL}. 29

2.11 Graphical depiction of the linear reconstruction described in Eq. 2.56. The discontinuous, thick, black lines through the points (x_j, U_j) show the piecewise linear nature of the interpolant $U(x)$. The slope in the j^{th} cell is determined by the slope of the line connecting U_j with U_{j+1} as indicated by the dashed lines through each cell. The cell interface values are simply the values of $U(x)$ at the boundaries of each cell. . . 32

2.12 A piecewise parabolic interpolation function $U(x)$ is shown with the three constraints on its shape: U_j, the cell averaged value which fixes the area under the interpolant; $U_{\mathrm{L},j}$ and $U_{\mathrm{R},j}$ the values of the reconstruction at the interfaces with the neighbouring two cells which are approximated from a higher order polynomial and modified to help prevent spurious oscillations in the solution. 34
2.13 After a piecewise parabolic reconstruction is achieved, the left and right input values to the Riemann problem at each cell interface ($U_{\mathrm{L},j+1/2}$ and $U_{\mathrm{R},j+1/2}$) are computed as shown. In a time interval Δt, corresponding to the current time step, only the shaded areas are causally connected to the interface at $x_{j+1/2}$ by waves travelling at c_j and c_{j+1}. The inputs to the Riemann solver are found by averaging the interpolant over these regions. 35
2.14 Toro test 1: PPM reconstruction with iterative Riemann solver. Initial discontinuity position was $x_0 = 0.3$. The numerical solution (symbols) and the exact solution (line) are shown at time $t = 0.2$. 39
2.15 Toro test 2: PPM reconstruction with iterative Riemann solver. Initial discontinuity position was $x_0 = 0.5$. The numerical solution (symbols) and the exact solution (line) are shown at time $t = 0.15$. 40
2.16 Toro test 3: PPM reconstruction with iterative Riemann solver. Initial discontinuity position was $x_0 = 0.5$. The numerical solution (symbols) and the exact solution (line) are shown at time $t = 0.012$. 41
2.17 Toro test 4: PPM reconstruction with iterative Riemann solver. Initial discontinuity position was $x_0 = 0.4$. The numerical solution (symbols) and the exact solution (line) are shown at time $t = 0.035$. 41
2.18 Toro test 5: PPM reconstruction with iterative Riemann solver. Initial discontinuity position was $x_0 = 0.8$. The numerical solution (symbols) and the exact solution (line) are shown at time $t = 0.012$. 43
2.19 L1 normalised error in mass density for each of the 1D Toro (1999) tests. The Courant number in each simulation was 0.4. The average slope in each plot is about unity which indicates 1^{st} order accuracy. . . 44
2.20 (a) L_1 normalised error in mass density for the 2D double Mach reflection test (Woodward and Colella, 1984). The Courant number in each simulation was 0.8. (b) CPU times as a function of grid size for the double Mach reflection problem. The CPU times have been normalised to the fastest computation (HLLE). 45

2.21 Density plots for the double Mach reflection problem computed with a resolution of 960×240 and Courant number 0.8 using the PPM scheme with various Riemann solvers. The faint (dark blue) line which starts at the top of the main shock front and cuts back into the red triangular region is a small underdense wave which is caused by "start up error" from the initial oblique shock and is also found by Woodward and Colella (1984). 47

3.1 The dependence of pressure with mass density for the two equations of state used in our simulations plotted with $k_B T = 0.13$ MeV and $Y_e = 0.15$. A logarithmic scale is used to allow the differences to be seen for the chosen quantities. Note the different gradients of the curves for $\rho \gtrsim 10^{14}$ g/cm^3 which indicates the different "stiffnesses" of the two state equations. 51

3.2 Panels (a) and (b) show contours of the neutrino chemical potential μ_ν (measured in MeV) in the temperature-density plane for fixed electron fraction Y_e. In each case the contours are spaced with increments of 10 and are labelled with their respective values. The presence of contour lines at the top-left of Panel (b) which is absent in Panel (a) is due to extrapolation of the LS-EoS to this range which was not required for the Shen-EoS. Panels (c) and (d) show a series of curves in the temperature-density plane at which the μ_ν is zero for different values of Y_e as indicated by the line labels. 52

3.3 Radial profiles of (clockwise from top-left) pressure, mass density, mass, and electron fraction for two neutron stars of equal mass (1.6 $M_\odot$) but with different state equations. The neutron star constructed with the equation of state of Lattimer and Swesty (1991) and Shen et al. (1998a,b) is plotted in each panel by solid and dashed curve, respectively. 58

3.4 Plots relating neutron star mass to density and the stellar radius. The left panels show results computed with the Newtonian equation of hydrostatic equilibrium while those on the right result from the solution of the Oppenheimer-Volkoff equations which include a relativistic gravitational potential. In all panels the thick black curves and the dashed curves represents the stars described by the Lattimer and Swesty (1991) EoS and the Shen et al. (1998a,b) EoS respectively. 59

3.5 Effective potentials for various values of the specific angular momentum h in geometric units in which $G = M = c = 1$. For each angular momentum value the corresponding effective potential is plotted for the Newtonian case (dotted curves) and the Schwarzschild case (solid curves). Note the maxima in the relativistic curves which signify an unstable circular orbit since a small perturbation will cause a particle to either fall without resistance to the singularity at $r = 0$ or escape to infinity. The lack of either a local maximum or minimum for the critical value of angular momentum $h = 2\sqrt{3}$ shows that a particle can have a non-zero angular momentum and still reach the singularity in the general relativistic case. These effects are in stark contrast to the Newtonian curves. 60

3.6 The effect of the rotational parameter a on the event horizon ($r_{\rm H}$), the radius of the innermost stable circular orbit ($r_{\rm ISCO}$) and $\beta \equiv r_{\rm ISCO}/r_{\rm H} - 1$, a dimensionless parameter which defines the gravitational potential used. The thick curve $r_{\rm bhkerr}$ is the arithmetic mean of the last stable orbit and the event horizon and this is the effective radius of the vacuum-sphere we use to simulate a black hole. The radii are in units of GM/c^2 or half the Schwarzschild radius and the dotted horizontal line thus corresponds to the Schwarzschild radius. This figure is adapted from Setiawan et al. (2006). 62

3.7 Schematic depiction of the multiple, nested, refined grids and their relative positions. Also shown is the outline of two neutron stars of equal mass; note how the finest grid covers the region where the "action" will occur during their coalescence. 69

3.8 Dynamical evolution of the coalescence of a neutron star and a black hole (the grey filled circle) shown as logarithmic density in the orbital plane for numerical model NBLA. The neutron star has a mass of 1.6 $M_\odot$ and the black hole is 10 $M_\odot$ and maximally rotating. The equation of state used in this simulation is from Lattimer and Swesty (1991). The velocity field of matter with density greater than 10^8 g cm^{-3} is shown by white arrows with the longest arrow corresponding to a velocity of about $0.3c$. 74

3.9 Continuation of the dynamical evolution of a merger event between a $1.6\,M_\odot$ neutron star and a maximally rotating $10\,M_\odot$ black hole. See Fig. 3.8 for more details. 75

3.10 (a) The separation distance between the neutron star and the black hole in all NSBH models as a function of time. (b) The mass of the neutron star defined as the mass within a 30 km volume around the neutron star's position. Panels (c) and (d) show the growth of the black hole during the course of the simulations. In all four panels the time has been normalised as described in the main text. 76

3.11 The effects of changing the resolution from 64^3 to 128^3 is shown for models NBLA and NBSA. Panel (a) shows the separation distance between the black hole and the neutron star. We stop plotting once the neutron star becomes tidally disrupted as spurious separations result from our determination of the position of the star by following the density maximum. The total neutrino luminosity over all neutrino flavours is shown in panel (b) and in panels (c) and (d) the effects of resolution on the cumulative energy in neutrinos and gravitational waves can be seen. As before, the time range has been normalised as described in the main text. 77

3.12 The mass accretion rates of the black hole in each of the NSBH models is plotted against time. Each panel compares LS-EoS results with Shen-EoS results for a particular model. 78

3.13 Comparison of various energies as functions of time for models NBLA, NBSA (left panels), NBLB and NBSB (right panels). The "L" and "S" tags in each plot refer to the equation of state. The total energy refers to the energy in all forms on the grid. This is obviously not conserved since neutrinos, gravitational waves and mass loss all carry energy out of the computational domain. It should be possible to quantify this loss by accumulating the fluxes at the edge of the grid. 80

3.14 The evolution of the distribution of angular momentum on the grid as a function of time. Panels (a) and (b) show the total angular momentum on the grid and the loss of angular momentum due to gravitational wave emission for models NBLA, NBSA, NBLB and NBSB. Panel (c) shows the cumulative angular momentum which has left the grid and panel (d) shows the change in specific angular momentum of the black hole through interaction with the gas. Note that we do not expect the total angular momentum to be constant due to losses via gravitational wave emission and material leaving the computational domain. 81

3.15 (a)Gravitationally unbound mass (mass which has a positive total energy) as a function of time for all NSBH models. (b) Maximum temperature in MeV shown for models NBLA and NBSA. 82
3.16 Maximum density on the grids as a function of time. The panel on the left exhibits damped oscillations for the first few milliseconds which are due to the tidal relaxation of the neutron stars. The panel on the right gives a magnified view of these oscillations. Time normalisation is as described in Sect. 3.2.2. 82
3.17 Cumulative energy radiated in all species of neutrino as a function of time for the NSBH models. 83
3.18 Neutrino luminosities as functions of time for the models NBLA (top) and NBSA (bottom) in each of the species tracked; electron $\nu_{\rm e}$, electron antineutrino $\bar{\nu}_{\rm e}$, and the tau and mu neutrinos and their respective antineutrinos $\nu_{\tau,\mu}$. We also plot the total luminosity in all species of neutrino, $\Sigma\nu_{\rm i}$. 85
3.19 Neutrino luminosities as functions of time for the models NBLB (top) and NBSB (bottom). For further details see Fig. 3.18. 85
3.20 Neutrino luminosities as functions of time for the models NBLC (top) and NBSC (bottom). For further details see Fig. 3.18. 85
3.21 Electron fraction in the orbital plane. Only the inner part of the computational domain is plotted. All of these cross-sections (and many more of the plots in this thesis) were made with the Interactive Data Language (IDL). 86
3.22 Electron fraction in the orbital plane (part2). 87
3.23 Temperature in the orbital plane. 88
3.24 Temperature in the orbital plane (part2). 89
3.25 Neutrino luminosities as functions of time for the models NNLA (top) and NNSA (bottom) in each of the species tracked; electron $\nu_{\rm e}$, electron antineutrino $\bar{\nu}_{\rm e}$, and the tau and mu neutrinos and their respective antineutrinos $\nu_{\tau,\mu}$. We also plot the total luminosity in all species of neutrino, $\Sigma\nu_{\rm i}$. 90
3.26 Dynamical evolution of the coalescence of two neutron stars shown as logarithmic density in the orbital plane. The neutron stars each have a mass of 1.6 $M_\odot$. The equation of state used in this simulation is from Lattimer and Swesty (1991). The white arrows show the velocity field with the longest arrow relating to a velocity of about $0.3c$. 92

3.27 Continuation of the dynamical evolution of a merger event between two 1.6 $M_\odot$ neutron stars. See Fig. 3.26 for more details. The high density central object (red with a sharp density drop near the yellow "crust") is a likely proto-black hole candidate but, as explained in the text, we cannot tell for certain without a full general relativistic treatment. . . 93
3.28 Temperature in the disk, NNLA and NNSA. 94
3.29 Electron fraction in the disk, NNLA and NNSA. 95
3.30 Two dimensional slices through the centre of the grid showing mass density in the disk for models NNLA and NNSA plotted as colour filled contours. The velocity field is shown as white arrows, the longest arrow corresponding to a velocity of about 0.3c. 96

4.1 Mass density in the orbital plane for the simulation of a neutron star merger with the LS-EoS and the iterative Riemann solver. Panel (a) shows an early snapshot after the neutron stars have begun shedding mass and (b) shows the distribution of mass at the end of the simulation. The arrows show the velocity field of the gas. The largest arrows correspond to velocities on the order of 0.3c. 102
4.2 Mass density in the orbital plane computed with the linearised Riemann solver of Roe (1981). All other details are the same as in Fig. 4.1. . . . 103
4.3 Mass density in the orbital plane computed with the approximate HLLE Riemann solver. All other details are the same as in Fig. 4.1. 103
4.4 The orbital paths of the two neutron stars computed using (a) the linearised Roe solver and (b) the approximate HLLE solver are plotted as plus symbols. The paths computed with the iterative Riemann solver are also shown as crosses for comparison. Only about the last 20% of the simulated data are plotted for clarity. 104
4.5 (a) Total neutrino luminosities as functions of time for the three simulations. (b) Comparison of the time dependence of neutrino luminosity for ν_e, $\bar{\nu}_e$ and the heavy neutrinos with their respective antineutrinos $\nu_{\tau,\mu}$. 104
4.6 Two dimensional slices through the centre of the computational domain showing temperature (in MeV) at the end of the simulation computed with the iterative Riemann solver. 105
4.7 Two dimensional slices through the centre of the computational domain showing temperature (in MeV) at the end of the simulation computed with the linearised Roe solver. 106

4.8 Two dimensional slices through the centre of the computational domain showing temperature (in MeV) at the end of the simulation computed with the approximate HLLE Riemann solver. 106
4.9 Two dimensional slices through the centre of the computational domain showing electron fraction at the end of the simulation computed with the iterative Riemann solver. 107
4.10 Two dimensional slices through the centre of the computational domain showing electron fraction at the end of the simulation computed with the linearised Roe solver. 107
4.11 Two dimensional slices through the centre of the computational domain showing electron fraction at the end of the simulation computed with the approximate HLLE Riemann solver. 108

B.1 Toro test 1: PPM reconstruction with iterative Riemann solver. Initial discontinuity position was $x_0 = 0.3$. The numerical solution (symbols) and the exact solution (line) are shown at time $T = 0.2$. This particular plot is identical to Fig. 2.14 in Sect. 2.7.1. 118
B.2 Toro test 1: PPM reconstruction with Roe solver. All other details are as Fig. B.1. 119
B.3 Toro test 1: PPM reconstruction with HLLE Riemann solver. All other details are as Fig. B.1. 120
B.4 Toro test 1: PPM reconstruction with HLLEM Riemann solver. All other details are as Fig. B.1. 120
B.5 Toro test 2: PPM reconstruction with iterative Riemann solver. Initial discontinuity position was $x_0 = 0.5$. The numerical solution (symbols) and the exact solution (line) are shown at time $T = 0.15$. 121
B.6 Toro test 2: PPM reconstruction with HLLE Riemann solver. All other details are as Fig. B.5. 122
B.7 Toro test 2: PPM reconstruction with HLLEM Riemann solver. All other details are as Fig. B.5. 122
B.8 Toro test 3: PPM reconstruction with iterative Riemann solver. Initial discontinuity position was $x_0 = 0.5$. The numerical solution (symbols) and the exact solution (line) are shown at time $T = 0.012$. 123
B.9 Toro test 3: PPM reconstruction with Roe solver. All other details are as Fig. B.8. 124
B.10 Toro test 3: PPM reconstruction with HLLE Riemann solver. All other details are as Fig. B.8. 124

B.11 Toro test 3: PPM reconstruction with HLLEM Riemann solver. All other details are as Fig. B.8. 125
B.12 Toro test 4: PPM reconstruction with iterative Riemann solver. Initial discontinuity position was $x_0 = 0.4$. The numerical solution (symbols) and the exact solution (line) are shown at time $T = 0.035$. 126
B.13 Toro test 4: PPM reconstruction with Roe solver. All other details are as Fig. B.12. 127
B.14 Toro test 4: PPM reconstruction with HLLE Riemann solver. All other details are as Fig. B.12. 127
B.15 Toro test 4: PPM reconstruction with HLLEM Riemann solver. All other details are as Fig. B.12. 128
B.16 Toro test 5: PPM reconstruction with iterative Riemann solver. Initial discontinuity position was $x_0 = 0.8$. The numerical solution (symbols) and the exact solution (line) are shown at time $T = 0.012$. 129
B.17 Toro test 5: PPM reconstruction with Roe solver. All other details are as Fig. B.16. 130
B.18 Toro test 5: PPM reconstruction with HLLE Riemann solver. All other details are as Fig. B.16. 130
B.19 Toro test 5: PPM reconstruction with HLLEM Riemann solver. All other details are as Fig. B.16. 131

C.1 Temperature in the $x - z$ plane. 133
C.2 Temperature in the $x - z$ plane (part2). 133
C.3 Temperature in the $y - z$ plane. 134
C.4 Temperature in the $y - z$ plane (part2). 134
C.5 Electron fraction in the $x - z$ plane. 135
C.6 Electron fraction in the $x - z$ plane (part2). 135
C.7 Electron fraction in the $y - z$ plane. 136
C.8 Electron fraction in the $y - z$ plane (part2). 136
C.9 Two dimensional slices through the centre of the grid showing mass density in the disk for models NBLB and NBSB plotted as colour filled contours. The velocity field is shown as white arrows, the longest arrow corresponding to a velocity of about $0.3c$. 137
C.10 Mass density and velocity field in the disk for models NBLC and NBSC. See Fig. C.9. 138
C.11 Temperature in the disk, NBLB and NBSB. 139
C.12 Temperature in the disk, NBLC and NBSC. 140
C.13 Electron fraction in the disk, NBLB and NBSB. 141

C.14 Electron fraction in the disk, NBLC and NBSC. 142

> "Tús maith, leath na h-oibre (a good start is half the work)."
>
> — Irish proverb

1 Introduction

1.1 Gamma-ray bursts: a brief history

Gamma-ray bursts (GRBs) are short-lived but extremely energetic transient events lasting anywhere from a few milliseconds to several minutes. During this time-span however, they are so luminous that they outshine the rest of the observable universe in gamma rays. GRBs were first detected serendipitously in 1967 by U.S. military satellites sent into orbit to ensure that the Soviet Union was complying with a ban on atmospheric testing of nuclear weapons. Nuclear explosions have a characteristic gamma-ray signature and so the military satellites were designed to detect short pulses of gamma-ray emission. The satellites began measuring energetic burst of gamma rays with energies in the range 0.2-1.5 MeV on average once per day. Understandably, the work was classified for several years until it was determined that the bursts were of astronomical origin (not, as the military feared, due to Soviet forces testing nuclear weapons on the far side of the moon!). The results for 16 short bursts in the previously mentioned energy range showing "significant time structure" were published in the public domain by Klebesadel et al. (1973).

Very little was known about these gamma-ray bursts until the launch of the

Compton Gamma Ray Observatory (for a summary of the results, see the paper by Fishman and Meegan, 1995) in 1991. This satellite recorded over 2,700 bursts with the Burst And Transient Source Experiment (BATSE). This instrument was an all-sky survey which showed that the GRBs were isotropically distributed across the sky with no correlation with the galactic plane implying an extra-galactic origin. The BATSE results showed the existence of two distinct populations of GRBs referred to as short-period and long-period GRBs. The former category typically last for less than a second and the latter for more than a second and, in many instances, they last for several minutes. The two populations vary spectroscopically too; short bursts tend to have a harder gamma ray spectrum than the long bursts with typical spectral indices of approximately 1 at energies $E_{\rm ph} \leq 100$ keV, breaking to -2 or -3 at $E_{\rm ph} \geq$ several hundred keV (e.g. Band et al., 1993).

Subsequent missions have added to our knowledge of what are often described as the "biggest bangs in the universe". The Italian satellite Beppo-SAX, launched in 1997, carried an X-Ray telescope to search for X-Ray afterglow which was expected from theoretical considerations. By locating the X-ray counterpart of GRB 970228 [1], Costa et al. (1997) were able to identify the corresponding host galaxy and thus obtain the red-shift. This showed unambiguously that GRBs were of cosmological origin. This posed a problem, however: at such great distances, the received fluxes imply energies $\lesssim 10^{54}$ erg if the emission is assumed to be isotropic. Also, the rapid variability in the light curves with time meant that, because of causality, the emitting region must be smaller than about 100 km (see Mészáros, 2002, and references therein).

The sensitivity of Beppo-SAX to bursts longer than about 5 to 10 seconds meant that it was more likely to return data on the long-period GRBs. To rectify this, the *Swift* satellite[2] was launched in 2004 and, within about half a year, it had identified the X-ray counterpart to the short-period GRB 050509b (Gehrels et al., 2005; Bloom et al., 2006). The identification of the host galaxy showed another difference between the two classes of GRBs; long bursts tended to be associated with star-forming regions in younger galaxies while GRB 050509b occurred in an old galaxy and was not associated with an accompanying supernova like many of the long-period bursts. The *Swift* mission has also provided some evidence for anisotropic beaming of the gamma-ray radiation and also the initial opening angle of this radiation (e.g. Soderberg et al. (2006); Grupe et al. (2006)). This considerably reduces the inferred total energy

[1] Gamma-ray burst identifiers refer to the date they were detected; the convention is YYMMDD. If there is more than one GRB detected on the same day, they are further labelled chronologically by an alphabetical letter, e.g. GRB 080319b.

[2] For technical details on the *swift* mission, see `http://swift.gsfc.nasa.gov`.

required to power a short-period GRB to about $\sim 10^{49}$ erg.

1.2 Theoretical models: GRB progenitors and central engines

The fundamental differences between the short and long-period GRBs suggest at least two different power sources. The collapse of super-massive stars (the "hyper-nova" or "collapsar" model) has been suggested (Woosley, 1993; Paczynski, 1998; MacFadyen and Woosley, 1999) as a model for the central engine of the long GRBs. In this thesis however, we concern ourselves with simulations of the gradual in-spiral and eventual coalescence of binary systems consisting of a neutron star with either another neutron star or a black hole which have been proposed as a power source for the short-period GRBs. These systems lose angular momentum due to emission of gravitational waves, the canonical example being the Hulse-Taylor pulsar system (Hulse and Taylor, 1975) which earned its discoverers the 1993 Nobel prize in physics.

If the merger of binary systems such as these are responsible for the short class of GRBs, there must be some way to extract the gravitational energy of the system and use it to power the gamma-ray event we observe. Some magnetohydrodynamical processes have been suggested including tapping the rotational energy of the central object if it collapses to a black hole through magnetic braking using a self-sustaining field produced by currents in an accretion disk (Blandford and Znajek, 1977; Mészáros and Rees, 1997). Regardless of the exact mechanism for converting the kinetic energy of the merging stars, high baryonic densities in excess of 10^{14} g/cm^3 generated during and immediately after coalescence lead to a medium which is opaque to photons. High temperatures are also created due to the violence of the event and this means that radiation of (anti)neutrinos will be the most prevalent mechanism for energy transport. Some simulations show that the density of neutrinos will be so high in the first few milliseconds after the merger that neutrino-antineutrino annihilation will take place with rates $\gtrsim 10^{52}$ erg s^{-1} (Birkl et al., 2007, and references therein). One scenario for producing a gamma-ray burst involves production of a fireball consisting of electron and positron pairs created via neutrino processes (e.g. Mészáros and Rees, 1992). This provides a test of a given model for a GRB; it must at least produce the correct amount of neutrinos and antineutrinos to provide the huge amount of energy required for a gamma ray burst.

1.3 Modelling the merger of compact stellar remnants

In this thesis we present simulation results of the merger of neutron stars with black holes and other neutron stars. Since neutrino processes are thought to be so important in transporting the massive amounts of energy liberated during the merger, we require some description of the micro-physics of the neutron star matter. In modern simulations, the nuclear physics of matter at the extreme densities found in these merger events is added to the model by including pre-calculated data in a tabular equation of state. This data is obtained from a theoretical model of nuclear physics which is then used to compute the relevant values at various conditions of density, temperature, etc. These data tables are described in more detail in Chap. 3 and in the literature (see for example, Ruffert et al., 1996; Rosswog and Davies, 2002).

Neutrino emission is very sensitive to temperature and, as temperature is determined in the aforementioned numerical simulations from the equation of state, changing the description of the neutron star material may impact neutrino emission. Changing the equation of state may also affect the dynamics which would in turn lead to different gravitational wave emission patterns as this has already been shown by Rasio and Shapiro (1994) to depend on the stiffness of the equation of state. To investigate the effect of the equation of state on the neutrino emission in simulations of this type, we intend to compare three dimensional simulations of merger events between binary systems containing either two neutron stars or a neutron star and black hole calculated with two different realistic state equations. Of the two equations of state, that proposed by Lattimer and Swesty (1991) has been in use in these types of simulation for over a decade. The other equation of state used, that of Shen et al. (1998a,b), has previously been used in mergers between two neutron stars (e.g. Rosswog and Davies, 2002) but only for smoothed particle hydrodynamics (SPH) codes. Rosswog and Davies (2002) describe some of the general differences caused by switching EoS but do not draw direct comparison with models computed with the EoS of Lattimer and Swesty (1991). Also, to the best of our knowledge, this is the first time a comparison can be drawn between simulations of neutron star–black hole mergers computed using the equations of state discussed above since other groups simulating the coalescence of neutron star - black hole binary systems with a realistic equation of state have only used one such EoS (e.g. Rosswog, 2005a).

Much more physics than the micro-physics and neutrino emission is required in modelling the merger of compact stellar remnants. We of course require some form of fluid dynamics to evolve the bulk motion of matter on the grid and, so that we can perform the solution on a computer, we must choose a method in which space and time can be discretized. If the stars are to merge at all we must include at least some

general relativity into our simulations; we include general relativistic corrections to Newtonian mechanics so that gravitational wave emission is taken into account.

An alternative mechanism to energy extraction via neutrino emission is extraction via magnetic fields. Since it has been shown in numerical simulations (see for example, Casse and Keppens, 2002) that an accretion disk threaded by a magnetic field can launch a continuous, self-collimating jet of plasma, we hypothesise that magnetic processes are important in the study of GRBs and may provide a mechanism through which gamma-ray emission may become highly directional, thus lowering the required energies to match the received fluxes[3]. Although some progress has been made using magnetohydrodynamics (MHD) in simulations of merging binary neutron stars with a realistic equation of state by Price and Rosswog (2006); Rosswog and Price (2007), there are still many unanswered questions such as the topology of the magnetic field outside of the stars and the resulting accretion disk, and the field's possible role in jet launching by acting as an energy reservoir and through its interaction with the top and bottom layers of the disk.

1.4 Organisation of the thesis

The thesis is laid out as follows: In chapter 2 we introduce some important concepts and background theory related to the numerical solution of the hydrodynamical equations. We also describe some numerical schemes for hydrodynamics and compare their performance in some standard one and two dimensional tests. Chapter 3 contains a full description of the features of the computer code we use to simulate the merging and coalescence of compact stellar remnants (i.e. neutron stars and black holes). We present the results of simulations designed to investigate whether the micro-physical description of matter under the extreme conditions present in a neutron star has any effect on the neutrino emission rates. Since it is thought that the energy we associate with the GRB is extracted from the merger event via neutrino-antineutrino annihilation, any variation in these rates is important as it may strengthen or weaken the case for mergers between compact objects as a central engine for the short period class of GRBs. We return to the subject of numerical schemes for hydrodynamics in chapter 4; we present results from current work on simplifying the numerical solver used in our compact merger code in preparation for the inclusion of magnetic field physics in our model. Finally, we conclude with a summary and discussion of results followed by some thoughts on the future direction of this research project.

[3]Note that this is speculative as the work by Casse and Keppens (2002) is non-relativistic and can never, therefore, lead to high Lorentz factor jets.

> We can't solve problems by using the same kind of thinking we used when we created them.
>
> — Albert Einstein

2

Hydrodynamics: Numerical Treatment and Tests

A long-term goal in our simulations of merger events between compact stellar remnants is the addition of magnetic field physics to the current computer model (described in detail in Chap. 3). In this thesis, we take some important first steps towards the accomplishment of this goal. For example, we must first understand the numerical solution of the augmented Euler equations in the context of that model and so, in this chapter, we introduce the basic mathematical theory of hydrodynamics and present numerical tests to show the development of suitable schemes for implementation in our astrophysical code.

2.1 Hydrodynamics

Hydrodynamics is the study of the motion of fluids where the fluid is described in the continuum limit, neglecting their discrete, molecular nature. In astronomy, the fluid in question is often compressible and so the term is used interchangeably with gas dynamics, the governing equations of which are the *Euler equations* which, in

conservation form, are written

$$\frac{\partial \mathbf{U}}{\partial t} + \nabla \cdot \mathbf{F}(\mathbf{U}) = \mathbf{S}(\mathbf{U}), \tag{2.1}$$

with the vectors

$$\mathbf{U} = \begin{pmatrix} \rho \\ \rho u_x \\ \rho u_y \\ \rho u_z \\ E \end{pmatrix}, \qquad \mathbf{F}(\mathbf{U}) = \begin{pmatrix} \rho u_x \\ \rho u_x^2 + p \\ \rho u_x u_y \\ \rho u_x u_z \\ (E+p)u_x \end{pmatrix}. \tag{2.2}$$

The state vector $\mathbf{U}$ contains the conserved quantities of mass density $\rho(x,t)$, the three components of linear momentum density $\rho(x,t)\mathbf{u}(x,t)$ and the total energy density $E(x,t)$.[1] $\mathbf{F}(\mathbf{U})$ is the vector of flux densities derived from the conserved quantities and $\mathbf{S}(\mathbf{U})$ is a vector containing source terms for the system.

The total energy $E = \rho\epsilon + \frac{1}{2}\rho|\mathbf{u}|^2$ is the sum of the internal and kinetic energy densities, $\rho\epsilon$ and $\frac{1}{2}\rho|\mathbf{u}|^2$, respectively. The quantity $\epsilon = \epsilon(p,\rho)$ which is a function of the mass density and the pressure, is known as the specific (per unit mass) internal energy and is determined by the *equation of state*.[2] As an example, consider the equation of state for an ideal gas (also known as a gamma-law gas) which is used for all the examples and tests throughout this chapter,

$$\epsilon = \frac{p}{\rho(\gamma - 1)}, \tag{2.3}$$

where γ is the ratio of the specific heats.

The Euler equations as shown in Eqs. 2.1-2.2 are a set of non-linear, coupled, partial differential equations (PDEs) and as such, a general, closed form, analytical solution has not yet been found. To proceed, we can make approximations to solve the equations in certain contexts or we can attempt to solve the equations numerically with the help of a computer. Since this thesis is concerned with the latter, we now consider the Euler equations, identifying any properties which may be useful in their numerical solution.

---

[1] Unless explicitly stated otherwise, "density" will mean *mass density* or mass per unit volume and all other fluid properties will be assumed to be densities.

[2] The equation of state completely describes the thermodynamical properties of the fluid medium and although it *can* be a function of just two variables (such as pressure and mass density as in this case), other more complicated or exotic types of fluid may require more data to uniquely determine the pressure for a given internal energy and so on. We will see an example of such an exotic equation of state in Chap. 3.

The Euler equations are examples of hyperbolic conservation laws. Hyperbolic in this context means that the flux Jacobian matrix

$$A \equiv \frac{\partial \mathbf{F}(\mathbf{U})}{\partial \mathbf{U}}, \tag{2.4}$$

is diagonalisable with real eigenvalues $\lambda_1 < \lambda_2 < ... < \lambda_n$ where n is equal to the number of coupled equations or the size of $\mathbf{U}$ and $\mathbf{F}$ ($\mathbf{U}, \mathbf{F} \in \mathbb{R}^n$). If the eigenvalues are also distinct, i.e. there are no degeneracies, then the system of equations exhibits *strict* hyperbolicity. These properties of the Jacobian matrix A are important and we shall return to them later in this chapter. For completeness, the eigenvectors of the Euler equations with the fluid quantities and fluxes given by 2.2 are

$$\begin{gathered}
\mathbf{r}_1 = \begin{pmatrix} 1 \\ u_x - c \\ u_y \\ u_z \\ H - u_x c \end{pmatrix}, \qquad \mathbf{r}_2 = \begin{pmatrix} 0 \\ 0 \\ u_y \\ 0 \\ u_y^2 \end{pmatrix}, \qquad \mathbf{r}_3 = \begin{pmatrix} 0 \\ 0 \\ 0 \\ u_z \\ u_z^2 \end{pmatrix}, \\
\mathbf{r}_4 = \begin{pmatrix} 1 \\ u_x \\ u_y \\ u_z \\ \frac{1}{2}|\mathbf{u}|^2 \end{pmatrix}, \qquad \mathbf{r}_5 = \begin{pmatrix} 1 \\ u_x + c \\ u_y \\ u_z \\ H + u_x c \end{pmatrix},
\end{gathered} \tag{2.5}$$

where c is the speed of sound which is related to the enthalpy $H \equiv (E+p)/\rho$ through the formula $c^2 = (\gamma - 1)(H - \frac{1}{2}|\mathbf{u}|^2)$. These eigenvectors have corresponding eigenvalues

$$\lambda_1 = u_x - c, \qquad \lambda_2 = u_x, \qquad \lambda_3 = u_x, \qquad \lambda_4 = u_x, \qquad \lambda_5 = u_x + c. \tag{2.6}$$

The Euler equations are examples of conservative equations which means that any of the special conserved quantities (mass, momentum and energy for the Euler equations) can only change in time in a given region of space, if we neglect any source or sink terms, if there is a net *flux* of that quantity into or out of the region. Any conservative equation is said to be in conservative form if it is written as Eq. 2.1.

A word on derivatives; the temporal derivative in Eq. 2.1 is an Eulerian derivative and measures the change in a quantity with respect to time at a *fixed* point in space and is thus written as a partial derivative. Another way to measure the evolution of a variable in time is to move along with the local flow, following a streamline. For example, consider a chemical tracer or a small concentration of dye added to a fluid flow. As this chemical flows past a point at which we might evaluate an Eulerian derivative, the local concentration of that chemical will change. The derivative of the

concentration evaluated by following the flow however, does not change unless there are sources or sinks caused by chemical reactions, etc. This derivative is a Lagrangian derivative and is related to the Eulerian derivative as follows,

$$\frac{\mathrm{D}}{\mathrm{D}t} = \frac{\partial}{\partial t} + \mathbf{u} \cdot \nabla. \tag{2.7}$$

These two derivatives lead to distinct formulations of fluid dynamics, namely the Eulerian and Lagrangian formulations. In order to solve the hydrodynamic equations numerically, we must first decide upon a way to represent the fluid in the computer. Since computer memory is finite and the fluid is thought of as a continuous medium in the Euler equations, this means we must choose a method of discretization. We can choose between the Eulerian and Lagrangian views in discretizing the fluid or use an "Arbitrary Lagrangian-Eulerian" (ALE) formulation, developed in an attempt to combine the advantages of the above classical descriptions while minimising their respective drawbacks as far as possible.

2.2 Numerical treatment

2.2.1 Discretization

One simple method of discretization is to split the fluid into cells which together form a grid in one, two and three spatial dimensions. In this context, choosing the Eulerian or Lagrangian formulation of hydrodynamics leads to two different types of computational grid. In the Eulerian framework the cells of the grid always occupy a fixed volume and any change in the conserved quantities is therefore due to flow through the cell, as expected from the definition of the Eulerian derivative. In the Lagrangian point of view, the grid is flexible and moves to follow "fluid particles" where a cell defines such a particle and the cell changes size to conserve the amount of mass within its volume. See Courant and Friedrichs (1948) or Richtmyer and Morton (1994) for more details. If the Lagrangian grid seems rather *ad hoc*, there is a conceptually simpler way of treating the Euler equations in their Lagrangian form; we can assign the fluid quantities to particles of fixed mass and follow these particles as they interact through the fluid forces. This point of view is followed in the smoothed particle hydrodynamics (SPH) approach, We do not use SPH in the present work, but simply direct the interested reader to some of the seminal papers in this field by Benz (1990), Monaghan (1992) and references therein.

The choice made in all the codes for which detailed results are presented in this thesis is to use an Eulerian grid based code. A discretization which is relevant in this case is to divide time and space into discrete lattice points $(x, t) \rightarrow (x_j, t_n)$ with

$j, n \in \mathbb{Z}$ as follows,

$$\begin{aligned} x_j &= j\Delta x, \\ t_n &= n\Delta t, \end{aligned} \tag{2.8}$$

where Δx and Δt are then the distance between the points in space and time respectively[3]. Note that this spatial discretization describes a uniform, equidistant mesh. It is of course possible to consider more complicated types of mesh which increase resolution in regions of interest or which utilise different coordinate systems (e.g. spherical) to better suit a particular problem. We do not consider such grids here since all codes presented in this work use the simple grids described above. Resolution is increased by nesting grids with decreasing Δx. See Sect. 3.1.7 for further details.

Using our discretization, any fluid variables can then be described in terms of these discrete coordinates as $\mathbf{U}(x_j, t_n)$ but it will be beneficial (as we shall see later) if we further consider the lattice points to be surrounded by cells of finite volume. In that case we must prescribe some value to the space between lattice points and one way to do this is to average the quantity over the cell volume,

$$\mathbf{U}_j^n \equiv \frac{1}{\Delta x_j} \int_{x_{j-1/2}}^{x_{j+1/2}} \mathbf{U}(x, t_n) \mathrm{d}x. \tag{2.9}$$

Note that we still refer to a cell *volume* even in one dimension. This finite volume discretization is shown graphically in one spatial dimension in Fig. 2.1.

2.2.2 Finite differences

We now have a discretization, in terms of a grid of finite volume cells, of the fluid described by the Euler equations, *viz.* the set of values $\{\mathbf{U}_j^n\}$. Solving the Euler equations, in the present numerical context, means to find approximations $\{\mathbf{U}_j^{n+1}\}$ to the fluid quantities at a time $t_{n+1} = t_n + \Delta t$ when the values at $t = t_n$ are known and form initial conditions. One obvious way of deriving numerical schemes is to rearrange the Taylor series approximations to the partial derivatives in the conservation laws. Consider for example, the one dimensional continuity equation of mass from the Euler equations in isolation in the case of a steady flow with constant velocity $u_x > 0$,

$$\frac{\partial \rho}{\partial t} + u_x \frac{\partial \rho}{\partial x} = 0. \tag{2.10}$$

This is often called the advection equation since any initial density profile is simply advected through a distance $u_x \Delta t$ each time step. We start by replacing each derivative

[3]The distance between any two lattice points, Δx, is trivially defined from the number of cells in any direction and by the physical length that this grid is meant to represent. The time step, Δt, however, requires a little more thought since, if chosen too large, the scheme may be numerically unstable. We defer the definition of the time step until Sect. 2.4.

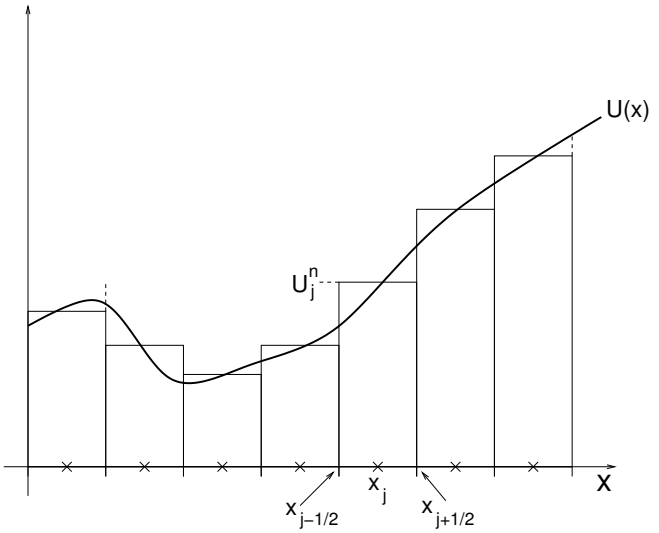

Figure 2.1: Graphical depiction of the discretization and cell averaged quantities in one spatial dimension.

with a finite difference approximation. There are many choices here, especially for the spatial derivative. The derivative could be one-sided, centred, first or second order, etc. and care should be taken since many choices produce inherently unstable schemes (see LeVeque (1994) for a survey). Since the flow has constant velocity, and hence always travels in the same direction, we can use a simple one sided representation of the spatial derivative,

$$\frac{\rho_j^{n+1} - \rho_j^n}{\Delta t} + u_x \frac{\rho_j^n - \rho_{j-1}^n}{\Delta x} = 0, \tag{2.11}$$

which we can then rearrange to find the density profile at the next time step

$$\rho_j^{n+1} = \rho_j^n - u_x \frac{\Delta t}{\Delta x} \left(\rho_j^n - \rho_{j-1}^n \right). \tag{2.12}$$

This is an example of an upwind scheme, so called because to update the value in any given cell it uses information from the neighbouring cell in the upstream or upwind direction. There are many more simple finite difference based schemes such as the upwind scheme. Many are robust but as a class they tend to suffer from high numerical diffusivity; they are fine when the solution is smooth but any steep gradients, such as in a hydrodynamical shock, become smeared out. A remedy for this is to construct a shock capturing scheme which preserves steep gradients in the fluid quantities. Just such a class of numerical schemes was first proposed by Godunov (1959).

2.2.3 Godunov's method

The upwind method defined in Sect. 2.2.2 has the interesting property that it exhibits less numerical diffusion than a scheme which uses a centred, finite difference

approximation to spatial derivatives (LeVeque, 1994). This makes sense if we consider that, since quantities in our grid cell can only change due to the flux into and out of the cell, only the upwind information will affect our chosen cell. Unfortunately for the Euler equations, we do not have the situation, essentially engineered in Eq. 2.10, that the velocity of the flow is a constant. However, Godunov (1959) managed to devise a method which effectively generalises the upwind method to all hyperbolic systems of PDEs including the Euler equations.

The Godunov scheme is conceptually intuitive and results from considering the integral form of the conservation law Eq. 2.1 (neglecting any source terms),

$$\int_{x_{j-1/2}}^{x_{j+1/2}} \mathbf{U}(x, t_{n+1})\mathrm{d}x - \int_{x_{j-1/2}}^{x_{j+1/2}} \mathbf{U}(x, t_n)\mathrm{d}x + \int_{t_n}^{t_{n+1}} \mathbf{F}\left(\mathbf{U}(x_{j+1/2}, t)\right)\mathrm{d}t - \int_{t_n}^{t_{n+1}} \mathbf{F}\left(\mathbf{U}(x_{j-1/2}, t)\right)\mathrm{d}t = 0. \quad (2.13)$$

The two integrals over x are equivalent to our definition of a cell averaged quantity, Eq. 2.9. If we also define the flux between cells

$$\mathbf{F}_{j+1/2}^{n+1/2} \equiv \frac{1}{\Delta t_n} \int_{t_n}^{t_{n+1}} \mathbf{F}\left(\mathbf{U}(x_{j+1/2}, t)\right)\mathrm{d}t, \quad (2.14)$$

then we can rewrite Eq. 2.13 as

$$\mathbf{U}_j^{n+1} = \mathbf{U}_j^n - \frac{\Delta t}{\Delta x}\left(\mathbf{F}_{j+1/2}^{n+1/2} - \mathbf{F}_{j-1/2}^{n+1/2}\right). \quad (2.15)$$

This scheme is clearly in conservative form and shows that if we can evaluate the inter-cell fluxes numerically, then we can advance the solution of the hyperbolic PDEs to the next time step. While this may seem difficult at first we note that, over the time interval $t \in [t_n, t_{n+1}]$, the integral in Eq. 2.14 is trivial since $\mathbf{U}$ is constant at $x = x_{j+1/2}$, the interface between the cells j and $j+1$. One way of computing $\mathbf{F}_{j+1/2}^{n+1/2}$ therefore, is to determine the value of $\mathbf{U}$ at the interface and then compute the fluxes based on these values. This is Godunov's method. At the interface between each cell, he solved the full non-linear Euler equations via an iterative method to obtain the values of fluid variables at that interface. By computing the fluxes according to their definition as in Eq. 2.2, he was then able to close the scheme and evolve the fluid quantities in time. The computation of the fluid quantities at the cell boundaries is accomplished by a Riemann solver. Let us now consider Godunov's iterative Riemann solver in more depth.

2.3 The Riemann problem and its solution

The general Riemann problem is the solution of a conservation law with piecewise constant initial data and a single discontinuity (LeVeque, 1994). In the special case

where the initial velocities on both sides of the discontinuity are zero, the term "shock tube" is also applied. Figure 2.2(a) shows the spatial profile of a given quantity in a typical Riemann problem. In general, discontinuities such as this are not stable in the sense that the dynamics represented by the conservation laws will act to break the original jump into smaller jumps which *are* stable and evolve in a self-similar manner. The solution of the Riemann problem then, can be thought of as the resolution of this discontinuity into characteristic jumps in the conserved quantities for that system of equations.

The canonical example of a hyperbolic PDE is the second order scalar wave equation

$$\frac{\partial^2 a}{\partial t^2} = c^2 \frac{\partial^2 a}{\partial x^2}, \tag{2.16}$$

where c is the speed of the waves and $a = a(x,t)$ is some arbitrary quantity such as the electric or magnetic field in the case of electro-magnetic waves, or gas pressure in the case of acoustic waves. Wave propagation is a property of all hyperbolic PDEs; perturbations in state variables spread outwards at characteristic speeds. It is this mechanism which is responsible for resolving a general Riemann problem; a general discontinuity may be thought of as a perturbation which excites one or more of the characteristic waves of the system of equations, each of which propagates outwards from the initial discontinuity as a stable jump in the fluid quantities. This is illustrated graphically in Fig. 2.2(b) where we have taken the resultant density profile in the Sod shock tube problem. This figure includes the three types of characteristic wave which the Euler equations support. There is a rarefaction fan (the smooth slope to the left of $x = 0$), a shock (the step discontinuity furthest on the right), and a contact discontinuity (between the shock and rarefaction). As these waves move outward from $x = 0$, they separate new piecewise constant regions as shown in Fig. 2.3. The "jump" in a given fluid variable as one of these waves pass satisfies the Rankine-Hugoniot jump condition

$$\mathbf{F}(\mathbf{U}_1) - \mathbf{F}(\mathbf{U}_2) = s\,(\mathbf{U}_1 - \mathbf{U}_2)\,, \tag{2.17}$$

which is derived directly from the integral form of the conservation law (e.g. LeVeque, 1994, 2002; Toro, 1999). It essentially states that a discontinuity in the fluid variables will be stable providing that it moves with velocity s. A side note which will be important later: this means we can have a "rarefaction shock" – a discontinuity which moves towards an area of high density leaving a rarefied, lower density state in its wake. This is unphysical however, but we can only see this if we consider the entropy change across the jump. The rarefaction shock, although a solution of the Rankine-

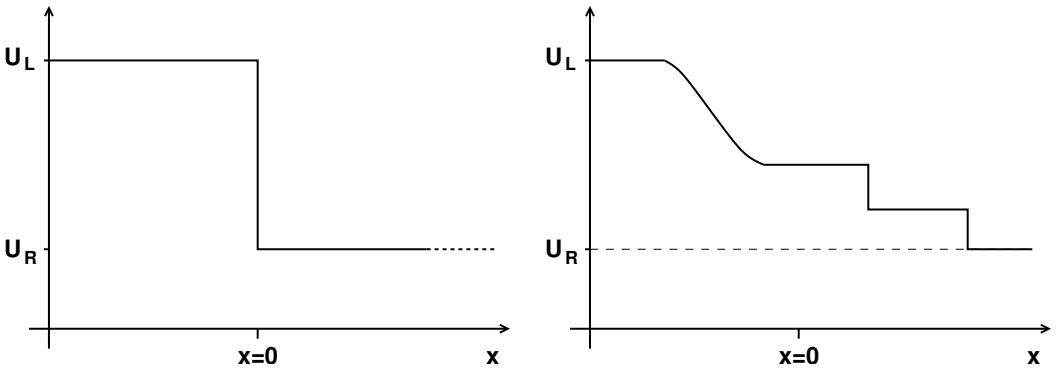

(a) (b)

Figure 2.2: (a) An example of the piecewise constant initial conditions in a Riemann problem showing a discontinuity in an arbitrary quantity as a function of x; (b) A possible solution (actually the mass density profile of the solution to the Sod shock tube Riemann problem) to the relaxation of the discontinuity in panel (a). From right to left the jumps correspond to a shock, a contact discontinuity and a rarefaction fan.

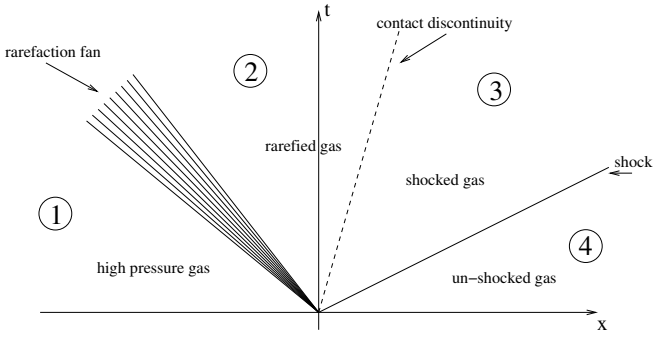

Figure 2.3: A space-time diagram of the self-similar solution of a Riemann problem showing the four zones which result and the three waves separating them. The waves shown here are, from left to right, a rarefaction wave, the contact discontinuity and a shock wave.

Hugoniot condition, is entropy violating[4] and should be replaced by a rarefaction fan.

A rarefaction wave has a head and a tail which travel with different speeds so that, over time, it spreads out in space into a self-similar structure called a rarefaction fan. As its name suggests, it connects regions of higher density and pressure with regions of lower values of those quantities. A shock is a simple discontinuity which obeys the Rankine-Hugoniot condition, Eq. 2.17. A shock causes an increase in density and

[4]The entropy in the unperturbed medium decreases as the wave passes which is in violation of the second law of thermodynamics. The implication is that the upstream and downstream states cannot be connected via a rarefaction "shock" without violating causality.

pressure as it passes. Also a simple discontinuity, a contact discontinuity is similar to a shock except that there is no jump in pressure as it passes. Since there is no pressure gradient, there will be no jump in velocity across the interface either and any discontinuity in density will simply be advected at the bulk flow velocity. When multi-dimensional flows are considered, shear flows can exist and in these cases the resolution is not just as simple as described in the preceeding sentence.

2.3.1 The shallow water equations[5]

To see how an understanding of these characteristic waves can help us solve the Riemann problem, let us consider a simpler set of hyperbolic conservation laws. We choose the shallow water equations as they are intuitive to understand and, since they consist of only two coupled PDEs, they have a two dimensional phase space which we can more easily visualise than the 3D phase space of the Euler equations. The shallow water equations, neglecting any bottom topography, can be written

$$\begin{aligned} \frac{\partial h}{\partial t} + \frac{\partial \left(hu\right)}{\partial x} &= 0, \\ \frac{\partial (hu)}{\partial t} + \frac{\partial}{\partial x}\left(hu^2 + \frac{1}{2}gh^2\right) &= 0, \end{aligned} \tag{2.18}$$

where $h = h(x,t)$ is the depth of the water, $u = u(x,t)$ is the local velocity of the water in the x-direction, and g is the acceleration due to gravity. Units in which $g = 1$ are often chosen when working with these equations and we follow this convention in the following discussion.

There are only two characteristic waves in the shallow water equations. Let us examine what effects these waves have on the height and momentum (hu, one of the conserved quantities in Eq. 2.18) of the water as they pass. We start by applying the Rankine-Hugoniot jump condition (Eq. 2.17) to the height and momentum to see which states can be connected to an arbitrary, constant state $(\hat{h}, \hat{h}\hat{u})$ by shocks of speed s. This gives us the two equations

$$\begin{aligned} m - \hat{m} &= s\left(h - \hat{h}\right), \\ \left(\frac{m^2}{h} + \frac{1}{2}gh^2\right) - \left(\frac{\hat{m}^2}{\hat{h}} + \frac{1}{2}g\hat{h}^2\right) &= s\left(m - \hat{m}\right), \end{aligned} \tag{2.19}$$

where we have defined momentum $m \equiv hu$. The shock speed s can easily be eliminated from these equations to give the momentum as a function of the initial, constant state

[5]Much of the discussion in this and the following few Sections can be found in many standard references in the literature, for example the excellent books by LeVeque (1994, 2002) and Toro (1999).

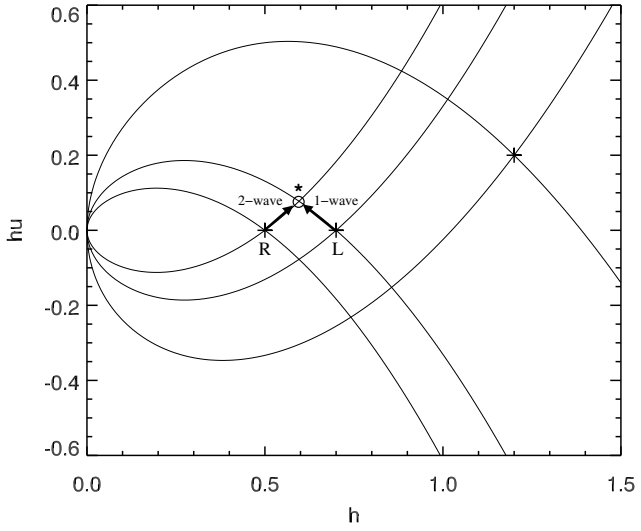

Figure 2.4: The Hugoniot curves associated with three arbitrary states (indicated by plus symbols) in the phase plane of the shallow water equations. The solution to the particular Riemann problem with left and right states marked by "L" and "R" respectively is shown by a circle with the label "$\star$". The characteristic waves referred to in the text are also highlighted by labelled arrows.

and the water depth

$$m(h) = \frac{\hat{m}h}{\hat{h}} \pm \sqrt{\frac{gh}{2\hat{h}}\left(h+\hat{h}\right)\left(h-\hat{h}\right)^2}. \tag{2.20}$$

Note the plus or minus sign; this function describes both shock types. We plot $m(h)$ in the phase space of the shallow water equations for various arbitrary initial points in Fig. 2.4. The constant states are indicated by plus symbols.

The set of states indicated by $m(h)$ are collectively known as the Hugoniot *locus* and represent the possible states to which an arbitrary initial state can be connected by means of a shock. This does not take into account whether a shock is entropy violating or not. To find the states which can be connected to the initial state by means of a rarefaction *wave*, we need to consider the integral curves for the system.

As is the case for shocks, there may not be a physically viable rarefaction wave branch leading from the initial state in phase space. In general though, given an arbitrary state in phase space, we can plot the points which can be connected to that state by a rarefaction wave. It turns out that these waves are subsets of the integral curves of the vector fields defined by the right eigenvectors of the Jacobian matrix of the system of equations (see for example LeVeque et al., 1998; LeVeque, 1994, 2002).

Integral curves are defined such that the tangent to the curve at any point lies in the direction of the eigenvector at that point. Due to their connection with the

eigenvectors of the Jacobian matrix, the integral curves are very similar in shape to the Hugoniot *locus* described earlier. This is especially true close to our arbitrarily chosen point in phase space and, it can be shown (Lax, 1973) that the curvature of both curves is the same. Although the integral curves diverge from the relevant Hugoniot locus, the overal shape is similar enough that we do not make any distinction in Fig. 2.4 since it is mainly for illustrative purposes.

An arbitrary point in the phase space of the shallow water equations can therefore be connected by two Hugoniot *loci* (one for each type of shock) and two integral curves (one for each type of rarefaction). Since it is either a shock or a rarefaction which modifies the piecewise constant states of a Riemann problem, the solution to the Riemann problem must lie at the intersection of two of these curves. The particular permutation of curves will be determined on physical grounds by the condition that entropy increases as the wave passes. To make this clearer, consider a Riemann problem for the shallow water equations[6] with initial conditions $\mathbf{U}_\mathrm{L} = (h = 0.7, hu = 0)$, $\mathbf{U}_\mathrm{R} = (h = 0.5, hu = 0)$. These are the two points side-by-side in the middle of the plot in Fig. 2.4 (marked "L" and "R"). The solution to this Riemann problem will be one of the intersection points on the curves through these initial states.

Intuition tells us that water will flow to the right, increasing the height of the water there at the expense of that on the left. If we look at the curves passing through $\mathbf{U}_\mathrm{L}$ and $\mathbf{U}_\mathrm{R}$, we see that they intersect in two locations. Both intersections have an intermediate water height which is higher than h_R and lower than h_L as we expected. In this instance we can choose between the two intersections because we know that the velocity at the point where the initial discontinuity was will be positive which makes the solution to this Riemann problem $h^\star \approx 0.6$, $m^\star \approx 0.75$. If we didn't have this insight however, we could still choose the correct intersection by considering the types of wave which are physically allowed. Contact discontinuities are not applicable in the shallow water equations. This leaves us with the two choices already discussed, shocks and rarefactions. Consider the right state ($h = 0.5$, $hu = 0.0$) of our Riemann problem and look at the curves for this state (Fig. 2.4). There are four paths of different states which we could follow from this point in phase space. If we label the left-most wave propagating from the discontinuity as the 1-wave and the right-most wave as the 2-wave then, by consulting the first of the jump conditions in Eq. 2.17, we can surmise that the curve which passes through $\mathbf{U}_\mathrm{R}$ from bottom-left to top-right is the wave with positive wave speed; the 2-wave. The other branch corresponds to the

[6] In this context, Riemann problems are often referred to as "dam break problems".

1-wave with negative wave speed[7]. We can eliminate the latter path because, as we have already stated, a rarefaction shock is an entropy violating, and thus unphysical, solution. We could perform a similar analysis on the left state but this is unnecessary as we have already uniquely identified the correct intersection and thus solved the Riemann problem.

2.3.2 Computing the inter-cell fluxes in Godunov's method

Returning to the original problem of determining the inter-cell fluxes for Godunov's scheme, we can think of the process schematically as in Fig. 2.5. Here we see four cells which form part of a 1D uniform computational grid. The cell centres are at positions marked as $\{x_j\}$ and a series of local Riemann problems are defined by the discontinuities between the different cell averaged values at positions $\{x_{j+1/2}\}$. In the figure, the vertical axis represents increasing time. The oblique lines originating from each Riemann problem represent some of the possible arrangements of the characteristics of the Euler equations; a thin solid line indicates a shock, a dashed line a contact discontinuity and the bundles of tightly packed lines show rarefaction fans. We have stated in Sect. 2.2.3 that we seek the value of all the fluid quantities evaluated at the interfaces between cells so that we may compute the fluxes. There are a few possibilities to consider: all of the characteristics could travel to the left of the interface, they could all travel to the right of the interface or, the interface could lie between waves going left and right. The first two scenarios are trivial since the values of the fluid variables at the interface will be direct copies of either the original left or right state. An example of this can be seen for the Riemann problem between the x_{j+1} and x_{j+2} cells in Fig. 2.5 where the fastest and slowest waves are both right travelling shocks. The interface values in the solution of this Riemann problem are just $\mathbf{U}_{j+1+1/2} = \mathbf{U}(x_{j+1})$. In the case where the waves travel in opposite directions we can use the idea developed above for the shallow water equations that the new state formed between the waves must be accessible from the left state through the wave which travels toward that state and also from the right state through the right-running wave. In the Euler equations there is a third wave, the contact wave, but this is not a problem so long as the solution is evaluated in terms of the primitive variables $(\rho, \mathbf{u}, p)$ since there is no jump in pressure or velocity across such a wave.

In the Euler equations, the phase space is now three dimensional[8] but we can still

[7] It just so happens that, in this case, the 1 and 2-waves are actually left and right-running. This is not always true in general.

[8] For simplicity, we assume that velocity only varies in the x-direction and only adds one dimension to the phase space as opposed to the three that would be added by considering more general flows.

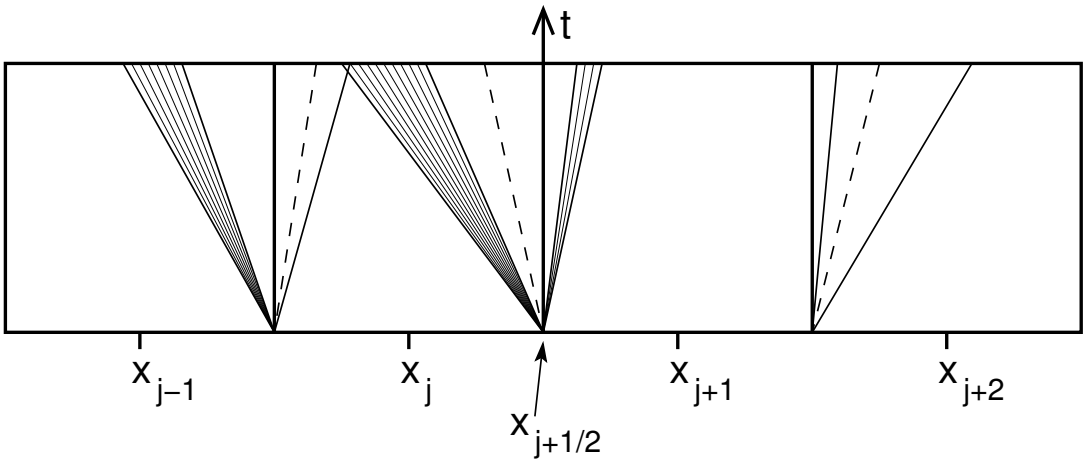

Figure 2.5: Godunov (1959) type methods advance the flow in time by solving local Riemann problems at cell interfaces to obtain inter-cell fluxes. This allows the fluid quantities to be updated in a conservative fashion.

derive an expression for the Hugoniot *locus* by applying the Rankine-Hugoniot jump condition to the Euler equations. If we project this three dimensional curve onto the pressure-velocity plane, then we have curves like those shown schematically in Fig. 2.6. Although the density varies along these curves, the energy is constant. In the figure we have assumed that the process of eliminating unphysical paths has already taken place, leaving the curves of a left travelling rarefaction, which reduces the pressure of the left state, and a right-going shock which increases the pressure and velocity of the right state. We label the constant state which forms between the two waves $(u^\star, p^\star)$. We now must address the crucial part of the method which was left out of our discussion on the shallow water equations; how to compute coordinates of the intersection point without resorting to graphical means since equating the curves in phase space leads to a non-linear equation.

The solution is to iterate. This can be done directly from the equations of the Hugoniot *locus* but, for the Euler equations, we describe a different method (see Richtmyer and Morton, 1994). We begin by rewriting the second Euler equation (describing the conservation of momentum of the fluid) in terms of the fluid variables on either side of some arbitrary wave

$$\rho_\star u_\star^2 + p_\star = \rho_0 u_0^2 + p_0, \tag{2.21}$$

where variables with a "0" subscript refer to material entering the wave (i.e. the initial left or right state of the Riemann problem) and a $\star$ subscript indicates material already processed by the wave. The fluid velocities in this equation are in the frame of the shock and so, to transform back to bulk flow velocities, we must add the speed

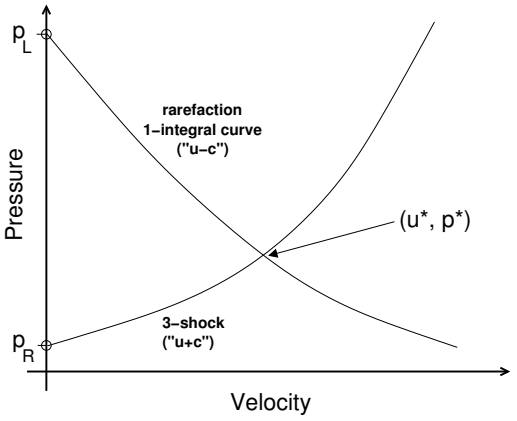

Figure 2.6: The loci of all possible states in a Riemann problem with a rarefaction moving to the left and a shock moving to the right in the velocity-pressure plane. The initial states are at left with zero velocity and the state marked (u^*, p^*) is the constant state formed between the shock and rarefaction wave.

of the wave.

From the equation of continuity of mass (the first Euler equation), we can define a mass flux $\rho_0 u_0 = \rho_\star u_\star \equiv M^\pm$, where "+" is used to distinguish a right-running wave from a left-running one, denoted by "−". Using this definition of mass flux, the equation above may be rewritten

$$M^\pm = \pm \frac{p_\star - p_0}{u_\star - u_0}. \tag{2.22}$$

The plus and minus signs continue to refer to the right and left characteristics respectively. If we recall the representation of the Riemann problem in the velocity plane (Fig. 2.6), then the above equation may be interpreted as the gradients of two lines in this plane. The lines have gradients of M^+ and $-M^-$ and, if we use p_R and p_L as values for p_0, the equations of the lines are

$$\begin{aligned} p &= M^+(u - u_\mathrm{R}) + p_\mathrm{R}, \\ p &= -M^-(u - u_\mathrm{L}) + p_\mathrm{L}. \end{aligned} \tag{2.23}$$

Assuming that these lines intersect at the point $(u_\star, p_\star)$ and eliminating $u_\star$ from the equations, we have

$$\frac{p_\star - p_\mathrm{R}}{M^+} + u_\mathrm{R} = u_\star = \frac{p_\star - p_\mathrm{L}}{-M^-} + u_\mathrm{L}, \tag{2.24}$$

which simplifies to

$$p_\star = \frac{M^+M^-(u_\mathrm{L} - u_\mathrm{R}) + M^+p_\mathrm{L} + M^-p_\mathrm{R}}{M^+ + M^-}. \tag{2.25}$$

To complete this equation for $p_\star$ we need values for $M^\pm$ which we can find by appealing to the first two fluxes of the Euler equations (see Eq. 2.2)

$$\begin{aligned} \rho_0 u_0 &= \rho_\star u_\star \equiv M^\pm, \\ p_0 + \rho_0 u_0^2 &= p_\star + \rho_\star u_\star^2, \end{aligned} \tag{2.26}$$

and combining them to arrive at

$$\left(M^{+,-}\right)^2 = \frac{p_\star - p_{\mathrm{R,L}}}{V_{\mathrm{R,L}} - V_\star}, \tag{2.27}$$

where $V \equiv 1/\rho$ and p, V assume values for the right or left states for M^+ and M^- respectively.

By substituting the equation of state for an ideal gas,

$$E = \frac{p}{\gamma - 1} + \frac{1}{2}\rho u^2, \tag{2.28}$$

into the third Euler flux (Eq. 2.2), $(E + p)u$, and using Eq. 2.27 above, the following ratio can be derived

$$\frac{\rho_{\mathrm{R,L}}}{\rho_\star} = \frac{p_{\mathrm{R,L}}(\gamma + 1) + p_\star(\gamma - 1)}{p_{\mathrm{R,L}}(\gamma - 1) + p_\star(\gamma + 1)}. \tag{2.29}$$

We use this ratio to eliminate $V_\star$ from Eq. 2.27, to give

$$M^{+,-} = \sqrt{p_{\mathrm{R,L}}\rho_{\mathrm{R,L}}}\sqrt{\frac{(\gamma+1)}{2}\left(\frac{p_\star}{p_{\mathrm{R,L}}}\right) + \frac{(\gamma-1)}{2}}, \tag{2.30}$$

for a shock. A similar expression can be derived for a rarefaction. Since a rarefaction wave is not a discontinuity, we can use the regular, isentropic theory straight from the Euler equations. We can of course write these equations in terms of the primitive (i.e. non-conservative) variables, replacing the equation for the conservation of energy with one for the conservation of entropy. Using these relations along with the relevant Riemann invariant ($u - \frac{2}{\gamma-1}c$ is a constant along the integral curve for rarefaction waves), we can find the expression for the mass flux for a rarefaction,

$$M^{+,-} = \sqrt{p_{\mathrm{R,L}}\rho_{\mathrm{R,L}}}\,\frac{(\gamma-1)}{2\sqrt{\gamma}}\,\frac{1 - (p_\star/p_{\mathrm{R,L}})}{1 - (p_\star/p_{\mathrm{R,L}})^{(\gamma-1)/2\gamma}}. \tag{2.31}$$

The full derivation can be found in Richtmyer and Morton (1994) for example. These formulæcan be combined into a single expression for the mass flux

$$M^{+,-} = \sqrt{p_{\mathrm{R,L}}\rho_{\mathrm{R,L}}}\;\phi\left(\frac{p_\star}{p_{\mathrm{R,L}}}\right), \tag{2.32}$$

if we define the function

$$\phi(x) = \begin{cases} \sqrt{\dfrac{\gamma+1}{2}x + \dfrac{\gamma-1}{2}}, & \text{for } x > 1 \\ \dfrac{\gamma-1}{2\sqrt{\gamma}}\,\dfrac{1-x}{1-x^{(\gamma-1)/2\gamma}}, & \text{for } x \le 1. \end{cases} \tag{2.33}$$

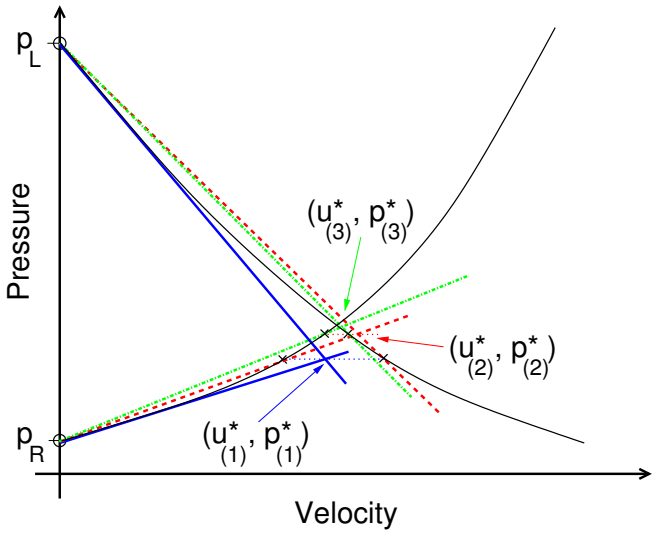

Figure 2.7: Graphical illustration of the iterative Riemann solver of Godunov. The true solution $(u^\star, p^\star)$ is the intersection of the black curves and the coloured lines show successive iterations $(u^\star_{(i)}, p^\star_{(i)})$ in search of this solution. Note how the intersection of one set of the coloured lines determines the gradient of the lines for the next iteration.

Note that $\phi(x)$ as written above is only valid for an ideal gas with constant γ. If a different, more general equation of state is used, this function must be modified.

To calculate the pressure in the region between the left and right characteristics in a Riemann problem using Eq. 2.25, we require the mass fluxes across both waves. Since the mass fluxes depend on $p_\star$, the solution is obviously iterative. We first make a guess at the pressure in regions (2) and (3) of Fig. 2.3, a reasonable starting point being the average value of p_L and p_R. We use this to calculate the gradients of the lines in the velocity-pressure plane and their intersection results in an improved value for $p_\star$ via Eq. 2.25. We insert this value into the equations to obtain new gradients and we repeat the process until convergence; that is, until there is no change in successive iterations to machine accuracy. The process is illustrated graphically in Fig. 2.7. The coloured lines show the successive approximations to the intersection of the correct, non-linear curves which are shown in black.

Once $p_\star$ is known to the desired accuracy, the velocity can be determined by eliminating $p_\star$ (instead of $u_\star$) from Eq. 2.24

$$u_\star = \frac{M^+ u_\mathrm{R} + M^- u_\mathrm{L} + p_\mathrm{L} - p_\mathrm{R}}{M^+ + M^-}. \tag{2.34}$$

The density can then be calculated in regions (2) and (3) of Fig. 2.3 once it is known which type of waves are present in the solution. To compute the density in region (2) or (3) (denoted $\rho^\star_\mathrm{L}$ and $\rho^\star_\mathrm{R}$ respectively) after a shock has passed, we can rearrange

Eq. 2.29, since it comes from the Rankine-Hugoniot jump conditions, to give

$$\rho^{\star}_{\mathrm{L,R}} = \rho_{\mathrm{L,R}} \left\{ \frac{\left(\frac{\gamma-1}{\gamma+1}\right) + \left(\frac{p_{\star}}{p_{\mathrm{L,R}}}\right)}{\left(\frac{\gamma-1}{\gamma+1}\right)\left(\frac{p_{\star}}{p_{\mathrm{L,R}}}\right) + 1} \right\}. \tag{2.35}$$

If the wave is a rarefaction, we can again use the isentropic law

$$p = k\rho^{\gamma}, \tag{2.36}$$

where k is a constant evaluated at the initial data state, and the relevant Riemann invariants to derive the following relation for the density

$$\rho^{\star}_{\mathrm{L,R}} = \rho_{\mathrm{L,R}} \left(\frac{p_{\star}}{p_{\mathrm{L,R}}}\right)^{\frac{1}{\gamma}}. \tag{2.37}$$

We now have all the necessary relations to find the fluid values in each region within the Riemann fan. Solving the Riemann problem is now just a matter of determining which of the states applies at $x_{j+1/2}$. Note that when the flow is *trans-sonic*, the solution may be found within the rarefaction fan and extra work is required to evaluate the fluid variables at $x_{j+1/2}$ in this instance. A further problem can occur in *degenerate* cases where the left and right state are connected by a single shock or rarefaction. Since any solution algorithm is required to select which of the correct mass flux formulæto apply (i.e. for a shock or a rarefaction) anyway, it can also monitor for these degenerate cases and perform the appropriate response which is usually to set, say, the right state equal to the left for a right travelling shock.

2.4 Choosing the time step

Until now we have left the computation of the time step undefined. The reason for this was to wait until the characteristic wave structure of hyperbolic conservation laws had been discovered.

The time step must be chosen carefully; too large and the whole numerical scheme could produce erroneous results which will likely lead to the total failure of the code. Choosing too small a time step is inefficient and wastes valuable CPU time.

The general rule when calculating a time step is that waves from one cell should not have time to interfere with the values in another, neighbouring cell. For some of the finite difference schemes described in Sect. 2.2.2, this means choosing a time step which is less than the time for a wave to reach the cell boundary. For example, in one dimension a time interval could be defined by $\Delta t < \Delta x/2(u_x + c)_{\max}$, where c is the sound speed and $(u_x + c)_{\max}$ is the fastest wave speed anywhere in the computational

domain. This definition of stability is known as the Courant-Friedrichs-Lewy (CFL) condition.

In Godunov's method, it doesn't matter if waves from neighbouring cells interact. All that is important is that the solution is constant at $\{x_{j+1/2}\}$ over the whole time step. In other words, the waves from a Riemann problem at $x_{j+1/2}$ must not be allowed to reach $x_{j-1/2}$ or $x_{j+1+1/2}$. This can be guaranteed as long as the time step is less than twice the time step defined in the previous paragraph.

In all our codes, we compute a time step which allows the maximum wave speed to just cover a distance Δx. This value is then scaled by multiplication by a number between zero and one. This parameter is referred to as the CFL parameter or Courant number and can be set anywhere less than 1.0 for Godunov schemes. Finite difference schemes like those mentioned above can use the same mechanism for computing the time step, but can only be expected to generate correct results if the time step thus calculated is scaled by a Courant number < 0.5.

2.5 Approximate Riemann solvers

From Sect. 2.3, we can see that the exact solution of arbitrary Riemann problems is computationally expensive; square root laden iterations must be performed at every cell interface on the computational grid, at every time step. Recall that, in Sect. 2.2.3, we saw how only the inter-cell fluxes are required to complete Godunov's numerical scheme. Much of the information acquired from computing the exact solution at the cell interfaces $\mathbf{U}^\star(x_{j\pm1/2}, t_n)$ is therefore discarded. Also, since the original Riemann problem was formed from left and right states which were computed from cell averaged approximations to the original solution anyway, we can increase computational efficiency without sacrificing accuracy if we can compute the inter-cell fluxes $\mathbf{F}^{n+1/2}_{j\pm1/2}$ directly through some form of approximation.

2.5.1 Roe's linearised solver

Linear hyperbolic equations like the advection equation (Eq. 2.10) are easily solved; the solution of a Riemann problem for such an equation will either be the left or right input state depending on the direction of the flow. By writing non-linear conservation laws like Eq. 2.1 in the form

$$\frac{\partial \mathbf{U}}{\partial t} + A\frac{\partial \mathbf{U}}{\partial x} = 0. \tag{2.38}$$

$A \in \mathbb{R}^{m\times m}$ is the flux Jacobian matrix for the system of equations where m is the number conservative equations. In general, A is still non-linear but if we linearise this matrix about some constant state which depends on the input states to a Riemann

problem, $\mathbf{U}_\mathrm{L}$ and $\mathbf{U}_\mathrm{R}$, then we can decouple the system of equations in Eq. 2.38 into m linear advection equations which are trivial to solve. We can do this because, as we mentioned in Sect. 2.1, one of the defining properties of a hyperbolic equation is having a Jacobian matrix which is diagonalisable with real eigenvalues.

If we write the linearised Jacobian matrix as $\hat{A} = \hat{A}(\mathbf{U}_\mathrm{L}, \mathbf{U}_\mathrm{R})$, then this matrix has right eigenvectors and eigenvalues defined by $\hat{A}\hat{\mathbf{r}}_i = \hat{\lambda}_i\hat{\mathbf{r}}_i$ where $(\hat{A} \in \mathbb{R}^{m\times m}, i = 1, m)$. As stated, the diagonalisability of $\hat{A}$ is guaranteed by hyperbolicity but Roe (1981) prescribed some other properties for the linearised Jacobian matrix.

(i) It constitutes a linear mapping from the vector space $\mathbf{U}$ to the vector space $\mathbf{F}$.

(ii) $\hat{A}(\mathbf{U}_\mathrm{L}, \mathbf{U}_\mathrm{R}) \rightarrow A(\hat{\mathbf{U}})$ smoothly as $\mathbf{U}_\mathrm{L}, \mathbf{U}_\mathrm{R} \rightarrow \hat{\mathbf{U}}$.

(iii) $\Delta\mathbf{F} = \hat{A}\Delta\mathbf{U} \quad \forall\, \mathbf{U}_\mathrm{L}, \mathbf{U}_\mathrm{R}$.

(iv) The eigenvectors of $\hat{A}$ are linearly independent.

Important for the development of an approximate Riemann solver are condition (iii) and condition (iv). Condition (iii) when compared to the Rankine-Hugoniot jump condition (Eq. 2.17) shows that the eigenvalues of $\hat{A}$ are the wave speeds of the (linearised) characteristic waves. Condition (iv) allows us to use the eigenvectors of the Jacobian matrix as basis vectors in the phase space of the system of equations, and therefore to decompose the jump $\Delta\mathbf{U} \equiv \mathbf{U}_\mathrm{R} - \mathbf{U}_\mathrm{L}$

$$\Delta\mathbf{U} = \sum_{i=1}^{m} \alpha_i\hat{\mathbf{r}}_i. \tag{2.39}$$

The solution of the Riemann problem can be found by starting with either the left or right input state and only counting those waves which affect that state. That is

$$\mathbf{U}(x_{j+1/2}) = \begin{cases} \mathbf{U}_\mathrm{L} + \sum\limits_{\hat{\lambda}_p<0} \alpha_p\hat{\mathbf{r}}_p, \\ \mathbf{U}_\mathrm{R} - \sum\limits_{\hat{\lambda}_p>0} \alpha_p\hat{\mathbf{r}}_p, \end{cases} \tag{2.40}$$

This construction allows Roe's solver to "recognise" shocks. Consider, for example, that a single shock is propagating to the right in the shallow water equations. In this case $\mathbf{U}_\mathrm{R}$ lies on the Hugoniot *locus* of $\mathbf{U}_\mathrm{L}$ and they are both connected by a single wave, as illustrated in Fig. 2.8(a). The solution at the interface will be the value of the left state and we show the solution predicted by the Roe solver using Eq. 2.40 as the box symbol at the end of the solid, thick black line. The line is in the direction of one of the two linearised eigenvectors of the shallow water equations and is a powerful illustration of the process of linearisation; the real, non-linear Hugoniot curve has been replaced by a straight line in phase space.

Figure 2.8(a) shows the importance of choosing the constant average state $\hat{\mathbf{U}}(\mathbf{U}_\mathrm{L}, \mathbf{U}_\mathrm{R})$ around which the Jacobian matrix is linearised. The dashed line and

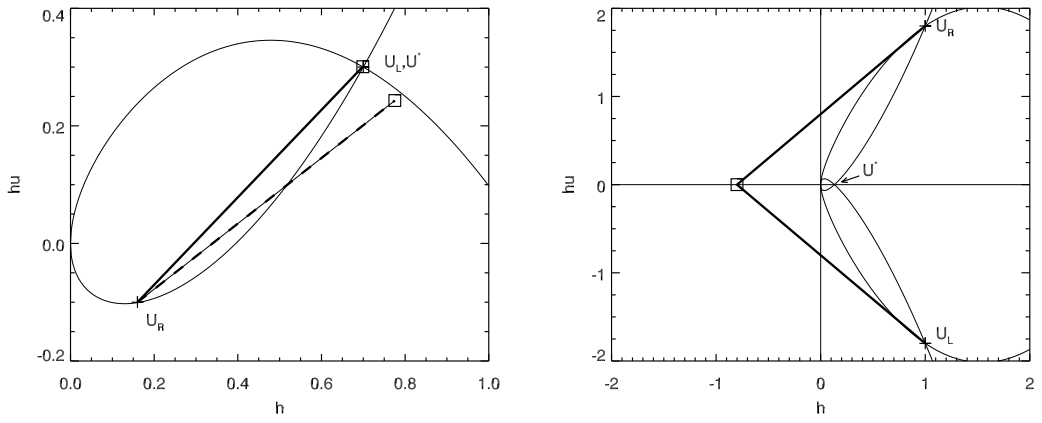

(a) (b)

Figure 2.8: Illustration of the Roe linearisation using the two dimensional phase space of the shallow water equations as an example. Two Riemann problems are shown here. In (a) a single shock moves with constant speed from left to right. The Roe approximation to the solution (square box with solid black line) matches the exact solution in this case. The dashed line and box symbol illustrate the importance of the average used to define the linearisation. The plot in (b) shows how the Roe solver can fail in the presence of strong rarefactions. Not only are the approximate and true solutions far apart, but the Roe solver computes an unphysical, negative depth.

connected box symbol in the plot show the result of computing the solution to the Riemann problem using the naive arithmetic average $\hat{\mathbf{U}} = (\mathbf{U}_\mathrm{L} + \mathbf{U}_\mathrm{R})/2$. The real art of constructing $\hat{A}$, the "Roe matrix", is finding "Roe averages" for each of the fluid quantities which ensure that the matrix satisfies each of Roe's properties (i)-(iv). For the shallow water equations, these averages become:

$$\hat{h} = \frac{h_\mathrm{L} + h_\mathrm{R}}{2}, \quad \text{and} \quad \hat{u} = \frac{u_\mathrm{L}\sqrt{h_\mathrm{L}} + u_\mathrm{R}\sqrt{h_\mathrm{R}}}{\sqrt{h_\mathrm{L}} + \sqrt{h_\mathrm{R}}}. \tag{2.41}$$

We have seen that Roe's linearisation allows us to solve the Riemann problem. All that is needed is the eigen-system of the Roe matrix which is already a saving on the iterative scheme. The real computational speed increase comes however, from the ability of the Roe method to return the information about the solution in a ready to use form; the Roe solver can compute the fluxes directly.

If we combine Roe's condition (iii)

$$\Delta\mathbf{F} = \hat{A}\Delta\mathbf{U}, \tag{2.42}$$

with the eigenvector decomposition for the jump $\Delta\mathbf{U}$, we get

$$\Delta\mathbf{F} = \hat{A}\sum_{p=1}^{m} \alpha_p \hat{\mathbf{r}}_p. \tag{2.43}$$

Since the $\hat{\mathbf{r}}_p$ are eigenvectors of $\hat{A}$, we arrive at the final expression for the jump in the fluxes between the left and right state,

$$\Delta\mathbf{F} = \sum_{p=1}^{m} \hat{\lambda}_p \alpha_p \hat{\mathbf{r}}_p. \tag{2.44}$$

Copying the form of Eq. 2.40,

$$\mathbf{F}_{j+1/2}^{n+1/2} = \begin{cases} \mathbf{F}(\mathbf{U}_\mathrm{L}) + \sum\limits_{\hat{\lambda}_p<0} \hat{\lambda}_p \alpha_p \hat{\mathbf{r}}_p, \\ \mathbf{F}(\mathbf{U}_\mathrm{R}) - \sum\limits_{\hat{\lambda}_p>0} \hat{\lambda}_p \alpha_p \hat{\mathbf{r}}_p, \end{cases} \tag{2.45}$$

Both forms are equivalent but for better stability, they are often combined by taking their arithmetic average

$$\mathbf{F}_{j+1/2}^{n+1/2} = \frac{1}{2}\left(\mathbf{F}(\mathbf{U}_\mathrm{L}) + \mathbf{F}(\mathbf{U}_\mathrm{R})\right) - \sum_{p=1}^{m} |\hat{\lambda}_p| \alpha_p \hat{\mathbf{r}}_p. \tag{2.46}$$

This is the Roe inter-cell flux which can be used to update the conservative variables using Eq. 2.15.

The Roe solver has the useful property that jumps which are already eigenvectors of the flux Jacobian matrix are solved exactly, despite the linearisation. Unfortunately the Roe solver has some shortcomings which we will now discuss.

2.5.2 Shortcomings of the Roe solver

One problem with the Roe solver is the treatment of rarefaction fans. Since the solution consists entirely of discontinuous jumps, the Rarefaction fan is just treated like a rarefaction shock. We have seen before (see Sect. 2.3) that rarefaction shocks are entropy violating and can lead to problems in the solution. For most Riemann problems it is not a problem since only the flux at $x_{j+1/2}$ is needed. When the solution contains a trans-sonic rarefaction fan however, the solution is expected to fall in the middle of the rarefaction fan which is simply not possible with the Roe solver. In this instance, the Roe solver can produce non-physical results (see Fig. 2.9 for example). This problem can be cured however, by the application of an "entropy fix". Roe (1981) himself discussed a possible fix as did Harten and Hyman (1983).

A more serious problem with the Roe solver, can be seen in Riemann problems with strong rarefactions which create a low density state. The phase space of such a Riemann problem for the shallow water equations is shown in Fig. 2.8(b). The two initial states for the Riemann problem are shown, labelled $\mathbf{U}_\mathrm{L}$ and $\mathbf{U}_\mathrm{R}$ as usual. Also indicated is the true solution of this Riemann problem, $\mathbf{U}^\star$, and the approximate

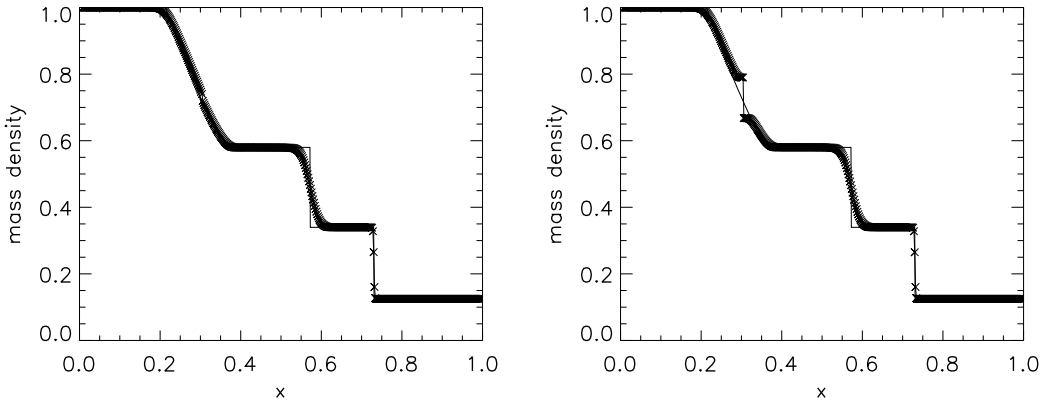

(a) (b)

Figure 2.9: The failure of the Roe solver for trans-sonic flows is demonstrated here with the solution to a modified Sod shock tube problem (Toro test 1). In panel (a) we see the numerical solution with an iterative Riemann solver and, in (b), the solution as computed using a linearised Roe solver. The exact solution is shown as a solid line in both plots. The resolution for both simulations was 500 cells with a Courant number of 0.9.

solution as computed using the Roe solver. The latter is shown as a box at the end of two thick black lines which show how the solution is found by following the eigenvector which represents either the left or right-running rarefaction wave, from either the left or right initial state. The problem is not just the error between the approximate and the true solution, it is the value of h found by the Roe solver. Remember that h represents the depth of water in the shallow water equations and a negative depth is obviously unphysical. More than that, this would actually lead to any computer code crashing since it would at some point have to evaluate characteristic speeds which require taking a square root of h. A similar problem exists in the Euler equations where mass density and pressure take on unphysical negative values which would also lead to failure of the scheme. Einfeldt et al. (1991) proved that for certain Riemann problems, e.g. the strong double rarefaction described here, *no* linearisation will maintain positivity of the solution. To solve this problem we must find an approximate Riemann solver which does not fail and which is at least as accurate as Roe's solver. If we cannot find a scheme which is as accurate as we desire, we can also build an adaptive code which detects Riemann problems for which the Roe solver will fail and, in these circumstances, uses the more robust but less accurate Riemann solver. Luckily, as well as showing the cases in which the Roe solver is doomed to failure, Einfeldt (1988) also proposed a more robust scheme which we now consider.

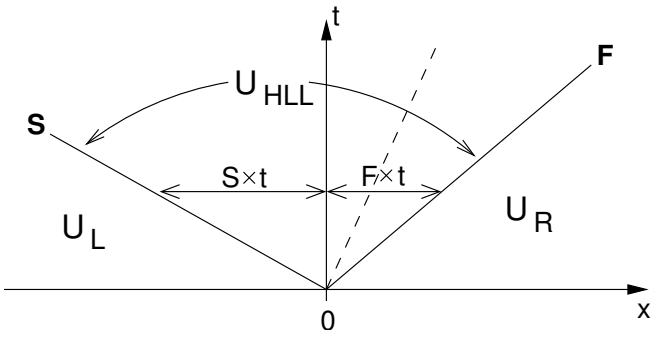

Figure 2.10: The three states in the HLL family of approximate Riemann solvers. F and S are the speeds of the fastest and slowest waves respectively. Between these waves, a region opens separating the original left and right states of the Riemann problem ($U_{\rm L}$ and $U_{\rm R}$) with a new constant state $U_{\rm HLL}$.

2.5.3 The HLL, HLLE and HLLEM schemes

In the previous section, we saw how the approximate solver of Roe may fail in regions of low density. We therefore consider another class of approximate Riemann solvers.

Harten et al. (1983) proposed a Riemann solver which used only the fastest left and right going waves emanating from the interface in a Riemann problem. Their method is often referred to as a three state solver since the two wave signals divide space and time into three distinct regions as shown in Fig. 2.10. The states $U_{\rm L}$ and $U_{\rm R}$ are the undisturbed left and right states of the Riemann problem and as the two waves propagate outward, the region between $x = -St$ and $x = +Ft$ assumes a new constant value $U_{\rm HLL}$. We can write the solution of this Riemann problem thus

$$U^{\star}(x,t) = \begin{cases} U_{\rm L} & \text{for } x \leq St, \\ U_{\rm HLL} & \text{for } St \leq x \leq Ft, \\ U_{\rm R} & \text{for } x \geq Ft. \end{cases} \tag{2.47}$$

In a Godunov type numerical scheme, the conserved quantities are evolved in time through the inter-cell fluxes via

$$U_i^{n+1} = U_i^n - \frac{\Delta t}{\Delta x}\left(f_{i+1/2}^n - f_{i-1/2}^n\right), \tag{2.48}$$

Using Eq. 2.47 in the integral form of the conservation laws (Eq. 2.13), the corresponding fluxes become

$$f_{i+1/2}^{\rm HLL} = \frac{b_{i+1/2}^+ f(U_i) - b_{i+1/2}^- f(U_{i+1}) + b_{i+1/2}^+ b_{i+1/2}^- (U_{i+1} - U_i)}{b_{i+1/2}^+ - b_{i+1/2}^-}. \tag{2.49}$$

Here the positive and negative wave signals are defined $b^+ \equiv \max\{b_{i+1/2}^{\rm R}, 0\}$ and $b^- \equiv \min\{b_{i+1/2}^{\rm L}, 0\}$. Harten et al. didn't specify a concrete choice for the wave speed

$b^{\mathrm{L}}_{i+1/2}$ and $b^{\mathrm{R}}_{i+1/2}$. The first implementation of such a scheme is due to Einfeldt (1988) who suggested the following choice for the wave speeds

$$\begin{aligned} b^{\mathrm{L}}_{i+1/2} &= \min\left\{\bar{u} - \bar{c}, u_i - c_i\right\}, \\ b^{\mathrm{R}}_{i+1/2} &= \max\left\{\bar{u} + \bar{c}, u_{i+1} + c_{i+1}\right\}, \end{aligned} \tag{2.50}$$

where u_i is the longitudinal velocity (that is, the component of the velocity vector which is orthogonal to the cell boundary) in the i^{th} cell, $c_i = \sqrt{\gamma p_i/\rho_i}$ is the sound speed in that cell and the over-bars denote the Roe average from Sect. 2.5.1. Note that $\bar{u} - \bar{c}$ and $\bar{u} + \bar{c}$ are the minimum and maximum eigenvalues of the Roe matrix for the Euler equations and so the so-called HLLE scheme avoids the cavitation problems experienced with the Roe solver by comparing the linearised characteristic speeds with their cell-centred values to the left and right of the interface and choosing whichever moves away from the cell interface fastest. This effectively provides extra diffusion which makes the HLLE scheme more robust.

Einfeldt et al. (1991) showed that although this choice was robust, it provided more numerical diffusion than was absolutely necessary. After a more rigorous investigation, they found that the sharpest possible results which still maintained positivity of the solution came from the modification

$$b^{\mathrm{L}}_{i+1/2} = \min\left\{\bar{u} - \bar{c}, u_i - \beta c_i\right\}, \tag{2.51}$$

$$b^{\mathrm{R}}_{i+1/2} = \max\left\{\bar{u} + \bar{c}, u_{i+1} + \beta c_{i+1}\right\}, \tag{2.52}$$

where $\beta = \sqrt{(\gamma - 1)/2\gamma}$. In the same paper, Einfeldt et al. also show that the HLLE scheme does not require an entropy fix as Roe's linearised scheme does.

The diffusivity of the HLLE scheme makes the scheme more robust but a diffusive scheme is normally very poor at resolving sharp gradients in the flow. HLLE is actually quite good at resolving shocks, even in a first order scheme, as can be seen in the tests at the end of this chapter (Figs. (B.3-B.18)). This is not so surprising since the scheme often defaults to the eigenvalues of the Roe matrix, bestowing the same shock-capturing properties as that scheme on HLLE. The problem is with the resolution of the contact discontinuity, however. In the three state description, this characteristic wave was omitted completely leading to a smeared representation of contacts. Two types of fix are proposed in the literature; the introduction of a third wave to represent the contact discontinuity such as in the HLLC scheme of Toro et al. (1994) (also described in Toro, 1999, Chap. 10) and Einfeldt's own modification, HLLEM. We choose to implement the latter fix since Wesenberg (2003) has shown that this may be easily extended to magnetohydrodynamics (although we note that MHD versions of HLLC also exist) with a tabulated equation of state (MHD-HLLEM); an important

consideration given the impetus of this work was the incorporation of magnetic field physics into a three-dimensional code for the simulation of mergers between compact stellar remnants (see Chap. 3 for a full description of this code).

Einfeldt's HLLEM modification adds anti-diffusion terms to the linear degenerate fields[9] (i.e. any discontinuities which are advected with the local flow) by modifying the numerical inter-cell fluxes

$$f^{\rm HLLEM}_{i+1/2} \equiv f^{\rm HLL}_{i+1/2} - \frac{b^+_{i+1/2} b^-_{i+1/2}}{b^+_{i+1/2} - b^-_{i+1/2}} \sum_p \delta^{(p)}_{i+1/2} \hat{\lambda}^{(p)}_{i+1/2} \hat{\mathbf{r}}^{(p)}_{i+1/2}, \tag{2.53}$$

where the

$$\delta^{(p)}_{i+1/2} \equiv \frac{\hat{c}_{i+1/2}}{\hat{c}_{i+1/2} + |\bar{u}_{i+1/2}|}, \qquad \forall p, \tag{2.54}$$

are referred to as anti-diffusion coefficients. They are defined such that excess dissipation is removed from the linear degenerate fields only (treating shear waves and the contact discontinuity on an equal footing). In this way, numerical stability of the scheme is maintained.

2.6 Higher Resolution Methods

2.6.1 Increasing the spatial accuracy of Godunov's method

Godunov's method (Sec. 2.2.3) can be thought of as the first order spatially accurate version of a whole class of reconstruct-solve-average (RSA) schemes. In the Godunov scheme, the reconstruction is a constant value function over the whole cell, i.e.

$$U(x) = U_j, \tag{2.55}$$

where U_j is the cell averaged value of a given quantity and $x \in [x_{j-1/2}, x_{j+1/2}]$. The value of the interpolated function $U(x)$ at the cell interfaces determines the left and right states of the Riemann problem which is then solved to update the quantity U_j at the next time step.

The next logical extension of this scheme is to use a piecewise linear interpolation for the reconstruction step such as

$$U(x) = U_j + (x - x_j)\frac{U_{j+1} - U_j}{x_{j+1} - x_j}. \tag{2.56}$$

A constraint on our interpolation is that it must still give the same cell average and this is implicitly achieved in Eq. 2.56 since the line passes directly through the point

[9] Characteristic waves, like the contact discontinuity, which are not genuinely non-linear are referred to as being "linear degenerate fields".

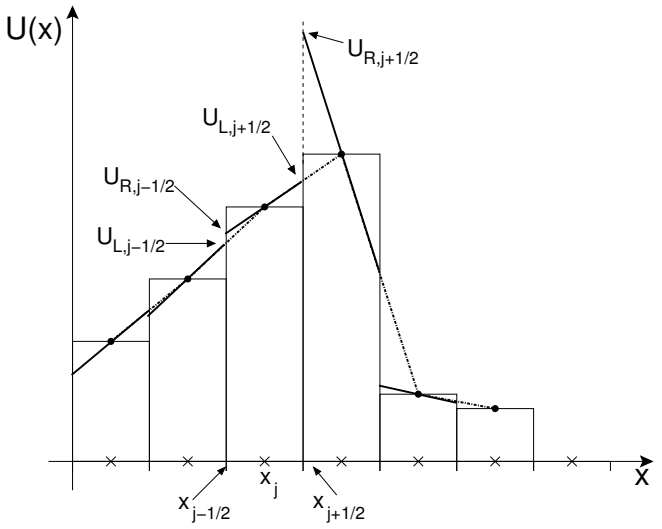

Figure 2.11: Graphical depiction of the linear reconstruction described in Eq. 2.56. The discontinuous, thick, black lines through the points (x_j, U_j) show the piecewise linear nature of the interpolant $U(x)$. The slope in the j^{th} cell is determined by the slope of the line connecting U_j with U_{j+1} as indicated by the dashed lines through each cell. The cell interface values are simply the values of $U(x)$ at the boundaries of each cell.

(x_j, U_j).[10] There is a problem with this simple reconstruction however; if the left and right interface values for input to the Riemann problem are computed from $U(x)$ as depicted graphically in Fig. 2.11, then spurious oscillations may arise in the solution near sharp discontinuities. Consider the slope at x_{j+1} from which the interface value $U_{\mathrm{R},j+1/2}$ is calculated; clearly the slope computed by Eq. 2.56 is too great leading to an interface value which is too large. It is not just because this point is an extremum of the original data either; the same slope would be generated regardless of the data on the left. Evolution of the conservation laws based on these interface values may generate a new value which is outside the range $[U_j, U_{j+1}]$. Therefore we have introduced a new extremum in the form of an *overshoot* which grows with time into an unphysical oscillation.

The oscillation in cell x_{j+1} develops because the slope is too large. We need therefore, to find a way of limiting the slope, at least in the region of discontinuities and extrema. We describe any scheme which does not introduce any new extrema as being *monotonicity* preserving. The first numerical method to make use of piecewise

[10] While a centred construction may seem more obvious to obtain the slope of $U(x)$ it turns out that the choice in Eq. 2.56 gives the same 2^{nd}-order accuracy (see for example LeVeque, 2002, §6.5) and so we are free to choose any of the three choices of upwind, centred or downwind. The choice made here, incidentally, is that of the Lax-Wendroff scheme.

linear interpolation and to address the issue of monotonicity in the solution is called MUSCL[11] and is described in detail in van Leer (1979) and references therein (the paper is the final in a series of five where van Leer develops the ideas required to make a stable scheme). MUSCL is an example of a total variation diminishing (TVD) scheme; if we define a quantity called the *total variation*

$$TV = \sum_j |u_{j+1} - u_j|, \tag{2.57}$$

then a TVD scheme is one in which the total variation does not grow from one time step to the next:

$$TV(u_{n+1}) \leq TV(u_n). \tag{2.58}$$

Since we do not make use of a piecewise linear scheme in the present work, we shall end our discussion at this point with the *nota bene* that any algorithm which modifies the slope in cell j based on U_j in relation to its neighbouring cells will thus lead to a nonlinear scheme by construction.

2.6.2 PPM - the piecewise parabolic method

We can continue to increase the order of the reconstruction polynomial $U(x)$ (see for example, the recent PQM method of White and Adcroft, 2008). In the astrophysically relevant, three dimensional code described in Chap. 3, we use the piecewise parabolic method (PPM) of Colella and Woodward (1984) which we will summarise here. It will be seen that, already with a parabolic reconstruction, the scheme is quite complicated and requires much more work to obtain the input values for each local Riemann problem than simply reading off the values of $U(x)$ at each cell interface.

As usual for an RSA scheme, our starting point is the discretized values of a given quantity $\{U_j\}$. We seek to construct a piecewise parabolic function $U(x)$ such that

$$U_j = \frac{1}{\Delta x_j} \int_{x_{j-1/2}}^{x_{j+1/2}} U(x) \mathrm{d}x, \tag{2.59}$$

i.e. the interpolation should preserve the cell averaged value U_j. The interpolant should not introduce any new extrema than are already present in $\{U_j\}$. The quadratic interpolant $U(x) = \alpha x^2 + \beta x + \gamma$, may be written (see App. A)

$$U(x) = U_{\mathrm{L},j} + \xi(\Delta U_j + U_{6,j}[1 - \xi]), \tag{2.60}$$

where

$$\xi \equiv \frac{x - x_{j-1/2}}{\Delta x_j}, \quad x \in [x_{j-1/2}, x_{j+1/2}], \quad \Delta U_j \equiv U_{\mathrm{R},j} - U_{\mathrm{L},j}, \tag{2.61}$$

[11] Monotonic Upwind-centred Scheme for Conservation Laws

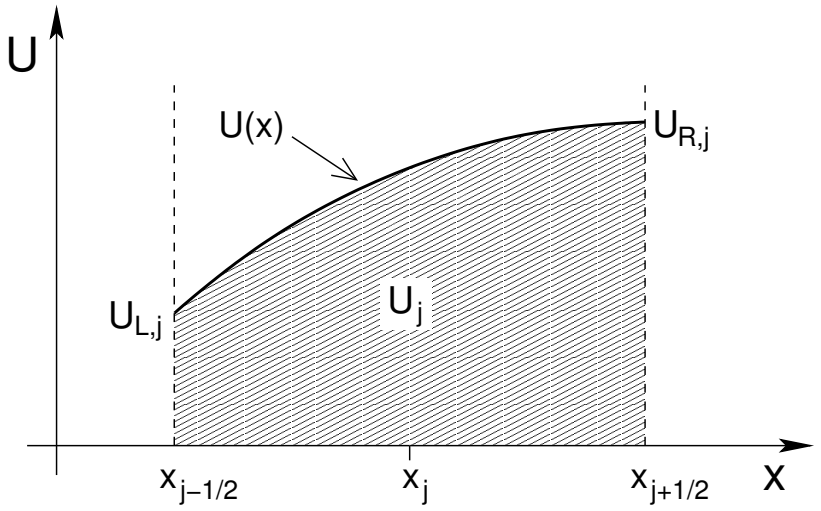

Figure 2.12: A piecewise parabolic interpolation function $U(x)$ is shown with the three constraints on its shape: U_j, the cell averaged value which fixes the area under the interpolant; $U_{\mathrm{L},j}$ and $U_{\mathrm{R},j}$ the values of the reconstruction at the interfaces with the neighbouring two cells which are approximated from a higher order polynomial and modified to help prevent spurious oscillations in the solution.

and

$$U_{6,j} \equiv 6\left(U_j - \frac{1}{2}\left[U_{\mathrm{L},j} + U_{\mathrm{R},j}\right]\right). \tag{2.62}$$

As illustrated in Fig. 2.12, the quadratic in Eq. 2.60 requires three constraints to fix its shape and position. One of these is provided by Eq. 2.59, but we still need to find values for $U_{\mathrm{L},j}$ and $U_{\mathrm{R},j}$, the values of $U(x)$ at the edges of cell j. To fix these values, Colella and Woodward use a higher order polynomial to obtain approximations to $U_{j\pm1/2}$ which are then modified by monotonization and discontinuity detection algorithms which we will describe in due course. In the PPM algorithm, a quartic polynomial is interpolated through the points $(x_{j+k\pm1/2}, V_{j+k\pm1/2})$, $k = 0, \pm1, \pm2$, where $V_{j\pm1/2}$ are the values of the indefinite integral

$$V(x) = \int U(x')\mathrm{d}x', \tag{2.63}$$

at the edges of cell j. This quartic function is then differentiated to provide a cubic approximation to $U_{j\pm1/2} = \mathrm{d}V/\mathrm{d}x|_{x_{j\pm1/2}}$. In regions far from extrema where the quantity U has a smooth profile, $U_{\mathrm{L},j+1} = U_{\mathrm{R},j} = U_{j+1/2}$, and the interpolation is continuous at $U_{j+1/2}$. The monotonization algorithm may change these initial guesses and it is at this point that the discontinuities are introduced between cells. In regions of smooth flow and using a computational grid with uniform cells, the interpolation scheme implemented in PPM leads to a scheme which is fourth order accurate.

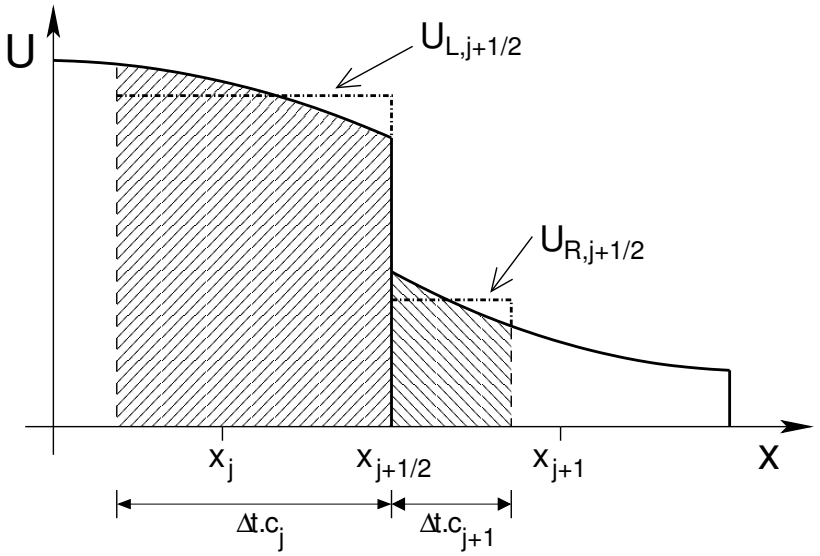

Figure 2.13: After a piecewise parabolic reconstruction is achieved, the left and right input values to the Riemann problem at each cell interface ($U_{\mathrm{L},j+1/2}$ and $U_{\mathrm{R},j+1/2}$) are computed as shown. In a time interval Δt, corresponding to the current time step, only the shaded areas are causally connected to the interface at $x_{j+1/2}$ by waves travelling at c_j and c_{j+1}. The inputs to the Riemann solver are found by averaging the interpolant over these regions.

In order to better capture shocks and contact discontinuities in the flow, PPM makes use of a detection algorithm which steepens the interpolated profile in a cell which is deemed to be within a discontinuity. Since the gradient of the interpolant in such a cell is determined from piecewise linear distributions in the neighbouring cells, the scheme does not drop below second-order accuracy in cases where a discontinuity was falsely detected.

Once the interpolation is completed such that we have a piecewise parabolic reconstruction of the data in each cell which fulfils the criteria for monotonicity etc., the left and right states for each local Riemann problem can be computed. Figure 2.13 graphically illustrates the procedure. There are two main choices to construct the input values for the Riemann problem; we can take the value of the interpolant on left and right sides of each cell boundary or we can average the interpolant over some region. Obviously choosing the cell average would be pointless since this has been conserved throughout the interpolation procedure and would leave us with Godunov's scheme. The values of $U(x)$ at each cell interface could be used but, in the PPM scheme, we choose the averaging route for which we must find a suitable region over which to integrate the interpolant such that we obtain a high resolution scheme.

The solution to a Riemann problem (see Sect. 2.3) depends on the number and type of characteristic waves crossing the interface during a single time step Δt. If we denote

the velocity of the fastest wave in the j^{th} cell which will influence the Riemann problem at $x_{j+1/2}$ by c_j, then we can express the domain of dependence for that Riemann problem by $[x_{j+1/2} - c_j\Delta t, x_{j+1/2} + c_{j+1}\Delta t]$. These are the shaded areas in Fig. 2.13. The left and right states for this Riemann problem are thus computed by averaging the interpolated profile of each quantity over the ranges $[x_{j+1/2} - c_j\Delta t, x_{j+1/2}]$ and $[x_{j+1/2}, x_{j+1/2} + c_{j+1}\Delta t]$ respectively. In practise, for the Eulerian formulation of PPM which we utilise, this step requires solving the characteristic form of the Euler equations. See Colella and Woodward (1984) for the details.

The left and right states having been calculated for all the local Riemann problems between each cell on the grid, the Riemann solver of choice computes a solution and the inter-cell fluxes are thus found. These fluxes allow the conservative quantities to be advanced to the next time step. Source terms etc. are applied and the process then begins again with the reconstruction of a new piecewise parabolic profile for each quantity.

A final note before we conclude our summary of the PPM scheme: Even though the PPM scheme is intended to be monotonicity preserving, there are certain conditions, under which, small amplitude, post-shock oscillations are observed. This is especially the case for shocks whose speed is small relative to the post-shock characteristic speed. Colella and Woodward proposed the application of extra dissipation (an artificial viscosity) and flattening of the interpolated profiles in cells around steep gradients in the data, essentially lowering the order of the scheme in such regions. We merely note here that we make use of the simplest scheme described in Colella and Woodward (1984) but that we normally do not add any extra numerical diffusion.

2.7 Numerical Tests

Before a numerical scheme can be used to solve any *real* problem, we must first be confident that it will produce valid results. Equally, even for tried and tested numerical schemes it is useful to know if we have implemented that scheme correctly. To eliminate the possibility of programming error and to evaluate the suitability of a numerical scheme for a particular task, we can compare results computed with that scheme to an analytic solution if one is available. In the case of non-linear equations such as the Euler equations this could be problematic but, since we have seen that an iterative Riemann solver can return results which are accurate to machine precision, we can at the very least find a reference solution by computing the problem with such an iterative Riemann solver at high resolution.

This is the approach taken here. In this section we present the results of some

standard tests for numerical hydrodynamics schemes and quantitatively evaluate their performance by comparing to a reference solution. After showing the actual solutions for some one and two dimensional problems, we compare them to the reference solution by means of a normalised error. We take the L_1 norm of the error in the computed mass density which is quite common in the field. This "L_1-error" is defined

$$\epsilon_{\mathrm{L1}} \equiv \sum_{i,j} |\rho_{ij}^{\mathrm{ref}} - \rho_{ij}| \Delta x_i \Delta y_j. \tag{2.64}$$

Obviously in one dimension it is only necessary to scale the sum by Δx.

We stated at the beginning of this chapter that we are interested in the inclusion of magnetic field physics in our astrophysically specialised computer code (see Chap. 3 for a full description of this code: CHARYBDIS). We are interested therefore, in numerical schemes which are as simple to code and as computationally efficient as possible so that they may be extended to solve the equations of magnetohydrodynamics. Our astrophysical code uses PPM (see Sect. 2.6.2) for its excellent treatment of contact discontinuities since for various reasons we are required to track chemical species which are advected in the same manner as contact discontinuities. The full astrophysical code came about as a considerable extension of the PROMETHEUS code which is an implementation of the PPM scheme – including advection of an arbitrary number of scalar quantities – by Fryxell et al. (1989). We have used the PPM skeleton of PROMETHEUS to compute all the tests in this section in conjunction with the various Riemann solvers discussed in preceding sections.

2.7.1 1D shock tube tests

In his excellent book on the subject of Riemann solvers, Toro (1999) lists five simple one dimensional shock tube problems.[12] A shock tube problem is the name given to what is essentially a real world Riemann problem. Imagine a length of tube which is thin enough to have negligible variation in the fluid variables in the directions perpendicular to the tube. If a diaphragm is placed in this tube so as to separate two regions of different but piecewise constant fluid states, then we have a Riemann problem; when the diaphragm is removed, various waves will propagate outwards, thus creating a distinct profile in each quantity which can be compared. The initial states for these five problems are listed in Table 2.1.

We computed solutions to the five Toro tests with PROMETHEUS using an iterative Riemann solver and the approximate Roe, HLLE and HLLEM solvers. For reference, we include the exact solution computed using code supplied by Toro (1999) which

[12]Strictly speaking, problem two is not a "shock tube" since the initial velocities are non-zero.

Test	ρ_L	ρ_R	u_L	u_R	p_L	p_R	x_0	t_{max}
1	1.0	0.125	0.0	0.0	1.0	0.1	0.3	0.2
2	1.0	1.0	-2.0	2.0	0.4	0.4	0.5	0.15
3	1.0	1.0	0.0	0.0	1000.0	0.01	0.5	0.012
4	1.0	1.0	0.0	0.0	0.01	100.0	0.4	0.035
5	5.99924	5.99242	19.5975	-6.19633	460.894	46.0950	0.8	0.012

Table 2.1: The initial conditions for the 1D Toro (1999) tests. The left and right states of the primitive variables are given for each Riemann problem along with the initial position of the discontinuity x_0 and the time at which the results are to be evaluated. In all cases, the ratio of the specific heats $\gamma = 1.4$.

uses the Riemann invariants and an iterative solver to deduce the structure of the entire self-similar Riemann fan. This reference solution is included in Figs. (2.14-2.18) as a solid line for comparison with the numerical solutions which are shown as unconnected symbols. Each solution was computed with 100 uniform cells over the domain $x \in [0, 1] \subset \mathbb{R}$. The Courant number was 0.4 for all these tests as in Toro (1999).

Figure 2.14 shows the solution of test 1 computed with the iterative Riemann solver. The other schemes produced results which are visually indistinguishable and so we omit them here. The full results for each test with each of the four solvers are presented in App. B, however. This first test is the least severe of the five and all the schemes pass with little problem. There is a noticeable oscillation behind the contact discontinuity (visible in the density and internal energy at $x \sim 0.5$) which is a known problem with PPM which could be further damped with artificial viscosity but, since we want to resolve the contact discontinuity as sharply as possible, we do not apply any extra viscosity. Note that this is exactly the same test used to show the entropy violating solution of the Roe solver in Sect. 2.5.1 but with PPM there is no such problem; we do not apply any entropy fix to the Roe solver here. For a more quantitative comparison of the four solvers for this test, see the L_1-error plots in Fig. 2.19.

The second Toro test is perhaps the toughest for any solver. It consists of two strong rarefaction waves which move apart from the initial discontinuity position, leaving a region of very low density. The Roe solver may not need an entropy fix when used with PPM, but it still fails this test because, as mentioned in Sect. 2.5.1, there are some Riemann problems for which it is impossible for linearised solvers to maintain positivity of all the fluid variables. In the present case, cavitation occurs for

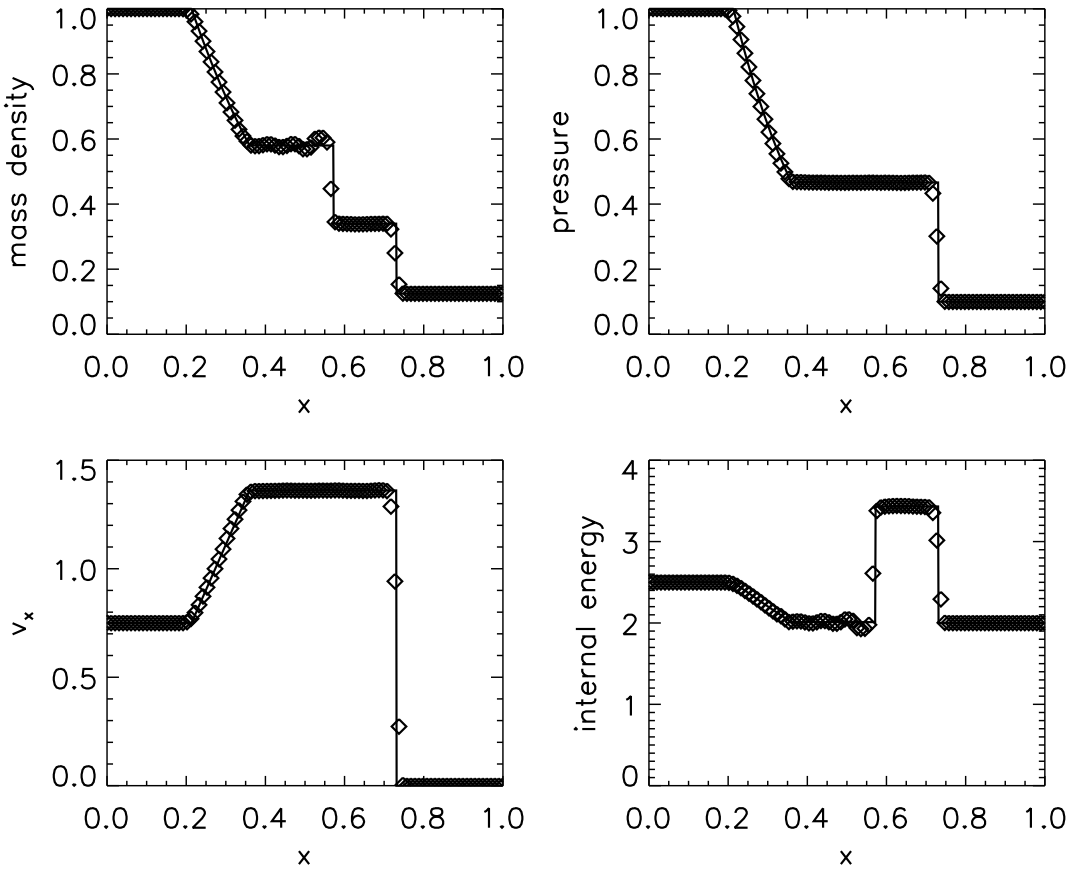

Figure 2.14: Toro test 1: PPM reconstruction with iterative Riemann solver. Initial discontinuity position was $x_0 = 0.3$. The numerical solution (symbols) and the exact solution (line) are shown at time $t = 0.2$.

the Roe solver and the code crashes when it tries to compute a sound speed based on the square root of a negative density. In Fig. 2.15 we show the density and internal energy for the iterative scheme at the end of the simulation. There is reasonable variance in the solution for the internal energy across the different solvers and so we also plot this quantity for the HLLE and HLLEM solvers. Part of the reason for these differences, and the reason why even the exact solver produces a spurious maximum which is not in the reference solution, is that the internal energy is computed from the ratio of mass density and pressure. As both of these quantities are small, the error in the computation of the internal energy is large.[13] This does not pose any

[13] Although not shown, a similar spurious maximum is observed in the entropy for this test. Entropy should be constant across rarefaction waves (it isn't because we compute it from the density and pressure) and so this could be used as a marker for related problems in a real simulation.

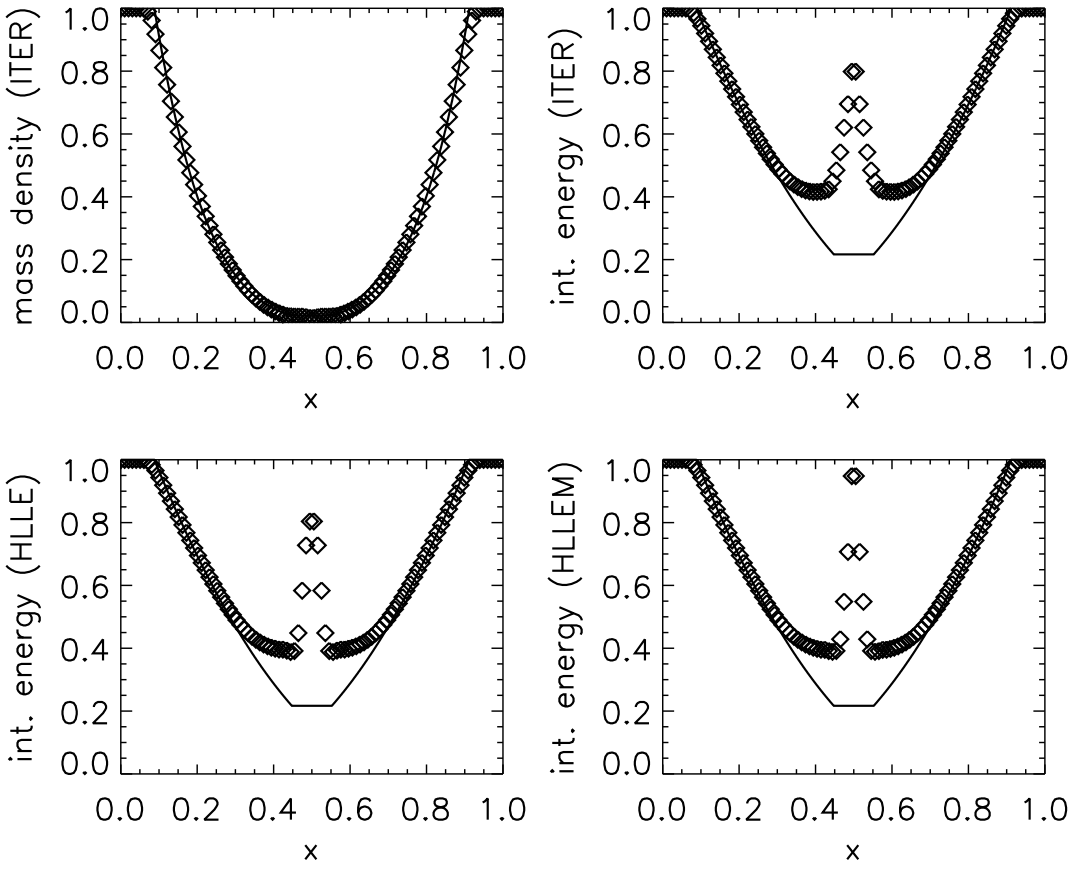

Figure 2.15: Toro test 2: PPM reconstruction with iterative Riemann solver. Initial discontinuity position was $x_0 = 0.5$. The numerical solution (symbols) and the exact solution (line) are shown at time $t = 0.15$.

danger for the astrophysical code, however; due to the difficulties associated with representing the huge density contrasts present in our simulations, we are forced to introduce a numerical "vacuum" state at finite density $\rho_{\rm background} > 10^8$ g cm^{-3}. It is not possible, therefore, that the density should become too small. For the same reason, we do not rule out the use of the Roe solver in the astrophysical code.

Test three, having an initially stationary fluid with no density gradient but a high pressure difference, is much like an explosion. A high Mach number blast wave propagates away from the initial pressure discontinuity in the positive x-direction. We find little difference between the four Riemann solvers in this test and this is reflected in the inclusion of the solution for density and internal energy only for the Roe solver in Fig. 2.16. Once again, the results for the other schemes are so similar as to be virtually indistinguishable.

This is also the case for test four, results of which are shown in Fig. 2.17. This

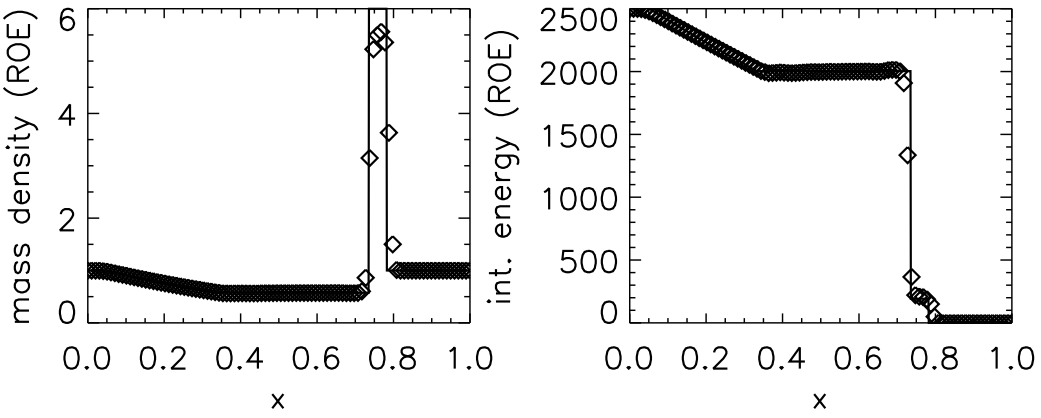

Figure 2.16: Toro test 3: PPM reconstruction with iterative Riemann solver. Initial discontinuity position was $x_0 = 0.5$. The numerical solution (symbols) and the exact solution (line) are shown at time $t = 0.012$.

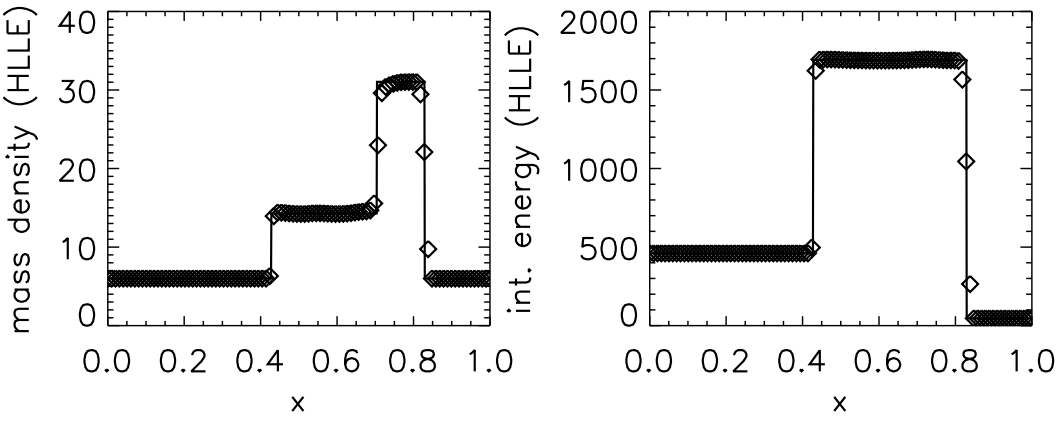

Figure 2.17: Toro test 4: PPM reconstruction with iterative Riemann solver. Initial discontinuity position was $x_0 = 0.4$. The numerical solution (symbols) and the exact solution (line) are shown at time $t = 0.035$.

time we present the density and internal energy for the HLLE solver for variety. This test produces a shock which moves very slowly relative to the grid. High resolution schemes are known to generate spurious oscillations behind such shocks (see for example LeVeque, 2002; Colella and Woodward, 1984), but we find that all the Riemann solvers with PPM cope well with this problem.

The final one dimensional test is very similar to test three. The only real difference is that the blast wave which develops moves very slowly relative to the grid (just like the situation in test four). This is devised to make for quite a stringent test of the accuracy of any numerical scheme. In that regard, this test works well because it

generates the biggest differences between the different Riemann solvers. In Fig. 2.18 we plot the density and internal energy for the iterative, Roe and HLLE solvers (the result for HLLEM is visually indistinguishable from that of Roe). HLLE has the worst performance in this test but, since the Roe and HLLEM solvers produce almost identical results, we note that the modification suggested by Einfeldt (1988) leads to an approximate Riemann solver which is as accurate as the Roe solver while also being more robust. Finally for the one dimensional tests, we plot the L_1-error in mass density as defined by Eq. 2.64 in Fig. 2.19. Panels (a) through (e) correspond to the five Toro tests in order. The reference solution shown in Figs. (2.14-2.18) was used in the computation of the error. From the plots we can clearly see that convergence is achieved as we increase the grid resolution. We can also see that all four of the Riemann solvers perform almost equally well for the first four problems. As we might expect, the divergence between the schemes is greatest for test five which is shown in panel (e). In this case we can see the poor performance of the HLLE scheme against the other two approximate solvers. The performance of HLLEM and Roe with respect to the iterative scheme is also quite clear in this plot, however. Although the total normalised error is still small, we should be wary of this result when we consider using approximate Riemann solvers in the astrophysical model.

Note that we must be careful in drawing direct comparisons between the relative performance of the schemes on the different tests; the L_1-error for test four (Fig. 2.19(d)), for example, is an order of magnitude higher than for any of the other four tests. This is not so surprising though when we consider that the maximum density in this problem is also an order of magnitude greater than in any of the other tests. In general, it would not be desirable for error comparison to depend on the actual density range of the problem. Since we are only interested in showing convergence and the order of accuracy of the schemes though, the absolute L_1-normed error is sufficient.

There is scope here for further work in this study; the comparison of the schemes through Toro's set of test problems could be extended with tests specifically designed to bring out the superior accuracy of PPM, for example.

2.7.2 Tests in two spatial dimensions

Any of the discrete, one-dimensional schemes described until now can be extended to multidimensional functionality by applying them alternately in the x, y and, if present, z-directions. This is known as dimensional splitting and a common second order accurate variant is known as Strang splitting (Strang, 1968).

The double Mach reflection of a strong shock is a standard two dimensional problem now used for code verification (see, amongst others, Mignone et al., 2007; Tóth and

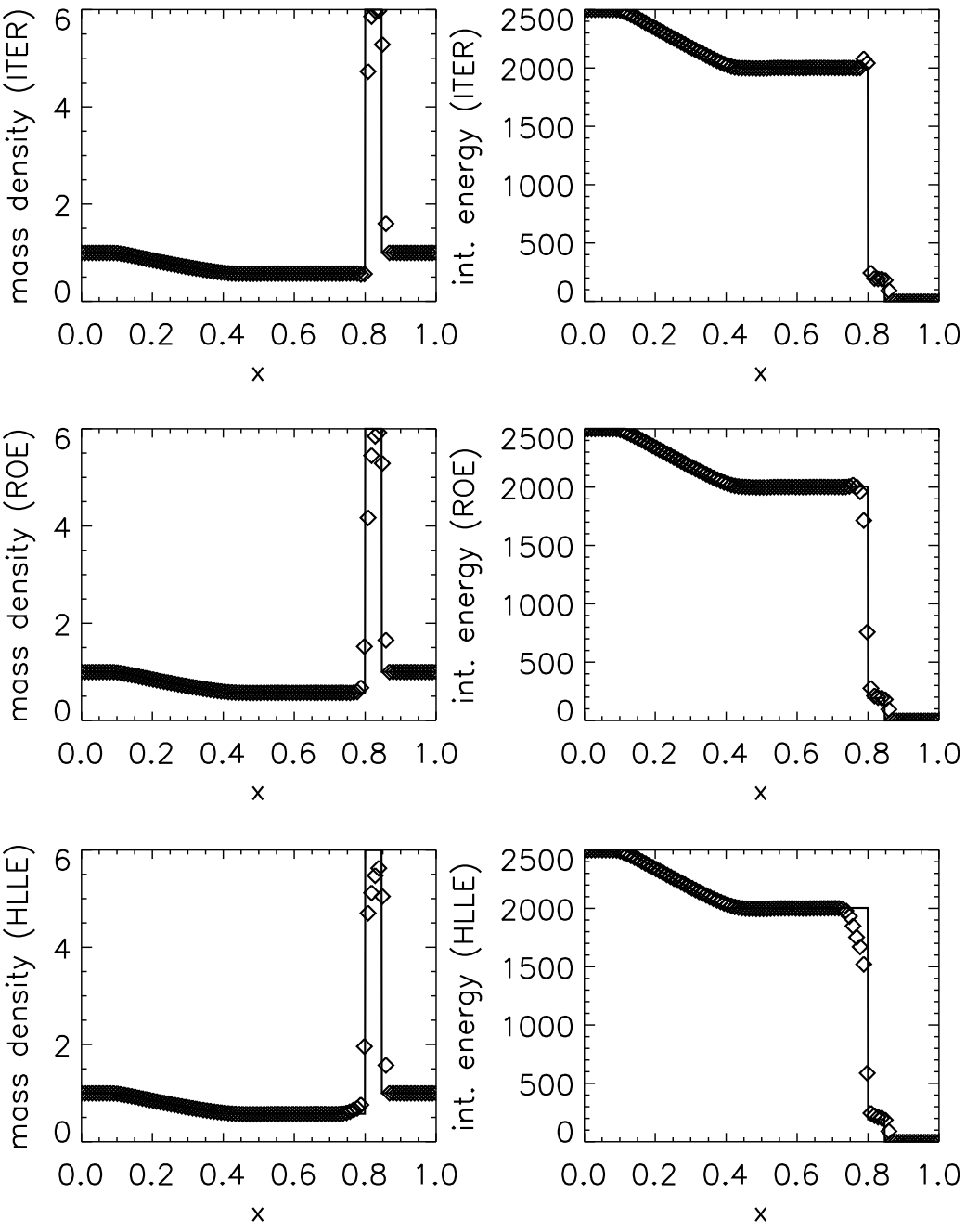

Figure 2.18: Toro test 5: PPM reconstruction with iterative Riemann solver. Initial discontinuity position was $x_0 = 0.8$. The numerical solution (symbols) and the exact solution (line) are shown at time $t = 0.012$.

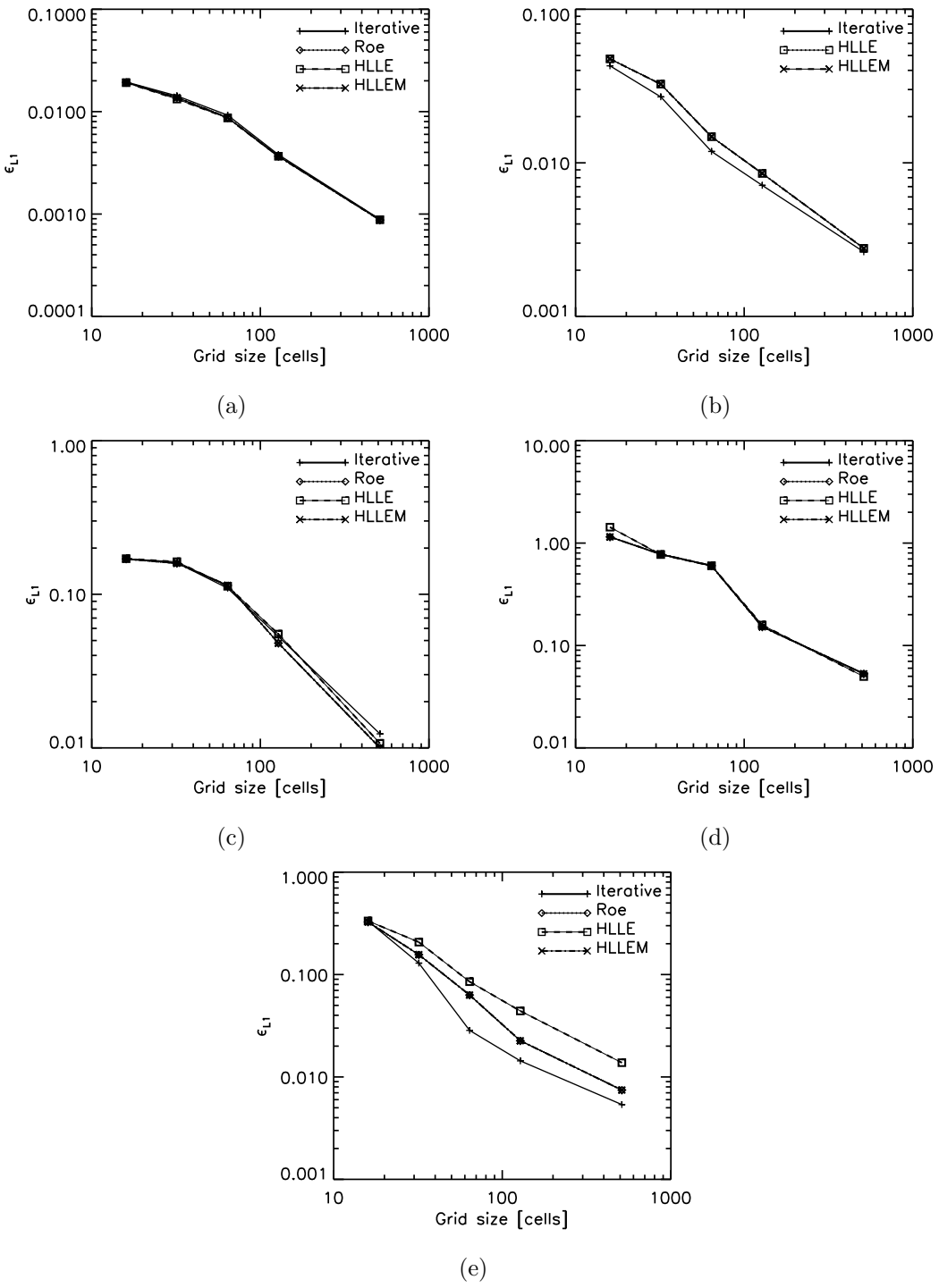

Figure 2.19: L1 normalised error in mass density for each of the 1D Toro (1999) tests. The Courant number in each simulation was 0.4. The average slope in each plot is about unity which indicates 1^{st} order accuracy.

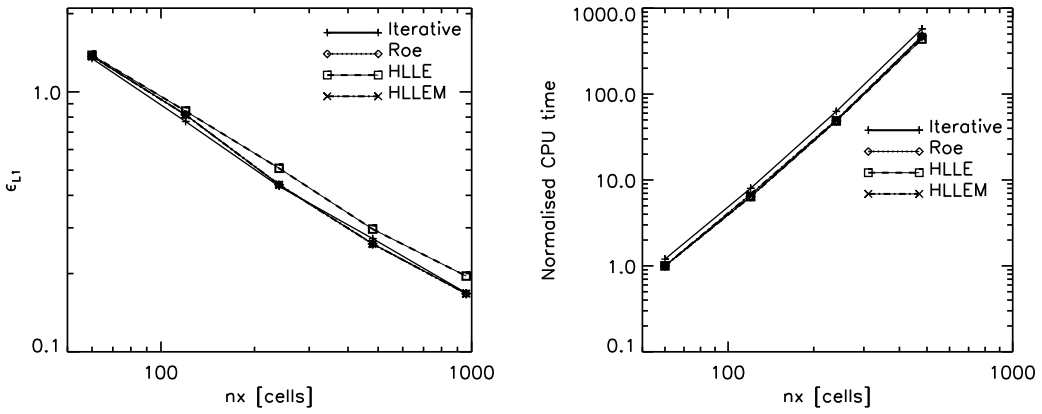

(a) (b)

Figure 2.20: (a) L_1 normalised error in mass density for the 2D double Mach reflection test (Woodward and Colella, 1984). The Courant number in each simulation was 0.8. (b) CPU times as a function of grid size for the double Mach reflection problem. The CPU times have been normalised to the fastest computation (HLLE).

Odstrčil, 1996). The test, which consists of a planar Mach 10 shock striking a reflecting wedge obliquely, can not only be compared with other numerical schemes, but also with direct experiment (Woodward and Colella, 1984). The problem is computed on a uniform, rectangular grid with $x \in [0, 4], y \in [0, 1]$. The initial conditions for the problem are as follows:

$$\mathbf{U}(x,0) = \begin{cases} \rho = 1.4, u_x = 0, u_y = 0, p = 1, & \text{if } x > \frac{1}{6} + \frac{y}{\tan 60^\circ}, \\ \rho = 8, u_x = 8.25 \sin 60^\circ, u_y = -8.25 \cos 60^\circ, p = 116.5, & \text{otherwise.} \end{cases} \tag{2.65}$$

The boundary conditions for this problem are quite involved. The left boundary is always set to the post-shock values (the bottom line of variables in Eq. 2.65) and the right boundary cells are copied from the edge of the active grid (an "out-flow" boundary condition). The top and bottom boundaries are split. To simulate the wedge upon which the shock impinges, the bottom boundary is reflecting for $x > 1/6$ and set to the post-shock values to the left of this. The top boundary is set to post-shock values for $x < x_s(t)$, where $x_s(t)$ is the current position of the shock at $y = 1$. For $x \geq x_s(t)$ the top boundary is continuous. The position of the shock at the top boundary as a function of time is $x_s(t) = 10t/\sin 60^\circ + 1/6 + 1/\tan 60^\circ$. The ratio of specific heats $\gamma = 1.4$ and the calculation is evaluated at $t = 0.2$.

We compute solutions to this double Mach reflection problem using implementation of PPM in PROMETHEUS with the same four Riemann solvers as in the previous section, *viz.* the exact or iterative solver and the approximate Riemann solvers of Roe, HLLE and HLLEM. So that we may evaluate the performance of each scheme,

we once again compute the L_1-error as Eq. 2.64. For this problem, we do not have the luxury of an exact solution with which to compare and so, we compute a reference solution with a resolution of $(x, y) \in [3,840 \times 960]$ using the iterative solver. Both the reference solution run and the lower resolution test runs were performed with a Courant number of 0.8.

The structure which forms in this problem is self-similar in that it maintains its proportions as it grows in time. This structure can be seen in Fig. 2.21 in which we plot the density as computed at $t = 0.2$ for each of the various Riemann solvers with a resolution of 960×240. Qualitatively, there is little difference between the four solutions, which of course is good news for our plan of setting these approximate schemes to work in a real, astrophysical problem. The easiest differences to spot are in the distinct "eye" structure which forms just behind the shock, close to the $y = 0$ axis. As we might expect, this fine structure is smeared out by HLLE but well represented with the other schemes.

To quantitatively compare the performance of each of the four Riemann solvers we once again plot the L_1-error in the mass density in Fig. 2.20(a). As with the 1D tests, we find that convergence is achieved as we increase grid resolution. We also find that the only scheme which deviates significantly is HLLE, which we might have expected already since it is overly diffusive by design. This boosts confidence that an approximate Riemann solver can be used without degradation of the results. Figure. 2.20(b) shows the results of an experiment in measuring the execution time of each of the runs at various resolutions. Here we find that all of the approximate solvers took about the same time to run, and that they were all consistently about 1.3 times faster than the iterative Riemann solver at each resolution. We are confident that this speed-up can be improved upon though, as the iterative solver is heavily optimised while the approximate solvers, having been programmed quickly as mere "proofs of concept", are not.

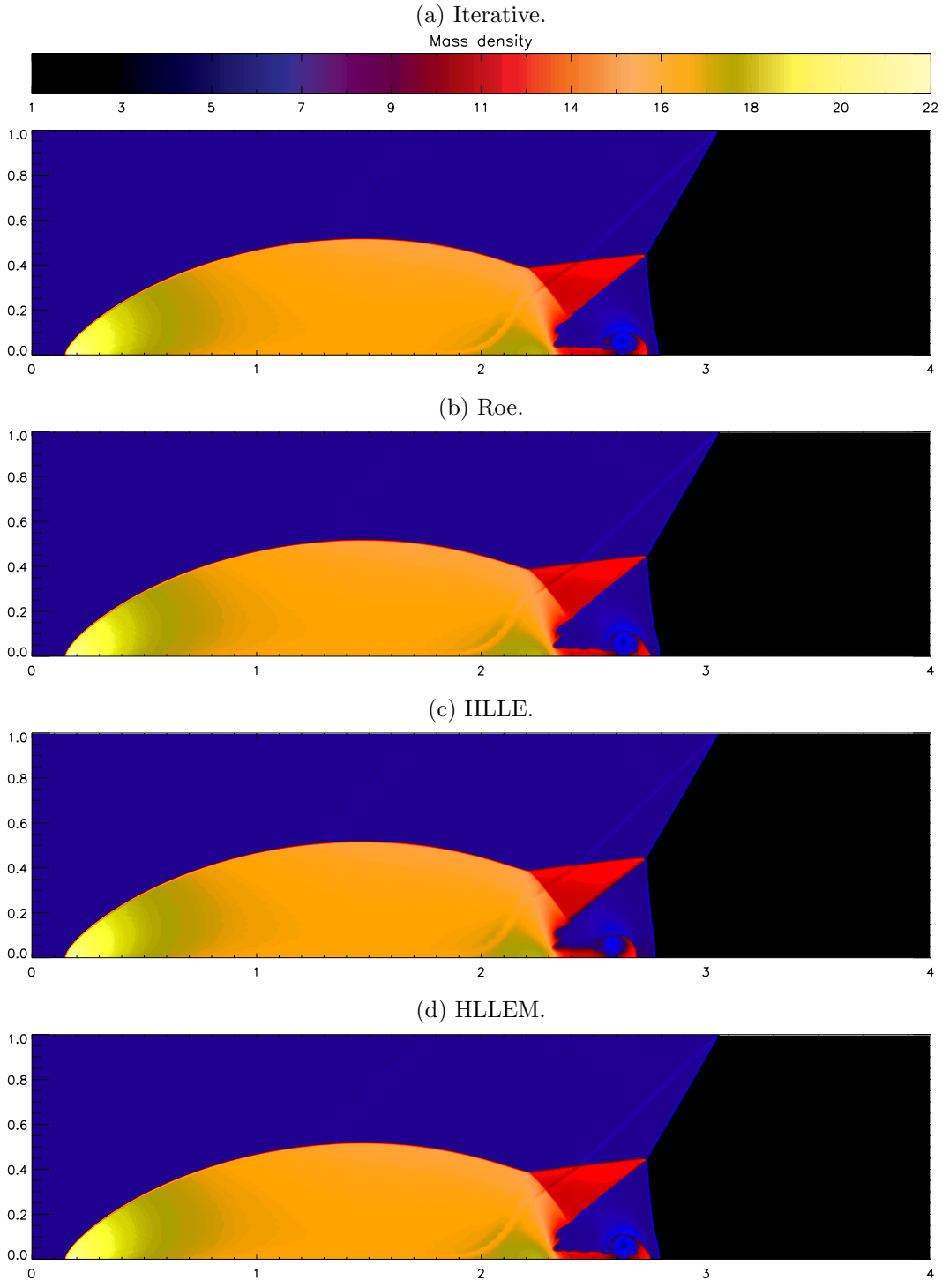

Figure 2.21: Density plots for the double Mach reflection problem computed with a resolution of 960×240 and Courant number 0.8 using the PPM scheme with various Riemann solvers. The faint (dark blue) line which starts at the top of the main shock front and cuts back into the red triangular region is a small underdense wave which is caused by "start up error" from the initial oblique shock and is also found by Woodward and Colella (1984).

> “The other of the two rocks is lower, as you, Odysseus, will see, and the distance between them is no more than a bow-shot. A great fig-tree with luxuriant foliage grows upon the crag, and it is below this that dread Charybdis sucks the dark waters down. Three times a day she spews them up, and three times she swallows them down once more in her horrible way. Heaven keep you from the spot when she is at work, for not even the Earth shaker could save you from disaster. No; you must hug Scyllas's rock and with all speed drive your ship through, since it is far better that you should have to mourn the loss of six of your company than that of your whole crew.”
>
> — The Odyssey, Book XII, Homer. “*A new translation*” by E. V. Rieu.

3

EoS: Numerical Treatment and Effects on GRB Simulations

In this chapter we present results from simulations of mergers between compact stellar remnants (neutron stars and black holes). The simulations are performed by a dedicated hydrodynamics code which we refer to as Charybdis.[1] Before presenting the results, we describe this code in detail and include a summary of relevant physics. We seek to compare simulations using two different descriptions of matter (equations of state, this is explained further in Sect. 3.1.1).

We mentioned in Chap. 1 that the coalescence of compact objects has been proposed as a central engine for the class of short-period gamma-ray bursts (GRBs). A possible mechanism for the conversion of the energy liberated during the merger event into the (huge) electromagnetic energy we observe during a GRB event, is the generation of a gamma-ray emitting fireball of electron and positron pairs through annihilation of neutrinos with their antimatter counterparts. We concentrate our analysis therefore, on the neutrino emission (since this can inform us on the magnitude

[1] Code for Hydrodynamic binARY star orBital Decay In Spirals.

of the energy available for a subsequent GRB) and investigate how it is affected by the change of equation of state.

3.1 Description of CHARYBDIS

3.1.1 Equation of state of nuclear material

At its most basic, an equation of state (EoS) relates pressure to the internal energy of a material. This minimum functionality is required, as we saw in Sect. 2.1, to close the system of partial differential equations (PDEs) which govern the hydrodynamics. In our astrophysical simulations, we require an EoS which will provide us with not only the basic thermodynamic properties such as temperature and pressure, but also the thermodynamic quantities required by our neutrino treatment (see Sect. 3.1.6). The description of matter at the high densities found in neutron stars ($\gtrsim 10^{14}$ g cm^{-3}) requires sophisticated nuclear physics. Real-time calculation of the required quantities would be impractical and so, in CHARYBDIS, we incorporate the necessary physics by using pre-calculated look-up tables for the EoS.[2] The value of a given quantity can be determined in the EoS data table from three input values: the mass density ρ, the electron fraction Y_e and the temperature $k_B T$.[3] In those instances during a simulation where the internal energy density $\rho\epsilon$ is known and the temperature is required, the EoS subroutine performs a bisection iteration and interpolation to find the temperature index which would return the relevant internal energy density within the table.

We compare results computed with two different equations of state, *viz.* those of Lattimer and Swesty (1991) and Shen et al. (1998a,b). Throughout, we shall refer to these by the abbreviations LS-EoS and Shen-EoS respectively. Previous work with CHARYBDIS (starting with Ruffert et al., 1996)) has used the LS-EoS in simulations of both neutron star-neutron star mergers (which we refer to as NSNS models) and in mergers between a single neutron star and a black hole (NSBH models). The present work is the first time the Shen-EoS has been used with CHARYBDIS.

The EoS tables contain data on the pressure P, the internal energy density $\rho\epsilon$, the adiabatic index $\Gamma \equiv (\partial \ln P / \partial \ln \rho)|_s$ and the degeneracy parameters of protons and neutrons (without rest masses). The tables span the ranges given in Tab. 3.1. The LS-EoS table has a resolution of 130 data points in density, 155 in temperature

[2] It is possible that discontinuities may be introduced in this way and our solution here is to smooth them out as described in Ruffert et al. (1996).

[3] Temperature can be measured in units of MeV by expressing it in the form of a thermal energy $k_B T$ where k_B is Boltzmann's constant.

EoS	$\rho^{\min}$ [g/cm^3]	$\rho^{\max}$ [g/cm^3]	$Y_e^{\min}$	$Y_e^{\max}$	$k_BT^{\min}$ [MeV]	$k_BT^{\max}$ [MeV]
LS-EoS	5.18×10^7	2.90×10^{15}	0.006	0.49	0.014	95.77
Shen-EoS	5.01×10^7	1.12×10^{15}	0.015	0.56	0.1	97.72

Table 3.1: The range of density ρ, electron fraction Y_e and temperature k_BT contained in our EoS tables for the equations of state of Lattimer and Swesty (1991) and Shen et al. (1998a,b).

and 25 in electron fraction. The Shen-EoS table has 180 data points in density, 120 in temperature and 50 in electron fraction. Further details on the specific implementation of the EoS tables can be found in Ruffert et al. (1996) for LS-EoS and in Oechslin and Janka (2006) for Shen-EoS.

Figure 3.1 shows the relationship between density and pressure for the two equations of state. Note that they match quite well at the lower end of the density range as we would expect but that there is a substantial difference in the high density regime above about $\rho \sim 10^{14}$ g/cm^3.[4] Above this critical value, the gradient is steeper for the Shen-EoS. This EoS is thus said to be "stiffer" than the LS-EoS; consider two fluid elements of equal mass and volume with an initial density above this critical value, one for each equation of state. If we compress each lump of matter by the same amount, Fig. 3.1 tells us the pressure will be higher in the Shen-EoS case. The Shen-EoS fluid element is therefore "stiffer" than the LS-EoS fluid element because this higher pressure provides a larger restoring force which makes the element more resistant to compression.

The EoS tables also contain information about the chemical potentials (or they can be deduced from other quantities in the case of the LS-EoS) for protons μ_p, neutrons μ_n, electrons μ_e and neutrinos μ_ν. To help understand the use of the chemical potentials, consider the β-process

$$n + \nu_e \leftrightharpoons e^- + p. \tag{3.1}$$

This reversible reaction is in equilibrium when

$$\mu_n + \mu_\nu = \mu_e + \mu_p. \tag{3.2}$$

Consider the special case of neutrino-less β-equilibrium in which any neutrinos produced via a β-process are immediately absorbed by the inverse process. In this

[4]This value indicates the density at which nuclei dissolve into free protons and neutrons known as the "nuclear density" $\rho_{\rm nuc} = 2.8 \times 10^{14}$ g cm^{-3} (Shapiro and Teukolsky, 1983).

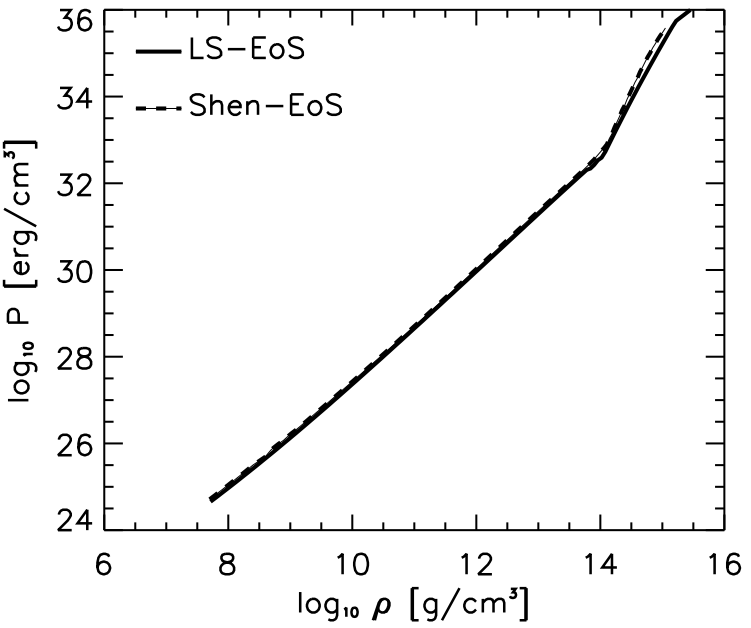

Figure 3.1: The dependence of pressure with mass density for the two equations of state used in our simulations plotted with $k_B T = 0.13$ MeV and $Y_e = 0.15$. A logarithmic scale is used to allow the differences to be seen for the chosen quantities. Note the different gradients of the curves for $\rho \gtrsim 10^{14}$ g/cm^3 which indicates the different "stiffnesses" of the two state equations.

equilibrium situation the chemical potential of the neutrinos

$$\mu_\nu = \mu_e + \mu_p - \mu_n, \tag{3.3}$$

equals zero because we are stating that the rates of production/destruction of neutrinos is the same. In Fig. 3.2 we display some contour plots of the chemical potential of neutrinos from the two equations of state. In the top two panels of that figure we show the dependence of μ_ν on density and temperature for a given electron fraction and draw special attention to the curve where $\mu_\nu = 0$. In the region contained by this curve the chemical potential is positive which, in a simplistic view, means that equilibrium will be restored by absorbing more neutrinos. Conversely, if equilibrium material is heated (through a hydrodynamic shock, for example) such that the chemical potential becomes negative then equilibrium will be established through the emission of neutrinos. From panels (a) and (b) of Fig. 3.2 we might therefore expect more neutrino emission in the high density regime with the Shen-EoS. We shall see whether or not this hypothesis is true in Sect. 3.2.

In panels (c) and (d) of Fig. 3.2 the variation in the equilibrium curves (the curves along which $\mu_\nu = 0$) with changes in the electron fraction of the matter is shown

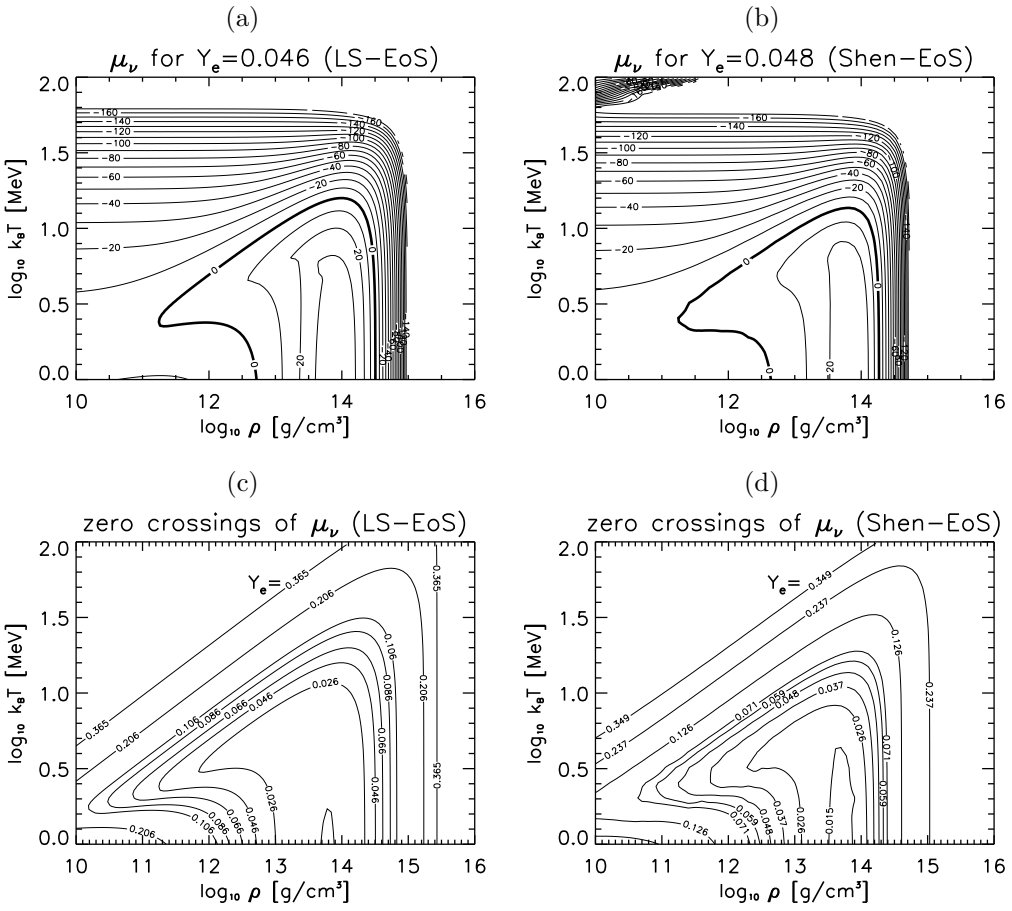

Figure 3.2: Panels (a) and (b) show contours of the neutrino chemical potential μ_ν (measured in MeV) in the temperature-density plane for fixed electron fraction Y_e. In each case the contours are spaced with increments of 10 and are labelled with their respective values. The presence of contour lines at the top-left of Panel (b) which is absent in Panel (a) is due to extrapolation of the LS-EoS to this range which was not required for the Shen-EoS. Panels (c) and (d) show a series of curves in the temperature-density plane at which the μ_ν is zero for different values of Y_e as indicated by the line labels.

for the two EoS tables. The region within which the neutrino chemical potential is positive shrinks as electron fraction increases. The difference between LS-EoS and Shen-EoS becomes more pronounced at lower values of Y_e.

3.1.2 Hydrodynamics

The form of the hydrodynamical equations solved in CHARYBDIS is modified slightly from the basic Euler equations presented in Sect. 2.1. We use the piecewise parabolic

method (PPM) as described in Sect. 2.6.2 to solve the following equations:

$$\frac{\partial \rho}{\partial t} + \frac{\partial \rho v^j}{\partial x^j} = 0, \tag{3.4}$$

$$\frac{\partial \rho w^i}{\partial t} + \frac{\partial \left(\rho w^i v^j + P\delta^{ij}\right)}{\partial x^j} = -\rho \frac{\partial \psi}{\partial x^i} - \rho \frac{\partial \phi}{\partial x^i}, \tag{3.5}$$

$$\frac{\partial E}{\partial t} + \frac{\partial \left(E + P\right) v^j}{\partial x^j} = -\rho v^j \frac{\partial \psi}{\partial x^j} + W + S_E, \tag{3.6}$$

where ρ denotes mass density, t time, v^i and w^i are the components of the kinematic and dynamic velocity[5] (see Blanchet et al., 1990) respectively, x^i the components of the position vector, P pressure, ψ the Newtonian gravitational potential, ϕ the back-reaction potential due to gravitational waves, E is the total energy (i.e. the sum of the internal energy $\rho\epsilon$ and the kinetic energy $\frac{1}{2}\rho w^i w^i$), G is the universal gravitational constant and c is the speed of light (not to be confused with the sound speed in chapter 2). The quantities W and S_{E} are the source or loss terms for gravitational wave and neutrino emission respectively. The energy source term due to gravitational waves

$$W = -\rho v^j \frac{\partial \phi}{\partial x^j} + \frac{4}{5}\frac{G}{c^5} \dddot{D}_{ij} v^i \left(\rho \frac{\partial \psi}{\partial x^j} + \frac{\partial P}{\partial x^j}\right), \tag{3.7}$$

in which D_{ij} is the quadrupole moment tensor of the mass distribution and the dots represent the third time derivative, is also discussed in Sect. 3.1.5. The neutrino source term S_{E} is the total energy loss rate in all flavours of neutrinos for the stellar gas, calculated by summing up their effective emission rates as described in full detail in the appendices of Ruffert et al. (1996). We perform full three dimensional simulations by computing one dimensional strips in first the x, y and z directions for half of the time step and then by reversing this order for the remaing half time step.

We can define all necessary quantities from the conserved quantities (ρ, ρw^i, E) by the following relations

$$E = \rho\epsilon + \frac{1}{2}\rho w^i w^i, \tag{3.8}$$

$$v^i = w^i + \frac{4}{5}\frac{G}{c^5}\dddot{D}_{ij} w^j, \tag{3.9}$$

$$\phi = \frac{2}{5}\frac{G}{c^5}\left(R - \dddot{D}_{ij} x^j \frac{\partial \psi}{\partial x^i}\right). \tag{3.10}$$

[5]The dynamic velocity is the "normal" velocity while the kinematic velocity is a transformed velocity which allows the emission of gravitational waves and their back-reaction on the fluid flow to be taken into account in a Newtonian setting. The transformation between the two velocities is given in Eq. 3.9.

As might be expected, the quadrupole moment tensor D_{ij} features in the back-reaction potential ϕ and in the transformation from dynamic to kinematic velocity. A full explanation of this post-Newtonian approximation is beyond the scope of this work but it is described in full in Blanchet et al. (1990). The computation of the third time derivative of D_{ij} is discussed in Sect. 3.1.5.

To compute the self-gravity of the gas we need to evaluate the Newtonian gravitational potential ψ everywhere on the grid. To do this, we solve the relevant Poisson equation. For the gravitational wave back-reaction, we also require the first time derivative of ψ and the quantity R in Eq. 3.10 to be defined. We therefore solve the following three Poisson equations

$$\nabla^2 \psi = 4\pi G \rho, \tag{3.11}$$

$$\nabla^2 \dot{\psi} = -4\pi G \frac{\partial \rho v^i}{\partial x^i}, \tag{3.12}$$

$$\nabla^2 R = 4\pi G \dddot{D}_{ij} x^j \frac{\partial \rho}{\partial x^i}. \tag{3.13}$$

We treat the integral form of the Poisson equations as convolution and compute the solution by Fast Fourier Transform (FFT) routines. The non-periodic boundary conditions, which are required to treat the merging system in isolation, are enforced by zero-padding (see for example, Press et al., 1992). The potentials are used to compute accelerations in each computational cell and added as source terms to Eqs. 3.4-3.6.

Other than the included source terms, the main difference between the hydrodynamical equations solved by CHARYBDIS and the basic Euler equations of gas dynamics presented in Sec. 2.1 is the post-Newtonian approximation implemented to include general relativistic effects up to the order at which gravitational waves become important. In some instances in Eqs. 3.4-3.6, the ordinary velocity of the matter is replaced by a relativistic velocity via the transformation in Eq. 3.9. At present, since CHARYBDIS uses an iterative Riemann solver which computes the complete solution to each Riemann problem, this transformation is easily performed on the velocities. As the approximate Riemann solvers described in chapter 2 only return the inter-cell flux of each conserved quantity, the relativistic switch poses a problem for these solvers.

The equations of hydrodynamics are supplemented by advection equations for the electron number density n_e and for entropy. The equation for the evolution of the electron number density

$$\frac{\partial n_e}{\partial t} + \frac{\partial n_e v^j}{\partial x^j} = S_{\mathrm{L}}, \tag{3.14}$$

is necessary for the neutrino treatment which we describe in Sect. 3.1.6. The lepton sink term S_{L} is described in Ruffert et al. (1996, App. B) and quantifies the total electron-lepton number loss rate of the stellar gas through neutrino emission. It is

found by summing the effective emission rates of neutrino number for the electron neutrino and electron anti-neutrino. The electron number density n_e is related to the electron fraction $Y_e = n_e u/\rho$ where u is the atomic mass unit.

We follow a separate equation for entropy as another means of calculating the temperature, rather than from the internal energy. As noted in Ruffert and Janka (2001), when temperature is computed from the internal energy of the gas (via the equation of state), large errors can result when the both the kinetic energy of the gas and the total energy are large. This is because internal energy is computed as the difference of these two quantities. Normally this does not pose a problem but, in the case of extremely degenerate matter, the noise in the temperature can be large as the heat capacity of degenerate matter is very small. We therefore track the entropy per nucleon of the matter s via a separate continuity equation for the entropy,

$$\frac{\partial(sn_b)}{\partial t} + \sum_j \frac{\partial(sn_b v^j)}{\partial x^j} = S_\nu + S_{\rm sh} + S_{\rm vis}, \tag{3.15}$$

where $n_b = \rho/u$ is the baryon number density (u is the atomic mass unit). The source terms account for change in the entropy density due to neutrino production, shock dissipation and shear and bulk viscosity effects. These terms are defined in Ruffert and Janka (2001). The temperature is computed from this equation in a predictor-corrector step which is second order accurate in time. Since the source terms depend on the temperature, the old temperature is first used to evaluate these terms. Solving Eq. 3.15 provides an estimate of the new entropy and thus for the new temperature. This estimate is then used to solve the entropy equation a second time with the source terms calculated using an average of the old and estimated new temperature. This procedure is not fully consistent but we are still free to evaluate the temperature from the internal energy in those cases where the kinetic and total energies are not both large.

3.1.3 Neutron star model

The widely accepted view today, that neutron stars represent the high density remnants of supernovæ, was first proposed at a meeting of the American Physical Society in Stanford by Baade and Zwicky (1934). When a massive star has fused every element up to iron in its core, the formation of elements with higher atomic numbers suddenly requires energy input rather than release. With no nuclear reactions in the core to release heat and therefore increase the gas pressure, the careful hydrostatic equilibrium between pressure and gravity fails and the outer envelope of the star enters free-fall. As the star contracts, the squeeze is so intense that electron clouds are pushed

into their parent nuclei. Protons and electrons bind to form neutrons in the reversible reaction

$$p + e^- \rightleftharpoons n + \nu_e. \tag{3.16}$$

The pressure gets so high that electrons become degenerate and so the decay of neutrons, which is normally the favoured direction for the above equation, is suppressed as there is no available quantum state for the electrons to exist. The contraction continues until a significant fraction of the stellar matter has been "neutronised" in this manner. At this point, the collapse is arrested when the pressure suddenly jumps up again as a result of the tremendous repulsive force exerted due to neutron degeneracy. The star's envelope is collapsing so rapidly though, that the equilibrium is overshot and most of the star's mass rebounds to be ejected in a tremendous explosion (a supernova) while about 1.4 $M_\odot$ (found empirically from observations) remains as an extremely dense remnant, the neutron star. There are many books which describe neutron stars and their formation in much more detail. See for example Ostlie and Carroll (1996), and Shapiro and Teukolsky (1983).

To model the hydrodynamic evolution of neutron stars with CHARYBDIS, we need to know how thermodynamic quantities like pressure, mass density, electron fraction, etc. vary within a neutron star. We therefore seek radial profiles for each quantity and use these profiles to place spherical neutron stars in hydrostatic equilibrium on the computational grid. To obtain these radial profiles, we must solve the equations of hydrostatic equilibrium in a Newtonian gravitational potential

$$\frac{dm(r)}{dr} = 4\pi r^2 \rho(r), \tag{3.17}$$

and

$$\frac{dP(r)}{dr} = -\frac{Gm(r)\rho(r)}{r^2}, \tag{3.18}$$

where r is the radial distance, $\rho(r)$ the mass density at distance r, $m(r)$ is the mass contained within the volume $\frac{4}{3}\pi r^3$ and G is the universal gravitational constant. The pressure at r, $P(r)$, will be dependent on the particular equation of state (see Sect. 3.1.1). Note that Eq. 3.18 becomes

$$\frac{dP(r)}{dr} = -\frac{G}{r^2}\left(m(r) + \frac{4\pi P(r) r^3}{c^2}\right)\left(\rho(r) + \frac{P(r)}{c^2}\right)\left(1 - \frac{2Gm(r)}{rc^2}\right)^{-1}, \tag{3.19}$$

when special relativity (needed because the particles move at speeds approaching the speed of light) and general relativity (needed because of the steep gravitational potential) are included. This is known as the Oppenheimer-Volkoff equation (Oppenheimer and Volkoff, 1939).

We solve the equations above using a fourth order Runge-Kutta scheme and some sample results in the Newtonian case are shown in Fig. 3.3 for two neutron stars of equal mass ($M = 1.6$ M$_\odot$) computed with the LS-EoS and the Shen-EoS. Here we can see the effect of a "stiffer" EoS on the neutron star's internal structure; the Shen-EoS star is more extended and as a result has less extreme conditions at its centre. In both cases, the neutron star can be divided into three main regions: a degenerate interior composed mainly of a neutron fluid within which mass density varies little ($\rho \gtrsim 10^{14}\,\mathrm{g\,cm^{-3}}$), an inner crust ($4.3 \times 10^{11}\,\mathrm{g\,cm^{-3}} \lesssim \rho \lesssim 10^{14}\,\mathrm{g\,cm^{-3}}$) and an outer crust ($\rho \lesssim 4.3 \times 10^{11}\,\mathrm{g\,cm^{-3}}$). The transition between the core and the inner crust is evidenced from the sharp turn or "knee" in the logarithmic mass density shown in Fig. 3.3(b). This transition occurs at 13-14 km for the LS-EoS and at about 15-16 km for the Shen-EoS and indicates the onset of neutron drip which occurs at $\rho_{\mathrm{drip}} \approx 4.3 \times 10^{11}$ g cm^{-3} (Shapiro and Teukolsky, 1983). At mass densities above this critical value, neutrons begin to "drip" out of nuclei and are able to survive as free neutrons. The ratio of free neutrons to nuclei increases with density until $\rho_{\mathrm{nuc}} \approx 2.8 \times 10^{14}$ g cm^{-3} at which point nuclei dissolve completely and merge together (Shapiro and Teukolsky, 1983). This corresponds to the density within the core.

The transition between the inner and outer crusts can be seen as a change of gradient in Fig. 3.3(b) and as a similar feature in Fig. 3.3(c) for the electron fraction. The electron fraction in the crust jumps up appreciably from its much lower (less than 10%) values in the interior of the star to values which are indicative of "normal" matter. This is non-degenerate matter in which electrons make up about half of the matter by number. Both phase transitions pointed out here are described in much more detail in, for example, the book by Shapiro and Teukolsky (1983).

In Fig. 3.4 we plot curves showing the allowed combinations of stellar mass, central mass density and radius for neutron stars with the LS-EoS and Shen-EoS. In the left panels we show the possible stars computed with a Newtonian gravitational potential and, on the right, we show the same relationships for a relativistic potential. Notice that in panel (b) (although it occurs above the maximum density in our EoS tables) we see the indication of a maximum allowed mass for a neutron star when we account for relativistic effects. This maximum mass depends strongly on the equation of state. We must be mindful of this result when choosing a mass for the neutron stars in our simulations. There is also a minimum mass at which a neutron star will be stable because neutrons at low density become susceptible to β-decay. A determination of this minimum mass requires a full stability analysis however, which we do not perform here.

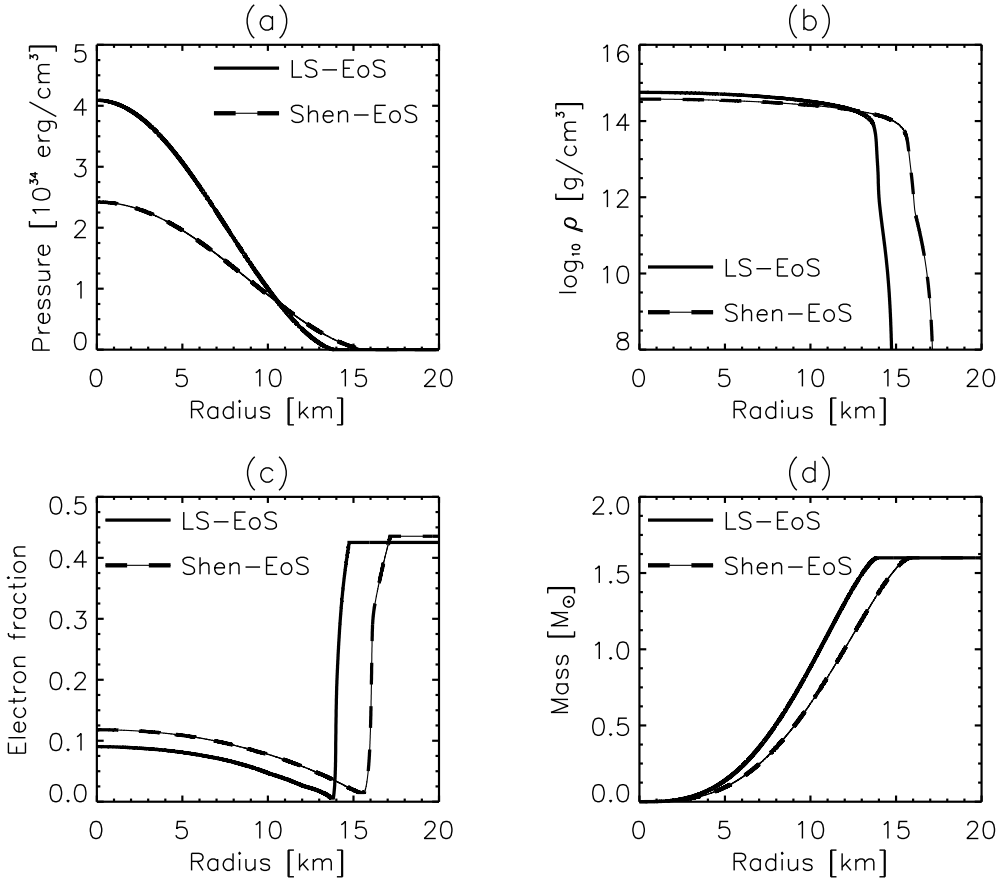

Figure 3.3: Radial profiles of (clockwise from top-left) pressure, mass density, mass, and electron fraction for two neutron stars of equal mass (1.6 $M_\odot$) but with different state equations. The neutron star constructed with the equation of state of Lattimer and Swesty (1991) and Shen et al. (1998a,b) is plotted in each panel by solid and dashed curve, respectively.

3.1.4 Implementation of black holes

First popularised by John Archibald Wheeler in an article in the popular-science publication *Scientific American* (Wheeler, 1968), the term *black hole* describes an object with a gravitational field so strong that it prevents light escaping. Although such objects were considered centuries ago in the framework of Newton's gravity and the corpuscular description of light, it has been through Einstein's general theory of relativity that we have come to be able to probe the strangeness of black holes.

Perhaps the most obvious feature of a black hole is the existence of an *event horizon*—a closed region of space within which nothing, not even light, is permitted to escape. This will naturally have a profound effect on the dynamics of material close to this region; some orbits, which would be parabolic or hyperbolic in Newton's

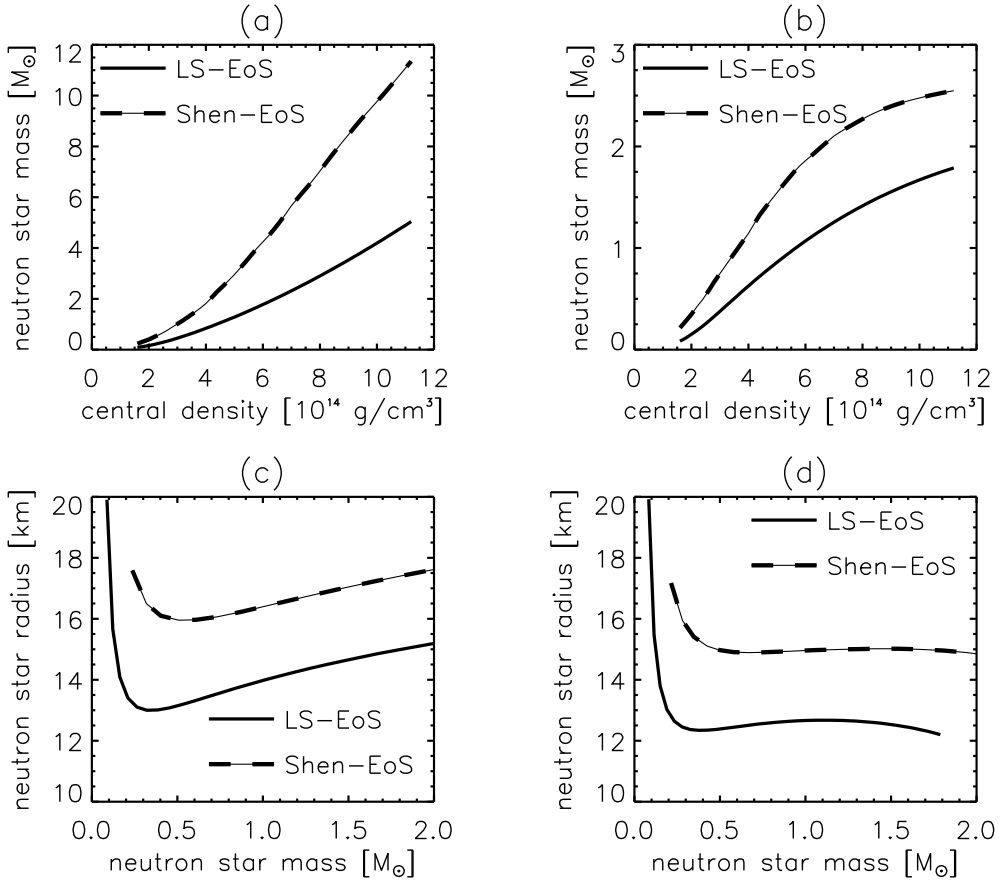

Figure 3.4: Plots relating neutron star mass to density and the stellar radius. The left panels show results computed with the Newtonian equation of hydrostatic equilibrium while those on the right result from the solution of the Oppenheimer-Volkoff equations which include a relativistic gravitational potential. In all panels the thick black curves and the dashed curves represents the stars described by the Lattimer and Swesty (1991) EoS and the Shen et al. (1998a,b) EoS respectively.

theory, will result in the disappearance of the matter into the black hole. Other effects, not present in Newtonian gravity, include a minimum radius for stable, circular orbits (outside the event horizon) and the lack of an angular momentum barrier to prevent particles from reaching $r = 0$. We can see the latter two effects in Fig. 3.5 which is a plot of effective potential in the Schwarzschild metric[6]. Stable orbits occur where the effective potential is concave and a stable circular orbit occurs at local minima of the potential. In the Newtonian case, there is only one circular orbit possible for a

[6]The solution to Einstein's field equations for a point mass in vacuum. It was found by Schwarzschild in 1916, only one month after the publication of Einstein's paper on GR.

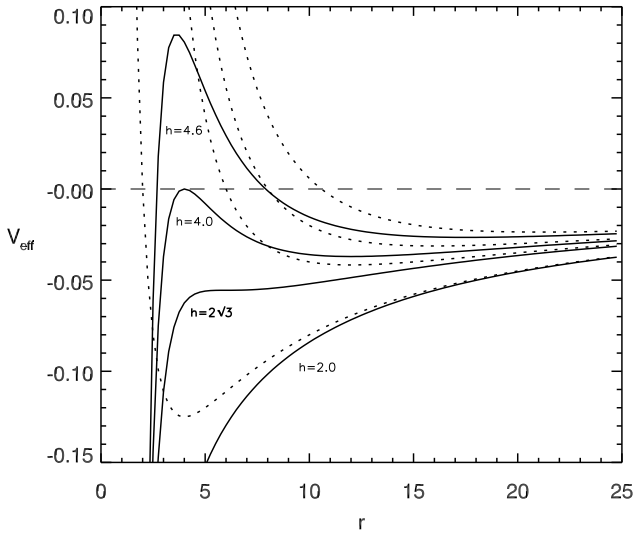

Figure 3.5: Effective potentials for various values of the specific angular momentum h in geometric units in which $G = M = c = 1$. For each angular momentum value the corresponding effective potential is plotted for the Newtonian case (dotted curves) and the Schwarzschild case (solid curves). Note the maxima in the relativistic curves which signify an unstable circular orbit since a small perturbation will cause a particle to either fall without resistance to the singularity at $r = 0$ or escape to infinity. The lack of either a local maximum or minimum for the critical value of angular momentum $h = 2\sqrt{3}$ shows that a particle can have a non-zero angular momentum and still reach the singularity in the general relativistic case. These effects are in stark contrast to the Newtonian curves.

given angular momentum and this orbit is stable to small perturbations. This stable circular orbit has a direct analogue in general relativity, but note that there is another point in this case where $\dot{r} = 0$ (the hump on the left-hand-side of the plot). This also corresponds to a circular orbit, but one which is unstable to perturbations; a small change in the angular momentum or radial distance will lead to a trajectory which falls into the black hole. There is no analogue for this behaviour in Newton's description of gravity where there is no way of reaching the centre of gravity with non-zero angular momentum; here an object with too much angular momentum can plunge into the black hole. One can see from the tracks for various values of specific angular momentum that there is a limiting value of h for which even the stable circular orbit disappears. In the geometric units used here this value is $h = 2\sqrt{3}$ and the radius of this *innermost stable circular orbit* is

$$r_{\mathrm{ISCO}} = \frac{6GM}{c^2} = 3r_{\mathrm{S}}, \tag{3.20}$$

where we have used the definition of the Schwarzschild radius ($r_{\mathrm{S}} = 2GM/c^2$) to obtain the final relation. Although the discussion so far has used the Schwarzschild metric

for illustration, the presence of angular momentum in nearly all astrophysical systems suggests that the formation of a black hole in a perfectly spherically symmetric fashion is unlikely. Luckily, we have a solution to the field equations which takes into account the rotation of a central gravitating mass – the Kerr metric. Since we do not employ a full general relativistic treatment in the simulations presented in this work, we shall just note that we still find the features described in the Schwarzschild metric, but now the event horizon is a function of the rotation which we will characterise by the *Kerr parameter* $a = J$ (in geometric units where $G = M = c = 1$)

$$r_{\mathrm{H}} = 1 + \sqrt{1 - a^2}. \tag{3.21}$$

Due to frame-dragging, where space-time is essentially twisted around by the motion of the gravitating mass, the radius of the innermost stable circular orbit in the Kerr solution also depends on the rotation of the central mass but, unlike the event horizon, it also depends on the "sense" of rotation; if a particle is in a pro-grade orbit (i.e. in the same direction as the black hole is rotating), then r_{ISCO} decreases and increases for a retrograde orbit. For a Kerr black hole, we have

$$\begin{aligned} r_{\mathrm{ISCO}} &= 3 + Z_2 \mp \sqrt{(3 - Z_1)(3 + Z_1 + 2Z_2)}, \\ Z_1 &\equiv 1 + \left(1 - a^2\right)^{\frac{1}{3}} \left[(1 + a)^{\frac{1}{3}} + (1 - a)^{\frac{1}{3}}\right], \\ Z_2 &\equiv \sqrt{3a^2 + Z_1^2}. \end{aligned} \tag{3.22}$$

Note that both Eq. 3.21 and Eq. 3.22 coincide with the Schwarzschild solution when $a = 0$. Figure 3.6 shows plots of the various radii discussed as functions of the specific angular momentum a or Kerr parameter.

The innermost stable circular orbit can be important dynamically as this is where the inner edge of any accretion disk which forms around the black hole will be (although the disk could also be truncated dynamically by magnetic fields as in the vicinity of some young stellar objects). It is important to include the general relativistic effects mentioned above in any simulation which involves an accreting black hole, such as the present work. Since the computer model we use is a Newtonian one, any general relativistic effects must be added as corrections or source terms (see also Sect. 3.1.5) to our code.

For simulations of a neutron star merging with a black hole, we model the black hole by a *vacuum sphere*, within which matter and angular momentum is removed from the grid and added to the black hole. The radius of this vacuum sphere (our "numerical event horizon") is taken to be the arithmetic mean of the true event horizon and the innermost stable circular orbit as computed from Eq. 3.21 and Eq. 3.22 respectively. While matching the radius of the vacuum sphere to the black hole's event horizon might

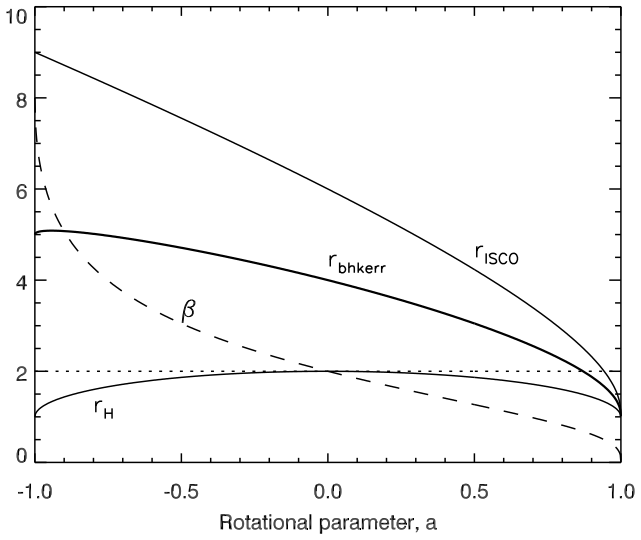

Figure 3.6: The effect of the rotational parameter a on the event horizon ($r_{\rm H}$), the radius of the innermost stable circular orbit ($r_{\rm ISCO}$) and $\beta \equiv r_{\rm ISCO}/r_{\rm H} - 1$, a dimensionless parameter which defines the gravitational potential used. The thick curve $r_{\rm bhkerr}$ is the arithmetic mean of the last stable orbit and the event horizon and this is the effective radius of the vacuum-sphere we use to simulate a black hole. The radii are in units of GM/c^2 or half the Schwarzschild radius and the dotted horizontal line thus corresponds to the Schwarzschild radius. This figure is adapted from Setiawan et al. (2006).

seem a more realistic choice, it is numerically problematic: the potential diverges at the event horizon. Since matter within $r_{\rm ISCO}$ is doomed to fall into the black hole anyway, the exact position of the numerical horizon should not influence the large-scale dynamics.

At every time step in the simulation, we compute the velocity of a point mass which represents the current position of the black hole taking into account the matter flowing into the black hole and the back-reaction from gravitational waves (see Sect. 3.1.5). The position of the point mass is then updated using a time-centred algorithm.

Although we use a point mass to keep track of the mass, position and velocity of the black hole, we do attribute a temporary mass distribution to the vacuum sphere when computing the potential for self-gravity of the gas in the simulation. This is to take advantage of the available nested-grid procedures which automatically generate a self-consistent potential. The alternative would be to add a point-mass potential as appropriate on each of the different grid levels. The distribution used is

$$\rho(r) = \max\left\{\left(e^{-4(r/r_{\rm bhkerr})^2} - 0.05\right),\ 1\times10^{-20}\right\}, \tag{3.23}$$

where r is the radial distance from the point mass and $r_{\rm bhkerr}$ refers to the hydrodynamical size (which is the numerical event horizon in our simulations) of

the vacuum sphere; $r_{\rm bhkerr} = (r_{\rm H} + r_{\rm ISCO})/2$. Figure 3.6 shows $r_{\rm bhkerr}$ along with the true event horizon and the radius of the last stable orbit as calculated from the Kerr solution to Einstein's field equations.

The calculation of $r_{\rm bhkerr}$ is one way to incorporate the general relativistic effects encountered close to a black hole, but this only affects matter once it crosses into the vacuum sphere. It is clear from Fig. 3.5 that the gravitational potential near the black hole differs from the Newtonian case. Since the gravitational force can be thought of in terms of the gradient of this potential, we can apply the necessary corrections by changing the momentum of the gas once we have an approximation for the general relativistic potential. In the case of a non-rotating black hole, Paczyński and Wiita (1980) present a potential which reproduces the event horizon and last stable orbit from the Schwarzschild metric. Since we wish to investigate the effect of black hole spin on the post-merger dynamics we use the potential derived by Artemova et al. (1996) following Paczyński and Wiita (1980) but modified to include the correct dependence on the Kerr parameter. The gravitational potential for the black hole $\phi_{\rm BH}(r)$ takes the form

$$\frac{{\rm d}\phi_{\rm BH}}{{\rm d}r} = -\frac{GM_{\rm BH}}{r^{2-\beta}(r - r_{\rm H})^{\beta}}. \tag{3.24}$$

The dependence on the black hole spin is provided through the dimensionless parameter β (see Fig. 3.6) defined

$$\beta \equiv \frac{r_{\rm ISCO}}{r_{\rm H}} - 1. \tag{3.25}$$

3.1.5 Gravitational waves in Newtonian setting

The crowning achievement of Einstein's General Theory of Relativity (GR) are the field equations (e.g. Shapiro and Teukolsky, 1983; Hobson et al., 2006)

$$R_{\mu\nu} - \frac{1}{2} g_{\mu\nu} R = -\frac{8\pi G}{c^4} T_{\mu\nu}. \tag{3.26}$$

These equations describe how the distribution of mass-energy prescribes the geometry of space-time. $T_{\mu\nu}$ is the stress-energy tensor which contains information about the distribution of mass, $R_{\mu\nu}$ is the Ricci tensor which is itself a contraction of the curvature tensor $R_{\mu\nu} \equiv R^{\sigma}_{\mu\nu\sigma}$, R is the Ricci (or curvature) scalar which is the trace of the Ricci tensor, and $g_{\mu\nu}$ is the metric tensor. The curvature tensor and its various contractions contain all the information necessary to describe the intrinsic curvature of the space-time manifold and the metric tensor allows us to measure distances and angles on the manifold. Together, these three terms describing the curvature and geometry of space-time define the Einstein tensor $G_{\mu\nu}$ as the left hand side of Eq. 3.26

which simplifies the field equations to

$$G_{\mu\nu} = -\frac{8\pi G}{c^4} T_{\mu\nu}, \tag{3.27}$$

which is perhaps their most familiar form. In the Newtonian or *weak field limit*, Eq. 3.26 reduces to the Poisson equation for gravity (see Sect. 3.1.2).

The field equations in either of the forms above are intricate and difficult to solve. A particular simplification though, comes from solving the *empty space* equations $R_{\mu\nu} = 0$, for a particular metric $g_{\mu\nu}$. Apart from this type of simplification and exploitation of symmetric situations, the field equations are generally intractable and so many researchers considered their general behaviour by linearising them. Much of the detail here can be followed in Hobson et al. (2006) amongst others.

We first make the physical assumption that the gravitational field is weak and can thus be considered as a perturbation against the background of a flat metric, i.e.

$$g_{\mu\nu} = \eta_{\mu\nu} + h_{\mu\nu} \tag{3.28}$$

where $|h_{\mu\nu}| \ll 1$ and the first and higher partial derivatives of $h_{\mu\nu}$ are also small. After making suitable gauge transforms and linearising the curvature terms in Eq. 3.26, we arrive at the linearised field equations

$$\Box^2 \bar{h}_{\mu\nu} = -\frac{16\pi G}{c^4} T_{\mu\nu}. \tag{3.29}$$

Here the $\bar{h}_{\mu\nu}$ is defined as the "trace reverse" of $h_{\mu\nu}$

$$\bar{h}_{\mu\nu} \equiv h_{\mu\nu} - \frac{1}{2}\eta_{\mu\nu} h, \tag{3.30}$$

and we assume that the $\bar{h}_{\mu\nu}$ are chosen to satisfy the gauge condition $\partial_\mu \bar{h}_{\mu\nu} = 0$. If we now enforce the condition $R_{\mu\nu} = 0$, we obtain the linearised field equations for empty space

$$\Box^2 \bar{h}_{\mu\nu} = 0. \tag{3.31}$$

Eq. 3.31 is a wave equation with plane-wave solutions of the form

$$\bar{h}_{\mu\nu} = A_{\mu\nu} \exp\{ik^\rho x_\rho\}, \tag{3.32}$$

where the amplitude coefficients $A_{\mu\nu} \in \mathbb{C}$ are constant components of a symmetric tensor and the $k^\mu \in \mathbb{R}$ are the constant components of a wave-vector. In the Lorentz gauge, the relationship $A_{\mu\nu} k^\mu = 0$ must be satisfied. Further analysis which we omit here (see Hobson et al., 2006, Chapter 18 for the details) shows that the amplitude coefficients $A_{\mu\nu}$ when transformed to a "transverse-traceless gauge" can

be decomposed into two independent polarisation tensors $h^{+}_{\mu\nu}$ and $h^{\times}_{\mu\nu}$ (note we have dispensed with the over-bar for simplicity).

We now turn our attention to the numerical treatment of the gravitational waves in CHARYBDIS. Gravitational waves are generated when a rotating object or mass distribution does not exhibit symmetry about the axis of rotation. The quadrupole moment tensor D_{ij} of the mass distribution allows us to quantify such axial asymmetry and the derivatives of this tensor with respect to time describe the gravitational wave emission. For example, we can compute the amplitudes of each of the so-called "plus" and "cross" polarised gravitational waves observed at a distance r perpendicular to the orbital plane by

$$h_{+} = \frac{G}{c^4}\frac{1}{r}\left(\ddot{D}_{xx} - \ddot{D}_{yy}\right), \tag{3.33}$$

and

$$h_{\times} = \frac{G}{c^4}\frac{2}{r}\ddot{D}_{xy}. \tag{3.34}$$

At arbitrary positions we can compute the wave amplitudes from the two above (Rasio and Shapiro, 1994).

To incorporate the effects of gravitational wave emission on the hydrodynamics in our simulations, we need to define the energy source term due to gravitational waves W which was given without explanation in Sect. 3.1.2. This term is computed by

$$W = -\rho v^j \frac{\partial \phi}{\partial x^j} + \frac{4}{5}\frac{G}{c^5}\dddot{D}_{ij} v^i \left(\rho \frac{\partial \psi}{\partial x^j} + \frac{\partial P}{\partial x^j}\right), \tag{3.35}$$

where ψ and ϕ are the Newtonian and gravitational wave back-reaction potentials respectively (the other symbols are as defined in Sect. 3.1.2). We can also evaluate the gravitational wave luminosity $\mathcal{L}$ either by summing up W over the whole emitting volume or via the classical quadrupole formula

$$\mathcal{L} = \frac{1}{5}\frac{G}{c^5}\dddot{D}_{ij}\dddot{D}_{ij}. \tag{3.36}$$

Summing up W yields the gravitational wave luminosity without averaging over time. When the orbit decays and therefore is not perfectly circular, the non-averaged luminosity is in general not identical with the value obtained by averaging over one orbital period.

Since only the 2$^{\text{nd}}$ and 3$^{\text{rd}}$ time derivatives of D_{ij} occur in the equations above, we do not need to calculate the quadrupole moment tensor explicitly. This allows us to skip computation of the numerical derivatives which would be less accurate and instead, we compute the derivatives directly from

$$\ddot{D}_{ij} = \mathrm{STF}\left[2\int \rho\left(v_i v_j - x_i \frac{\partial \psi}{\partial x_j}\right)\mathrm{d}V\right], \tag{3.37}$$

and

$$\ddot{\bar{D}}_{ij} = \mathrm{STF}\left[2\int\left(2P\frac{\partial v_i}{\partial x^j} + \frac{\partial\psi}{\partial x^j}\left\{x_i\frac{\partial\rho v^k}{\partial x^k} - 2\rho v_i\right\} - \rho x_i\frac{\partial\dot{\psi}}{\partial x^j}\right)\mathrm{d}V\right], \tag{3.38}$$

where STF stands for *symmetric and trace free* and is equivalent to gauge transforming a tensor to the transverse-traceless gauge (again, the details are to be found in Hobson et al. (2006)). The transformation is

$$\mathrm{STF}\left[X_{ij}\right] \equiv \frac{1}{2}X_{ij} + \frac{1}{2}X_{ji} - \frac{1}{3}\delta_{ij}X_{kk}. \tag{3.39}$$

3.1.6 Neutrino emission

CHARYBDIS contains an "elaborate neutrino leakage scheme" which is described in detail in the appendices of Ruffert et al. (1996). We summarise the treatment of neutrinos in the code here.

Emission and absorption of the electron-type neutrinos ν_e and $\bar{\nu}_e$ are tracked separately. The heavier neutrino species, the τ and μ neutrinos and their anti-particles are considered together and denoted as ν_x. The reason for this seeming disinterest in the heavy neutrinos is due to the emission and absorption processes for the various species as we shall now see.

Any of the three types of neutrino (and their corresponding antineutrinos) can be produced in so-called thermal processes like the annihilation of an electron-positron pair,

$$e^- + e^+ \longrightarrow \nu_i + \bar{\nu}_i, \tag{3.40}$$

where the subscript i refers to all three species of neutrino, and by the decay of photons,

$$\tilde{\gamma} \longrightarrow \nu_i + \bar{\nu}_i. \tag{3.41}$$

The latter process dominates in regions of high density and high electron degeneracy. Electron-type neutrinos however, are special in that they interact with "normal" matter, i.e. matter made up of protons and neutrons, through the charged-current β-processes

$$e^- + p \leftrightharpoons n + \nu_e, \tag{3.42}$$

$$e^+ + n \leftrightharpoons p + \bar{\nu}_e. \tag{3.43}$$

Reactions involving the right arrows in Eq. 3.42 and Eq. 3.43 correspond to emission of neutrinos while the reverse reactions describe absorption of neutrinos by matter. Absorption in general is dominated by these inverse β-processes but with an important

contribution from neutral-current scattering of the neutrinos by nucleons,

$$\nu_i + \left\{ \begin{array}{c} n \\ p \end{array} \right\} \longrightarrow \nu_i + \left\{ \begin{array}{c} n \\ p \end{array} \right\}. \tag{3.44}$$

The nucleonic equation above indicates that the only change in the particles involved is the distribution of energy between them. The latter is the dominant source of opacity for the heavy-lepton neutrinos. Note: for the reason that we wish to keep the memory usage of the equation of state look-up table as low as possible, we do not track nuclei but instead assume that they fully dissociate into a gas of protons and neutrons. The error from this simplification is estimated to be on the order of a few 10% (Ruffert et al., 1996). This may seem to be quite a large error but the accuracy is in keeping with the other parts of the model like the treatment of gravitational waves in a Newtonian framework, for example. The philosophy has been that it is better to simulate as many different physical elements of the model and to gradually improve the treatment than to study only a few phenomena exactly.

Since the electron and anti-electron neutrinos interact with matter, the ratio of ν_e to $\bar{\nu}_e$ may change as conditions within the gas change. It is for this reason that we must track the electron and anti-electron neutrinos independently. Since we do not have any reason to suspect that the heavy lepton neutrinos or their respective antineutrinos might occur in different abundances, we can treat them all as being equivalent.

At low optical depths, the production and emission of neutrinos is computed directly from the rates of the above processes (Eq. 3.40-3.43). At high optical depths, equilibration happens much faster than the timescale of diffusion and hydrodynamic changes. In this case we assume chemical equilibrium abundances for the neutrinos and emission rates on the timescale of diffusion (see appendix B of Ruffert et al., 1996). A smooth transition between these two regimes is achieved by interpolation.

The neutrino leakage scheme has been tested by comparison to a one dimensional (spherically symmetric) calculation for the neutrino diffusion from proto-neutron stars and found to be in agreement on the order of a few 10% (Ruffert et al., 1996). This order of error is introduced by assumptions made to simplify what is already a computationally expensive treatment. For example, transport effects by neutrino diffusion and momentum transfer by neutrinos are both assumed to be negligible.

3.1.7 Nested, refined grid structure

To simulate a problem with length scales which vary from the order of tens of kilometres for the orbits of the neutron stars, down to the typical lengths which

characterise turbulence (metres, centimetres, and smaller), some form of hierarchical grid structure is essential if the computation is to be completed in a reasonable time.[7] There are two main approaches here: adaptive mesh refinement (AMR) and nested refined grids. Both methods are structured, hierarchical collections of grids where a larger, coarser (i.e. larger discretized volume per computational cell) grid contains one or more smaller, finer (higher resolution) grids. AMR is more general but consequently more complicated to implement, especially in an existing code. With AMR, resolution is increased where it is needed by testing each cell for the violation of a specified criterion. This criterion for re-gridding can range from local measures of compressibility, rotationality, current density, etc. (Powell et al., 1999) to the spatial gradient of quantities like the speed of sound (Ziegler, 1999). The problem of choosing a successful indicator for applying refinement in AMR aside, there are other difficulties such as maintaining global conservation of the numerical scheme during the creation, evolution and destruction of the refined grids. For a discussion of the latter problem see, for example, Keppens et al. (2003) and for a detailed description of the AMR method see Berger and Colella (1989), Bell et al. (1994), Friedel (1997), etc.

In the simulations presented in this work, we are fortunate that the regions of the computational volume which require the highest resolutions are localised to the centre of the grid. This allows for a more specialised type of grid refinement which we refer to as a nested, refined grid Ruffert (1992). The number of grids is fixed throughout (we use four in all simulations here) and, although the code we use permits the grids to move relative to one-another, they are also fixed in space. Figure 3.7 shows the configuration of the grids. Each grid has a simple relation to the other grids of different resolution; all grids are Cartesian with the same *logical size*, i.e. they share the same number of equidistant computational cells. The *physical size* of each grid however, varies in length by a factor of two between the next coarsest or finest grid (so in the 2D case depicted in Fig. 3.7, each finer grid level covers a physical area of space which is half as large as that covered by its host grid). In the simulations presented in this thesis, we only use one grid at each level of refinement.

The hydrodynamic equations are evolved on each grid, independently of all others, neglecting any overlap of grids. It is important however, that each grid (except the coarsest grid) is nested in such a way that it is surrounded by a grid which differs in refinement by only one level. This requirement makes the calculation of inter-grid

[7] This assumes that we are using a grid based code, of course. Another approach would be to dispense with the grid entirely and use smooth particle hydrodynamics (SPH). We do not consider SPH here, but simply direct the interested reader to Benz (1990), Monaghan (1992) and references therein.

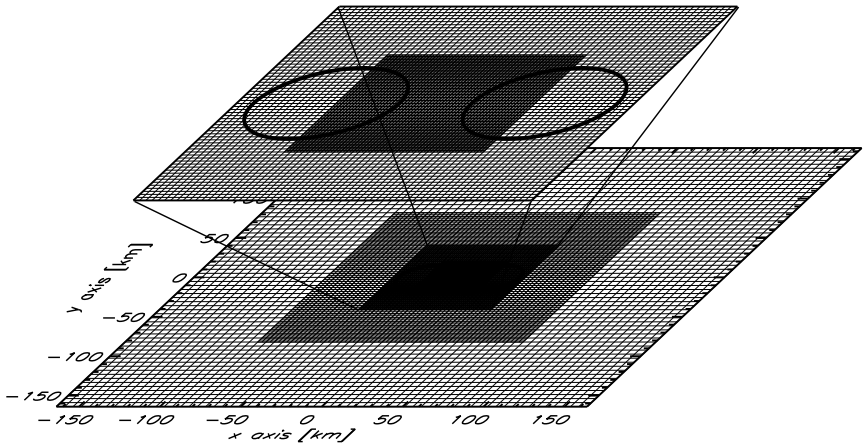

Figure 3.7: Schematic depiction of the multiple, nested, refined grids and their relative positions. Also shown is the outline of two neutron stars of equal mass; note how the finest grid covers the region where the "action" will occur during their coalescence.

Level	Time step	1	2	3	4	5	6	7
1, coarse	$4\Delta t$	$\star$						
2, medium	$2\Delta t$		$\star$			$\star\uparrow$		
3, fine	Δt			$\star$	$\star\uparrow$		$\star$	$\star\uparrow$

Table 3.2: An example of the "w-cycle" of the time step schedule for three levels of nested, refined grids. A star represents computation on that grid level and an up arrow indicates a fine grid being copied onto the next coarsest grid. A full cycle is shown for this level of refinement (from Ruffert, 1992).

fluxes on the boundary of each fine grid consistent for any level of refinement.

Even though the grids are evolved independently, we are required to follow a certain sequence in their computation due to the Courant-Friedrichs-Lewy stability criterion (see Sect. 2.4). Grids which are a factor of two finer must be calculated twice as often as their parent grid. In Ruffert (1992), a *time step schedule* is implemented which we refer to as the "W-cycle" and which is also used in the present simulations; the reason for the name becomes apparent when the schedule is represented as in Tab. 3.2. Computation starts on the coarsest grid (the *root* grid) using a time step which is appropriate for the hydrodynamic conditions on that grid. Computation cannot resume on this grid now until the next finest grid has been evolved twice with a time step equal to half the time step on the root grid. The recursive nature of the scheme should now be apparent, for the second grid cannot be evolved for the second time until any grid finer than itself undergoes two cycles of computation. When the finest grid is reached, it may be computed twice in succession for there are no child

grids to evolve. After this finest grid has been dealt with, its immediate parent is allowed to advance by another step. Information must be communicated between the grids at some point, otherwise there would be no point in the whole operation. We treat the quantities computed on finer grids to be more important than the quantities on the coarse grid which they overlap. So any time we complete calculations on a finer grid and return to computing its parent, we average the values from the fine grid to the coarse grid. This is indicated by an arrow in Tab. 3.2. The procedure described here continues in this recursive fashion until we are ready to evolve the hydrodynamic quantities on the root grid again, at which point the cycle restarts.

From Tab. 3.2 it can be seen that finer grids are computed twice as often as their coarser parent grid. We have already stated that each grid is the same logical size and therefore it should take the same time to complete computation on each grid. Since a finer grid is required to be computed more often than all levels coarser than itself, the largest amount of computer time is spent evolving the finest grids.

A note on inter-grid communication: copying from a fine grid to a coarse grid as discussed above is accomplished here by multi-dimensional arithmetic averaging of the hydrodynamic quantities. The situation is complicated somewhat by the fluxes on the boundary between coarse grid and fine grid not being equal; an adjustment must be made to the simple average to maintain global conservation which is obviously desirable. In some instances we require information computed on a coarse grid to be "promoted" to that on a finer grid. This is accomplished by a monotonic, multi-dimensional interpolation scheme. We use the procedure of van Leer (1977) which is described in detail, along with the rest of the refined grid treatment outlined here, in Ruffert (1992). Ruffert and Janka (2001) also describes the utilisation of the fixed nested grid structure for the problem of mergers between compact objects as studied here.

3.2 Numerical simulations

3.2.1 Initial conditions

To quantify the effect of the equation of state on the mergers of neutron stars and black holes, we run several computer simulations in which we vary the initial positions of the objects and, in the case of models containing a black hole, the initial mass and spin of the black hole. For any given set of initial conditions we ran a simulation with both equations of state so that we could make direct comparisons. Table. 3.3 shows the initial conditions for each of the models presented in this chapter.

Each model has a unique identification code. The first two letters of this code

Model ID	EoS	$M_{\rm NS}$	$M_{\rm BH}$	Separation	$a_{\rm Kerr}$	Grid length	n_x
NBLA	L&S	1.6 $M_\odot$	10 $M_\odot$	90 km	0.99	1 600 km	128
NBSA	Shen	1.6 $M_\odot$	10 $M_\odot$	90 km	0.99	1 600 km	128
NBLB	L&S	1.6 $M_\odot$	2.5 $M_\odot$	55 km	0.90	800 km	64
NBSB	Shen	1.6 $M_\odot$	2.5 $M_\odot$	55 km	0.90	800 km	64
NBLC	L&S	1.6 $M_\odot$	2.5 $M_\odot$	57 km	0.00	800 km	64
NBSC	Shen	1.6 $M_\odot$	2.5 $M_\odot$	57 km	0.00	800 km	64
NNLA	L&S	1.6 $M_\odot$	–	65 km	–	800 km	64
NNSA	Shen	1.6 $M_\odot$	–	65 km	–	800 km	64

Table 3.3: Initial conditions for simulations aimed at investigating the importance of the equation of state (EoS) for the short class of gamma-ray bursts. Separation refers to the initial centre to centre distance of the two objects, $a_{\rm Kerr}$ is the rotational parameter for the black hole (see Sect. 3.1.4), and grid length is the size of the coarsest grid in the x or y directions. n_x is the number of cells in the x-direction on each computational grid.

specify the types of compact stellar object simulated; a model with a code starting "NB" simulates the merger of a neutron star and a black hole while "NN" indicates that the merging objects are both neutron stars. The third letter dictates the equation of state used; "L" for the LS-EoS and "S" for the Shen-EoS. The final letter in the code identifies the particular set of initial conditions as described in Tab. 3.3.

In Tab. 3.3, the resolution of a particular simulation is quoted in terms of the number of cells in the x-direction of each grid. We will often use the shorthand n_x^3 to describe a particular resolution even though the total number of cells in the computational volume is not as large as n_x^3. The number of cells in the y-direction $n_y = n_x$ but this is not true in the z-direction where $n_z = n_x/4$. The number of cells in the z-direction, being perpendicular to the orbital plane of the merging system, is halved because we assume the gas evolution above and below the orbital plane to be symmetric. The reduction of n_z by a further factor of two is possible since, as reported by Ruffert et al. (1996), test calculations showed that hardly any matter moves out to more than one neutron star radius away from the orbital plane.

Due to the restriction of computing time, only models NBLA and NBSA are computed at a resolution of 128^3. The other simulations were computed with half the amount of cells in each dimension. At 64^3, we can obtain the solution over about 30 ms (or for about $5,000$ time steps) on a dual-processor, desktop machine (using OpenMP parallelisation) in a few days. The same calculation at 128^3 resolution, on the same hardware is on the order of a month. The two high-resolution models for which we do have data were run on eight processor, shared-memory nodes at the Edinburgh

Compute and Data Facility (ECDF). In each simulation we used four refine, nested grids with an equal number of cells in each. Figure 3.11 shows a comparison between the high resolution NBLA and NBSA models with 64^3 counterparts. While for the LS-EoS the general trends in the data are the same, the Shen-EoS simulations seem to be much more sensitive to the change in resolution.

Before we allow the compact objects to freely orbit each other losing angular momentum via gravitational waves, we "tidally relax" all neutron stars on the grid. If we omit this step, the stars oscillate violently and are found to transfer matter spuriously as a result. The oscillations result from the neutron star having been constructed in hydrostatic equilibrium in a spherically symmetric gravitational potential. When it is placed next to either another neutron star or a black hole, this equilibrium no longer applies and the star "rings" as it tries to settle down into the tear-drop equilibrium shape of this new potential. By performing tidal relaxation we speed up this process of readjustment and ensure that no spurious mass transfer occurs due to the star's oscillation. The relaxation procedure involves transforming all velocities to a co-rotating frame of reference in which we can easily detect and nullify the radial velocity of the star(s). Even if we do nothing else the star would eventually settle down into equilibrium since numerical viscosity will damp the oscillations. To speed up the equilibration, we remove the excess kinetic energy of the star each time step and also, since we do not want the diffusion to cause spurious heating of the star, we cool the star to maintain the temperature profile set in the initialisation subroutine.

We will now present the results obtained from these numerical simulations divided into two sections. In the first section we analyse the data from the models in which a single neutron star merges with a black hole, and in the section after that we present the results for the single neutron star binary system.

3.2.2 NSBH results and discussion

Although the details of each model vary, Figures 3.8 and 3.9 show the dynamical evolution of a typical merger between a neutron star and a black hole. Plotted in the figures are the logarithmic mass density (selected contours as well as shaded colour) and the velocity field where the density is greater than a critical value around 10^8 g cm^{-3}. We omit material of lower density since it is a numerical background value intended to represent a vacuum surrounding our merging system.

The first panel shows the initial conditions for the simulation after the neutron star has been tidally relaxed; the neutron star and black hole are given velocities for an approximately circular orbit for their separation distance (which in this simulation is 90 km) about the centre of mass which is at the origin. Within an orbit or so, the

neutron star begins to transfer matter to the black hole through the inner Lagrange point (panel (b) in Fig. 3.8). Material is also lost through the 2$^{\text{nd}}$ Lagrange point, most of which forms extended spiral arms which may escape the system. The neutron star will, within a few orbits, venture close enough to the black hole that tidal forces will elongate the star which cause some of the more dense material to be transferred directly across the event horizon as in Fig. 3.8(d) and Fig. 3.9(a). We find that the bulk of the neutron star may survive this elongation and matter transfer for a few approaches before finally being tidally disrupted to form a thick accretion disk around the black hole (panels (b)-(d) of Fig. 3.9). Some material which was ejected into the spiral structures around the merger rains down onto the accretion disk further bulking it up as can be seen just entering the bottom right of the last panel in Fig. 3.9.

Before presenting the detailed results for each model, we make a few remarks about the data processing. In the case of each direct comparison between a simulation with the LS-EoS and the Shen-EoS, the objects start with the same separation distance at time zero. Since the neutron star with the Shen-EoS is more extended however, the dynamical evolution may be markedly different leading to, for example, the two models undergoing similar events at very different simulated times. Clearly if there are more interesting events that we wish to compare directly, we can just shift the time scale to synchronise one of these events. In all the following plots we have redefined the time axis such that $t = 0$ corresponds to the peak accretion rate of the first substantial mass transfer between neutron star and black hole. In other words, we choose the first tidal shredding of the neutron star by the black hole to be the origin of our time coordinate. This can be seen in Fig. 3.12, for example.

Figure 3.10(a) shows the separation distance between the black hole and neutron star measured from centre to centre for the three models in which a neutron star and a black hole merge (we shall abbreviate such systems as NSBH). In this plot we see the first major difference between the LS-EoS and Shen-EoS models. After the first substantial transfer of mass or shredding event at $t = 0$, both stars (much reduced in mass as evidenced from panels (b) and (c) of Fig. 3.12) are flung out on an elliptical orbit. For the LS-EoS, the neutron star is likely to become completely destroyed through tidal shredding on its next approach to the black hole and what is left of it forms an accretion disk. In the Shen-EoS models though, the neutron star tends to survive for several complete orbits more intact before its destruction by tidal forces. During the closest approaches (the orbits are elliptical) the neutron star transfers mass as can be seen in all three panels of Fig. 3.12. Note that in Fig. 3.12(c) the peak accretion rate of the black hole is higher for the Shen-EoS in only this model. We are somewhat sceptical of this result however, since in model NBSC the neutron

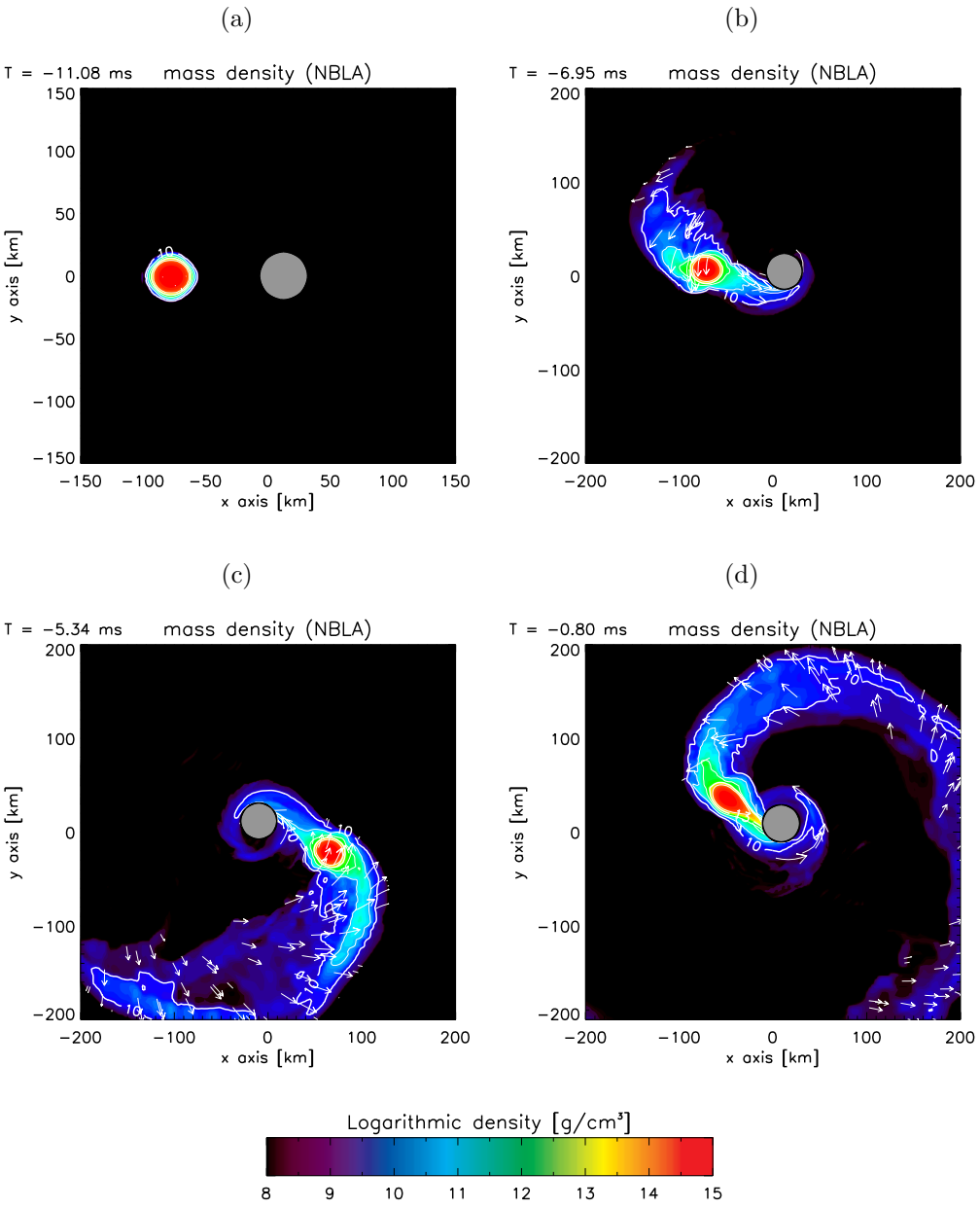

Figure 3.8: Dynamical evolution of the coalescence of a neutron star and a black hole (the grey filled circle) shown as logarithmic density in the orbital plane for numerical model NBLA. The neutron star has a mass of 1.6 $M_\odot$ and the black hole is 10 $M_\odot$ and maximally rotating. The equation of state used in this simulation is from Lattimer and Swesty (1991). The velocity field of matter with density greater than 10^8 g cm^{-3} is shown by white arrows with the longest arrow corresponding to a velocity of about $0.3c$.

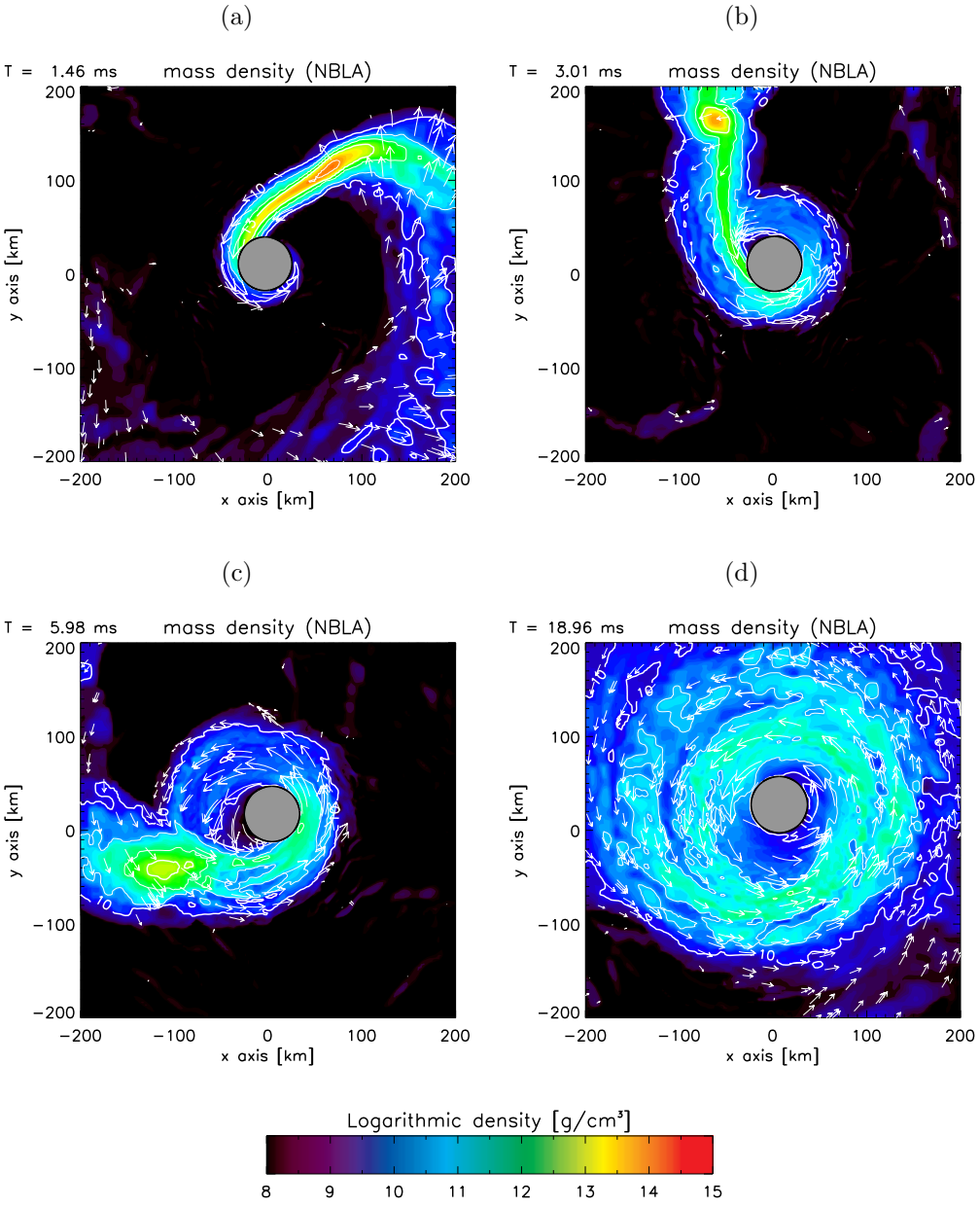

Figure 3.9: Continuation of the dynamical evolution of a merger event between a $1.6\,M_\odot$ neutron star and a maximally rotating $10\,M_\odot$ black hole. See Fig. 3.8 for more details.

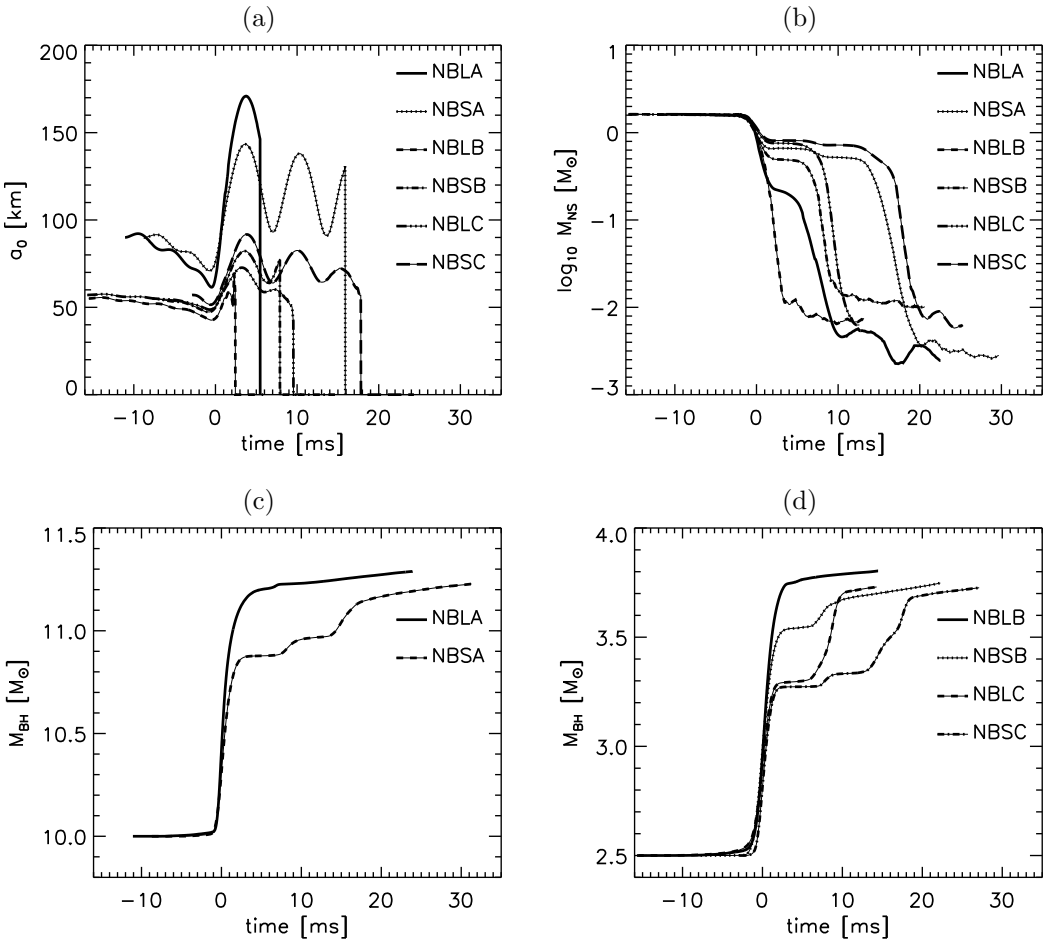

Figure 3.10: (a) The separation distance between the neutron star and the black hole in all NSBH models as a function of time. (b) The mass of the neutron star defined as the mass within a 30 km volume around the neutron star's position. Panels (c) and (d) show the growth of the black hole during the course of the simulations. In all four panels the time has been normalised as described in the main text.

star transfers a large amount of material directly across the black hole's event horizon within a single orbit. This probably indicates that the initial conditions are poorly chosen and that both this model and its partner NBLC should start with a greater initial separation between neutron star and black hole.

In previous work with CHARYBDIS it has been noted (Ruffert et al., 1996, 1997; Ruffert and Janka, 2001) that when two neutron stars merge, the neutrino luminosity is powerful but too short in duration to be the sole cause of a gamma-ray burst (GRB). It is thought, since the merger event will likely lead to the birth of a black hole, that the gamma-ray burst could be powered by cumulative neutrino emission from an accretion disk of hot neutron star debris which persists around this black hole for

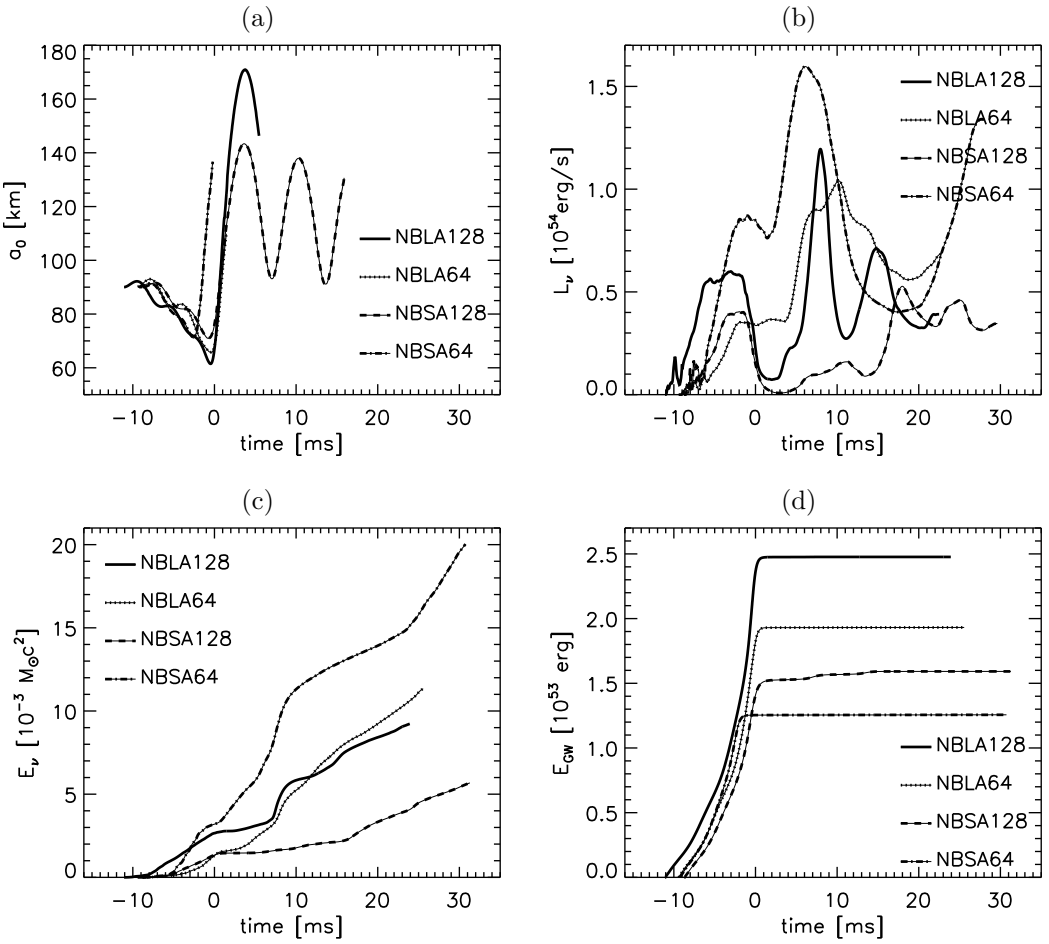

Figure 3.11: The effects of changing the resolution from 64^3 to 128^3 is shown for models NBLA and NBSA. Panel (a) shows the separation distance between the black hole and the neutron star. We stop plotting once the neutron star becomes tidally disrupted as spurious separations result from our determination of the position of the star by following the density maximum. The total neutrino luminosity over all neutrino flavours is shown in panel (b) and in panels (c) and (d) the effects of resolution on the cumulative energy in neutrinos and gravitational waves can be seen. As before, the time range has been normalised as described in the main text.

several hundred milliseconds. For this reason, Setiawan et al. (2004, 2006) and Janka et al. (1999) concentrate their neutrino analysis on the thick, quasi-steady accretion disk which forms around the black hole in their NSBH simulations. We follow this approach and, with the exception of Figs. 3.21-C.4 in which we plot two dimensional slices of various quantities through the centre of the computational domain at several different stages of the simulations, we focus our comparisons on the late stages of each

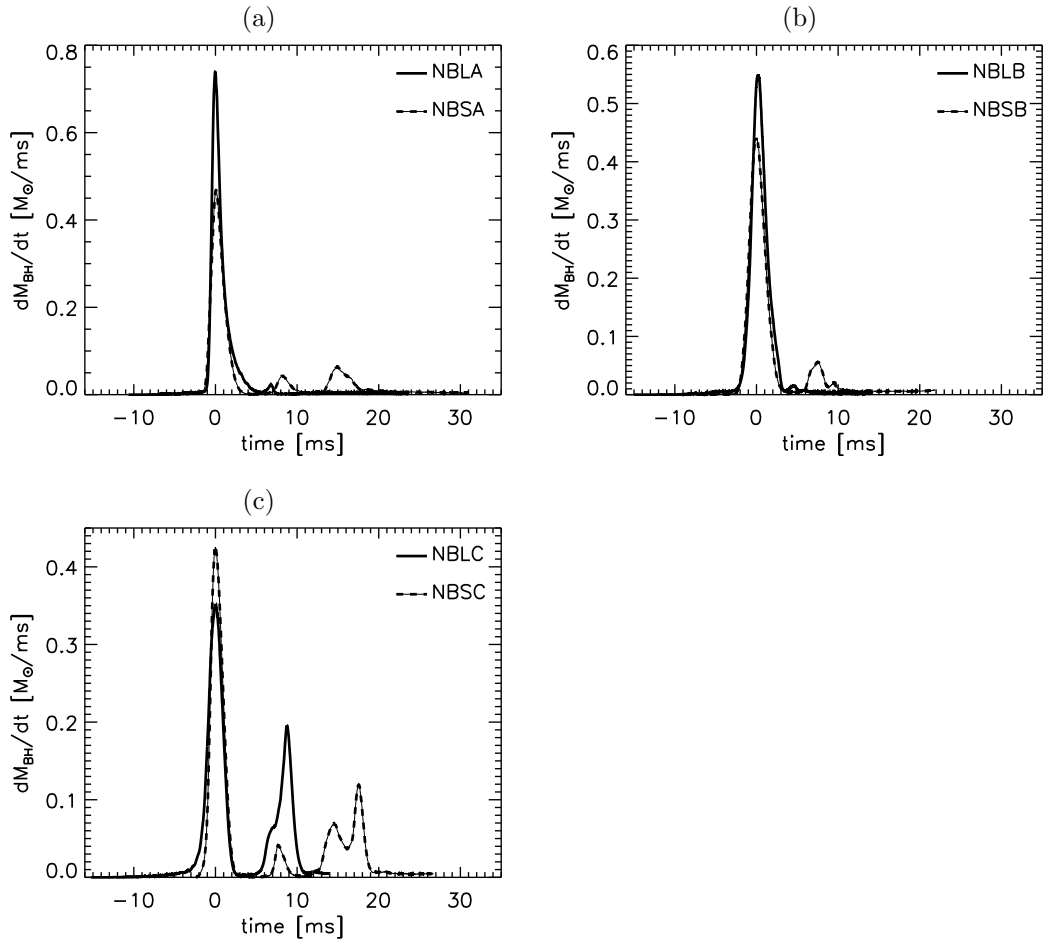

Figure 3.12: The mass accretion rates of the black hole in each of the NSBH models is plotted against time. Each panel compares LS-EoS results with Shen-EoS results for a particular model.

simulation where an accretion disk has formed.[8]

Figure 3.10(b) shows the mass of the neutron star in NSBH simulations as a function of time. The mass is measured by considering the gas within a sphere of diameter 30km centred on the density maximum. By evaluating the total gas mass on the grid at the end of the simulation, we can obtain an estimate of the mass of the accretion disk which forms after the neutron star has been shredded. It is interesting that, despite the differences in time-scale and the shape of each profile in general, all the simulations generate an accretion disk with roughly similar mass 2.87×10^{-1} M$_\odot \lesssim M_{\rm disk} \lesssim 5.35 \times 10^{-1}$ M$_\odot$. This seems to be independent of the

[8]For completeness, we also include these cross sectional plots but, since they take up several pages, they can be found in Appendix C.

equation of state. The corresponding growth in the black hole mass can be seen in panels (c) and (d) in Fig. 3.10.

Before considering the results for neutrino emission, let us briefly consider some global properties of the simulations. The huge energy scales involved in NSBH merger events are presented for models NBLA, NBSA, NBLB and NBSB in Fig. 3.13. The results for models NBLC and NBSC are similar to models NBLB and NBSC. The EoS has the greatest effect on internal energy of the gas as might be expected and on the gravitational potential energy of the system. The latter effect is likely due to the varying orbital paths taken by stars as computed with the different equations of state. In Fig. 3.14 the effects of gravitational wave emission on the angular momentum of the merging systems can plainly be seen. The effect of the accretion process on the black hole is evident in panel (d) in which the Kerr parameter (see Sect. 3.1.4) is plotted against time. Note how the accretion disk can brake a rapidly rotating black hole (the top four curves) or spin up a black hole with zero initial spin (the bottom two curves). The changes are consistent between the two equations of state except in models NBLC and NBSC. As mentioned before though, we should be careful about drawing any radical conclusions from this model due to a possible error in the initial conditions.

Neutrino emission depends on the hydrodynamic and thermodynamic state of the neutron star material, especially the temperature and electron fraction (see Ruffert et al., 1997, for a detailed discussion). We plot the global maximum temperature in Fig. 3.15(b) for model A. We only plot this model since the others show the same trend; the Shen-EoS leads to lower temperatures (and less extreme conditions) in general. This is the first indication that our hypothesis from Sect. 3.1.1, that the Shen-EoS might lead to higher neutrino emission in general, might be wrong. Further work is required to properly investigate why this is the case. The global maximum of mass density as a function of time is shown in Fig. 3.16. Once again we find slightly less extreme conditions produced when the Shen-EoS is used in the simulation. Small scale, damped oscillations can be seen in this figure (a magnified portion of the original plot is shown in panel (b)) despite the tidal relaxation of the neutron star. The oscillations decay within a few milliseconds however, and do not appear to affect the evolution of the density in any of the models.

We now turn our attention to the neutrino emission, starting with the global luminosity. Figures 3.18-3.20 show the total luminosity from the entire computational domain evaluated at each time step. In each of these three plots, with the exception of Fig. 3.20, the neutrino luminosity is higher for the LS-EoS than with the Shen-EoS. The difference between the two equations of state is not large, though; in each model

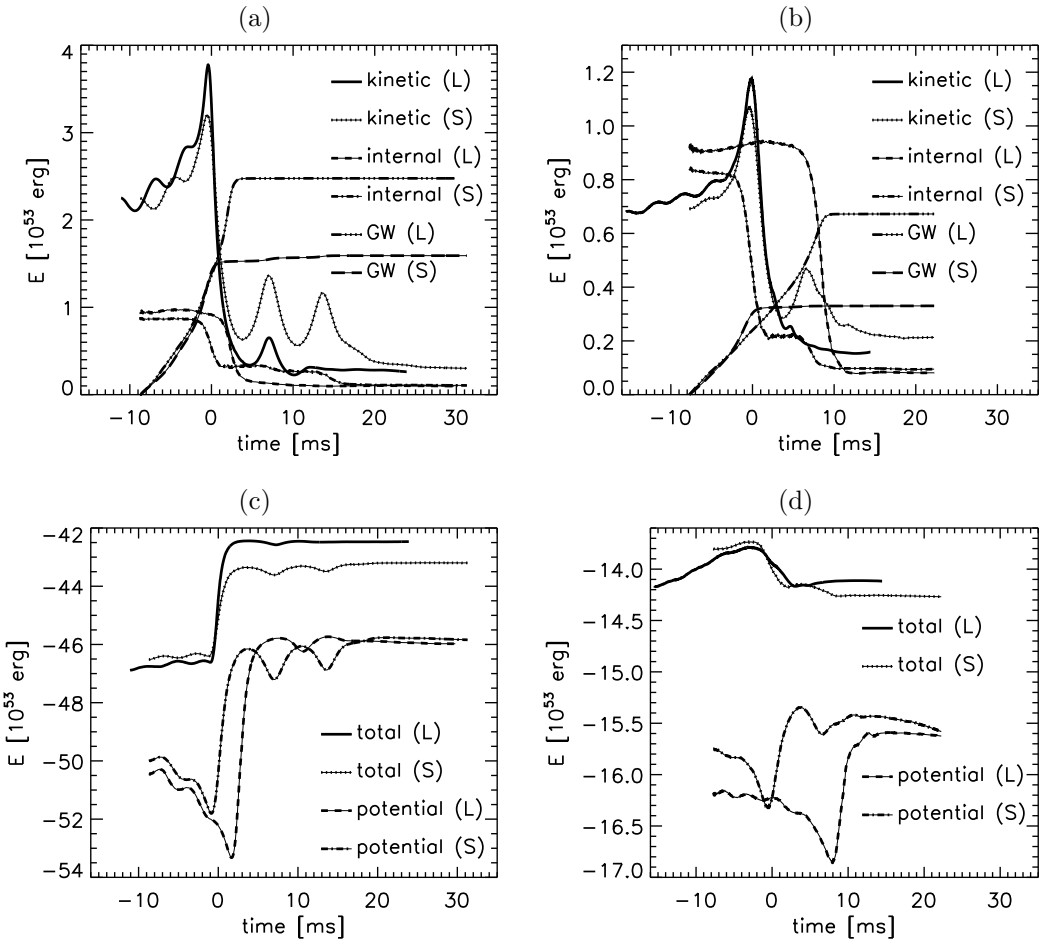

Figure 3.13: Comparison of various energies as functions of time for models NBLA, NBSA (left panels), NBLB and NBSB (right panels). The "L" and "S" tags in each plot refer to the equation of state. The total energy refers to the energy in all forms on the grid. This is obviously not conserved since neutrinos, gravitational waves and mass loss all carry energy out of the computational domain. It should be possible to quantify this loss by accumulating the fluxes at the edge of the grid.

the emission is within the same order of magnitude as can be seen in Tab. 3.4. The largest difference for the peak luminosity rate is between models NBLB and NBLC and even then the LS-EoS results is only about 2.3 times greater than the Shen-EoS result. This is good news since it means that uncertainties in the nuclear physics which go into describing the dense material of neutron stars do not seem to affect the generation of neutrinos.

The main features of the neutrino luminosity can be explained by considering the conditions throughout the computational volume. Consider Fig. 3.18, for example. The striking features in this plot are the round plateau feature which develops as

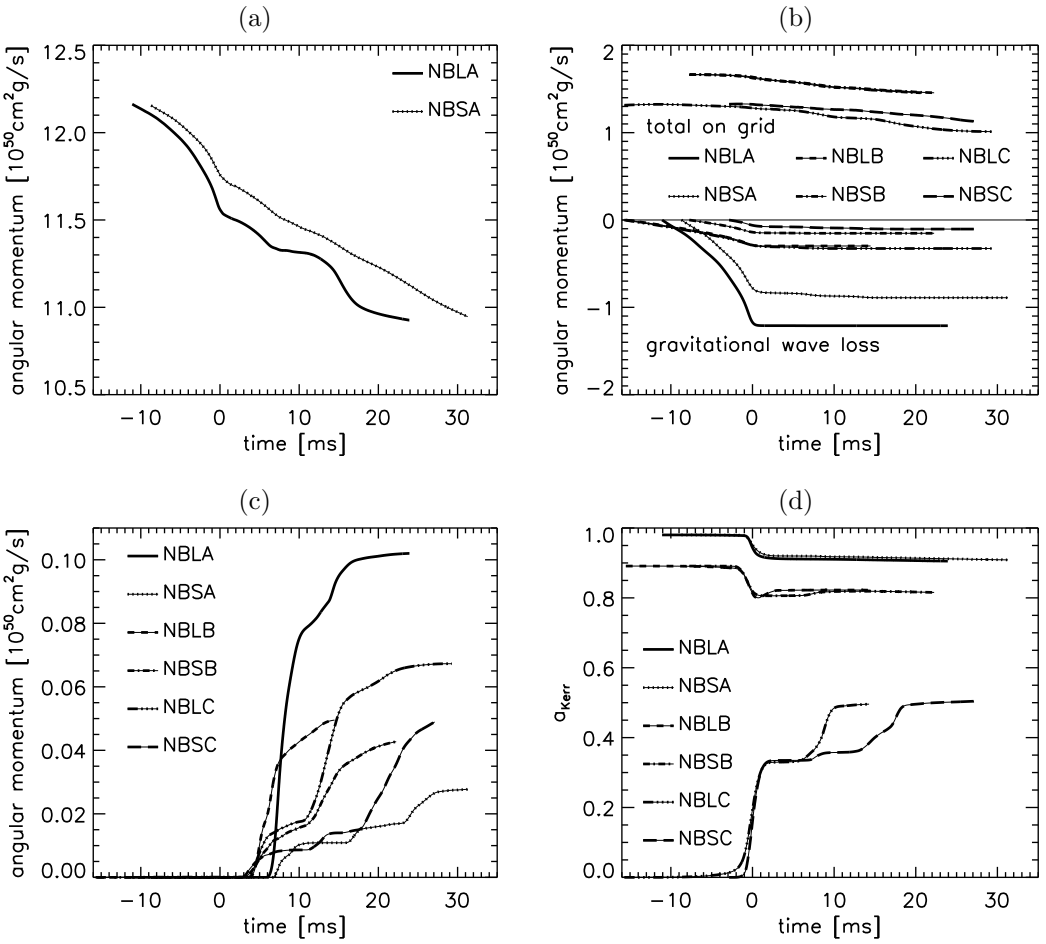

Figure 3.14: The evolution of the distribution of angular momentum on the grid as a function of time. Panels (a) and (b) show the total angular momentum on the grid and the loss of angular momentum due to gravitational wave emission for models NBLA, NBSA, NBLB and NBSB. Panel (c) shows the cumulative angular momentum which has left the grid and panel (d) shows the change in specific angular momentum of the black hole through interaction with the gas. Note that we do not expect the total angular momentum to be constant due to losses via gravitational wave emission and material leaving the computational domain.

soon as the simulation starts and the subsequent peaks and troughs, one of which in particular is very pronounced in the NBLA model and appears absent in the NBSA case. We have chosen six points in time ($t = -3, 2, 8, 15, 18$) at which we plot detailed two dimensional slices through the computational domain for the electron fraction Y_e (Figs. 3.21-3.22) and the temperature (Figs. 3.23-3.24). From these plots we can explain the aforementioned features of Fig. 3.18.

The rounded plateau at the start of each simulation occurs because of a shock wave heating the leading edge of the neutron star to temperatures in excess of 10 MeV. This

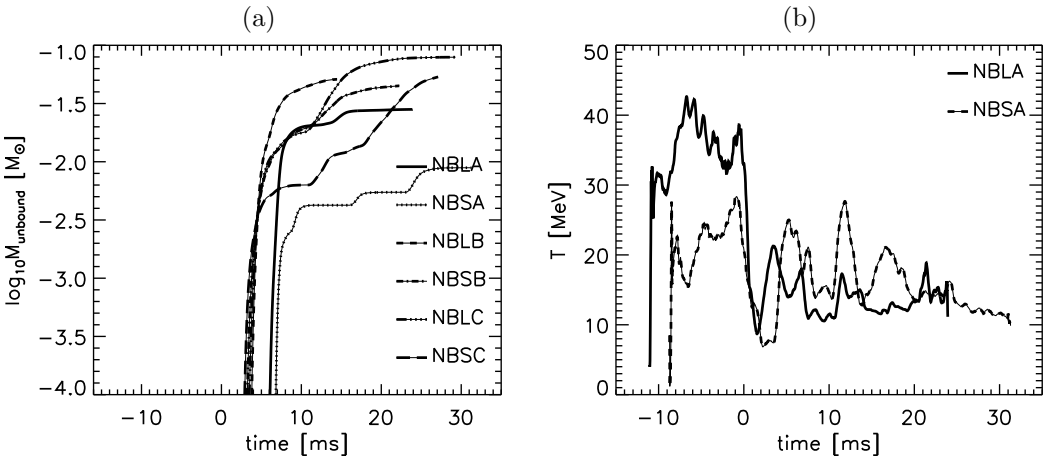

Figure 3.15: (a)Gravitationally unbound mass (mass which has a positive total energy) as a function of time for all NSBH models. (b) Maximum temperature in MeV shown for models NBLA and NBSA.

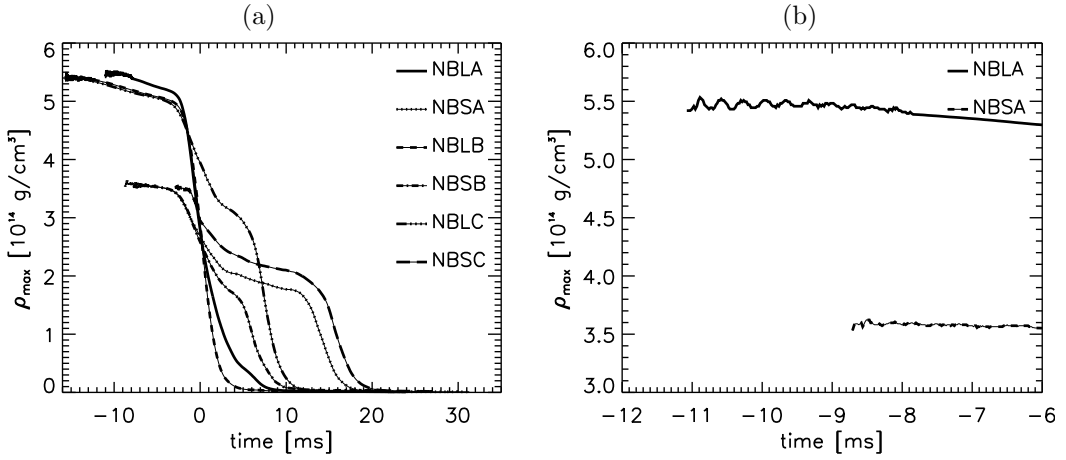

Figure 3.16: Maximum density on the grids as a function of time. The panel on the left exhibits damped oscillations for the first few milliseconds which are due to the tidal relaxation of the neutron stars. The panel on the right gives a magnified view of these oscillations. Time normalisation is as described in Sect. 3.2.2.

shock develops due to friction between the star and the "low-density" ambient matter which must be present in our code for numerical reasons. It is unlikely that such heating would occur in reality as the ambient density in the NSBH system would be many orders of magnitude lower than the 10^8 g/cm^3 required in our simulations. This heating is short-lived however, and eventually the neutrino emission settles down again before the large spike seen at $t \approx 8$ ms in the NBLA model. Although this feature appears absent from the NBSA plot, it actually just occurs later in time at

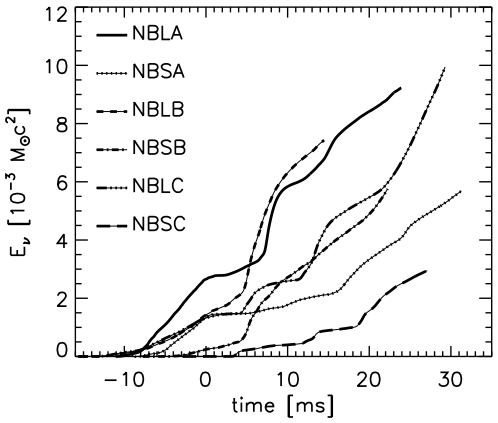

Figure 3.17: Cumulative energy radiated in all species of neutrino as a function of time for the NSBH models.

Model ID	$M_{\rm disk}$ [10^{-1} $M_\odot$]	$T^{\rm max}$ [MeV]	$L^{\rm max}_{\nu_e}$ [10^{53} erg/s]	$L^{\rm max}_{\bar{\nu}_e}$ [10^{53} erg/s]	$L^{\rm max}_{\nu_x}$ [10^{53} erg/s]	$L^{\rm max}_{\nu}$ [10^{53} erg/s]
NBLA	4.86	52.36	2.25	7.50	2.78	11.95
NBSA	5.35	41.78	1.06	3.33	1.72	5.27
NBLB	3.39	39.45	3.20	11.96	2.36	17.60
NBSB	3.85	36.06	1.87	4.96	1.95	7.65
NBLC	2.87	44.87	1.75	8.04	2.37	11.52
NBSC	4.06	30.69	1.34	3.70	0.25	5.31

Table 3.4: A summary of results from the NSBH simulations. $M_{\rm disk}$ is the estimated mass of the accretion disk around the black hole as measured at the end of the simulation. $T^{\rm max}$ is the maximum gas temperature during the simulation in energy units, $L^{\rm max}_{\nu_i}$ denotes the maximum luminosity in neutrino species i. The notation L_{ν_x} is shorthand for the combined luminosity of the heavy neutrinos and their antineutrinos ($\nu_\tau, \bar{\nu}_\tau, \nu_\mu$ and $\bar{\nu}_\mu$).

$t \approx 18$ ms. These peaks are due to the final tidal disruption of the neutron star into the accretion disk which decreases the opacity of the medium to neutrinos but also causes viscous heating as can be seen in the temperature plots. A similar analysis can be performed on the other models but for brevity we only include detailed 2D slices for these simulations once the matter has settled into an accretion disk. These plots are to be found in Figs. C.9-3.29.

We complete our discussion of the NSBH models by considering the total cumulative energy emitted in neutrinos of all species over time (see Fig. 3.17). The difference between the two equations of state is most marked here; the different slopes of the plots indicate that perhaps, over the lifetime of the accretion disk, the equation

of state may prove more important than we have suspected until now. Further study, extending the simulation time of the accretion disk may increase our understanding of this process.

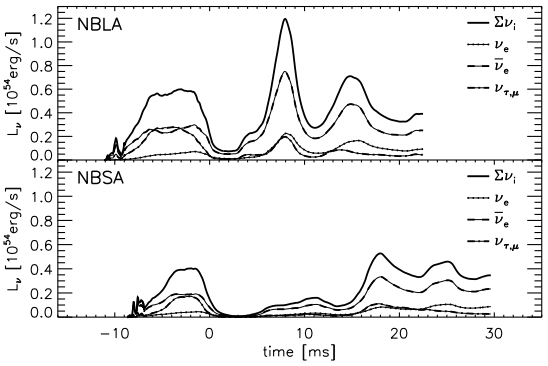

Figure 3.18: Neutrino luminosities as functions of time for the models NBLA (top) and NBSA (bottom) in each of the species tracked; electron $\nu_{\rm e}$, electron antineutrino $\bar{\nu}_{\rm e}$, and the tau and mu neutrinos and their respective antineutrinos $\nu_{\tau,\mu}$. We also plot the total luminosity in all species of neutrino, $\Sigma\nu_{\rm i}$.

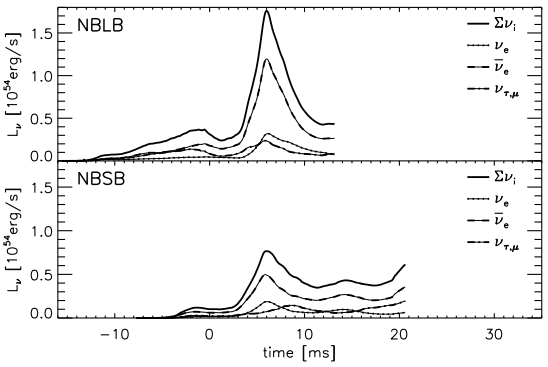

Figure 3.19: Neutrino luminosities as functions of time for the models NBLB (top) and NBSB (bottom). For further details see Fig. 3.18.

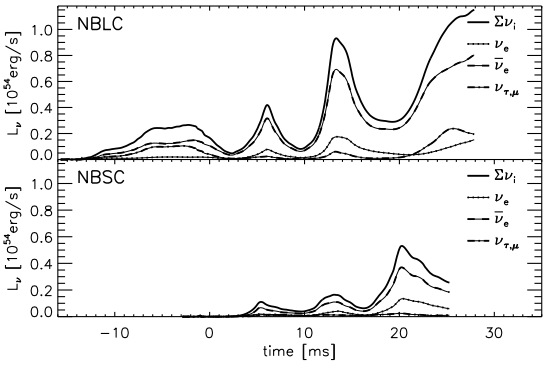

Figure 3.20: Neutrino luminosities as functions of time for the models NBLC (top) and NBSC (bottom). For further details see Fig. 3.18.

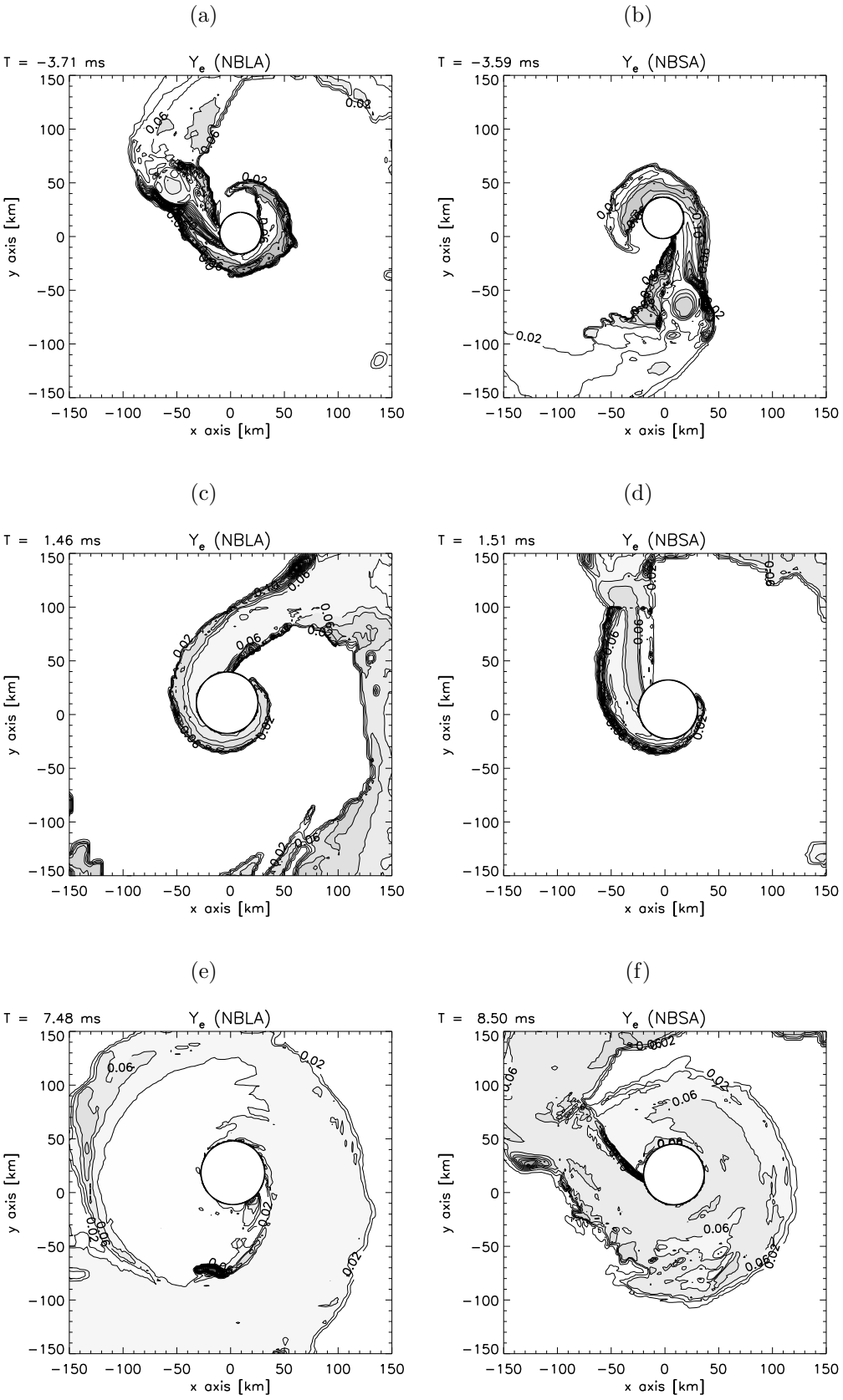

Figure 3.21: Electron fraction in the orbital plane. Only the inner part of the computational domain is plotted. All of these cross-sections (and many more of the plots in this thesis) were made with the Interactive Data Language (IDL).

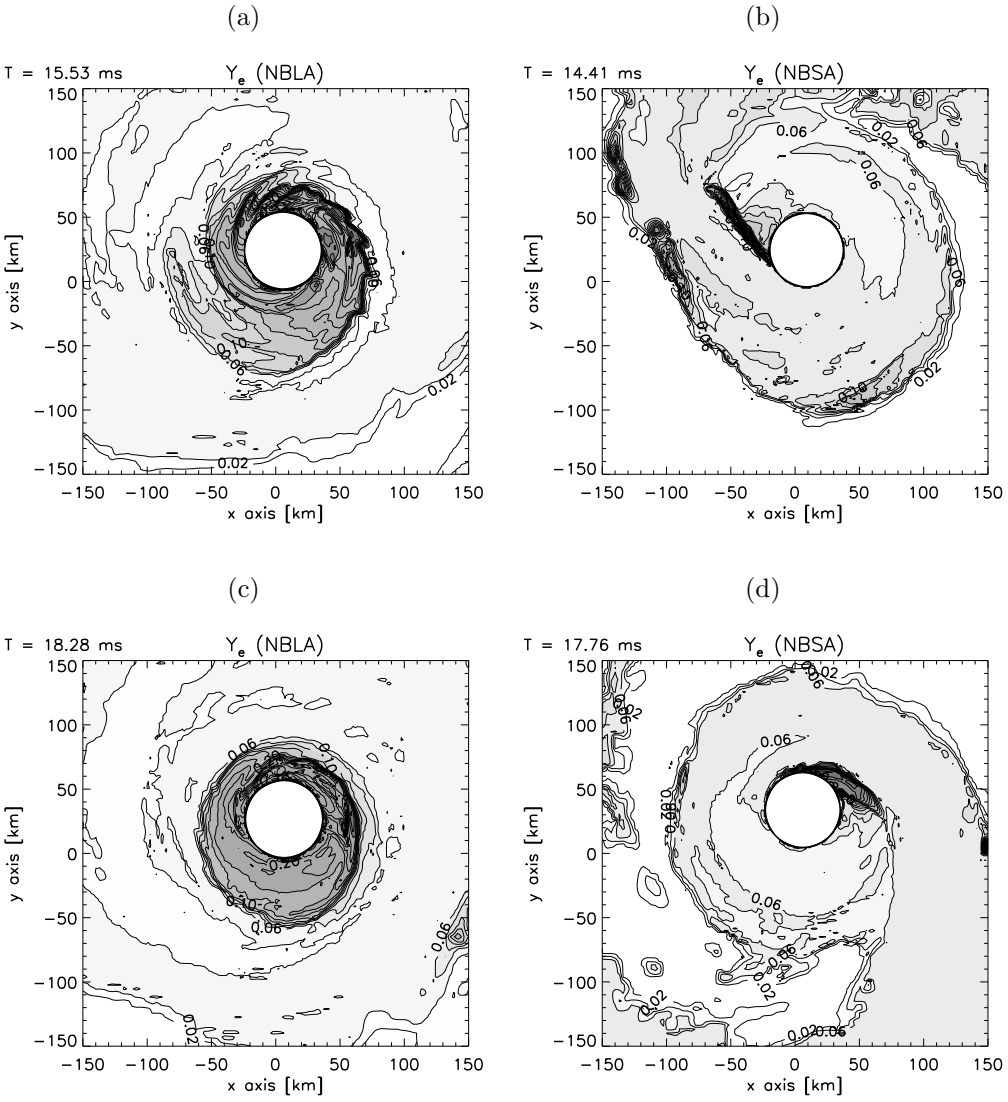

Figure 3.22: Electron fraction in the orbital plane (part2).

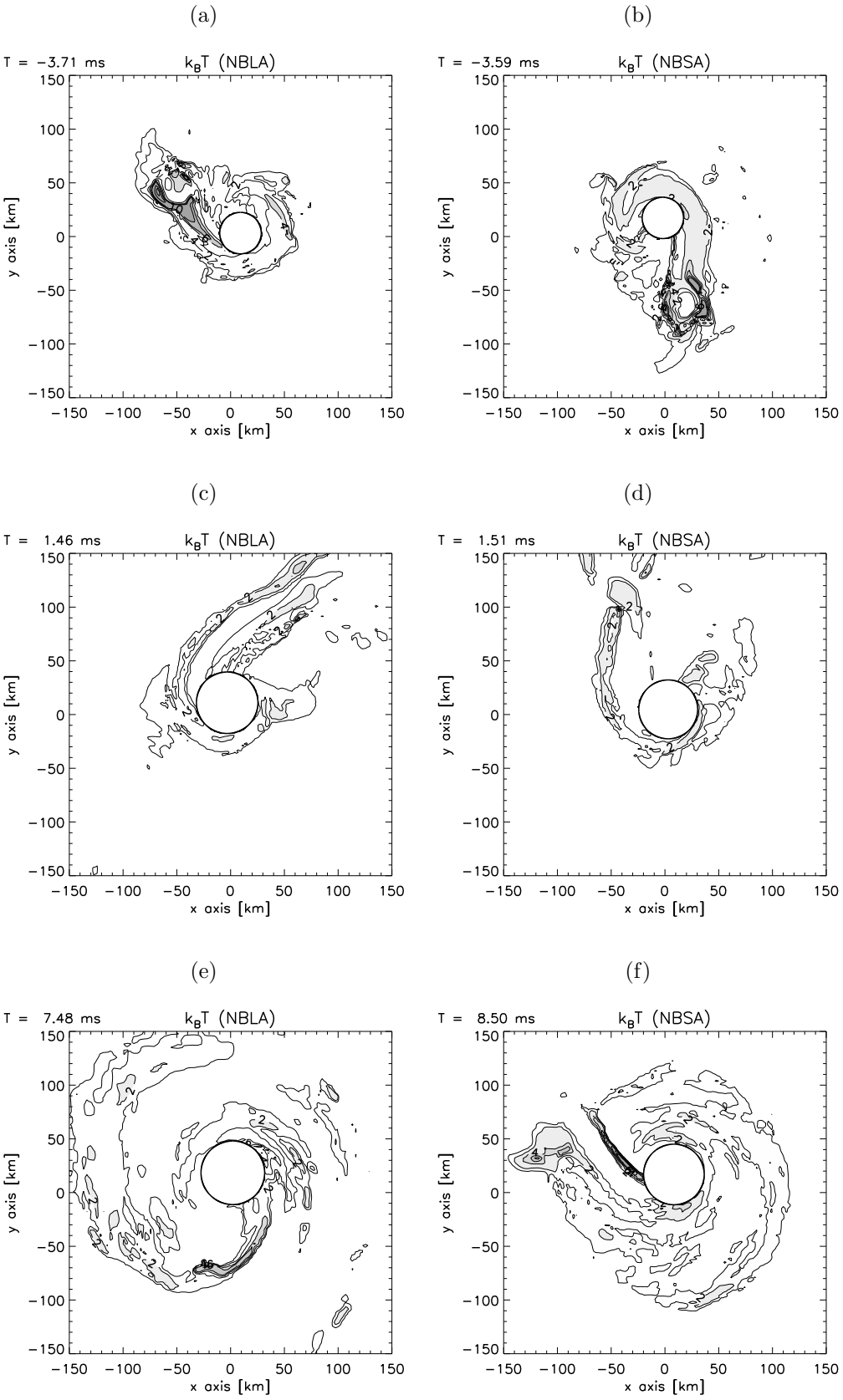

Figure 3.23: Temperature in the orbital plane.

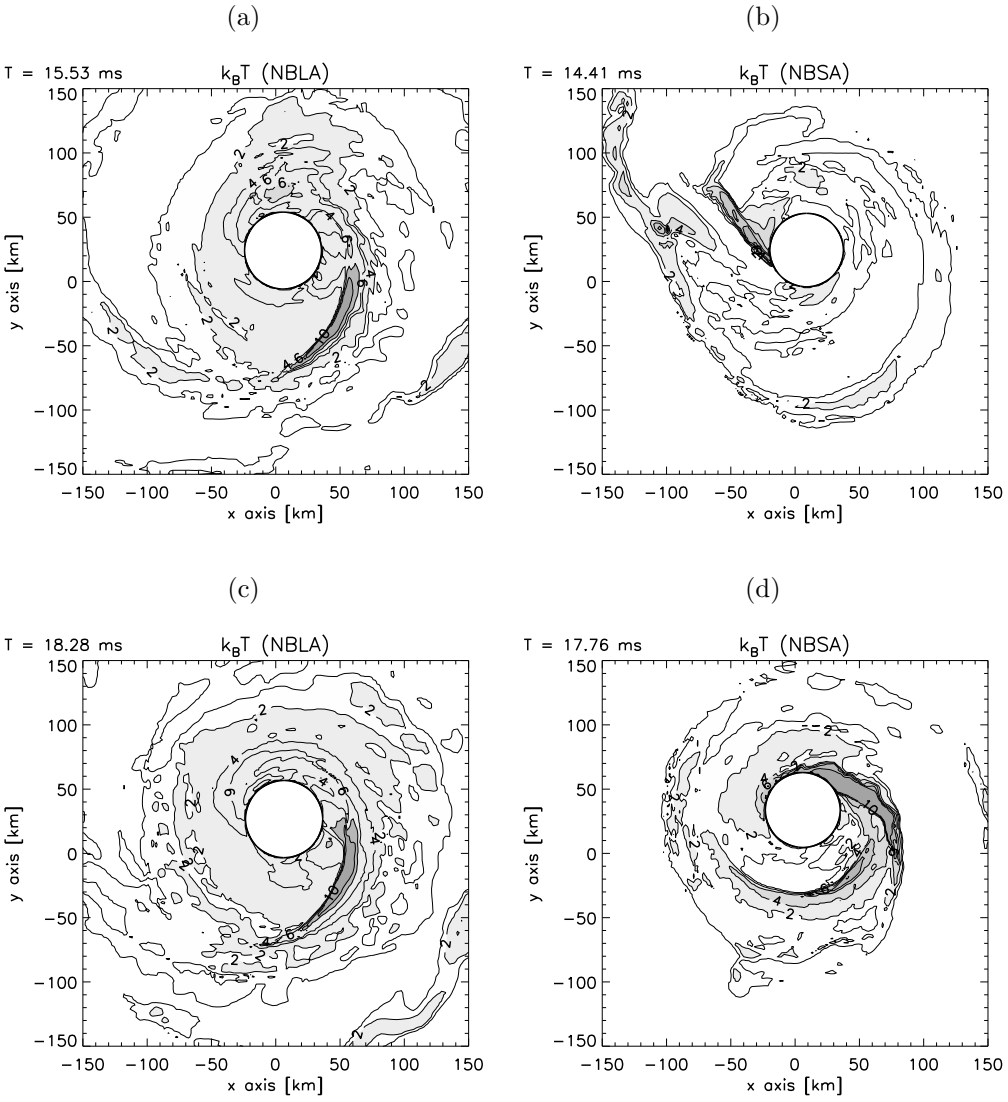

Figure 3.24: Temperature in the orbital plane (part2).

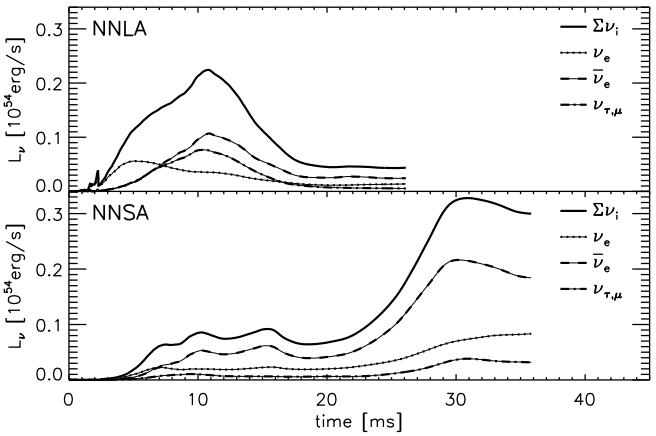

Figure 3.25: Neutrino luminosities as functions of time for the models NNLA (top) and NNSA (bottom) in each of the species tracked; electron $\nu_{\rm e}$, electron antineutrino $\bar{\nu}_{\rm e}$, and the tau and mu neutrinos and their respective antineutrinos $\nu_{\tau,\mu}$. We also plot the total luminosity in all species of neutrino, $\Sigma\nu_{\rm i}$.

Model ID	$T^{\rm max}$	$L^{\rm max}_{\nu_e}$	$L^{\rm max}_{\bar{\nu}_e}$	$L^{\rm max}_{\nu_x}$	$L^{\rm max}_{\nu}$
	[MeV]	[10^{53} erg/s]	[10^{53} erg/s]	[10^{53} erg/s]	[10^{53} erg/s]
NNLA	53.21	2.29	6.85	1.56	10.40
NNSA	62.37	3.88	9.24	3.26	15.96

Table 3.5: A summary of results from the NSNS simulations. $T^{\rm max}$ is the maximum gas temperature during the simulation in energy units, $L^{\rm max}_{\nu_i}$ denotes the maximum luminosity in neutrino species i. The notation L_{ν_x} is shorthand for the combined luminosity of the heavy neutrinos and their antineutrinos ($\nu_\tau, \bar{\nu}_\tau, \nu_\mu$ and $\bar{\nu}_\mu$).

3.2.3 NSNS results and discussion

The dynamics of the merger of a neutron star binary system is similar to the NSBH system we have just discussed. The two stars orbit each other until matter escapes into long spiral arms. The main difference here is that there is no chance for either of the two stars to be given a stay of execution by being flung out into an elliptic orbit; drag caused by turbulence at the point of contact between the stellar surfaces accelerates the merging process and the two stars coalesce into a hot, rapidly oscillating blob. This new high mass neutron star will likely be unstable and should therefore collapse to form a black hole. Since we do not have a full general relativistic treatment yet, we do not speculate on how long it would take before the collapse happened and how much of the matter would form the initial black hole. The in-spiral and eventual merger of the two stars is depicted in Figs. 3.26 and 3.27.

We skip immediately to the neutrino emission, the results for which are surprising in comparison to the results for the NSBH models. The luminosity of neutrinos is plotted in Fig. 3.25 for models NNLA and NNSA and peak luminosities for each flavour is shown in Tab. 3.5. Here we find the Shen-EoS produces more neutrinos. In fact, even after the luminosity has dropped to a quasi-steady state in model NNLA, the emission remains high in the Shen-EoS case. If we look at the temperature sections in Fig. 3.28 we find that the temperatures are highest for the LS-EoS. It seems that in this case, quantity is better since, although the peak temperature is lower in model NNSA, a greater volume of the thick (proto-)accretion disk is at a temperature of around 6 MeV. Perhaps this is due to the difference in stiffness of the two equations of state leading to more extreme conditions (i.e. the higher temperature) in what is in effect a new, larger mass neutron star.

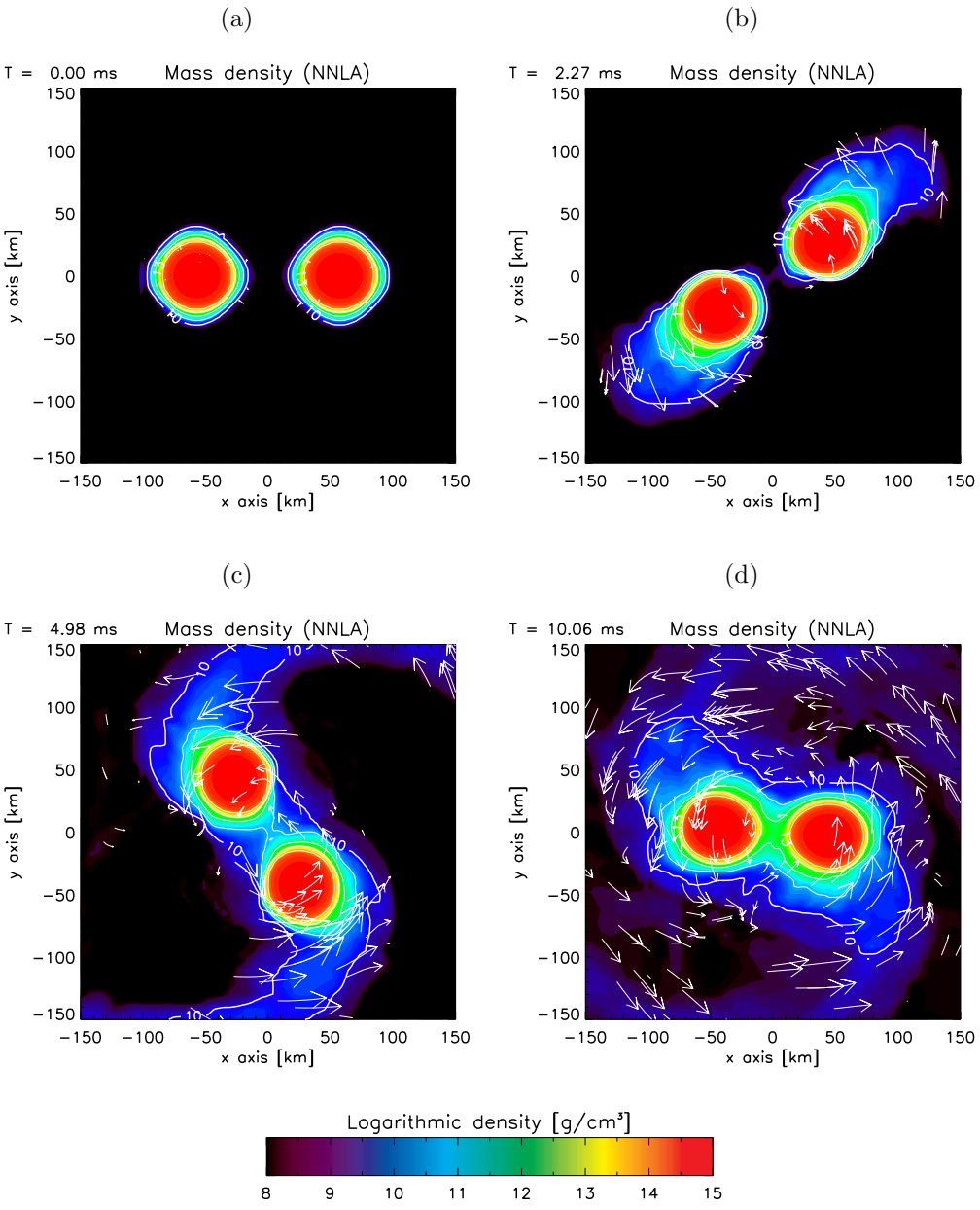

Figure 3.26: Dynamical evolution of the coalescence of two neutron stars shown as logarithmic density in the orbital plane. The neutron stars each have a mass of 1.6 $M_{\odot}$. The equation of state used in this simulation is from Lattimer and Swesty (1991). The white arrows show the velocity field with the longest arrow relating to a velocity of about $0.3c$.

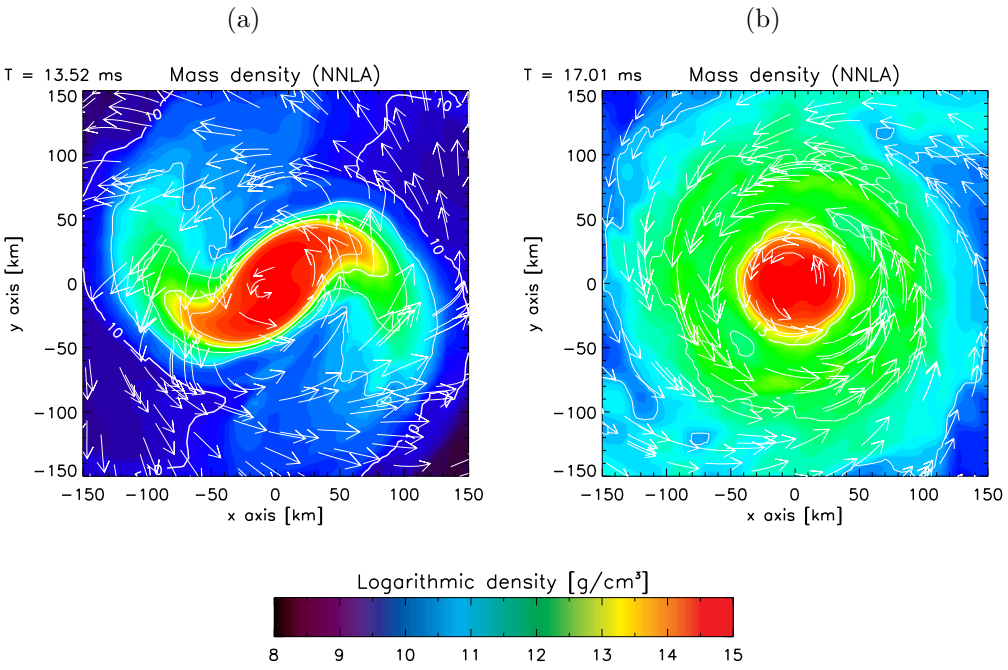

Figure 3.27: Continuation of the dynamical evolution of a merger event between two 1.6 $M_{\odot}$ neutron stars. See Fig. 3.26 for more details. The high density central object (red with a sharp density drop near the yellow "crust") is a likely proto-black hole candidate but, as explained in the text, we cannot tell for certain without a full general relativistic treatment.

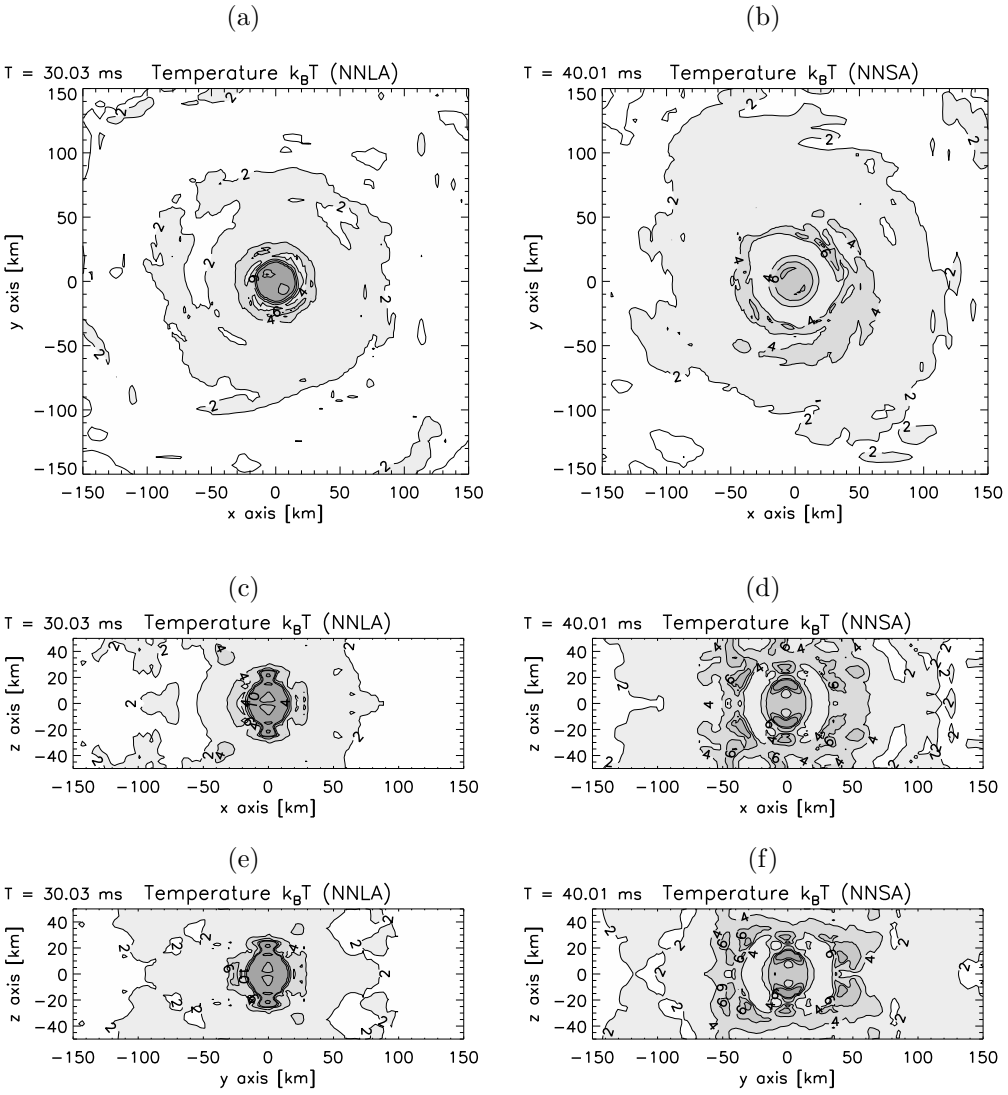

Figure 3.28: Temperature in the disk, NNLA and NNSA.

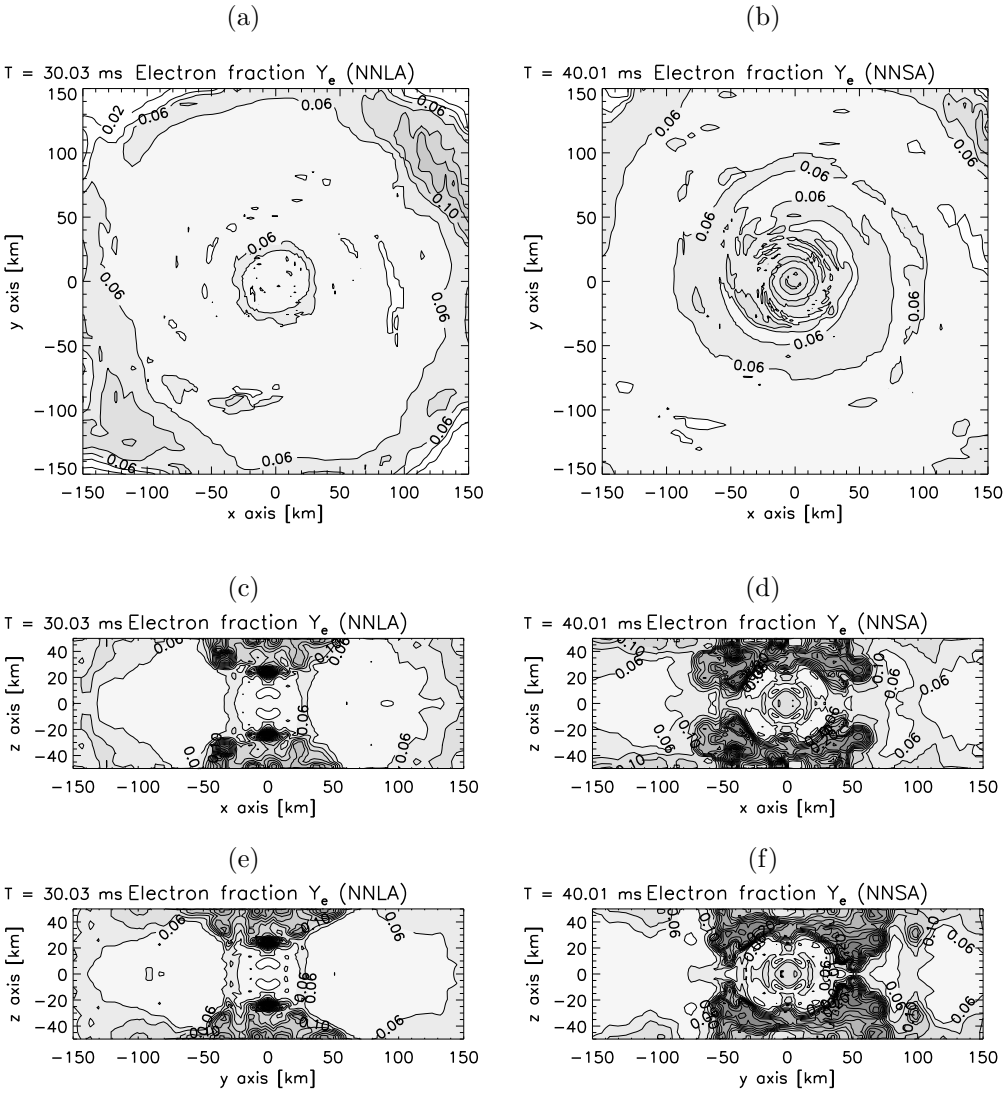

Figure 3.29: Electron fraction in the disk, NNLA and NNSA.

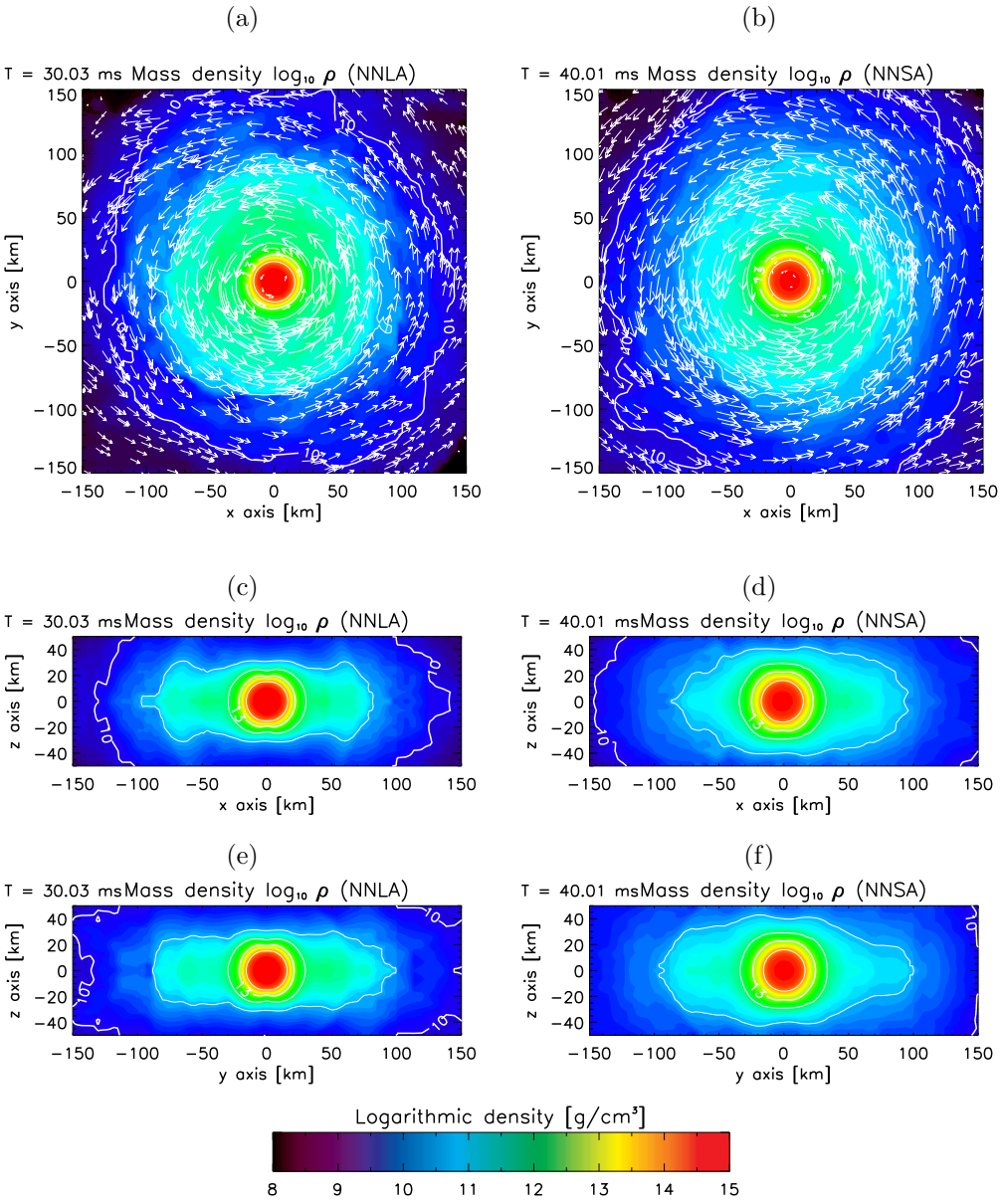

Figure 3.30: Two dimensional slices through the centre of the grid showing mass density in the disk for models NNLA and NNSA plotted as colour filled contours. The velocity field is shown as white arrows, the longest arrow corresponding to a velocity of about $0.3c$.

> “The best laid schemes o’ Mice an’ Men,
> Gang aft agley,
> An’ lea’e us nought but grief an’ pain,
> For promis’d joy!
> (The best laid schemes of Mice and Men
> oft go awry,
> And leave us nothing but grief and pain,
> For promised joy!)”
>
> — Robert Burns, *excerpt from “To a Mouse”*

4

Application of Approximate Riemann Solvers in Charybdis

In chapter 3 we have introduced our astrophysical code for the simulation of mergers of compact stellar remnants, Charybdis. In this chapter we continue with our investigations on the suitability of the approximate Riemann solvers presented in chapter 2 for solving astrophysically relevant gas-dynamic problems.

Our ultimate goal will be to employ one of these more computationally efficient Riemann solvers (or possibly to incorporate more than one in a hybrid scheme) in the solution of the equations of magnetohydrodynamics (MHD), modified to account for the back-reaction of gravitational wave emission and augmented by the advection equations for entropy and chemical species (see Sect. 3.1.2).

We now present a brief summary of the MHD system to motivate the use of a conceptually simpler Riemann solver than the exact or iterative solver currently used in Charybdis. Although such an exact MHD Riemann solver has already been developed for the piecewise parabolic scheme (PPM) (Dai and Woodward, 1994), we argue that the computational expense of this solver is prohibitive and that its complexity would make the inclusion of the gravitational back-reaction and advection

terms more challenging than necessary.

4.1 The challenge of magnetohydrodynamics

The equations of MHD can be derived by supplementing the Euler equations (see Sect. 3.1.2) by Maxwell's equations of electrodynamics. Choosing a set of units in which the magnetic permeability of free space μ_0 is taken to be unity, the system of equations in the conservative form of Eq. 2.1 is as follows (Goedbloed and Poedts, 2004)

$$\frac{\partial \mathbf{U}}{\partial t} + \nabla \cdot \mathbf{F}(\mathbf{U}) = \mathbf{S}(\mathbf{U}), \tag{4.1}$$

with the vectors

$$\begin{aligned} \mathbf{U} = \begin{pmatrix} \rho \\ \rho\mathbf{u} \\ E \\ \mathbf{B} \end{pmatrix}, \qquad \mathbf{F}(\mathbf{U}) = \begin{pmatrix} \rho\mathbf{u} \\ \rho\mathbf{u}\mathbf{u} + \left(p + \frac{B^2}{2}\right)\mathbf{I} - \mathbf{B}\mathbf{B} \\ \left(\frac{1}{2}\rho u^2 + \rho e + p\right)\mathbf{u} + (\mathbf{B} \times \mathbf{u} + \eta\mathbf{j}) \times \mathbf{B} \\ \mathbf{u}\mathbf{B} - \mathbf{B}\mathbf{u} \end{pmatrix}, \\ \text{and } \mathbf{S}(\mathbf{U}) = \begin{pmatrix} 0 \\ 0 \\ 0 \\ -\nabla \times (\eta \nabla \times B) \equiv \eta\nabla^2\mathbf{B} + \mathbf{j} \times \nabla\eta \end{pmatrix}, \end{aligned} \tag{4.2}$$

along with the solenoidal constraint on the magnetic field: $\nabla \cdot \mathbf{B} = 0$. The relevant variables are the mass density ρ, the momentum density $\rho\mathbf{u}$, the total energy density (made up of kinetic, internal and magnetic contributions)

$$E \equiv \frac{1}{2}\rho u^2 + \rho e + \frac{B^2}{2}, \tag{4.3}$$

the magnetic field $\mathbf{B}$ and the current density $\mathbf{j}$.

The respective elements of the flux vector are the momentum density, the Maxwell stress tensor (in which $\mathbf{I}$ is the unit tensor), the energy flux and a term composed of the anti-symmetric tensor product of the fluid velocity and the magnetic field $\mathbf{B}$, and a term which allows for the possibility of change to the magnetic topology. This last equation is called the induction equation.

The parameter η is often referred to as either the magnetic resistivity or diffusivity. The first name refers to the effect of the parameter on the behaviour of electrical currents. With $\eta = 0$, currents can flow but they do so with no dissipation of energy, the up-shot of which is that there can be no spontaneous changes in the magnetic topology (i.e. no reconnection). The other name is much more obvious when the induction equation is written in the following form. If we suppose that we

are interested in a structure which consists of stationary plasma which is threaded by a magnetic field (e.g. a solar prominence), the induction equation simplifies to

$$\frac{\partial \mathbf{B}}{\partial t} = \eta \nabla^2 \mathbf{B}. \tag{4.4}$$

This equation is of the form of a diffusion equation for the magnetic field. Clearly η is the diffusion constant in this equation and when it is set to zero, the magnetic field will never decay independently of the motion of the plasma.

An additional constraint on the evolution of the magnetic field, which can cause problems for numerical solutions, is

$$\nabla \cdot \mathbf{B} = 0. \tag{4.5}$$

This implies that there are no sources or sinks of magnetic field within a closed system.

The formulation of both the Euler equations and MHD leads to a system of non-linear, hyperbolic equations as we have already discussed in some detail in chapter 2. The addition of the magnetic field in the MHD equations leads to a much richer mathematical model. For example, by linearising the Euler equations, one can derive a wave equation which corresponds to ordinary acoustic waves. In MHD by contrast, the forces introduced by the Maxwell stress tensor $\frac{1}{2}(\mathbf{B} \cdot \mathbf{B})\mathbf{I} - \mathbf{BB}$ mean that the magnetic field effectively provides a pressure force orthogonal to the field lines and a tension force along bent field lines. These contributions to the dynamics mean that linearisation of the MHD equations yields three types of wave. The fast and slow magneto-sonic waves are pressure waves which we would expect from ordinary gas dynamics. They propagate with different speeds because they correspond to the situations where the gas pressure and the pressure exerted by the magnetic field work together or against each other, respectively. There is also a third wave in MHD though, which has no analogue in pure gas dynamics, the Alfvén wave. Whereas the magneto-sonic waves are longitudinal compression waves, the Alfvén wave is a transverse wave *along* the magnetic field lines, like waves on a guitar string.

4.2 Implementation of the approximate schemes

Since CHARYBDIS evolved from the PROMETHEUS code we described in chapter 2, we can easily incorporate the Roe and HLLE schemes into CHARYBDIS without much programming effort since the same subroutines and variable names are still present in the inner workings of the hydrodynamic solver. There are some fundamental differences in the equations solved by PROMETHEUS and CHARYBDIS, however. In the latter, as described in chapter 3, there are extra equations to be solved for advected

quantities such as entropy and the electron number density. Since the conservation equation for a passively advected scalar quantity is equivalent to the equation of mass conservation, we simply treat these extra equations in exactly the same manner as the mass density in our calculations. At present, we do not use the HLLEM scheme since the modification which is intended to improve the accuracy of contact waves (see Sect. 2.5.3) requires anti-diffusion terms to be added to the linearly degenerate fields (Einfeldt, 1988; Einfeldt et al., 1991). Further work is required to determine the correct course of action for the advected quantities which, of course, travel as linearly degenerate contact waves. We expect the electron fraction and temperature distributions to be much more diffuse when compared with the iterative solver.

A final unresolved problem at this time is the treatment of gravitational wave emission and the back-reaction of these waves on the gas dynamics. At present, the Riemann solver in CHARYBDIS returns the cell interface values of each individual fluid quantity. In the system of equations defined in Sect. 3.1.2 two velocities occur; the "kinematic" and "dynamic" velocities (recall these are used as part of a relativistic correction to allow us to study gravitational wave emission and feedback). The Riemann solver is entirely non-relativistic and uses the transformation in Eq. 3.9 to complete the solution of the hydrodynamical equations. It is much more difficult to apply the required transformations in the case of an approximate scheme which returns the cell interface flux values directly. Without recourse to the interface values of the conservative/primitive variables it is not straightforward to apply the transformation in the form of Eq. 3.9 to the fluxes computed by the approximate schemes. The solution to this problem may involve changing the way gravitational wave emission is handled in CHARYBDIS. As a temporary solution, so that we may actually have some results to compare, we simply turn off the gravitational wave effects in all the simulations in this chapter. We will still see some orbital decay though because angular momentum conservation is not guaranteed numerically.

4.3 Numerical results

In this section we compare the results of hydrodynamical simulations of the coalescence (due to numerical dissipation!) of two neutron stars computed with CHARYBDIS. We choose the same initial conditions for the tests as model NNLA in the previous chapter (see Sect. 3.2.1), i.e. two 1.6 $M_\odot$ neutron stars are placed 57 km apart in an approximately circular orbit. All the tests in this chapter are computed using the tabulated equation of state of Lattimer and Swesty (1991). The initial conditions are summarised in Tab. 4.1.

Model ID	EoS	NS Masses	Separation	Grid length	Resolution
ITER	L&S	1.6 $M_\odot$	57 km	800 km	64^3
ROE	L&S	1.6 $M_\odot$	57 km	800 km	64^3
HLLE	L&S	1.6 $M_\odot$	57 km	800 km	64^3

Table 4.1: Initial conditions for simulations run to test the performance of the approximate Riemann solvers (ROE and HLLE) against the exact, iterative solver (ITER). Separation refers to the initial centre to centre distance of the two neutron stars, and grid length is the size of the coarsest grid in the x or y directions.

We have already described the basic dynamics of the merger and coalescence of a neutron star binary system in Sect. 3.2.3 and so in Figs. 4.1-4.3 we only plot the mass density and velocity fields for two snapshots in time; one near the beginning of the simulation and one at the very end. Note that, in contrast to the results for NSBH simulations in Sect. 3.2.2, there is no renormalisation of time and $t = 0$ merely refers to the beginning of the simulation. Figures. 4.1-4.3 show that the dynamics of the simulation are similar for the three different numerical schemes. The approximate solvers do not show such pronounced mass loss as is seen in Fig. 4.1(a) for the iterative solver. The Roe solver is worst in this respect with no appreciable mass loss despite the fact that Fig. 4.2(a) shows a later physical time than the equivalent plots for the iterative and HLLE solvers. This is not to say that the HLLE solver performs better than the Roe's scheme as can be seen in the later snapshot in Figs. 4.1-4.3. Here the general qualitative shape of the spiral arms and the coalescing stars is very similar for the iterative and Roe solvers despite the difference in the amount of material in these structures. The rather poor performance of the HLLE solver is seen in Fig. 4.3(b); the neutron stars have completely merged by the end of the simulation time ($t = 25$ ms). This is to be expected since we knew that this scheme would be much more diffusive than the other two.

Despite the differences mentioned above, these results are encouraging since we at least find similar dynamical behaviour for the approximate Riemann solver based schemes. This is further confirmed in Fig. 4.4 in which we directly compare the orbital paths for the two neutron stars computed with each of the approximate Riemann solver to the result computed with the iterative solver. To avoid confusion from the overlap of the initial few orbits we only plot the last "20%" or so of the data.

The more rapid orbital decay exhibited in the simulation computed with the HLLE solver is largely due to the large numerical viscosity inherent in this scheme. Other discrepancies of the merger dynamics may be caused by our assumption to treat the

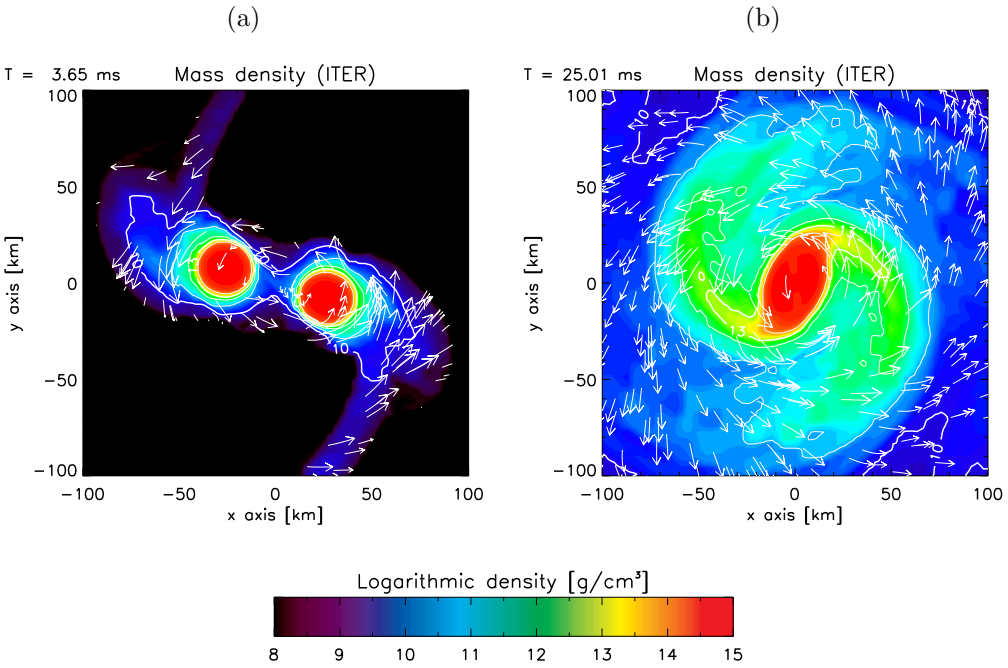

Figure 4.1: Mass density in the orbital plane for the simulation of a neutron star merger with the LS-EoS and the iterative Riemann solver. Panel (a) shows an early snapshot after the neutron stars have begun shedding mass and (b) shows the distribution of mass at the end of the simulation. The arrows show the velocity field of the gas. The largest arrows correspond to velocities on the order of $0.3c$.

advected quantities just as we treat the mass density. Our reason for suspecting this treatment to be insufficient comes from comparing the neutrino luminosities (both total radiation in neutrinos and the individual luminosities) (Fig. 4.5). Since neutrino emission depends strongly on the local temperature and electron fraction (themselves derived from the advected quantities), the large differences between the neutrino emission as computed by the approximate schemes and by the iterative scheme imply that the problem may lie in the advected quantities. This is a problem we are currently working to resolve and shows the direction of our future work in this area.

For completeness and, for consistency with chapter 3, we plot two dimensional slices of the temperature and electron fraction through the centre of the computational domain for each of the three solvers. See Figs. 4.6-4.11. A summary of some global quantities from each simulation is presented in Tab. 4.2. Note that the HLLE simulation exceeds the maximum tabulated value for temperature with the LS-EoS (which is 95.77 MeV. See Tab. 3.1). The difference in the neutrino luminosity between the iterative and approximate solvers is an order or magnitude in some species. The difference is not as pronounced between models ROE and HLLE, however.

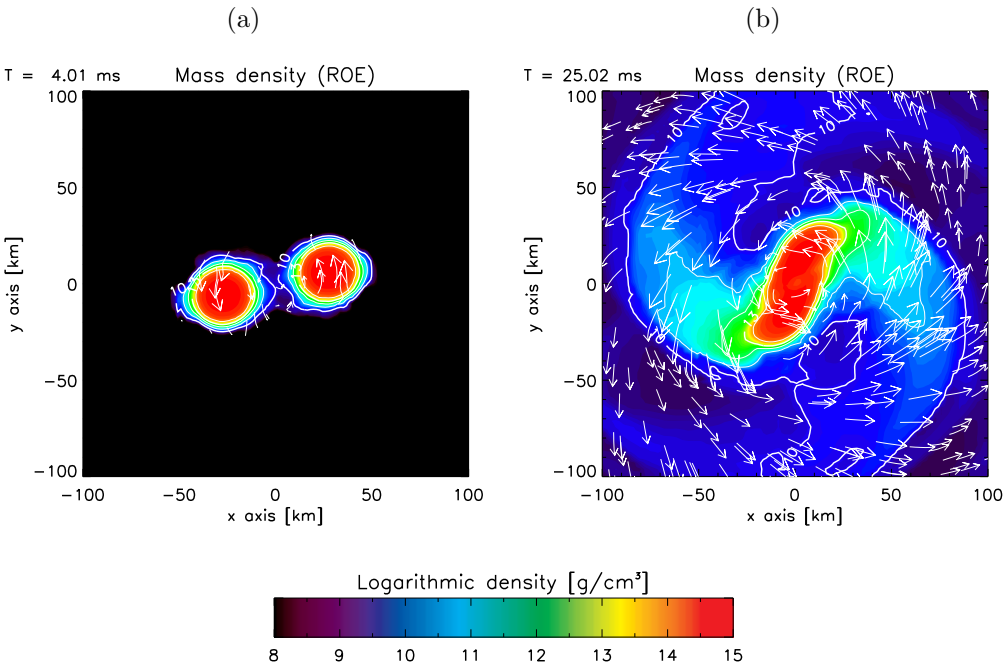

Figure 4.2: Mass density in the orbital plane computed with the linearised Riemann solver of Roe (1981). All other details are the same as in Fig. 4.1.

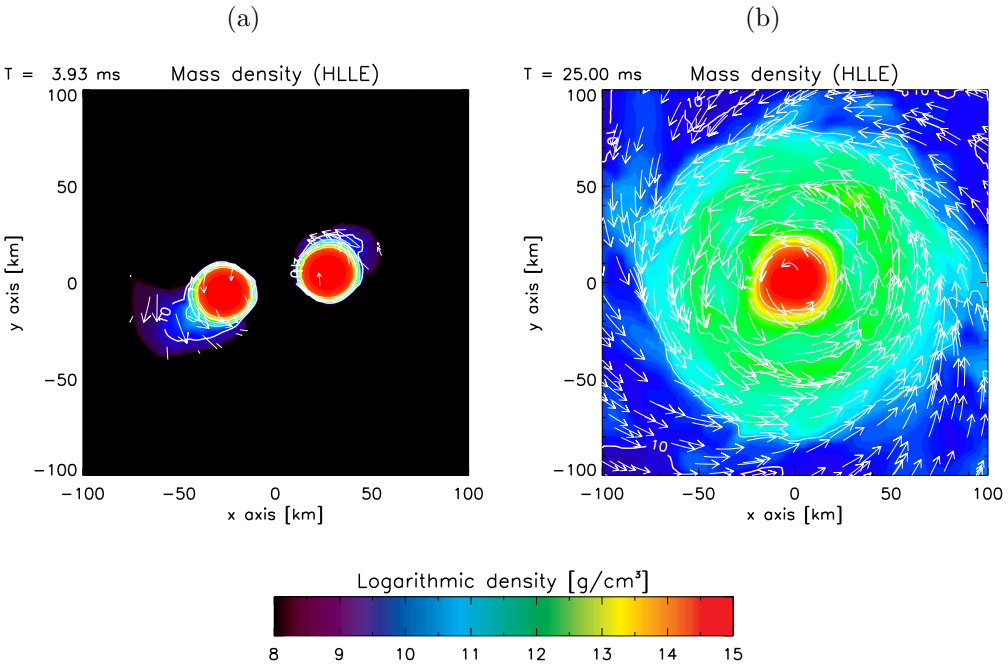

Figure 4.3: Mass density in the orbital plane computed with the approximate HLLE Riemann solver. All other details are the same as in Fig. 4.1.

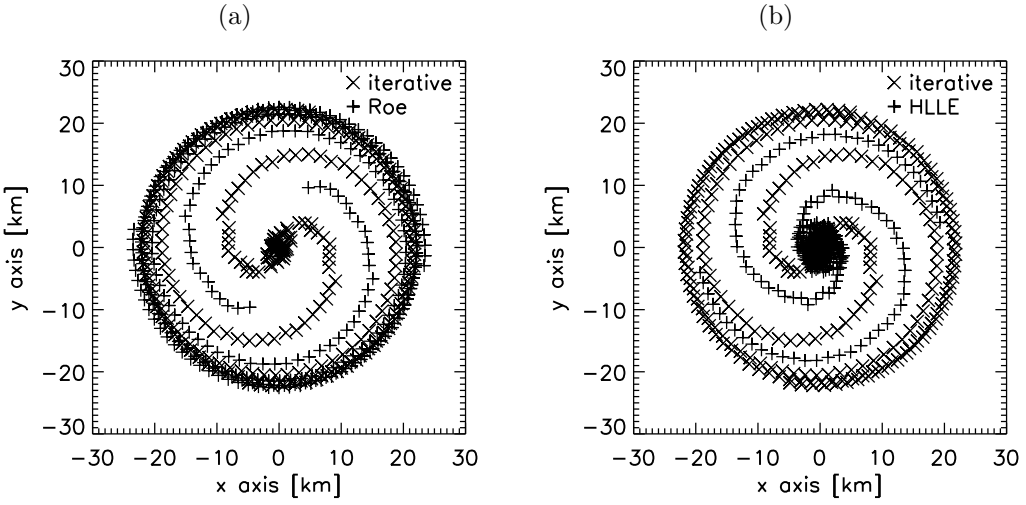

Figure 4.4: The orbital paths of the two neutron stars computed using (a) the linearised Roe solver and (b) the approximate HLLE solver are plotted as plus symbols. The paths computed with the iterative Riemann solver are also shown as crosses for comparison. Only about the last 20% of the simulated data are plotted for clarity.

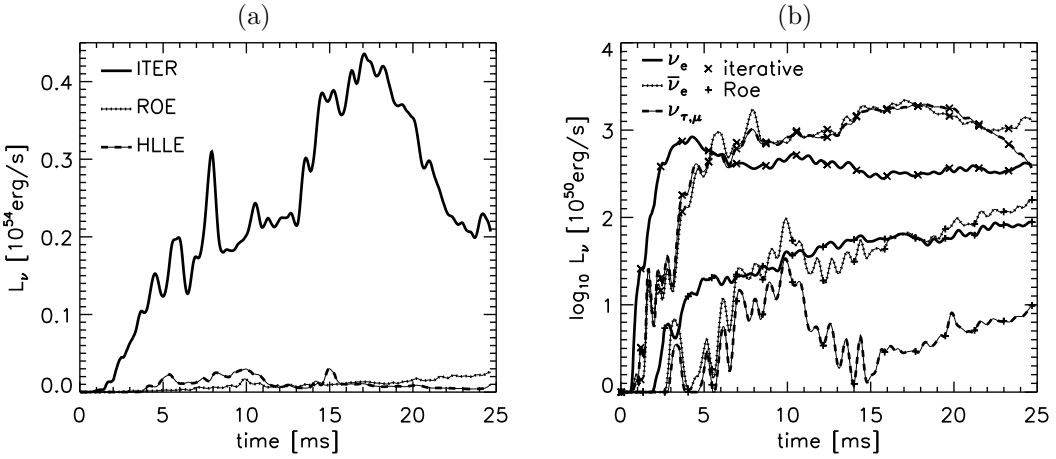

Figure 4.5: (a) Total neutrino luminosities as functions of time for the three simulations. (b) Comparison of the time dependence of neutrino luminosity for ν_e, $\bar{\nu}_e$ and the heavy neutrinos with their respective antineutrinos $\nu_{\tau,\mu}$.

Model ID	$T^{\max}$ [MeV]	$L_{\nu_e}^{\max}$ [10^{52} erg/s]	$L_{\bar{\nu}_e}^{\max}$ [10^{52} erg/s]	$L_{\nu_x}^{\max}$ [10^{52} erg/s]	$L_{\nu}^{\max}$ [10^{52} erg/s]
ITER	50	8.37	22.00	19.82	43.57
ROE	34	0.89	1.59	0.34	2.57
HLLE	> 100	0.89	2.29	0.69	3.02

Table 4.2: A summary of results from the three simulations with the iterative Riemann solver (ITER) and the two approximate solvers (ROE and HLLE). $T^{\max}$ is the maximum gas temperature during the simulation in energy units, $L_{\nu_i}^{\max}$ denotes the maximum luminosity in neutrino species i. The notation L_{ν_x} is shorthand for the combined luminosity of the heavy neutrinos and their antineutrinos ($\nu_\tau, \bar{\nu}_\tau, \nu_\mu$ and $\bar{\nu}_\mu$).

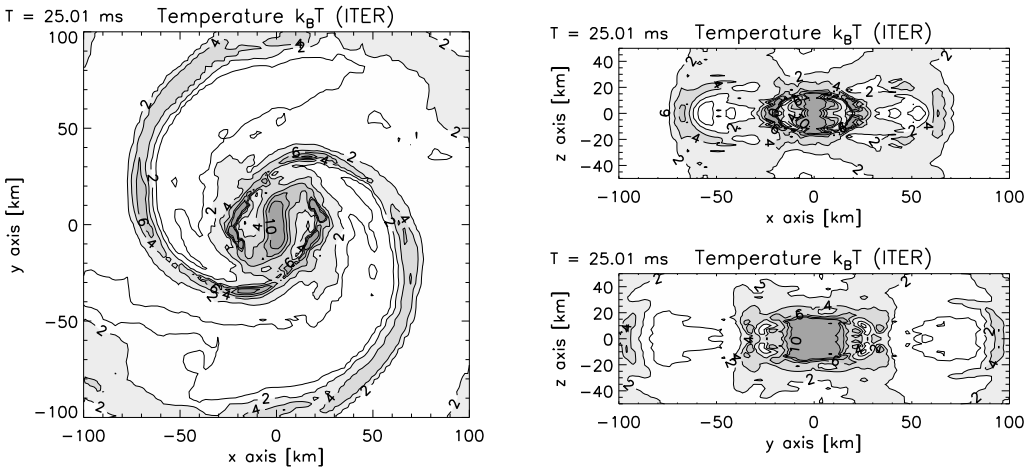

Figure 4.6: Two dimensional slices through the centre of the computational domain showing temperature (in MeV) at the end of the simulation computed with the iterative Riemann solver.

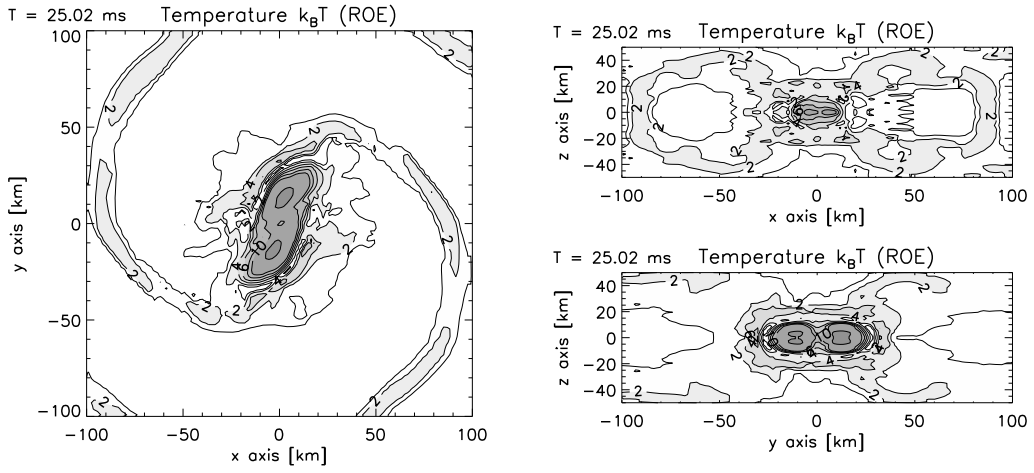

Figure 4.7: Two dimensional slices through the centre of the computational domain showing temperature (in MeV) at the end of the simulation computed with the linearised Roe solver.

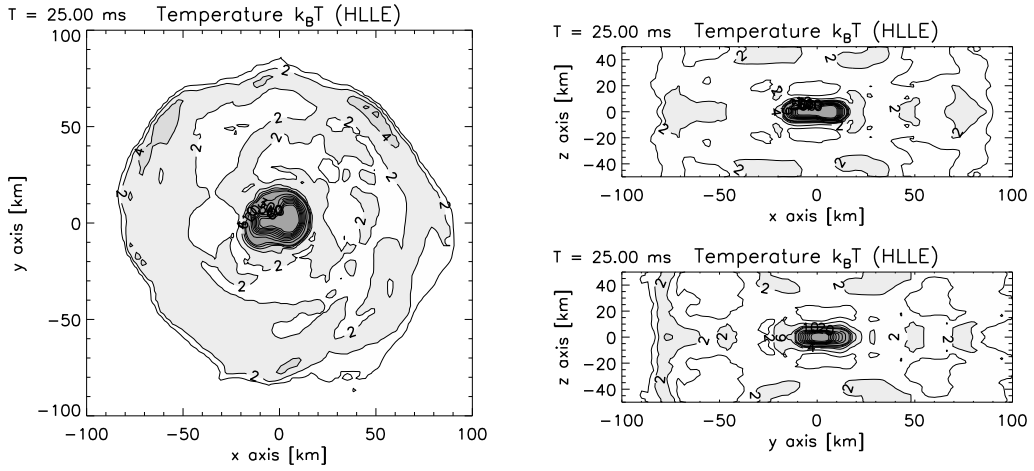

Figure 4.8: Two dimensional slices through the centre of the computational domain showing temperature (in MeV) at the end of the simulation computed with the approximate HLLE Riemann solver.

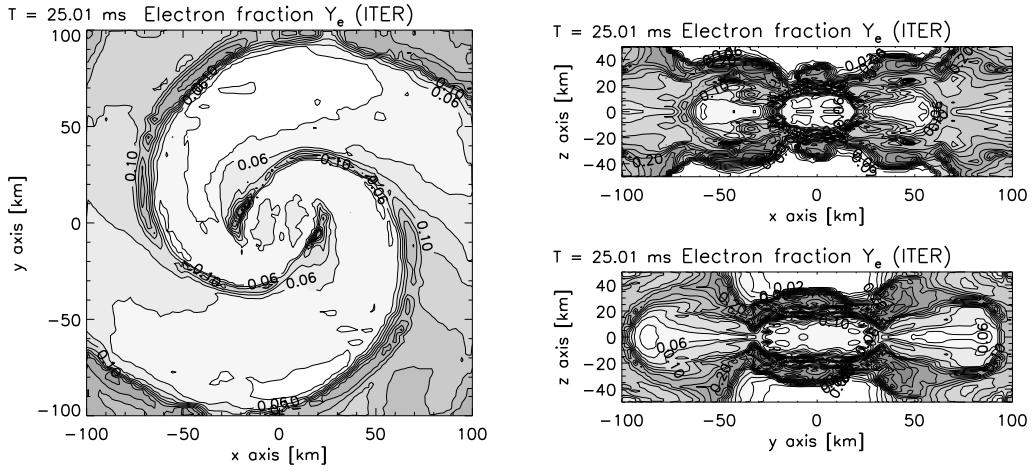

Figure 4.9: Two dimensional slices through the centre of the computational domain showing electron fraction at the end of the simulation computed with the iterative Riemann solver.

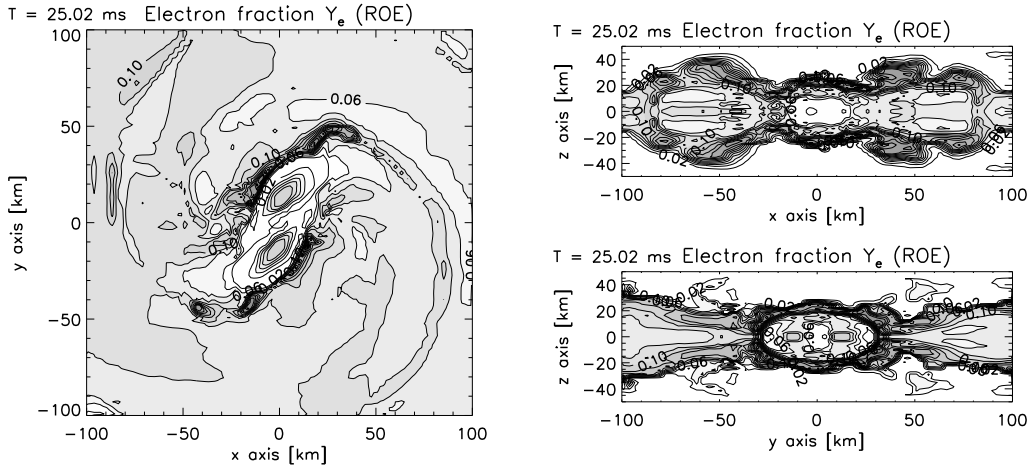

Figure 4.10: Two dimensional slices through the centre of the computational domain showing electron fraction at the end of the simulation computed with the linearised Roe solver.

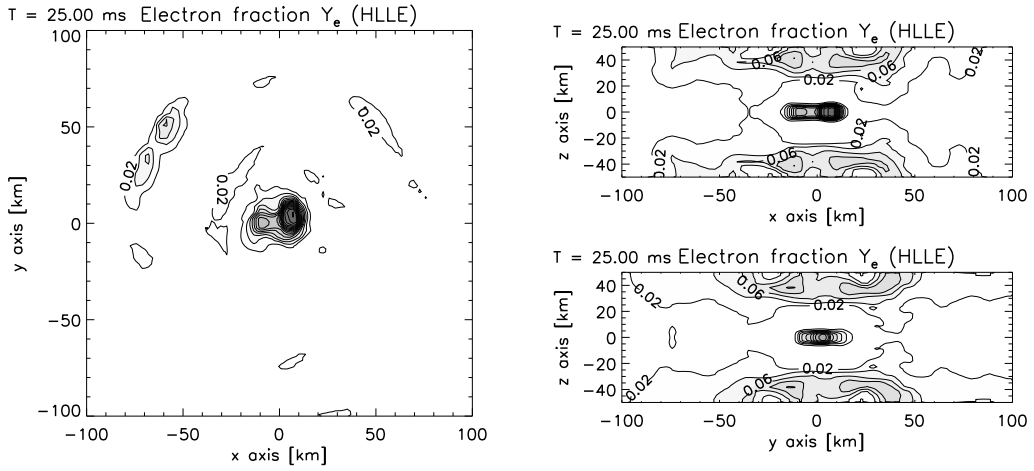

Figure 4.11: Two dimensional slices through the centre of the computational domain showing electron fraction at the end of the simulation computed with the approximate HLLE Riemann solver.

> We shall not cease from exploration, and the end of all our exploring will be to arrive where we started and know the place for the first time.
>
> — T. S. Eliot

5 Conclusions and Outlook

We have presented two main themes in this thesis; in chapter 2 we reported on the implementation of the approximate Riemann solvers of Roe (1981), HLLE and HLLEM (Harten et al., 1983; Einfeldt, 1988; Einfeldt et al., 1991) in the piecewise parabolic method (PPM) of Colella and Woodward (1984). We found that the schemes performed very well in tests with L_1-normed errors which were very close those for the iterative solver when compared with an exact or high resolution reference solution. In chapter 4, we presented some results showing the current state of a project in which we utilise the aforementioned approximate solvers in an astrophysical model for the merging of compact stellar remnants. We introduced this model in chapter 3 when we presented results from an investigation into the effect of the equation of state (EoS) used to describe neutron star material on the dynamics of the merger and on the emission of neutrino radiation. In the next two sections we will provide a brief résumé of the main results from each of these research projects.

5.1 The importance of the equation of state in GRB simulations

In chapter 3 we presented the results from four different merger scenarios; three neutron star - black hole (NSBH) mergers and one binary neutron star merger (NSNS). In each case we compute the solution with the EoS of Lattimer and Swesty (1991) (LS-EoS) and of Shen et al. (1998a,b) (Shen-EoS). Our aim was to investigate whether or not the change of EoS would significantly affect the results.

Our results show that simulations with the stiff Shen-EoS tend to yield less extreme conditions of mass density and temperature during the merging process than in simulations using the LS-EoS (that is to say, the energies involved in the merging event are approximately higher in the LS-EoS case). As a result, the peak neutrino emission is smaller by a factor between 1.5 and 2.0. This is not an appreciable difference when we consider the approximations made in order to obtain a numerical solution (e.g. gravitational waves and the black hole are present in an essentially Newtonian setting).

We find the Shen-EoS results to be more sensitive to changes in the resolution of the computation than the LS-EoS simulations. The initial encounter with the black hole causes the Shen-EoS neutron star to enter a series of elliptic orbits before its final destruction in the highest resolution case (128^3), but not in the lower resolution simulation (64^3). This suggests that the larger radius of the Shen-EoS star combined with the internal forces under the Shen-EoS make it more susceptible to being flung out to greater separation distances through tidal interaction with the black hole. We believe that this may be due in part to the high mass ratio between the black hole and neutron star in the particular model chosen to compare the effects of resolution ($M_{\rm BH} = 10\ M_\odot, M_{\rm NS} = 1.6\ M_\odot$) since Rosswog (2005a) describes simulations (also using the Shen-EoS) with high mass ratios of $M_{\rm BH}/M_{\rm NS} > 14/1.4$ in which a similar reduced mass neutron star can survive as many as eight encounters with the black hole.

Direct comparison of our results for neutrino emission with the simulations in Rosswog (2005a) is not possible since we do not have any models which match their initial conditions which have much higher black hole to neutron star mass ratios

than our models[1]. It has been noted that NSBH mergers with a high mass ratio form much reduced accretion disks with temperatures $\lesssim 2.5$ MeV (Rosswog, 2005b) and therefore inherently lower neutrino emission. Since we find temperatures in our simulated accretion disks to exceed about 10 MeV, it would be interesting to consider similar mass ratios to Rosswog to see whether our grid based calculation agrees with his SPH simulations.

We can draw some comparisons with other simulations using CHARYBDIS. Janka et al. (1999) present NSBH mergers (computed with the LS-EoS) including models with a 1.6 $M_\odot$ neutron star merging with black holes with masses 2.5 $M_\odot$ and 10 $M_\odot$. We find good agreement between their results for maximum neutrino emission and our own; both are of the order of a few 10^{53} erg s^{-1}. This may not seem surprising at first but, considering that they did not use the updated method for computing the temperature from the entropy equations (see Sect. 3.1.2) this is a reassuring result. Setiawan et al. (2004, 2006) simulate the neutrino emission from the accretion disk after it has already formed. We note that they find maximum neutrino luminosities of the order 10^{53} erg s^{-1} in those cases where the mass of the accretion disk is similar to that found in our simulations, i.e. about $\frac{1}{10}$ $M_\odot$. The values of their peak neutrino luminosity are certainly consistent with the quasi-steady emission reached at the end of our NSBH simulations once the accretion disk has formed.

5.2 Using approximate Riemann solvers in Charybdis

In chapter 2 we described Godunov's method (Sect. 2.2.3) and the high resolution derivative of this scheme, the piecewise parabolic method (PPM) (Sect. 2.6.2), on which our astrophysical code CHARYBDIS is based. We also introduced three approximate Riemann solvers – the linearised solver of Roe (1981) and the approximate HLLE and HLLEM solvers (Harten et al., 1983; Einfeldt, 1988; Einfeldt et al., 1991) – and evaluated their performance against an exact, iterative solver (see Sect. 2.3) in several numerical tests in one and two spatial dimensions. Comparing the one dimensional shock-tube tests with an exact solution, we found that, relative to this

[1]The higher the mass of the black hole with respect to the neutron star in the case of NSBH binaries, the more elongated the neutron star's trajectory becomes after the initial encounter. The longer period of this elliptical orbit means more computational time is required to simulate the merger event. This is made worse in our simulations since we must increase the grid size to accurately track the neutron star which leads to higher computational time for each timestep of the whole simulation. This is one reason why we do not draw exact comparison with those particular models in the work of Rosswog et al.

reference solution, all three approximate solvers had very similar L_1-error as the iterative solver. This performance was repeated when we considered a two dimensional test where a high Mach shock impinges on a reflecting surface at an angle to the bulk flow. We also noted decrease in computational time for the approximate solvers relative to the iterative Riemann solver by a factor of about 1.3.

We present some early results of the attempt to incorporate these approximate Riemann solvers in CHARYBDIS in chapter 4. We found that, although the approximate schemes performed well in the tests in chapter 2, they were not as effective at simulating the merging of two neutron stars when compared with the results for the iterative Riemann solver. The differences in the computed solutions are greatest in quantities which depend on local conditions in the gas, such as neutrino emission. The actual dynamics of the merger are qualitatively correct for each scheme however, leading us to suspect that the problems are due to our assumption that the modifications to the basic Euler equations of Sect. 2.1 do not require any special treatment in the approximate solvers.

5.3 Outlook

There is still tremendous scope to improve our models for the merger of compact stellar remnants. Currently, the numerical implementation of some aspects of the physical model are only correct to first order. The treatment of gravitational waves in a Newtonian framework is an example of this. We reason that, since a fully general relativistic code would take a long time to develop, it is better to have some approximation to the true gravitational wave effects than not include them at all. The transfer to a fully general relativistic code can be considered a long term goal for CHARYBDIS and one for which no plans are currently being advanced. Similarly, there are assumptions made in our neutrino treatment (see Sect. 3.1.6) which lead to an error of the order of a few 10% when compared with results from diffusion calculations in one dimensional situations (Ruffert et al., 1996, 1997). This is adequate as it is consistent with the rest of the code.

Some less ambitious modifications and additions can be considered within the context of the current code, a few of which can be thought of as medium term goals. They include the extension of the equation of state (EoS) tables to lower tabulated values of density than our current version (5.01×10^7 g cm$^{-3} \leq \rho \leq 1.12\times10^{15}$ g cm^{-3}). The minimum density in this table is already much higher than the value of $\rho_{\min} = 1.26 \times 10^5$ g cm^{-3} given by Shen et al. (1998b). Extension of our data tables down to this new lowest density would be straightforward but we could do better by following

the example of Rosswog and Davies (2002) who assume that, below this density, the gas consists of a mixture of protons, neutrons, electrons and alpha particles. Currently, neutrino annihilation rates are computed after the hydrodynamic simulation using a radiative transfer code. By incorporating the radiative transfer calculations into CHARYBDIS, we could begin to approximate the effects of neutrino pressure on the fluid flow.

We are limited, at present, in the maximum resolution we choose for our simulations by computing time. The use of a nested, refined grid structure (see Sect. 3.1.7) already permits us to simulate a larger computational volume which allows us to follow the evolution of the long spiral arms of material lost from the neutron stars without compromising the resolution at the location of the merger. Even so, the resolutions which are feasible when running our code on current computer hardware do not allow us to observe the small-scale turbulence which is known to form (see, for example Ruffert et al., 1996; Rosswog and Davies, 2002) in the shear motion at the contact point between the two neutron stars as they begin to coalesce. To investigate this turbulence (probably due to the Kelvin-Helmholtz instability) with the 3D code would require a full parallelisation which would allow us to take advantage of large, distributed memory machines. At present, we exploit an OpenMP parallelisation which restricts us to a relatively small number of processors and does not provide us with the several orders of magnitude speed increase we could gain by using hundreds of processors and parallelising with, for example, the Message Passing Interface (MPI). As a medium term project, a two dimensional PPM code could be constructed to make use of the realistic equation of state of neutron star matter so that resolution could be increased enough to investigate the Kelvin-Helmholtz rolls in isolation.

Looking to the immediate future, the results presented in this thesis can of course be improved by the application of higher resolution. The comparison of neutrino emission in the simulations of chapter 3 can be extended and made more rigorous by considering two dimensional plots showing the local emission rates of neutrinos in all species. The question of how the EoS changes the amount of energy which could be available to power a gamma-ray burst could be addressed more quantitatively by computing the annihilation rates for neutrinos and antineutrinos. This has been done before with CHARYBDIS using a post-processing step which is described (along with examples for the merger of neutron star binary systems) in (Ruffert et al., 1997). Such results were not included in this thesis due to constraints on computing time; the post-processing involves a radiative transfer code which takes the same order of computing time as the main hydrodynamics code (which, for a typical 128^3 resolution simulation, takes about two weeks on Edinburgh University's compute and data facility, EDDIE.

On a dual core desktop machine, each simulation can take up to three months).

Although the addition of magnetic field physics was not achieved within the time limit of my PhD studies, this goal has been a driving force for much of the work presented in this thesis. In Sect. 4.1 we presented the equations of magnetohydrodynamics (MHD) to showcase the differences with the Euler equations of ordinary hydrodynamics. There are many complications which arise when the MHD equations are considered such as the extra wave structure which adds more work to Riemann solver based numerical schemes, magnetic pressure and tension forces on the plasma and the condition that the magnetic field should remain solenoidal (i.e. $\nabla \cdot \mathbf{B}$) at all times during its evolution. Depending on the numerical treatment, this can be a real headache when multi-dimensional calculations are considered. Clearly the addition of an MHD solver to CHARYBDIS is not something which can be done in one step. First, we intend to continue improving the implementation of the approximate Riemann solvers in CHARYBDIS (see chapter 4) until they are able to accurately reproduce the fine detail results computed by the iterative Riemann solver. When we have achieved that milestone we can repeat the entire development cycle for an MHD Riemann solver; starting with one dimensional shock tube problems and leading on to multi-dimensional tests with the ideal gas equation we hope to eventually find ourselves implementing the MHD Riemann solver in CHARYBDIS, ready to start investigating the parameter space of the merger of magnetised[2] neutron star binary systems.

[2]A new-born neutron star can have a typical magnetic field strength on the order of 10^{12} Gauss. This will likely have decayed by the time it would take for two neutron stars to merge by emission of gravitational waves and the gas pressure (which is of the order 10^{34} erg/cm^3 within the star) will dominate the initial merging. It is the effect of the magnetic field on the accretion disk which we are interested in, however. Gas pressures in the disk are much lower and with amplification of the magnetic fields due to turbulence in the merging event by about three orders of magnitude (Price and Rosswog, 2006), plasma beta could drop from values in excess of $\beta \sim 10^4$ to around $\beta \sim 10^{-10}$.

A

The interpolant of PPM

Here we describe the method by which the quadratic interpolant $U(x) = \alpha x^2 + \beta x + \gamma$ becomes

$$U(x) = U_{\mathrm{L},j} + \xi(\Delta U_j + U_{6,j}[1 - \xi]), \tag{A.1}$$

where

$$\xi \equiv \frac{x - x_{j-1/2}}{\Delta x_j}, \qquad x \in [x_{j-1/2}, x_{j+1/2}], \tag{A.2}$$

as presented in Sec. 2.6.2

We seek a quadratic interpolation formula of the form

$$a(\xi) = \alpha\xi^2 + \beta\xi + \gamma \tag{A.3}$$

over the cell width ($\xi_{j-\frac{1}{2}} \leq \xi \leq \xi_{j+\frac{1}{2}}$). To make this algebraically cleaner, we introduce the transformation

$$x \equiv \frac{\xi - \xi_{j-\frac{1}{2}}}{\Delta\xi_j},$$

where $\Delta\xi_j \equiv \xi_{j+\frac{1}{2}} - \xi_{j-\frac{1}{2}}$.

We need three constraints to arrive at values for the three unknown coefficients of the interpolated function. These values are found using the relations

$$a(0) = a_{L,j}, \tag{A.4}$$

$$a(1) = a_{R,j}, \tag{A.5}$$

and

$$\frac{1}{\Delta\xi_j}\int_{\xi_{j-\frac{1}{2}}}^{\xi_{j+\frac{1}{2}}} a(\xi)d\xi = a_j^n.$$

The last constraint can be rewritten using the transformation given above and, if we substitute for the interpolation function, we can integrate as follows:

$$\begin{aligned}
\int_0^1 a(x)dx &= a_j^n, \\
\int_0^1 \left(\alpha x^2 + \beta x + \gamma\right) dx &= a_j^n, \\
\left[\frac{1}{3}\alpha x^3 + \frac{1}{2}\beta x^2 + \gamma x\right]_0^1 &= a_j^n, \\
2\alpha + 3\beta + 6\gamma &= 6a_j^n.
\end{aligned} \tag{A.6}$$

So we now have our three constraints. The first two can be rewritten

$$\alpha + \beta + \gamma = a_{R,j} \tag{A.7}$$

$$\gamma = a_{L,j}, \tag{A.8}$$

by expanding (A.4) and (A.5) using the definition of the interpolation function (A.3). Equations (A.6)-(A.8) can be represented by the matrix equation

$$\begin{pmatrix} 2 & 3 & 6 \\ 1 & 1 & 1 \\ 0 & 0 & 1 \end{pmatrix} \begin{pmatrix} \alpha \\ \beta \\ \gamma \end{pmatrix} = \begin{pmatrix} 6a_j^n \\ a_{R,j} \\ a_{L,j} \end{pmatrix},$$

which after Gaussian elimination becomes

$$\begin{pmatrix} 1 & 0 & 0 \\ 0 & 1 & 0 \\ 0 & 0 & 1 \end{pmatrix} \begin{pmatrix} \alpha \\ \beta \\ \gamma \end{pmatrix} = \begin{pmatrix} 3\left(a_{L,j} + a_{R,j} - 2a_j^n\right) \\ 2\left(3a_j^n - 2a_{L,j} - a_{R,j}\right) \\ a_{L,j} \end{pmatrix}.$$

Returning to the definition of $a(\xi)$ and applying some algebra

$$\begin{aligned}
a(\xi) &= 3(a_{L,j} + a_{R,j} - 2a_j^n)x^2 + 2(3a_j^n - 2a_{L,j} - a_{R,j})x + a_{L,j}, \\
&= a_{L,j} + \left[6\left(a_j^n - \frac{1}{2}(a_{L,j} + a_{R,j})\right) - a_{L,j} + a_{R,j}\right]x - \\
&\quad - 6\left(a_j^n - \frac{1}{2}(a_{L,j} + a_{R,j})\right)x^2.
\end{aligned} \tag{A.9}$$

Defining $a_{6,j} \equiv 6\left[a_j^n - \frac{1}{2}\left(a_{L,j} + a_{R,j}\right)\right]$ and $\Delta a_j \equiv a_{R,j} - a_{L,j}$, we arrive at

$$a(\xi) = a_{L,j} + x\left[\Delta a_j + a_{6,j}(1-x)\right],$$

which is the form of the quadratic interpolation function as presented in Colella & Woodward Colella and Woodward (1984).

B

Numerical results

In this appendix we present the complete list of plots for the 1D PPM Toro tests from Chap. 2.

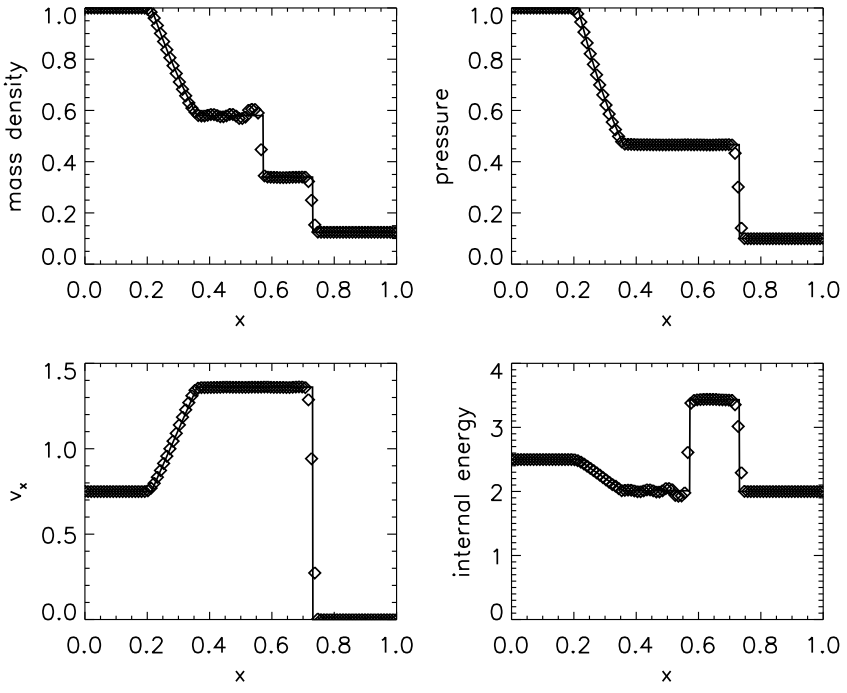

Figure B.1: Toro test 1: PPM reconstruction with iterative Riemann solver. Initial discontinuity position was $x_0 = 0.3$. The numerical solution (symbols) and the exact solution (line) are shown at time $T = 0.2$. This particular plot is identical to Fig. 2.14 in Sect. 2.7.1.

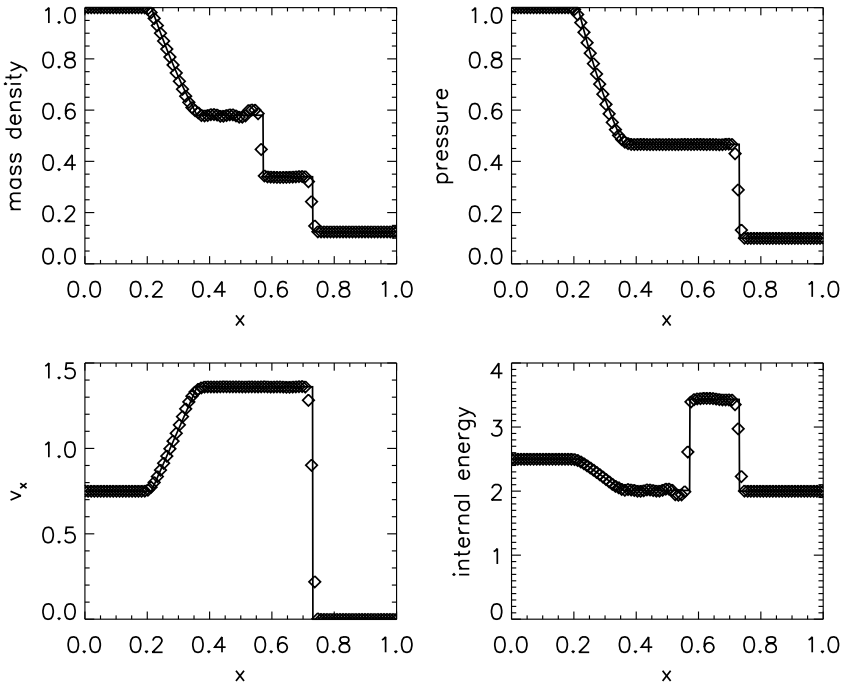

Figure B.2: Toro test 1: PPM reconstruction with Roe solver. All other details are as Fig. B.1.

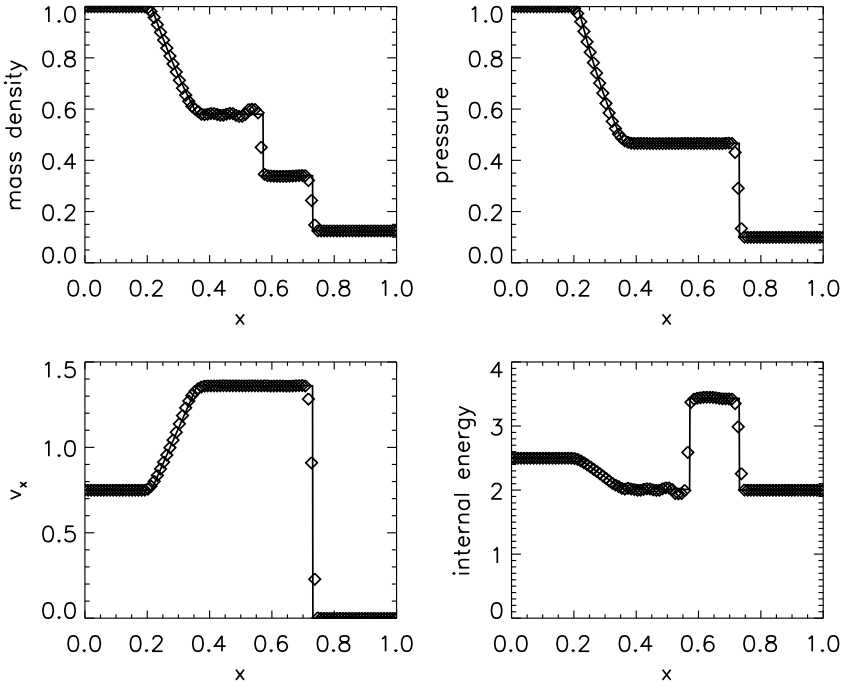

Figure B.3: Toro test 1: PPM reconstruction with HLLE Riemann solver. All other details are as Fig. B.1.

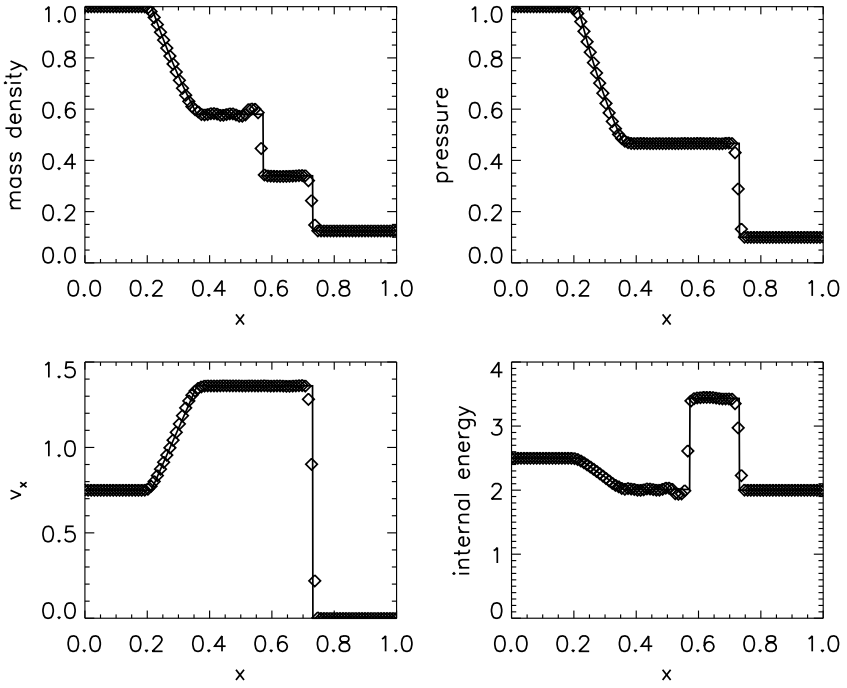

Figure B.4: Toro test 1: PPM reconstruction with HLLEM Riemann solver. All other details are as Fig. B.1.

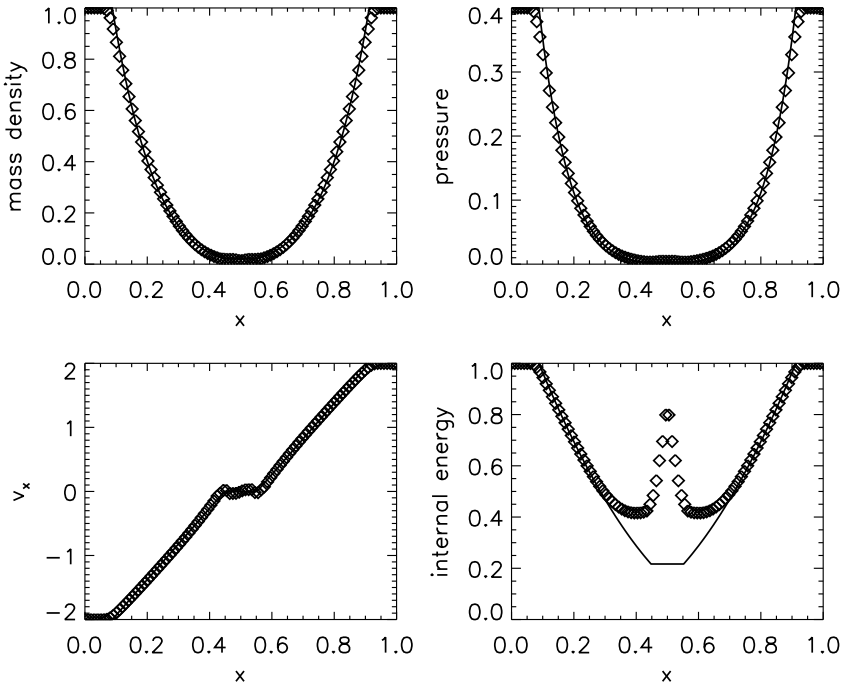

Figure B.5: Toro test 2: PPM reconstruction with iterative Riemann solver. Initial discontinuity position was $x_0 = 0.5$. The numerical solution (symbols) and the exact solution (line) are shown at time $T = 0.15$.

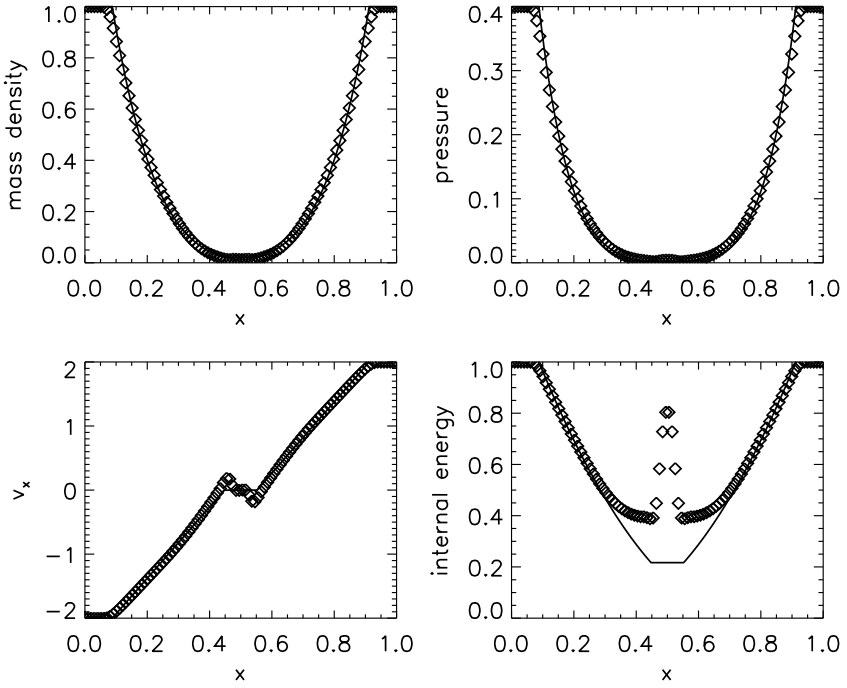

Figure B.6: Toro test 2: PPM reconstruction with HLLE Riemann solver. All other details are as Fig. B.5.

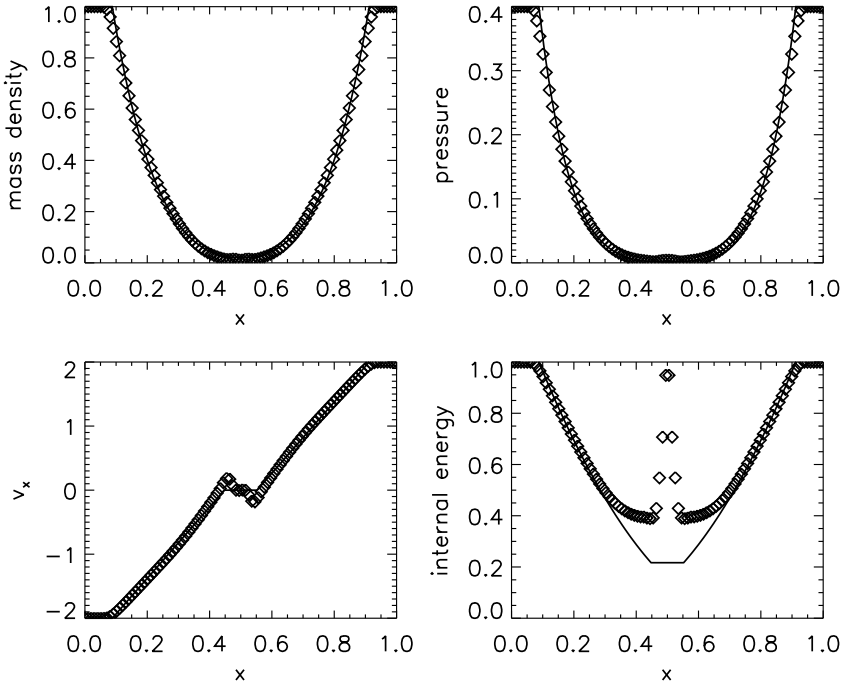

Figure B.7: Toro test 2: PPM reconstruction with HLLEM Riemann solver. All other details are as Fig. B.5.

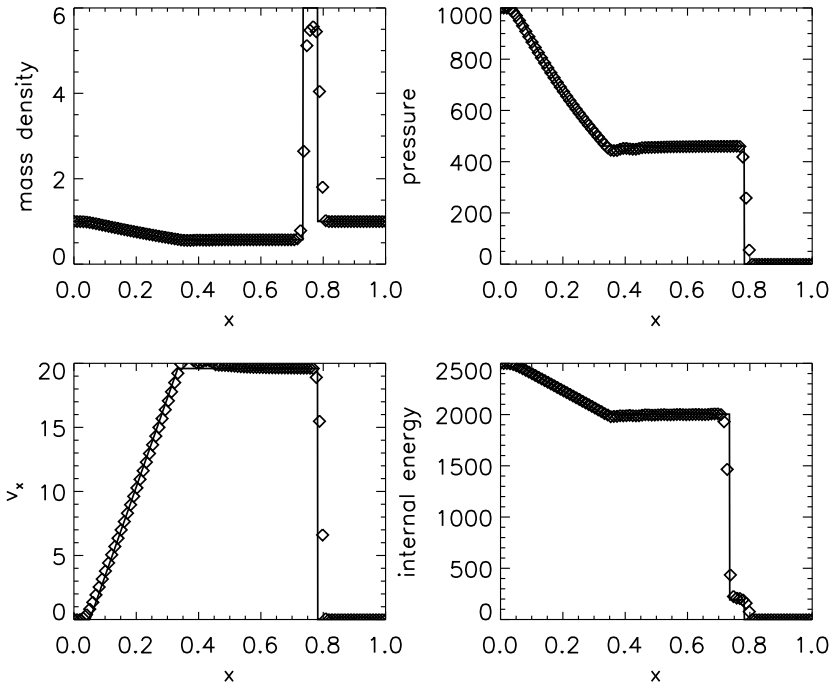

Figure B.8: Toro test 3: PPM reconstruction with iterative Riemann solver. Initial discontinuity position was $x_0 = 0.5$. The numerical solution (symbols) and the exact solution (line) are shown at time $T = 0.012$.

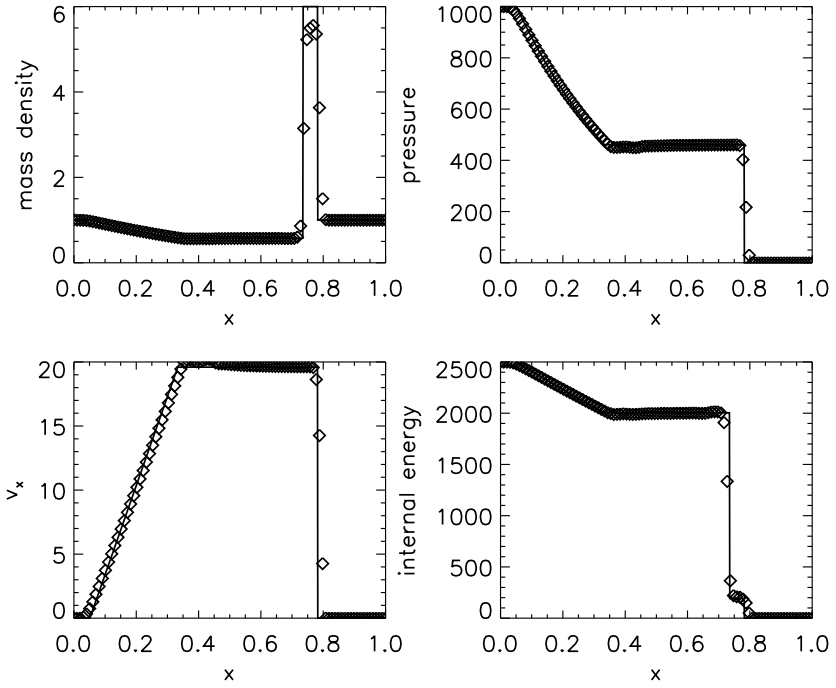

Figure B.9: Toro test 3: PPM reconstruction with Roe solver. All other details are as Fig. B.8.

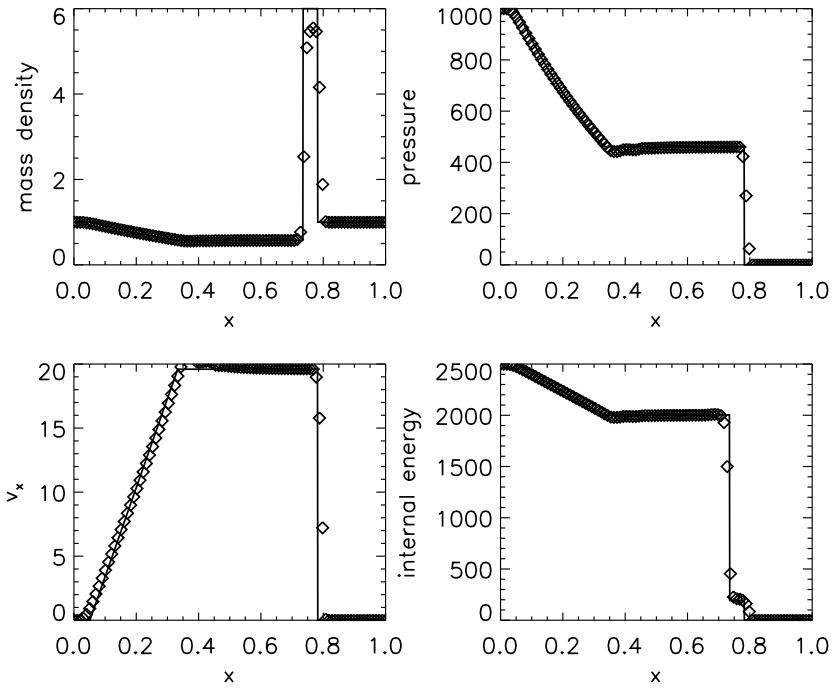

Figure B.10: Toro test 3: PPM reconstruction with HLLE Riemann solver. All other details are as Fig. B.8.

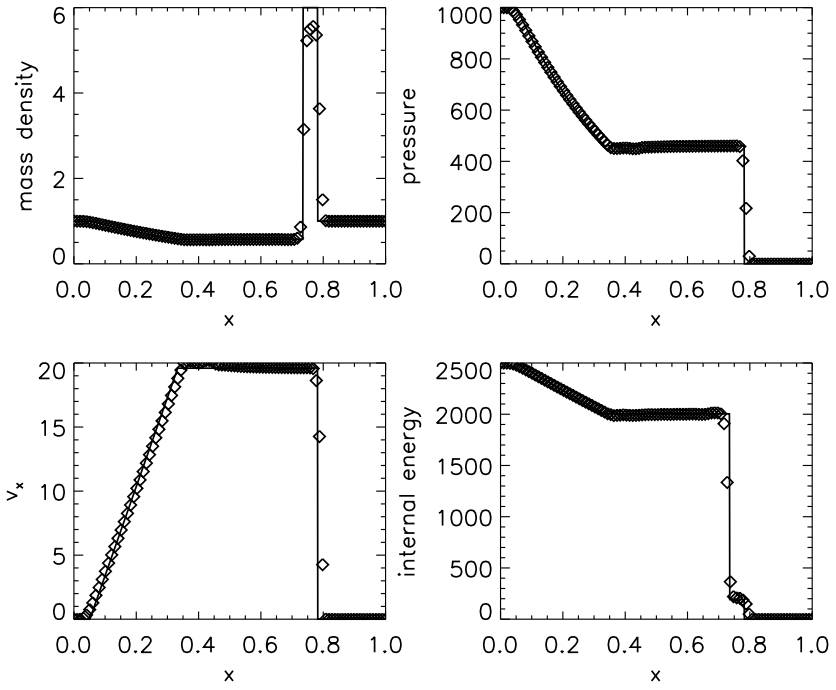

Figure B.11: Toro test 3: PPM reconstruction with HLLEM Riemann solver. All other details are as Fig. B.8.

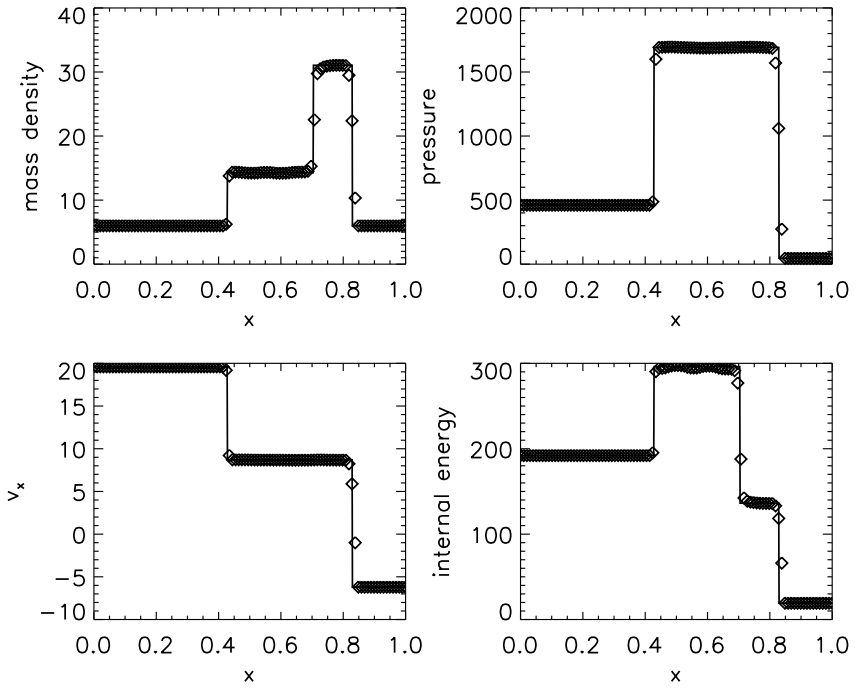

Figure B.12: Toro test 4: PPM reconstruction with iterative Riemann solver. Initial discontinuity position was $x_0 = 0.4$. The numerical solution (symbols) and the exact solution (line) are shown at time $T = 0.035$.

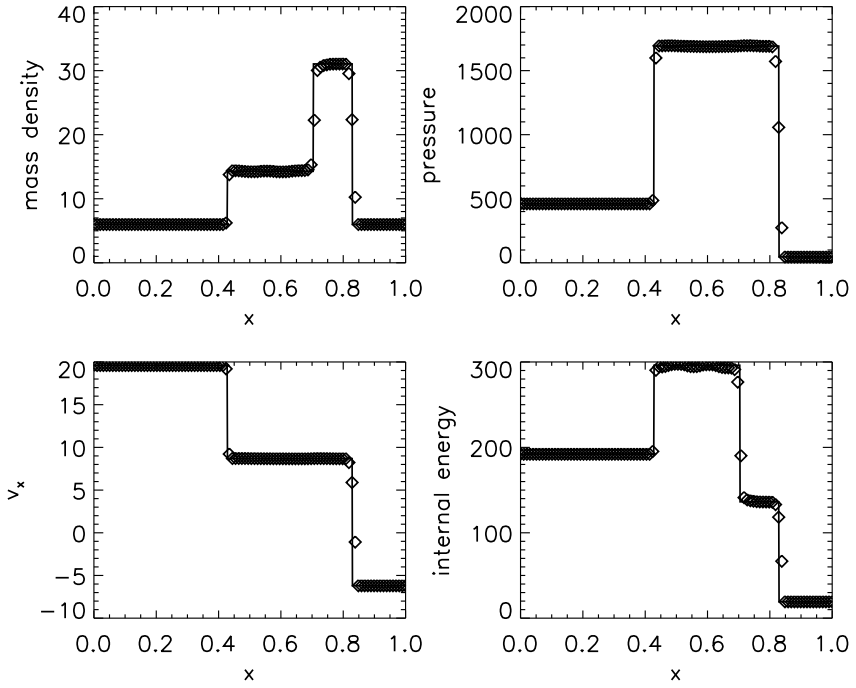

Figure B.13: Toro test 4: PPM reconstruction with Roe solver. All other details are as Fig. B.12.

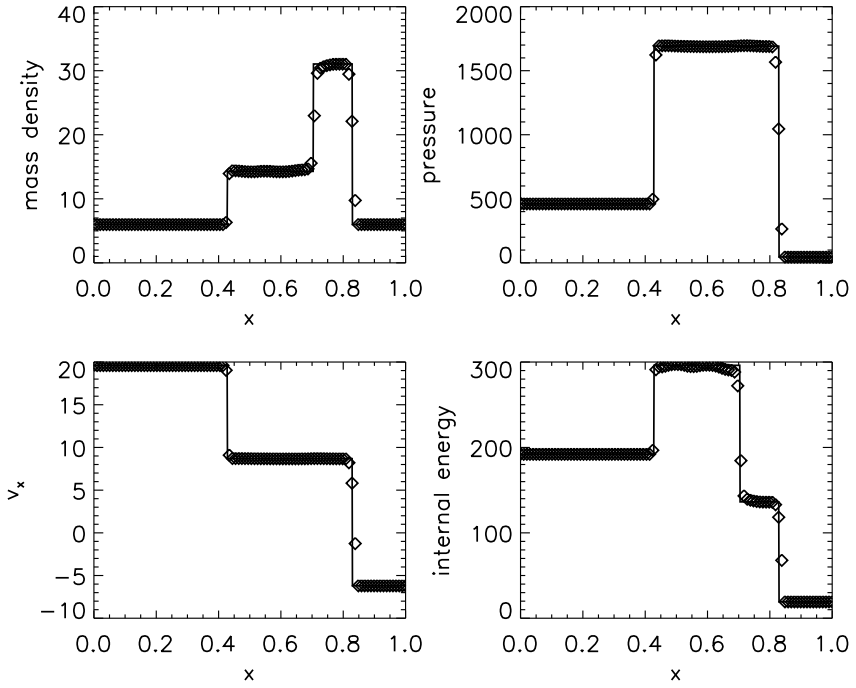

Figure B.14: Toro test 4: PPM reconstruction with HLLE Riemann solver. All other details are as Fig. B.12.

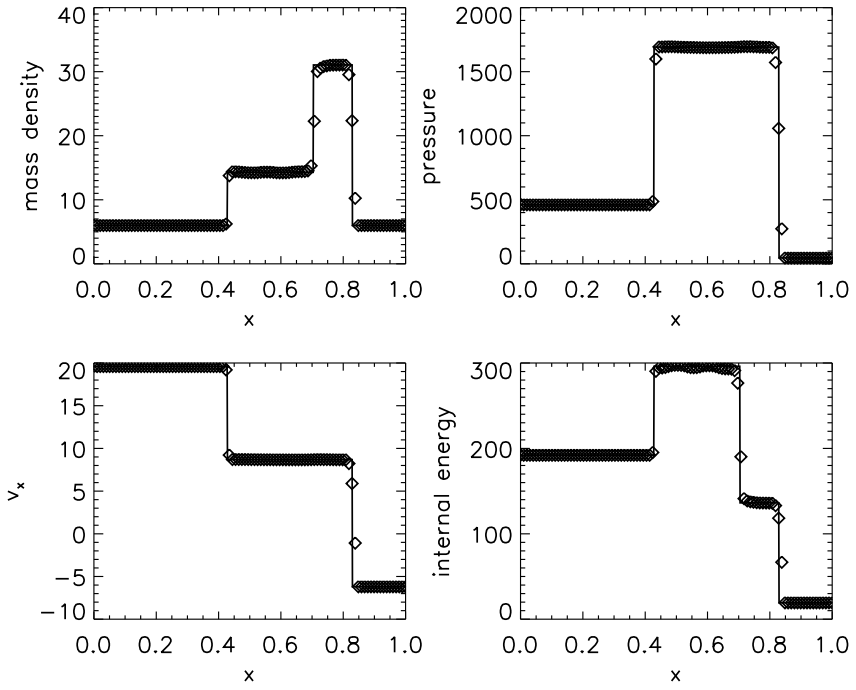

Figure B.15: Toro test 4: PPM reconstruction with HLLEM Riemann solver. All other details are as Fig. B.12.

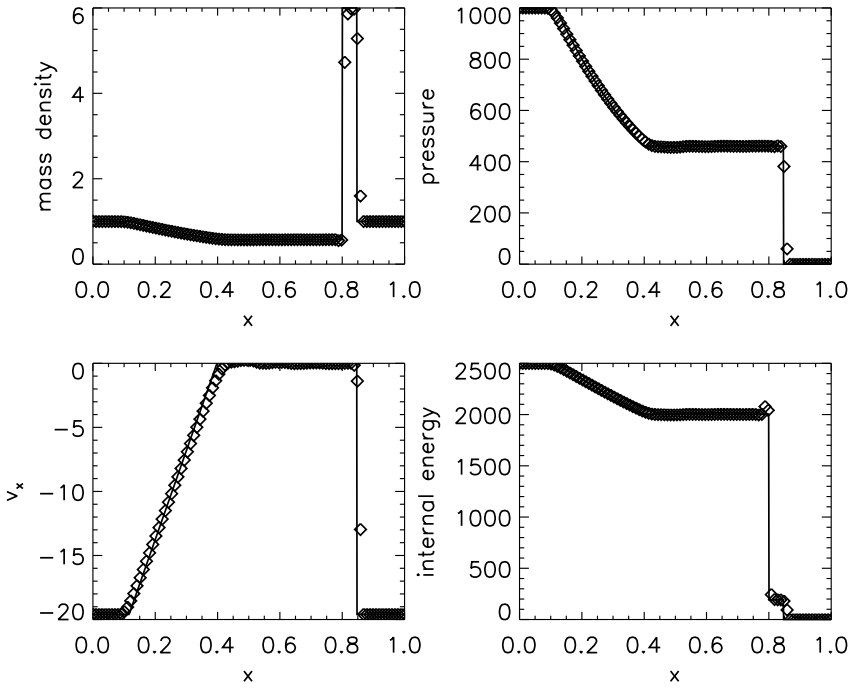

Figure B.16: Toro test 5: PPM reconstruction with iterative Riemann solver. Initial discontinuity position was $x_0 = 0.8$. The numerical solution (symbols) and the exact solution (line) are shown at time $T = 0.012$.

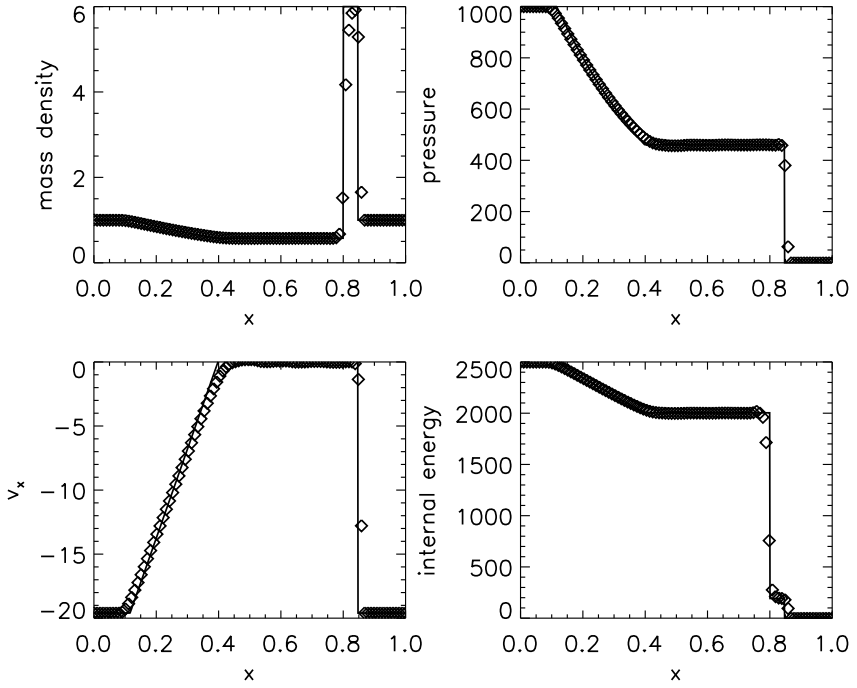

Figure B.17: Toro test 5: PPM reconstruction with Roe solver. All other details are as Fig. B.16.

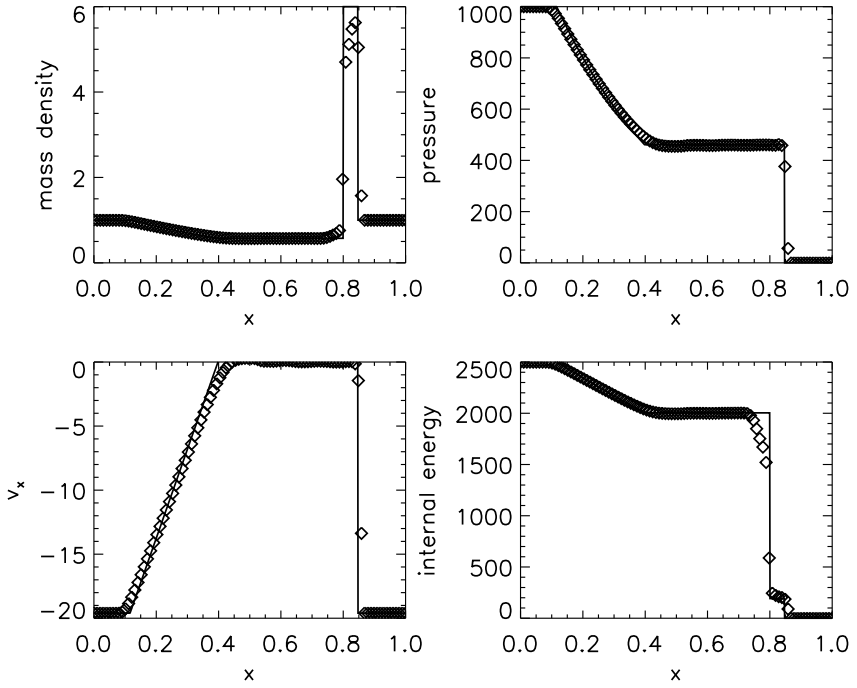

Figure B.18: Toro test 5: PPM reconstruction with HLLE Riemann solver. All other details are as Fig. B.16.

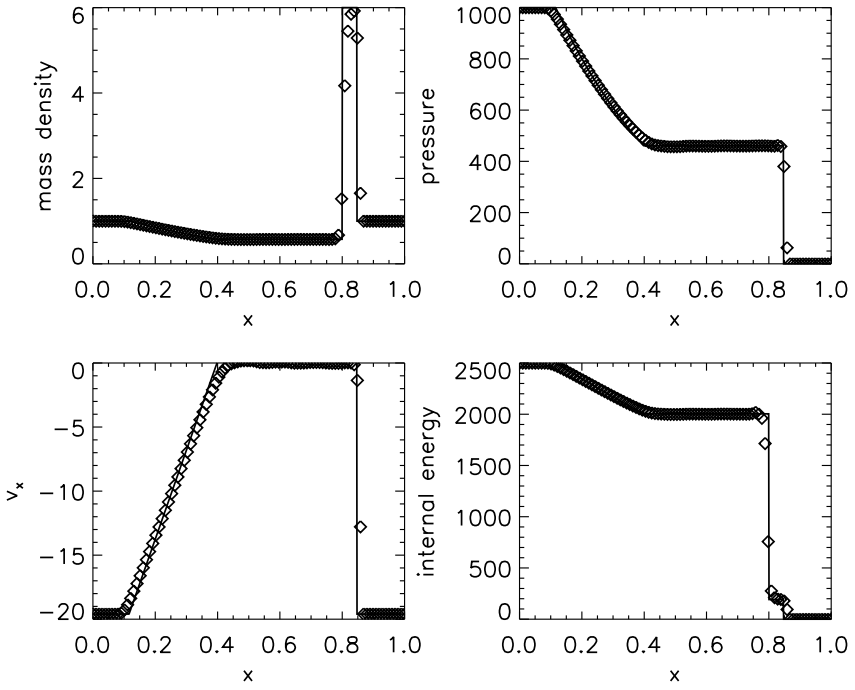

Figure B.19: Toro test 5: PPM reconstruction with HLLEM Riemann solver. All other details are as Fig. B.16.

C

Two Dimensional Plots of NSBH Simulations

In this appendix we present the complete list of the 2D cross-sectional plots for the NSBH and models described in Chapter 3 which there wasn't enough cause to include in the Chapter itself.

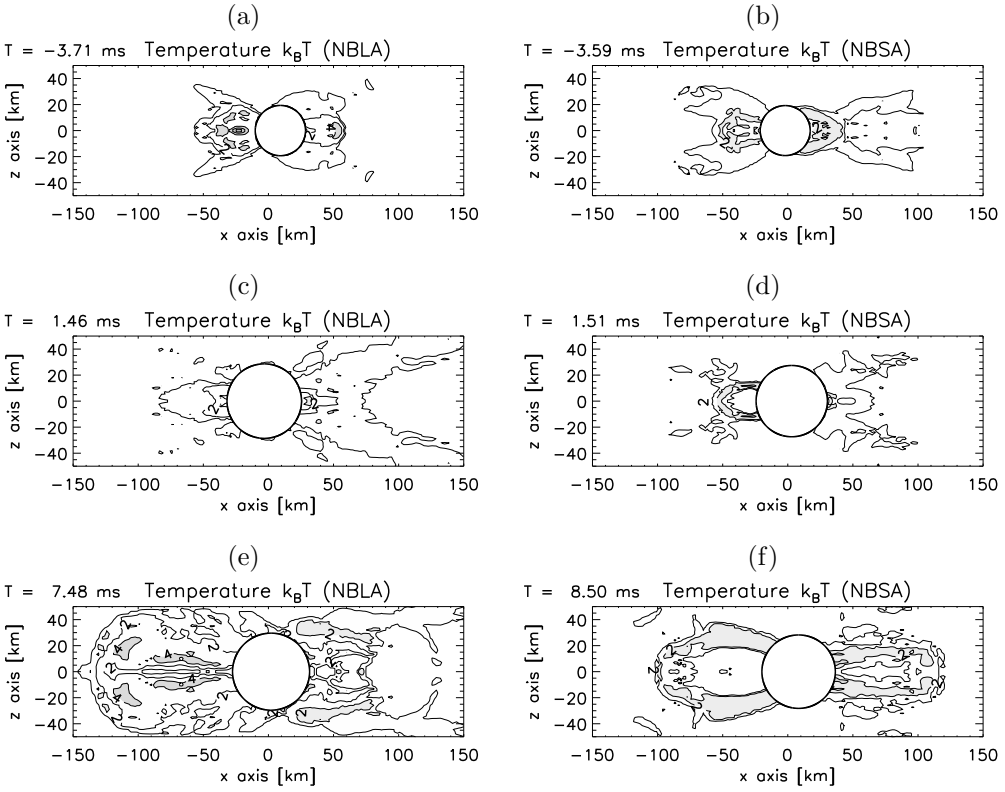

Figure C.1: Temperature in the $x - z$ plane.

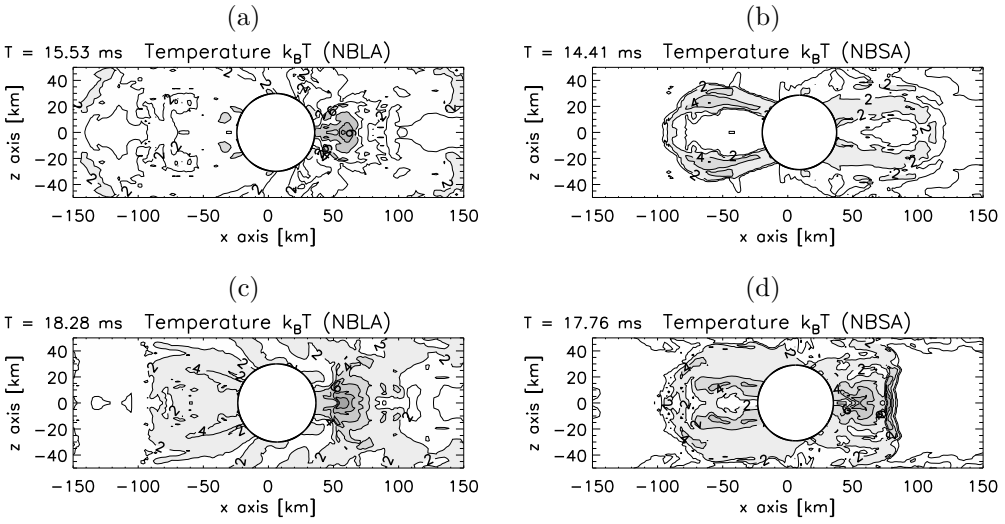

Figure C.2: Temperature in the $x - z$ plane (part2).

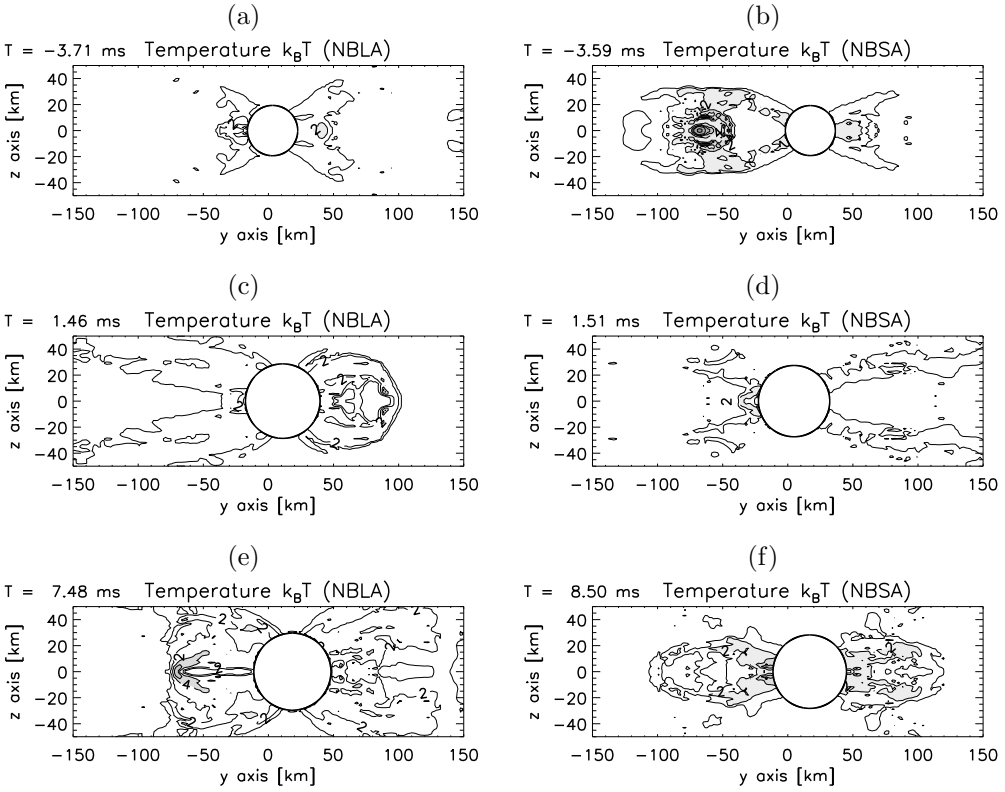

Figure C.3: Temperature in the $y - z$ plane.

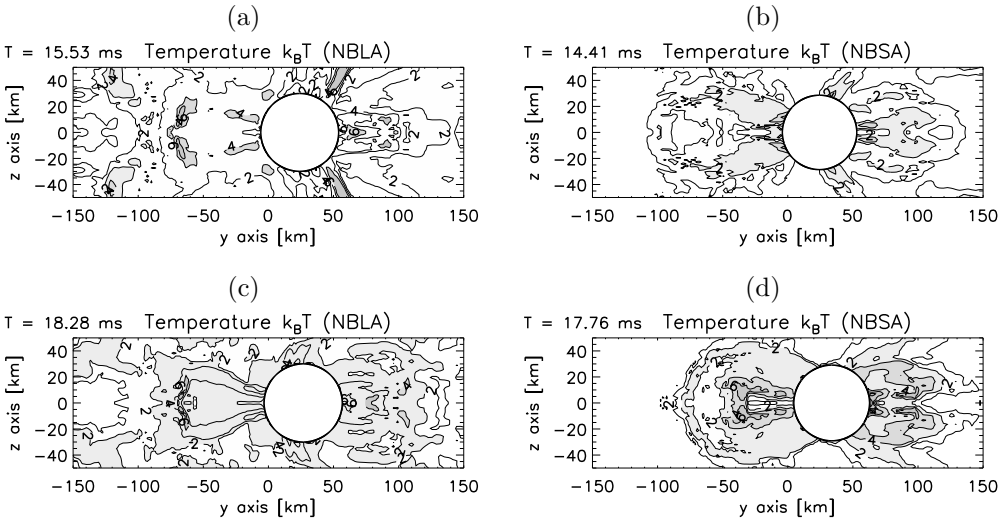

Figure C.4: Temperature in the $y - z$ plane (part2).

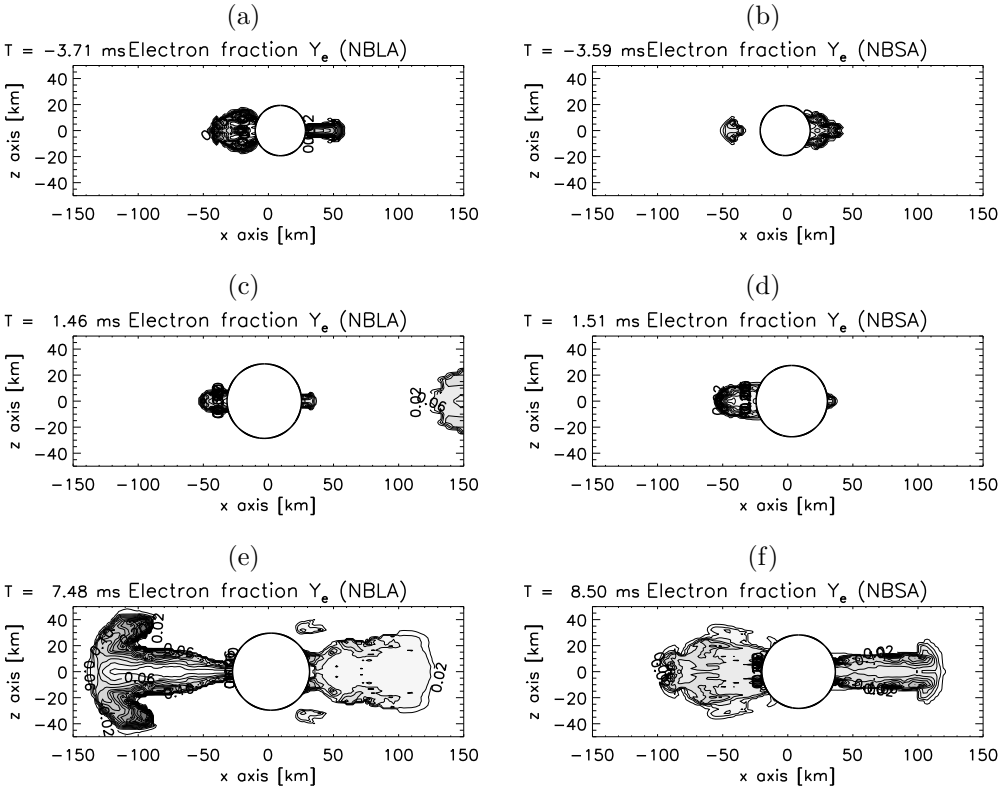

Figure C.5: Electron fraction in the $x - z$ plane.

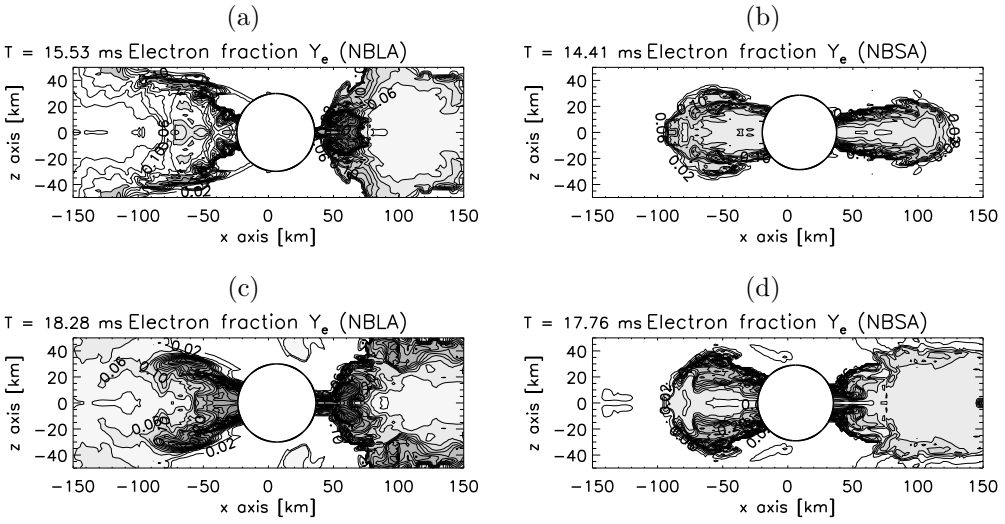

Figure C.6: Electron fraction in the $x - z$ plane (part2).

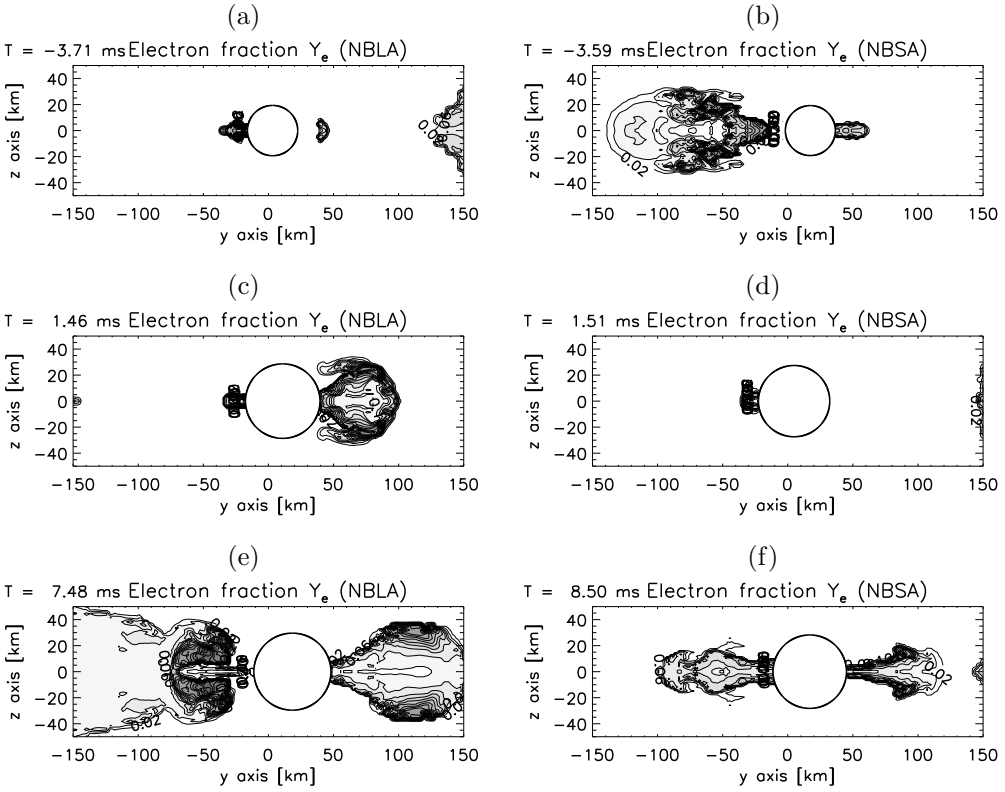

Figure C.7: Electron fraction in the $y - z$ plane.

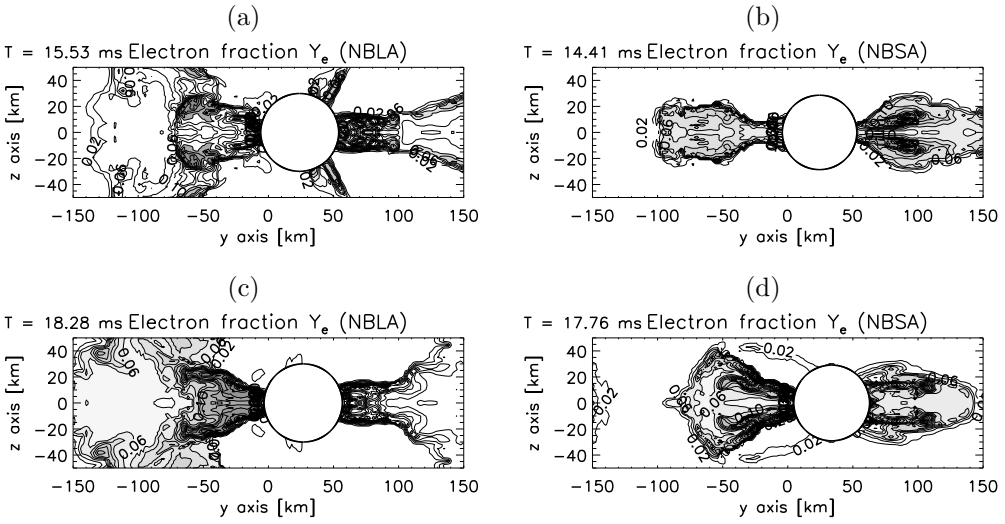

Figure C.8: Electron fraction in the $y - z$ plane (part2).

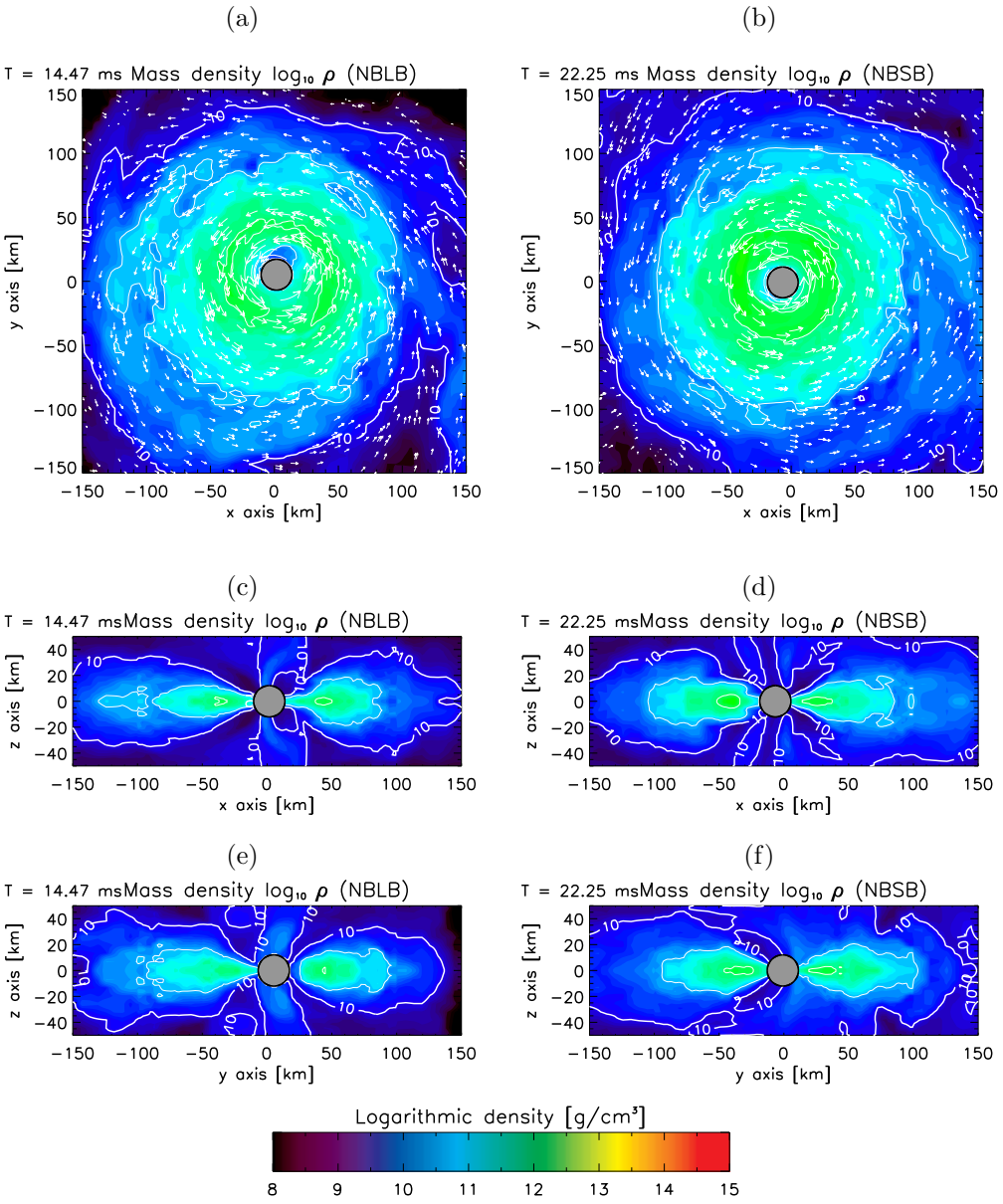

Figure C.9: Two dimensional slices through the centre of the grid showing mass density in the disk for models NBLB and NBSB plotted as colour filled contours. The velocity field is shown as white arrows, the longest arrow corresponding to a velocity of about $0.3c$.

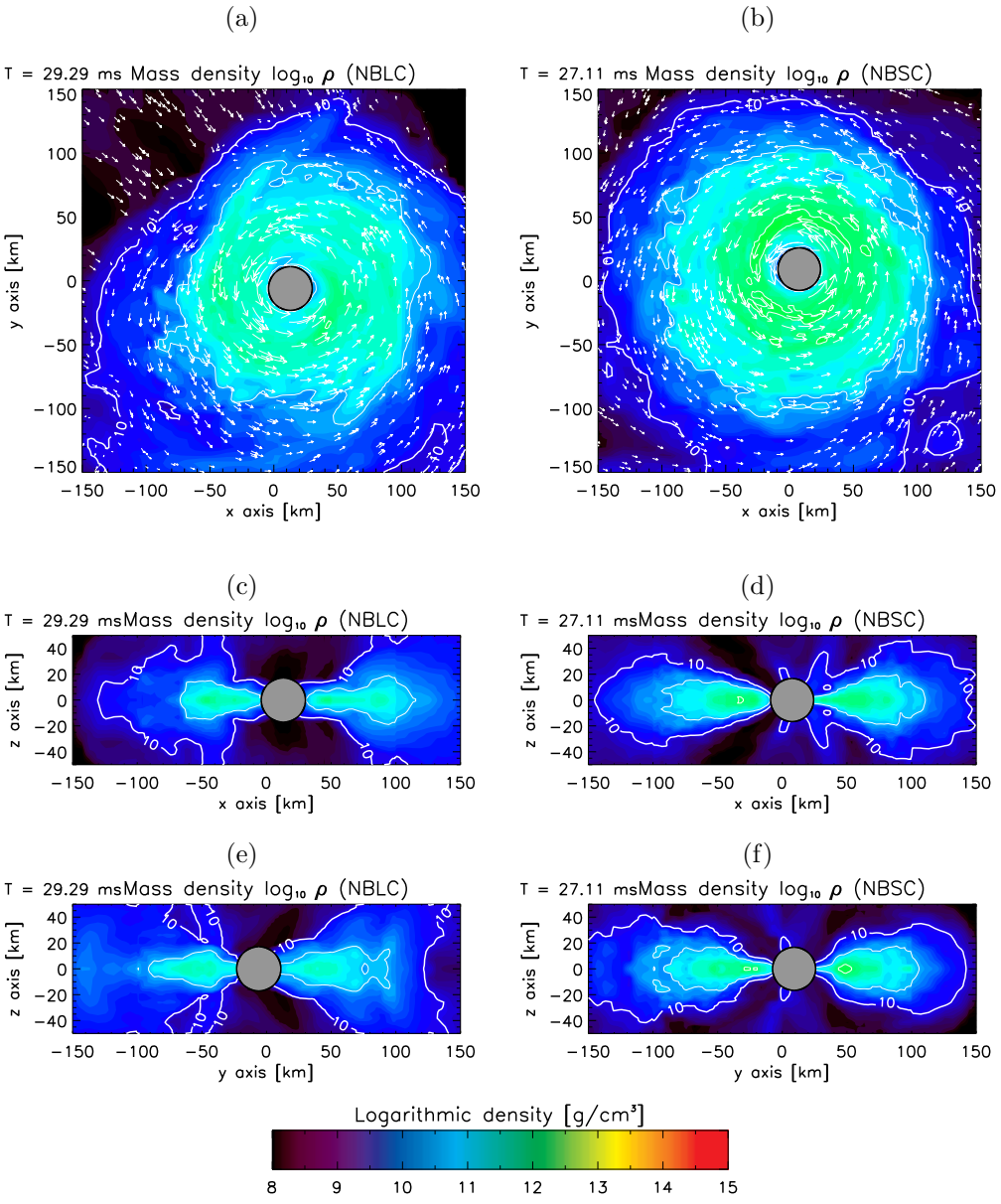

Figure C.10: Mass density and velocity field in the disk for models NBLC and NBSC. See Fig. C.9.

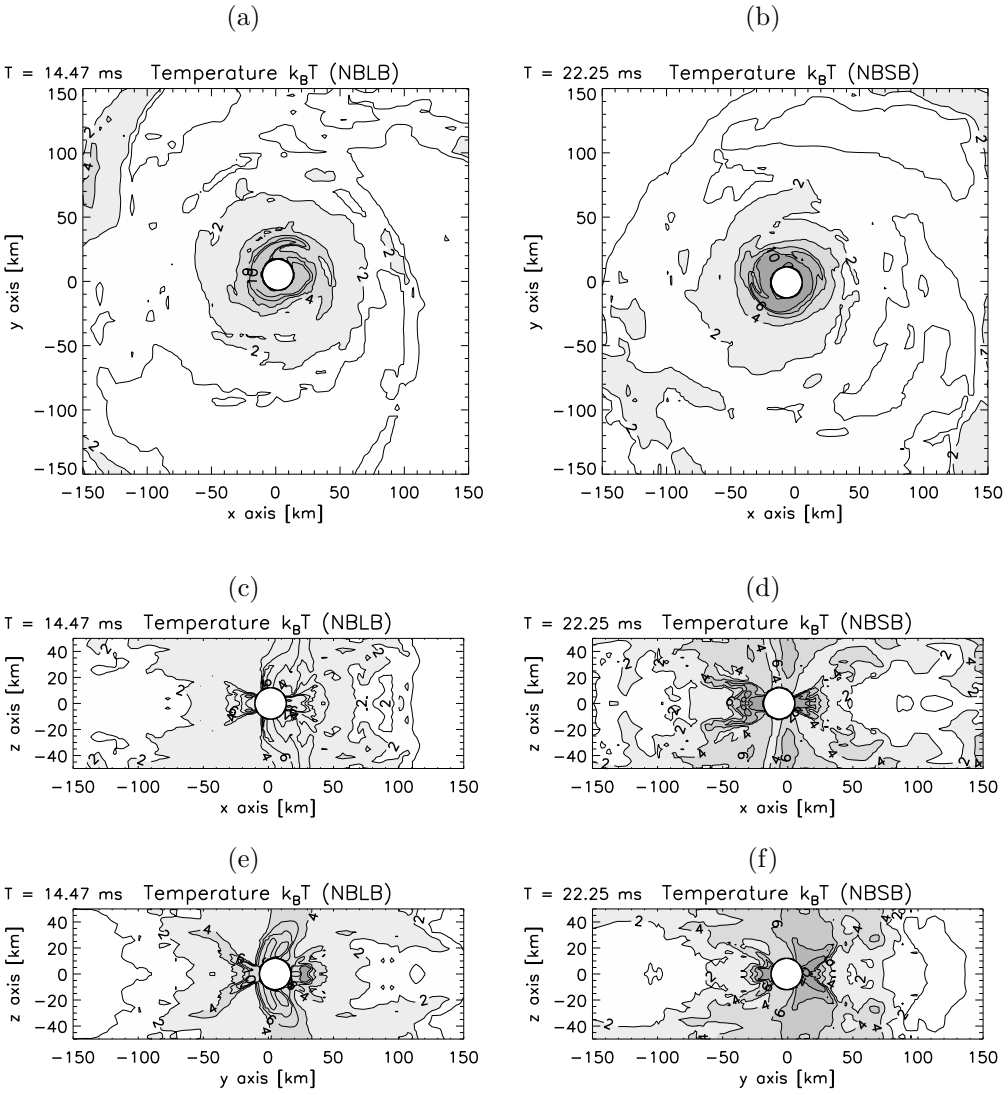

Figure C.11: Temperature in the disk, NBLB and NBSB.

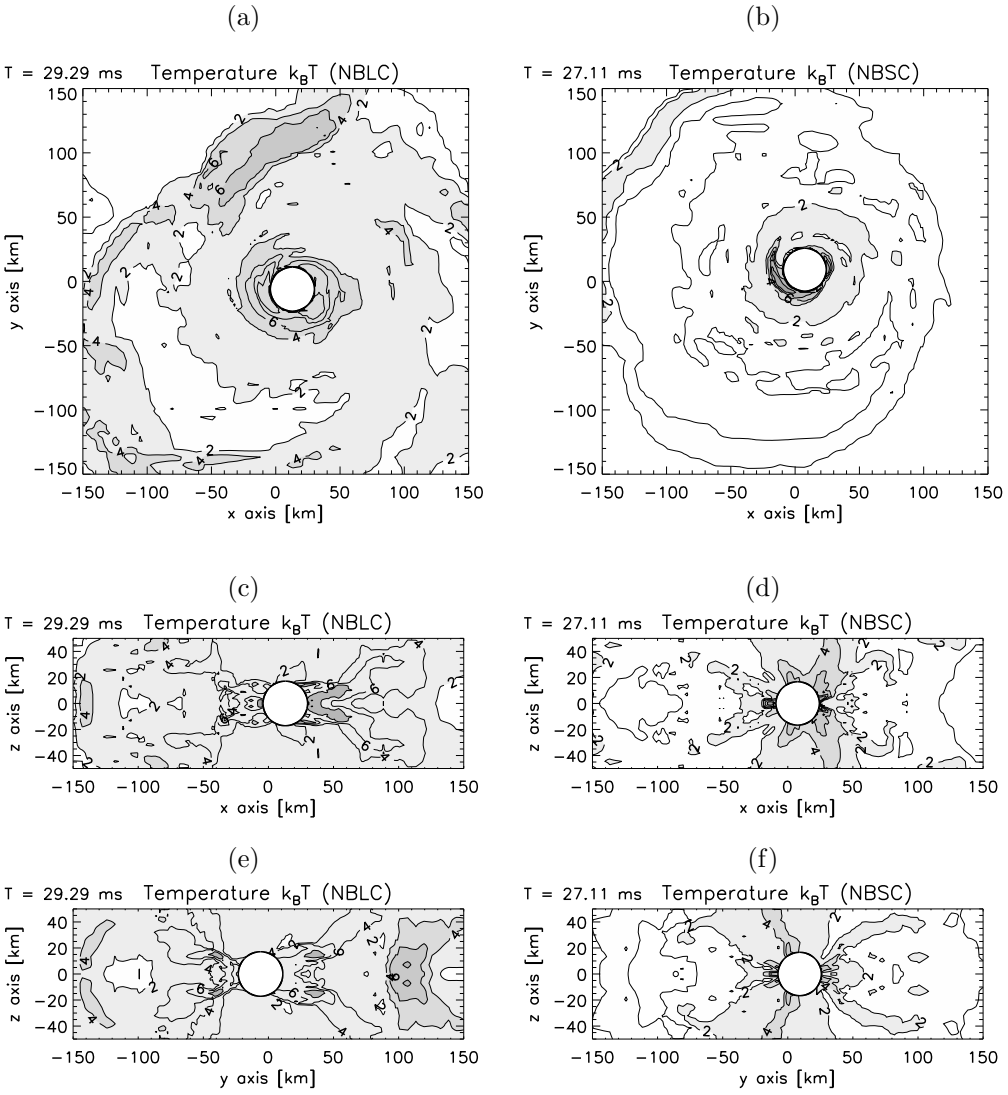

Figure C.12: Temperature in the disk, NBLC and NBSC.

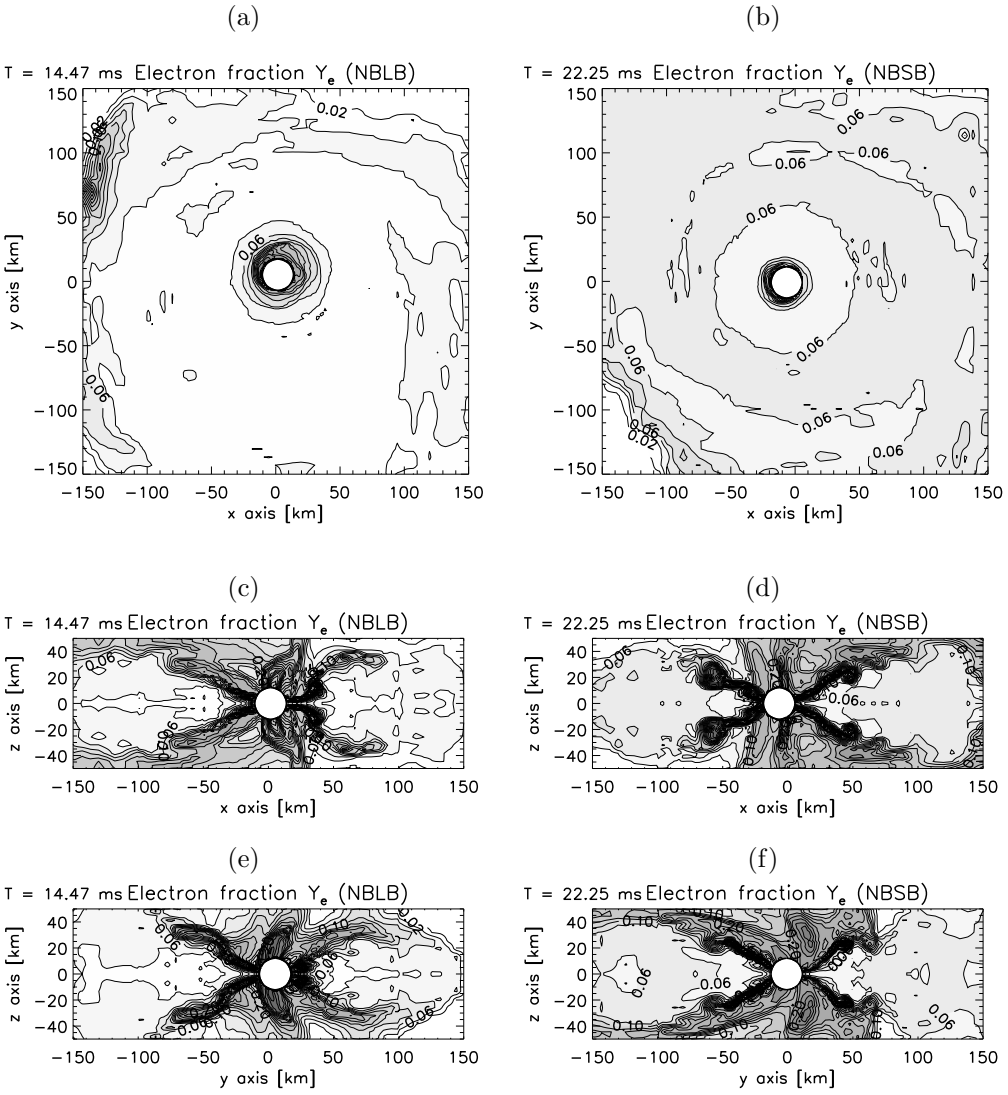

Figure C.13: Electron fraction in the disk, NBLB and NBSB.

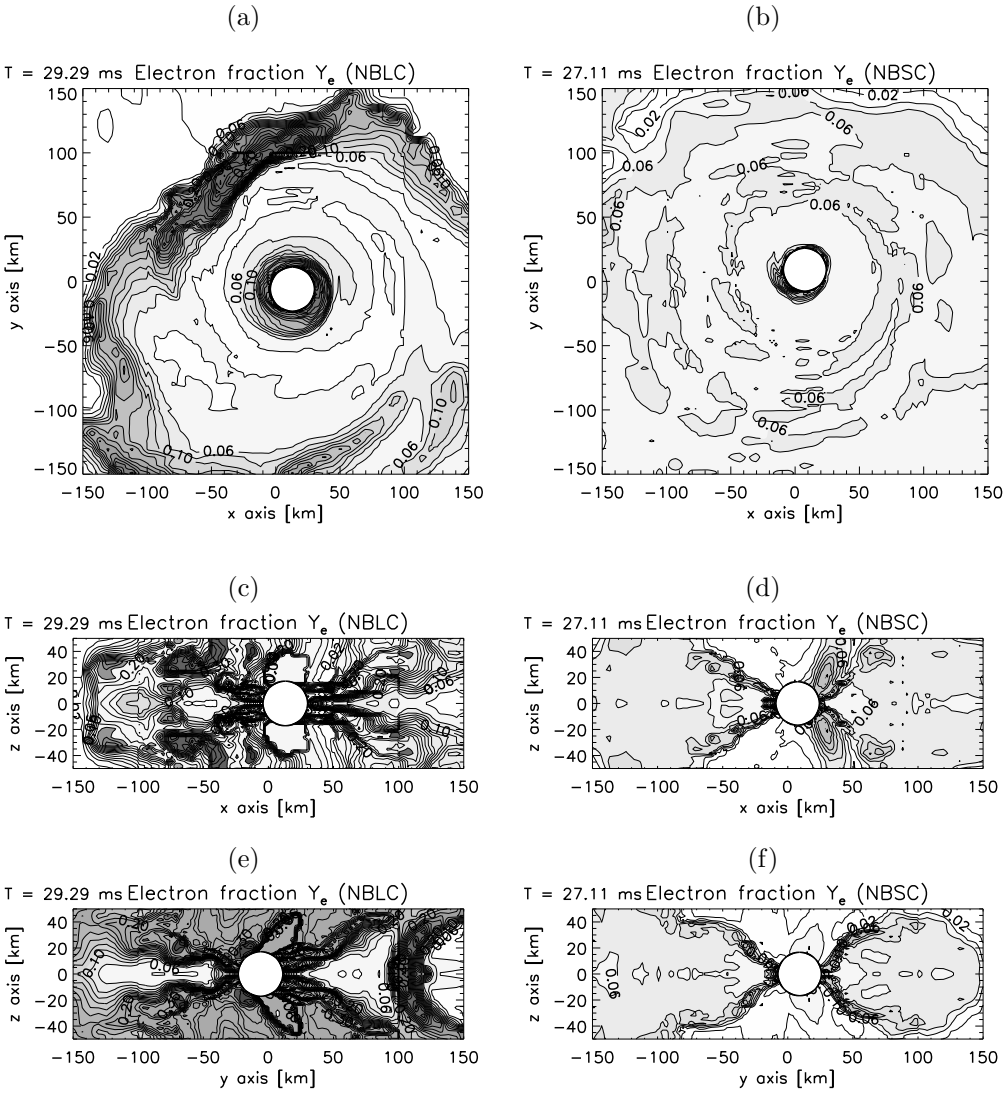

Figure C.14: Electron fraction in the disk, NBLC and NBSC.

Bibliography

Artemova, I. V., Bjoernsson, G., and Novikov, I. D.: 1996, *Astrophys. J.* **461**, 565

Baade, W. and Zwicky, F.: 1934, *Phys. Rev.* **45(2)**, 138

Band, D., Matteson, J., Ford, L., Schaefer, B., Palmer, D., Teegarden, B., Cline, T., Briggs, M., Paciesas, W., Pendleton, G., Fishman, G., Kouveliotou, C., Meegan, C., Wilson, R., and Lestrade, P.: 1993, *Astrophys. J.* **413**, 281

Bell, J., Berger, M., Saltzman, J., and Welcome, M.: 1994, *SIAM Journal on Scientific Computing* **15(1)**, 127

Benz, W.: 1990, in J. R. Buchler (ed.), *Numerical Modelling of Nonlinear Stellar Pulsations Problems and Prospects*, pp 269–+

Berger, M. J. and Colella, P.: 1989, *J. Comp. Phys.* **82**, 64

Birkl, R., Aloy, M. A., Janka, H.-T., and Müller, E.: 2007, *Astron. Astrophys.* **463**, 51

Blanchet, L., Damour, T., and Schäfer, G.: 1990, *Mon. Not. R. Astron. Soc.* **242**, 289

Blandford, R. D. and Znajek, R. L.: 1977, *Mon. Not. R. Astron. Soc.* **179**, 433

Bloom, J. S., Prochaska, J. X., Pooley, D., Blake, C. H., Foley, R. J., Jha, S., Ramirez-Ruiz, E., Granot, J., Filippenko, A. V., Sigurdsson, S., Barth, A. J., Chen, H.-W., Cooper, M. C., Falco, E. E., Gal, R. R., Gerke, B. F., Gladders, M. D., Greene, J. E., Hennanwi, J., Ho, L. C., Hurley, K., Koester, B. P., Li, W., Lubin, L., Newman, J., Perley, D. A., Squires, G. K., and Wood-Vasey, W. M.: 2006, *Astrophys. J.* **638**, 354

Casse, F. and Keppens, R.: 2002, *Astrophys. J.* **581**, 988

Colella, P. and Woodward, P. R.: 1984, *J. Comp. Phys.* **54**, 174

Costa, E., Frontera, F., Heise, J., Feroci, M., in't Zand, J., Fiore, F., Cinti, M. N., Dal Fiume, D., Nicastro, L., Orlandini, M., Palazzi, E., Rapisarda#, M., Zavattini, G., Jager, R., Parmar, A., Owens, A., Molendi, S., Cusumano, G., Maccarone, M. C., Giarrusso, S., Coletta, A., Antonelli, L. A., Giommi, P., Muller, J. M., Piro, L., and Butler, R. C.: 1997, *Nature* **387**, 783

Courant, R. and Friedrichs, K. O.: 1948, *Supersonic Flow and Shock Waves*, Interscience Publishers

Dai, W. and Woodward, P. R.: 1994, *J. Comp. Phys.* **115(2)**, 485

Einfeldt, B.: 1988, *SIAM Journal on Numerical Analysis* **25(2)**, 294

Einfeldt, B., Roe, P. L., Munz, C. D., and Sjogreen, B.: 1991, *J. Comp. Phys.* **92**, 273

Fishman, G. J. and Meegan, C. A.: 1995, *Annu. Rev. Astron. Astrophys.* **33**, 415

Friedel, H.: 1997, *J. Comp. Phys.* **134**, 190

Fryxell, B. A., Müller, E., and Arnett, D.: 1989, *Preprint series of the Max-Plank-Institut für Physik und Astrophysik, Institut für Astrophysik* 449

Gehrels, N., Sarazin, C. L., O'Brien, P. T., Zhang, B., Barbier, L., Barthelmy, S. D., Blustin, A., Burrows, D. N., Cannizzo, J., Cummings, J. R., Goad, M., Holland, S. T., Hurkett, C. P., Kennea, J. A., Levan, A., Markwardt, C. B., Mason, K. O., Meszaros, P., Page, M., Palmer, D. M., Rol, E., Sakamoto, T., Willingale, R., Angelini, L., Beardmore, A., Boyd, P. T., Breeveld, A., Campana, S., Chester, M. M., Chincarini, G., Cominsky, L. R., Cusumano, G., de Pasquale, M., Fenimore, E. E., Giommi, P., Gronwall, C., Grupe, D., Hill, J. E., Hinshaw, D., Hjorth, J., Hullinger, D., Hurley, K. C., Klose, S., Kobayashi, S., Kouveliotou, C., Krimm, H. A., Mangano, V., Marshall, F. E., McGowan, K., Moretti, A., Mushotzky, R. F., Nakazawa, K., Norris, J. P., Nousek, J. A., Osborne, J. P., Page, K., Parsons, A. M., Patel, S., Perri, M., Poole, T., Romano, P., Roming, P. W. A., Rosen, S., Sato, G., Schady, P., Smale, A. P., Sollerman, J., Starling, R., Still, M., Suzuki, M., Tagliaferri, G., Takahashi, T., Tashiro, M., Tueller, J., Wells, A. A., White, N. E., and Wijers, R. A. M. J.: 2005, *Nature* **437**, 851

Godunov, S. K.: 1959, *Mat. Sb. (N.S.)* **47 (89)**, 271

Goedbloed, J. P. H. and Poedts, S.: 2004, *Principles of Magnetohydrodynamics: With Applications to Laboratory and Astrophysical Plasmas*, Cambridge University Press

Grupe, D., Burrows, D. N., Patel, S. K., Kouveliotou, C., Zhang, B., Mészáros, P., Wijers, R. A. M., and Gehrels, N.: 2006, *Astrophys. J.* **653**, 462

Harten, A. and Hyman, J. M.: 1983, *J. Comp. Phys.* **50**, 235

Harten, A., Lax, P. D., and Leer, B. V.: 1983, *SIAM Review* **25(1)**, 35

Hobson, M. P., Efstathiou, G. P., and Lasenby, A. N.: 2006, *General Relativity: An Introduction for Physicists*, Cambridge University Press

Hulse, R. A. and Taylor, J. H.: 1975, *Astrophys. J.* **195**, L51

Janka, H.-T., Eberl, T., Ruffert, M., and Fryer, C. L.: 1999, *Astrophys. J., Lett.* **527**, L39

Keppens, R., Nool, M., Tóth, G., and Goedbloed, J. P.: 2003, *Computer Physics Communications* **153**, 317

Klebesadel, R. W., Strong, I. B., and Olson, R. A.: 1973, *Astrophys. J., Lett.* **182**, L85+

Lattimer, J. M. and Swesty, D. F.: 1991, *Nucl. Phys. A* **535**, 331

Lax, P.: 1973, *Hyperbolic systems of conservation laws and the mathematical theory of shock waves*, Vol. 11 of *CBMS-NSF Regional Conference Series in Applied Mathematics*, Society for Industrial and Applied Mathematics, Philadelphia, U.S.A.

LeVeque, R. J.: 1994, *Numerical Methods for Conservation Laws*, Lectures in Mathematics, Birkhäuser Verlag, 2nd edition

LeVeque, R. J.: 2002, *Finite Volume Methods for Hyperbolic Problems*, Cambridge Texts in Applied Mathematics, Cambridge University Press, 1st edition

LeVeque, R. J., Mihalas, D., Dorfi, E. A., and M uller, E.: 1998, *Computational Methods for Astrophysical Fluid Flow*, Saas Fee Advanced Courses; 27, Springer-Verlag

MacFadyen, A. I. and Woosley, S. E.: 1999, *Astrophys. J.* **524**, 262

Mészáros, P.: 2002, *Annu. Rev. Astron. Astrophys.* **40**, 137

Mészáros, P. and Rees, M. J.: 1992, *Astrophys. J.* **397**, 570

Mészáros, P. and Rees, M. J.: 1997, *Astrophys. J.* **482**, L29

Mignone, A., Bodo, G., Massaglia, S., Matsakos, T., Tesileanu, O., Zanni, C., and Ferrari, A.: 2007, *Astrophys. J., Suppl. Ser.* **170**, 228

Monaghan, J. J.: 1992, *ARA&A* **30**, 543

Oechslin, R. and Janka, T.: 2006, *ArXiv Astrophysics e-prints*

Oppenheimer, J. R. and Volkoff, G. M.: 1939, *Phys. Rev.* **55**, 374

Ostlie, D. A. and Carroll, B. W.: 1996, *An Introduction to Modern Stellar Astrophysics*, Addison-Wesley Publishing Company, Inc.

Paczynski, B.: 1998, *Astrophys. J., Lett.* **494**, L45+

Paczyński, B. and Wiita, P. J.: 1980, *Astron. Astrophys.* **88**, 23

Powell, K. G., Roe, P. L., Linde, T. J., Gombosi, T. I., and de Zeeuw, D. L.: 1999, *J. Comp. Phys.* **154**, 284

Press, W. H., Teukolsky, S. A., Vetterling, W. T., and Flannery, B. P.: 1992, *Numerical recipes in FORTRAN. The art of scientific computing*, Cambridge: University Press, —c1992, 2nd ed.

Price, D. J. and Rosswog, S.: 2006, *Science* **312**, 719

Rasio, F. A. and Shapiro, S. L.: 1994, *Astrophys. J.* **432**, 242

Richtmyer, R. D. and Morton, K. W.: 1957, 1967, 1994, *Difference Methods for Initial-Value Problems*, Krieger Publishing Company, Malabar, Florida, USA, 2nd edition reprinted edition

Roe, P. L.: 1981, *J. Comp. Phys.* **43**, 357

Rosswog, S.: 2005a, *Astrophys. J.* **634**, 1202

Rosswog, S.: 2005b, *ArXiv Astrophysics e-prints*

Rosswog, S. and Davies, M. B.: 2002, *Mon. Not. R. Astron. Soc.* **334**, 481

Rosswog, S. and Price, D.: 2007, *Mon. Not. R. Astron. Soc.* **379**, 915

Ruffert, M.: 1992, *Astron. Astrophys.* **265**, 82

Ruffert, M. and Janka, H.-T.: 2001, *Astron. Astrophys.* **380**, 544

Ruffert, M., Janka, H.-T., and Schäfer, G.: 1996, *Astron. Astrophys.* **311**, 532

Ruffert, M., Janka, H.-T., Takahashi, K., and Schaefer, G.: 1997, *Astron. Astrophys.* **319**, 122

Setiawan, S., Ruffert, M., and Janka, H.-T.: 2004, *Mon. Not. R. Astron. Soc.* **352**, 753

Setiawan, S., Ruffert, M., and Janka, H.-T.: 2006, *Astron. Astrophys.* **458**, 553

Shapiro, S. L. and Teukolsky, S. A.: 1983, *Black Holes, White Dwarfs, and Neutron Stars: The Physics of Compact Objects*, John Wiley & Sons, Inc.

Shen, H., Toki, H., Oyamatsu, K., and Sumiyoshi, K.: 1998a, *Nucl. Phys. A* **637**, 435

Shen, H., Toki, H., Oyamatsu, K., and Sumiyoshi, K.: 1998b, *Prog. Theor. Phys.* **100**, 1013

Soderberg, A. M., Berger, E., Kasliwal, M., Frail, D. A., Price, P. A., Schmidt, B. P., Kulkarni, S. R., Fox, D. B., Cenko, S. B., Gal-Yam, A., Nakar, E., and Roth, K. C.: 2006, *Astrophys. J.* **650**, 261

Strang, G.: 1968, *SIAM Journal on Numerical Analysis* **5(3)**, 506

Toro, E. F.: 1999, *Riemann Solvers and Numerical Methods for Fluid Dynamics*, Springer-Verlag, 2nd edition

Toro, E. F., Spruce, M., and Speares, W.: 1994, *Shock Waves* **4**, 25

Tóth, G. and Odstrčil, D.: 1996, *J. Comp. Phys.* **128**, 82

van Leer, B.: 1977, *J. Comp. Phys.* **23**, 276

van Leer, B.: 1979, *J. Comp. Phys.* **32**, 101

Wesenberg, M.: 2003, *Ph.D. thesis*, Fakultät für Mathematik und Physik der Albert-Ludwigs-Universität Freiburg im Breisgau

Wheeler, J. A.: 1968, *American Scientist* **56**, 1

White, L. and Adcroft, A.: 2008, *Journal of Computational Physics* **227**, 7394

Woodward, P. and Colella, P.: 1984, *J. Comp. Phys.* **54**, 115

Woosley, S. E.: 1993, *Astrophys. J.* **405**, 273

Ziegler, U.: 1999, *Computer Physics Communications* **116**, 65